

A Micro to Macro Evaluation of Evaporation Considering the Pore-Scale Mechanisms through Unsaturated Soil Profiles

ジュマナ ジ エヌ フサリ

<https://hdl.handle.net/2324/7157340>

出版情報 : Kyushu University, 2023, 博士 (工学) , 課程博士
バージョン :
権利関係 :



**A M I C R O T O M A C R O
EVALUATION OF EVAPORATION CONSIDERING
THE PORE-SCALE MECHANISMS THROUGH
UNSATURATED SOIL PROFILES**

JUMANA G. N. HUSSARY

SEPTEMBER 2023

**A M I C R O T O M A C R O
EVALUATION OF EVAPORATION CONSIDERING
THE PORE-SCALE MECHANISMS THROUGH
UNSATURATED SOIL PROFILES**



**A THESIS SUBMITTED
IN PARTIAL FULFILLMENT OF THE REQUIREMENTS
FOR THE DEGREE OF
DOCTOR OF ENGINEERING**

BY

JUMANA G. N. HUSSARY

TO THE

**DEPARTMENT OF CIVIL ENGINEERING
GRADUATE SCHOOL OF ENGINEERING
KYUSHU UNIVERSITY
FUKUOKA, JAPAN**

2023

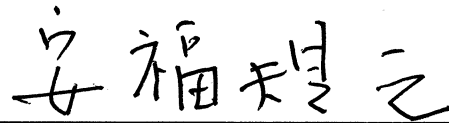
GEOTECHNICAL ENGINEERING LABORATORY
DEPARTMENT OF CIVIL ENGINEERING
GRADUATE SCHOOL OF ENGINEERING
KYUSHU UNIVERSITY
FUKUOKA, JAPAN

CERTIFICATE

*The undersigned hereby certify that they have read and recommended to the Graduate School of Engineering for the acceptance of this dissertation entitled, “**A MICRO TO MACRO EVALUATION OF EVAPORATION CONSIDERING THE PORE-SCALE MECHANISMS THROUGH UNSATURATED SOIL PROFILES**” by **JUMANA G. N. HUSSARY** in partial fulfillment of the requirements for the degree of **DOCTOR OF ENGINEERING**.*

Dated: July 2023

Supervisor:



Professor Noriyuki YASUFUKU, Dr. Eng.

Examining Committee:



Professor Shinichiro YANO, Dr. Eng.



Professor Kiyonobu KASAMA, Dr. Eng.

Dedication

To my beloved parents

George and Manal Hussary

For their endless love, support and encouragement

To my five Siblings

Areej, Naseef, Nour, Nadi and Amin Hussary

To my family and friends

Acknowledgment

First and foremost, I would like to express my sincere gratitude and appreciation to my supervisor, Professor Noriyuki Yasufuku, for his support and guidance throughout my Doctoral course. His motivation, enthusiasm, encouragement, and immense knowledge enriched my experience. I would like to thank Associate Professor Ryohei Ishikura, Geotechnical Engineering Laboratory, Kyushu University, for his unwavering support and contribution to this research. I would like to extend my heartfelt thanks to Assistant Professor Adel Alowaisy, Geotechnical Engineering Laboratory, Kyushu University, for his significant assistance at every stage of this research project. His invaluable advice, encouragement, and patience during my research has greatly improved the content and outcome of this study. Special gratitude to the examining committee, Professor Shinichiro Yano, and Professor Kiyonobu Kasama. Their time and effort are highly appreciated.

I am forever indebted to my parents for their continuous and unparalleled love, help, and support. I sincerely thank my family, my sister RPh. Areej Hussary, and her husband Adv. Saleem Hinnawi, my brothers, grandparents, aunts and their families, uncle Haitham, my cousins and friends. Their belief in me has kept my spirit and motivation high during this process. I am deeply grateful to my uncle Doctor Nakhleh Hussary for being a true source of inspiration in my career path. I would like to thank Associate Professor Monther Abdelhadi, Dean of the Faculty of Engineering, American University of Madaba, for his advice and encouragement since day one of this long journey and for contributing and believing in this project.

I would like to acknowledge the crucial role of the technical staff in the Geotechnical Engineering Laboratory, Mrs. Aki Ito and Mr. Michio Nakashima, for their great assistance and technical support in the laboratory. Additionally, I would like to thank Mrs. Yasura Oiwa for her help in many personal and professional situations. My heartfelt thanks to my research colleagues and friends for filling my life with love and care. Finally, thanks to the MEXT Scholarship and Kyushu University for the great opportunity and valuable experience in Japan.

Abstract

Climate change has become a global concern over the past decades. From global warming to shifting weather patterns, the impacts of climate change are global in scope and unprecedented in scale. Drylands worldwide cover around 46.5% of the global land area and are home to around 38.6% of its population. Besides the hot and dry conditions, the global warming ramifications, such as the increased drought frequency, extensive water evaporation, and precipitation deficit, are causing a reduction in soil moisture availability, water scarcity, and land degradation in such regions. All these factors are exacerbating the desertification phenomenon where over the past several decades, it has extended to about 9.4% of drylands, affecting more than 500 million people, most of whom are in developing countries. Therefore, providing simple and economical technologies is essential to mitigate soil degradation and combat desertification.

Ground surface boundary fluxes and water movement through unsaturated soils are critical for many engineering and water management applications. Despite the proposed methods to predict and control such fluxes in the literature, solving unsaturated soils related issues requires developing more comprehensive and easily applied models. Generally, the upward evaporation flux from soil profiles is dominant in drylands. It is a complex multiphase pore-scale process involving coupled heat-mass transfer, liquid-gas phase change, and liquid-vapor transport through its pores. From bare soil profiles, evaporation is a function of the surface's atmospheric demand and the soil's ability to supply water, which depends on soil pore properties. Most existing research tackles the evaporation process from a phenomenological point of view. It is usually considered a boundary flux where the mechanisms occurring at the pore level are neglected due to the lack of suitable techniques. Moreover, previous evaporation estimation models usually consider complicated parameters to estimate the evaporation rate. However, for a complete description of the evaporation process and an accurate evaluation of its rate, the atmospheric demand should be solved in conjugation with the water supply and considering its mechanisms through unsaturated soils based on a simplified parameter.

This thesis investigates and evaluates the evaporation process from unsaturated soils by tackling the evolving micro-mechanisms occurring at the soil pore level and reflecting them

on the macroscale behavior of evaporation. Moreover, it considers developing natural soil covers to control and suppress evaporation from bare soil profiles in drylands as a step toward combating desertification. Four objectives are drawn to satisfy the goals of the thesis. It starts with the parameterization of the soil pore structure through an experimental approach and investigates its influence on evaporation behavior. Secondly, experimental visualization of the formation and development of the unsaturated soil layer and its boundaries during evaporation and investigation of their role in the process. Thirdly, to formulate an empirical and theoretical framework for accurately estimating the evaporation rate based on the soil pore structure parametrization and the visualization of the unsaturated layer dynamics. Finally, optimization of a conceptual framework for a natural soil cover that suppresses evaporation and maximizes water retention in drylands by identifying the role of the relative soil properties between the natural ground and the applied soil cover.

At the beginning of the thesis, a thorough background related to the desertification phenomenon was presented. The scientific understanding of climatic changes and how they exacerbate desertification was discussed. The global warming ramifications and its threat to humanity and the ecosystem were reviewed. Moreover, recent facts and statistics on drylands were discussed, and the necessity to combat desertification and the vital role and need to accurately evaluate the ground surface boundary fluxes, mainly the dominant evaporation flux, for many engineering applications, were highlighted. An inclusive literature review of the current research scopes and related objectives was presented. It presents an inclusive view of the potential and actual evaporation fluxes and their micro and macroscale definitions. The most used models and methods to evaluate the evaporation rates in practice were discussed. The influencing factors of the actual evaporation behavior were delineated, while the importance of bridging the atmospheric demand and water supply through the soil profile was reviewed. Moreover, the latest methods used to suppress water evaporation from soil profiles were explained.

The influence of the soil pore structure on evaporation behavior was investigated through experimental testing. Consequently, a comprehensive and robust index that reflects the pore structure variations and considers the factors affecting the capillary and diffusion flow was proposed. The Pore Size Distribution Index (I_{PSD}) correlated well with the duration and evaporated water during Stages 1 and 2. Moreover, the influence of the pore structure was investigated where generally, it was found that sandy soils with larger I_{PSD} exhibit longer stages resulting in more water losses. The proposed index is systematically determined using only the

soil retention properties, specifically the Soil Water Characteristics Curve (SWCC). The proposed index was utilized to propose an actual evaporation estimation model. Moreover, it is expected to be a fundamental parameter in water movement and solute transport through unsaturated soil profiles.

A novel and effective image analysis-based technique was developed. The experimental technique is confirmed to be a reliable and definitive tool in tracing the development of the unsaturated layer during drying soil column tests. The setup included an image acquisition unit comprised of a digital camera and a lighting setup to capture high-quality images remotely. Additionally, two-reference soil columns are set up next to the primary tested soil column to calibrate the color changes in the primary column and allow the detection of the saturated, unsaturated, and dry zones within the profile. Finally, image processing operations are applied to accurately and directly detect the zones' boundaries, the drying front, and the vaporization plane.

Using the image analysis-based technique, the dynamics of the drying front, vaporization plane, and the film region, where capillary water flow is dominant, were studied, and new insights regarding their significant contribution to the evaporation process were concluded. It was found that the drying front tends to recede faster during Stage 1, with a slight reduction in its rate with each consecutive stage. The unsaturated layer thickness is maintained during Stage 2, where water mainly gets lost from the smaller embedded pores rather than the large pores at the drying front, where water is lost gradually from the vaporization plane, causing an increase in the air-dry layer thickness and the length of the diffusion pathways to the surface. The vaporization plane forms instantly at the onset of Stage 2, followed by a sudden increase in its depth at the onset of Stage 3, which explains the inflection points of the actual evaporation curve at the onset of Stages 2 and 3. The sharper reduction at the onset of Stage 2 is associated with the change of the mechanism from capillary during Stage 1 to vapor diffusion during Stage 2.

Consequently, a strong correlation was found between the vaporization plane receding rate and the pore structure presented by the newly proposed I_{PSD} . Generally, soil profiles with a broader pore size distribution, characterized by bigger I_{PSD} , tend to have a slower receding rate of the vaporization plane during Stage 2. Accordingly, a robust empirical formula was derived for homogenous sandy soil profiles under unified atmospheric conditions to predict the receding rate of the vaporization plane. Based on the empirical formula and by solving Fick's law of diffusion, a semi-empirical actual evaporation rate estimation model from homogeneous

soil profiles was proposed. The simple pore-scale-based estimation model is reliable in predicting the normalized evaporation rate. It considers the evaporation process's internal and external influencing factors: the atmospheric demand and water supply capabilities. It is simple, reliable, and expected to be utilized efficiently for many engineering applications.

Finally, a novel design concept for an environmental-friendly natural soil cover was proposed to suppress evaporation rates and increase water storage in soil profiles. The simple concept considers the micro-mechanisms and dynamics occurring during evaporation between the soil cover, natural ground, and the textural contrast boundary between them. It comprises two design criteria; the relative soil properties (C1) and the relative cover thickness (C2). C1 is deduced from the retention properties of both soils, while C2 considers the drying front during the sufficient capillary supply and its relation to the textural contrast boundary. It was found that the most effective design of the natural soil cover can be achieved by applying a proper cover material over the natural ground that keeps C1 and C2 smaller than 1. The proposed design concept is a simple, economical, and environmental-friendly solution to combat desertification in many arid and semi-arid regions and developing countries.

Table of Contents

DEDICATION	V
ACKNOWLEDGMENT	VII
ABSTRACT	IX
TABLE OF CONTENTS	XIII
LIST OF FIGURES	XVII
LIST OF TABLES	XXIII
CHAPTER 1: INTRODUCTION	1
1.1 CLIMATE CHANGE AND GLOBAL WARMING RAMIFICATIONS	2
1.1.1 GLOBAL WARMING AND RISING TEMPERATURE	2
1.1.2 EXTENSIVE EVAPOTRANSPIRATION AND PRECIPITATION DEFICIT	5
1.1.3 WATER SCARCITY AND LIMITED SOIL MOISTURE	6
1.1.4 DROUGHTS	8
1.2 DRYLANDS AND DESERTIFICATION	9
1.2.1 DRYLANDS	9
1.2.2 LAND DEGRADATION AND DESERTIFICATION	11
1.2.3 COMBATING DESERTIFICATION	13
1.3 GROUND SURFACE BOUNDARY FLUXES AND WATER FLOW THROUGH SOIL PROFILES	14
1.4 RESEARCH OBJECTIVES	17
1.5 THESIS FRAMEWORK AND OUTLINES	18
REFERENCES	21
CHAPTER 2: LITERATURE REVIEW	23
2.1 WATER BALANCE AT THE GROUND SURFACE AND EVAPORATION FLUXES	24

2.2	POTENTIAL EVAPORATION FLUX	25
2.2.1	DEFINITION OF THE POTENTIAL EVAPORATION	25
2.2.2	DIRECT MEASUREMENTS OF POTENTIAL EVAPORATION	26
2.2.3	DETERMINATION METHODS OF THE POTENTIAL EVAPORATION	28
2.3	ACTUAL EVAPORATION FLUX	32
2.3.1	ACTUAL EVAPORATION PROCESS AND ITS STAGES	32
2.3.2	FACTORS INFLUENCING THE ACTUAL EVAPORATION BEHAVIOR	42
2.3.3	DIRECT MEASUREMENT OF THE ACTUAL EVAPORATION	44
2.3.4	DETERMINATION METHODS OF THE ACTUAL EVAPORATION	50
2.4	SUPPRESSING EVAPORATION AND MAXIMIZING WATER RETENTION IN SOIL PROFILES	57
2.5	RESEARCH ORIGINAL CONTRIBUTIONS RELATIVE TO THE LITERATURE	59
	REFERENCES	60

CHAPTER 3: PORE STRUCTURE PARAMETERIZATION AND ITS INFLUENCE ON EVAPORATION FROM HOMOGENEOUS SOIL PROFILES

3.1	INTRODUCTION	69
3.2	MATERIALS	70
3.3	METHODOLOGY AND EXPERIMENTAL CONSIDERATIONS	75
3.3.1	EXPERIMENTAL SETUP	75
3.3.2	SOIL COLUMN PREPARATION	79
3.3.3	TESTING PROCEDURE AND BOUNDARY CONDITIONS	81
3.4	ACTUAL EVAPORATION AND ITS STAGES	82
3.4.1	INFLUENCE OF SOIL TEXTURE	84
3.4.2	INFLUENCE OF RELATIVE DENSITY	86
3.5	WATER REDISTRIBUTION AND UNSATURATED LAYER FORMATION	87
3.5.1	INFLUENCE OF SOIL TEXTURE	87
3.5.2	INFLUENCE OF RELATIVE DENSITY	93
3.6	SIGNIFICANCE OF THE FALLING RATE STAGE (STAGE 2)	94
3.7	PORE STRUCTURE AND EVAPORATION STAGES	97
3.7.1	PORE STRUCTURE AND PORE SIZE DISTRIBUTION	98
3.7.2	PORE SIZE DISTRIBUTION INDEX (I_{psd})	101
3.7.3	PORE SIZE DISTRIBUTION INDEX AND EVAPORATION STAGES	104
3.8	SUMMARY AND CONCLUSIONS	106
	REFERENCES	107

**CHAPTER 4: VISUALIZATION OF THE UNSATURATED SOIL LAYER USING A NOVEL
IMAGE ANALYSIS-BASED TECHNIQUE**

109

4.1	INTRODUCTION	109
4.2	MATERIALS	110
4.3	METHODOLOGY AND EXPERIMENTAL SETUP DEVELOPMENT	112
4.3.1	EVAPORATION TESTING UNIT AND PREPARATION	116
4.3.2	IMAGE ACQUISITION UNIT	118
4.3.3	TESTING PROCEDURE AND BOUNDARY CONDITIONS	120
4.4	IMAGE ANALYSIS-BASED TECHNIQUE	120
4.4.1	IMAGE PROCESSING	120
4.4.2	EXTRACTING INFORMATION FROM PROCESSED IMAGES	124
4.5	RELIABILITY AND ACCURACY OF THE IMAGE ANALYSIS-BASED TECHNIQUE	126
4.6	DRYING FRONT DYNAMICS	131
4.6.1	SPATIAL DEVELOPMENT OF THE DRYING FRONT	131
4.6.2	GEOMETRY AND TEMPORAL DEVELOPMENT OF THE DRYING FRONT	131
4.7	VAPORIZATION PLANE DYNAMICS	133
4.7.1	SPATIAL DEVELOPMENT OF THE VAPORIZATION PLANE	133
4.7.2	GEOMETRY AND TEMPORAL DEVELOPMENT OF THE VAPORIZATION PLANE	134
4.8	FILM REGION DYNAMICS	135
4.9	SUMMARY AND CONCLUSIONS	137
	REFERENCES	138

**CHAPTER 5: PORE-SCALE-BASED ESTIMATION MODEL OF THE ACTUAL
EVAPORATION**

139

5.1	INTRODUCTION	139
5.2	THEORETICAL CONSIDERATIONS	140
5.2.1	STAGE 1: CAPILLARY LIQUID FLOW AND THE CHARACTERISTIC LENGTH	140
5.2.2	STAGE 2: VAPOR DIFFUSION FROM A RECEDING VAPORIZATION PLANE	143
5.3	DERIVATION OF THE SEMI-EMPIRICAL EVAPORATION MODEL	144
5.3.1	MODEL ASSUMPTIONS	144
5.3.2	FICK'S LAW OF DIFFUSION TO ESTIMATE THE ACTUAL EVAPORATION REDUCTION RATE DURING STAGE 2	145
5.3.3	EMPIRICAL CORRELATION OF THE VAPORIZATION PLANE RECEDING RATE AND PORE SIZE DISTRIBUTION INDEX	147
5.3.4	ESTIMATION OF THE NORMALIZED ACTUAL EVAPORATION CURVE	150

5.4	RELIABILITY AND LIMITATIONS OF THE PORE-SCALE-BASED EVAPORATION MODEL	151
5.5	SUMMARY AND CONCLUSIONS	156
	REFERENCES	157

CHAPTER 6: OPTIMIZATION OF A SOIL COVER DESIGN TO SUPPRESS EVAPORATION	159
---	------------

6.1	INTRODUCTION	159
6.2	EVAPORATION FROM DOUBLE-LAYERED SOIL PROFILES	161
6.3	SOIL COVER CONCEPT AND DESIGN CRITERIA	162
6.3.1	RELATIVE RETENTION PROPERTIES	165
6.3.2	RELATIVE COVER THICKNESS	166
6.3.3	SOIL COVER DESIGN AND ITS EMPLOYMENT	167
6.4	MATERIALS AND SOIL PROFILES CONFIGURATIONS	168
6.5	METHODOLOGY AND EXPERIMENTAL CONSIDERATIONS	170
6.5.1	EXPERIMENTAL SETUP	170
6.5.2	SOIL COLUMNS PREPARATION	174
6.5.3	TESTING PROCEDURE AND BOUNDARY CONDITIONS	175
6.6	VALIDATION OF THE SOIL COVER EFFICIENCY	177
6.6.1	SOIL COVER AND ACTUAL EVAPORATION STAGES	177
6.6.2	SOIL COVER AND WATER REDISTRIBUTION	178
6.6.3	SOIL COVER DESIGN CONCEPT AND ITS EFFICIENCY	182
6.7	SUMMARY AND CONCLUSIONS	183
	REFERENCES	184

CHAPTER 7: SUMMARY AND CONCLUSIONS	187
---	------------

7.1	RESEARCH ACHIEVED OBJECTIVES	187
7.2	CONCLUSIONS	188
7.3	FUTURE WORK	190

GLOSSARY AND PARAMETER NOTATION	- 1 -
--	--------------

List of Figures

Number	Title	Page
Figure 1.1	Global emissions of greenhouse gases.	2
Figure 1.2	Global land average temperature anomalies.	3
Figure 1.3	Global average Earth's surface temperature anomalies (with respect to a 1991-2020 period)	4
Figure 1.4	Global average Earth's surface temperature percentiles in 2022.	4
Figure 1.5	Global land average precipitation anomalies.	5
Figure 1.6	Global average annual precipitation from 1960-1990.	6
Figure 1.7	Global average Earth's surface precipitation percentiles in 2022.	7
Figure 1.8	Global average annual evapotranspiration from 1970-2000	7
Figure 1.9	Global projected water scarcity in 2025.	8
Figure 1.10	Global drought-vulnerability index in 2022.	10
Figure 1.11	Global geographical distribution of drylands.	10
Figure 1.12	Current and projected population in drylands.	11
Figure 1.13	Global desertification-vulnerability level based on a reclassification of the global soil climate map and global soil map.	12
Figure 1.14	Categorized problems that require proper determination of boundary fluxes and water flow through soil profiles.	15
Figure 1.15	Research objectives.	17

Figure 1.16	Thesis framework and organization.	20
Figure 2.1	Water fluxes at the ground surface.	23
Figure 2.2	Atmometer device.	27
Figure 2.3	Standard U.S. Weather Bureau ‘Class A’ evaporation pan.	28
Figure 2.4	Actual evaporation stages and corresponding air-water phase distribution.	34
Figure 2.5	Actual evaporation stages and unsaturated layer configuration.	36
Figure 2.6	L_C and Stage 1 conceptualization: (a) simplified hydraulically interacting pair of capillaries. (b) homogeneous soil profile.	38
Figure 2.7	Typical initial drying and main wetting SWCCs.	39
Figure 2.8	Linearization of the drying SWCC to determine L_C .	39
Figure 2.9	Determination of L_{Comp} for double-layered soil profiles.	40
Figure 2.10	Schematic diagram of a soil saturation profile during Stage 2.	41
Figure 2.11	Weighing lysimeter test.	46
Figure 2.12	Thin soil section drying test.	47
Figure 2.13	Drying soil column test.	48
Figure 2.14	Resistances associated with evaporation when the top soil layer is (a) moist and (b) dry.	54
Figure 3.1	Particle size distribution curves.	72
Figure 3.2	Drying soil water characteristic curves.	74
Figure 3.3	Hydraulic conductivity functions.	75
Figure 3.4	Experimental setup of the drying soil column test.	76-77
Figure 3.5	Drying soil column preparation and compaction method.	80

Figure 3.6	Average atmospheric conditions of the tested profiles.	82
Figure 3.7	Fluctuations of the atmospheric conditions during testing the K-7 profile.	83
Figure 3.8	Normalized actual evaporation curves – Influence of soil texture.	84
Figure 3.9	Normalized actual evaporation reduction rate during Stage 2.	85
Figure 3.10	Normalized actual evaporation curves – Influence of relative density.	86
Figure 3.11	Cumulative evaporated water mass – Influence of soil texture.	88
Figure 3.12	Water redistribution profiles during evaporation - Influence of soil texture.	89
Figure 3.13	Relationship between the normalized actual evaporation reduction rate and vaporization plane during Stage 2.	92
Figure 3.14	Cumulative evaporated water mass – Influence of relative density.	94
Figure 3.15	Water redistribution profiles during evaporation - Influence of relative density.	95
Figure 3.16	Significance of Stage 2.	96
Figure 3.17	Pore size distribution curves and lognormal distribution fitting.	101
Figure 3.18	Pore Size Distribution Index (I_{PSD}) determination process. [Flowchart]	103
Figure 3.19	Pore Size Distribution Index (I_{PSD}) and evaporation stages.	104
Figure 4.1	Particle size distribution curves.	112
Figure 4.2	Drying soil water characteristic curves.	112
Figure 4.3	Hydraulic conductivity functions.	113
Figure 4.4	Pore size distribution curves and lognormal distribution fitting.	113
Figure 4.5	Developed experimental setup and image acquisition.	114-115
Figure 4.6	Brilliant blue dye tracer and its specifications.	117

Figure 4.7	Evaporation testing unit. [Picture]	118
Figure 4.8	Two-point lighting setup.	119
Figure 4.9	Average atmospheric conditions of the tested profiles.	121
Figure 4.10	Image processing. [Flowchart]	122
Figure 4.11	Extracting information from the processed images (a) grayscale processed image. (b) corresponding contouring plot.	124
Figure 4.12	K-6 soil profile (a) Processed images. (b) Corresponding water redistribution.	127
Figure 4.13	K-4 soil profile (a) Processed images. (b) Corresponding water redistribution.	128
Figure 4.14	K-3.5 soil profile (a) Processed images. (b) Corresponding water redistribution.	129
Figure 4.15	Geometry and temporal development of the drying front.	132
Figure 4.16	Geometry and temporal development of the vaporization plane.	134
Figure 4.17	Film region dynamics.	136
Figure 5.1	Normalized actual evaporation curves – Influence of the atmospheric demand.	142
Figure 5.2	Evaporation depth during drying.	142
Figure 5.3	Fick's law of diffusion during Stage 2.	146
Figure 5.4	Saturation profiles of the soil columns.	148
Figure 5.5	Vaporization plane receding rate and I_{PSD} relationship.	149
Figure 5.6	Empirical determination of the inverse of the vaporization plane receding rate based on I_{PSD} .	150
Figure 5.7	Estimation of the normalized actual evaporation curve using the semi-empirical evaporation model.	151
Figure 5.8	Pore-scale-based estimation model of the actual evaporation. [Flowchart]	152
Figure 5.9	Comparison between the estimated and experimental $\Delta NAE/\Delta t$ of Stage 2.	153

Figure 5.10	Reliability of the pore-scale-based actual evaporation estimation model.	155
Figure 6.1	Principle of soil covers and their practical application.	163
Figure 6.2	Influence of the soil cover on cumulative water losses.	164
Figure 6.3	Relative retention properties, C1 criterion of the soil cover design.	165
Figure 6.4	Relative cover thickness, C2 criterion of the soil cover design.	167
Figure 6.5	The proposed soil cover design concept.	168
Figure 6.6	Particle size distribution curves.	169
Figure 6.7	Drying soil water characteristic curves.	169
Figure 6.8	Soil cover design concept and the tested double-layered soil profiles.	170
Figure 6.9	Experimental setup of the double-layered drying soil column tests.	172-173
Figure 6.10	Preparation of the double-layered drying soil columns.	175
Figure 6.11	Average atmospheric conditions of the double-layered tested groups.	176
Figure 6.12	Normalized actual evaporation curves of the double-layered tested groups: a) fine-overlying-coarse. b) coarse-overlying-fine.	178
Figure 6.13	Water redistribution profiles of the double-layered tested groups during evaporation.	180
Figure 6.14	Suction profiles of the double-layered tested groups during evaporation.	181
Figure 6.15	Efficiency of the proposed soil cover design concept.	182

List of Tables

Number	Title	Page
Table 2.1	Determination methods of the potential evaporation	29-30
Table 2.2	Soil-atmosphere boundary models for the determination of the actual evaporation	52
Table 2.3	Surface-resistance-based methods for the determination of the actual evaporation	55
Table 3.1	Soil profiles' physical and hydrological properties	73
Table 3.2	Soil profiles' pore structure parameters and Pore Size Distribution Index (I_{PSD})	105
Table 4.1	Soil profiles' physical and hydrological properties	111
Table 6.1	Double-layered soil profile's physical and hydrological properties.	171

1

Introduction

CHAPTER

Climate change has become a global concern over the past decades. It is the defining environmental issue of the 21st century. From shifting weather patterns to the increase of seawater levels, the impacts of climate change are global in scope and unprecedented in scale. Climate change is the significant and lasting changes in Earth's environmental conditions over time. Changes happen due to many internal and external factors, including natural and various human activities. The Earth's climate had constantly changed even long before humans became involved. However, investigations have observed unusual changes recently.

Global warming is an example; the Earth's average temperature is increasing faster than ever during human history. Scientists are confident that human activities are leading to this phenomenon. The extensive and expansive releases of greenhouse gases, Figure 1.1, have changed the Earth's atmosphere making it better at trapping Sun's heat. Therefore, exacerbating the greenhouse effect and consequently increasing the temperature. The consequences of climate change are broad and differ from region to region. Some areas face increasing droughts and heat waves, which lead to land degradation and water scarcity. Due to the extensive water

evaporation, others suffered from intense storms and increased torrential rainfall events, which drive flooding and land erosion. All those impacts and others have critical consequences on plants, animals, human life, and development.

This chapter reviews the scientific understanding of the primary climatic changes that have led many worldwide lands to degrade and their soils to lose productivity. It presents facts and statistics about drylands and the efforts to combat desertification. Besides, the importance of evaluating the soil boundary fluxes and water flow in unsaturated soils to find innovative solutions is discussed. Finally, the current research objectives and the thesis framework are addressed.

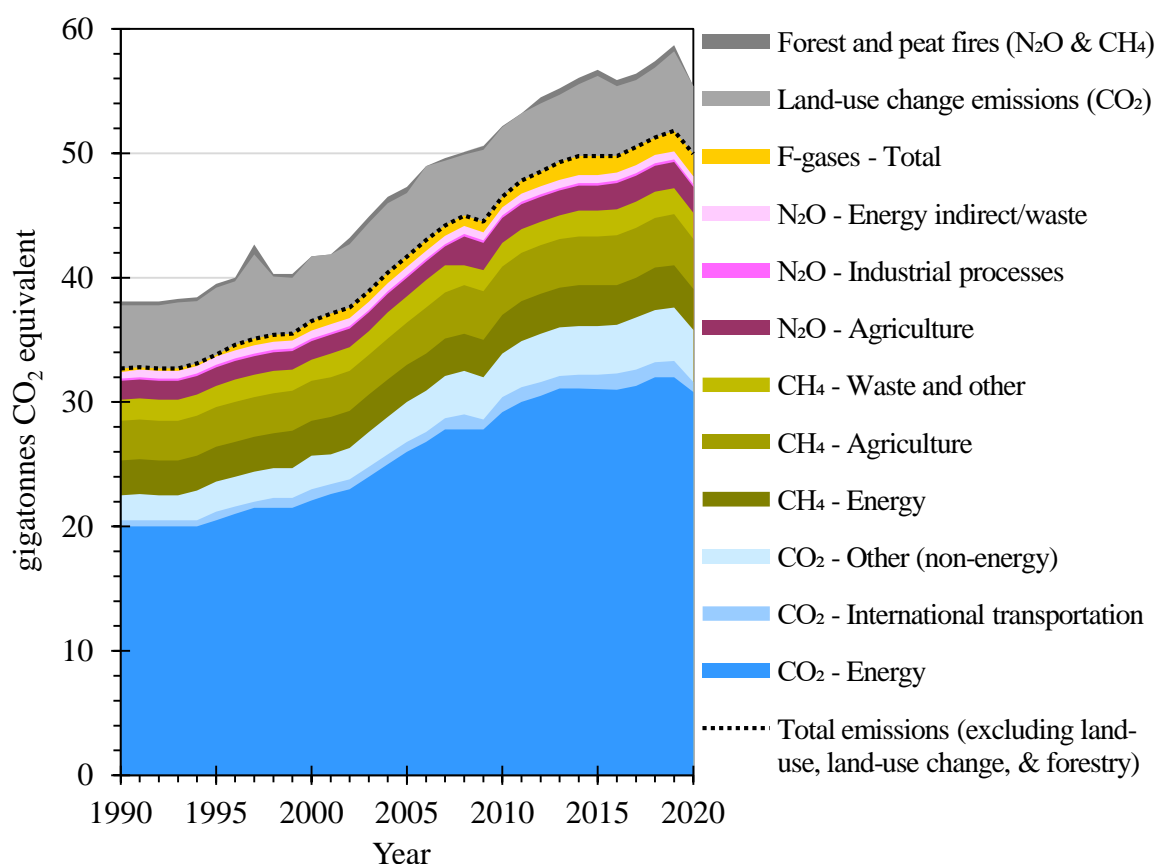


Figure 1.1: Global emissions of the greenhouse gases. (Olivier et al., 2017)

1.1 Climate Change and Global Warming Ramifications

1.1.1 Global warming and rising temperature

A special report by the Intergovernmental Panel on Climate Change (IPCC, 2019) stated that since the pre-industrial period (1850-1900), the land surface air temperature had risen nearly twice the global average temperature. Figure 1.2 delineates the global land average temperature

changes from 1850 to 2022. The data was adopted from Berkeley Earth, the National Aeronautics and Space Administration (NASA), and National Oceanic and Atmospheric Administration (NOAA), where the average was determined relative to different time series, as indicated in the legend. These groups produce a similar understanding of recent global warming patterns, where the average temperature in 2022 is estimated to be around $1.24 \pm 0.3^\circ\text{C}$ above the average temperature from 1850-1900, making it the fifth warmest year in the past century (Berkeley Earth). The world map in Figure 1.3 shows how Earth's surface temperature, including land and ocean, has increased relative to the average temperature in 1991-2000. It can be observed that the temperature rises broadly distributed over the globe, affecting nearly all land and ocean. According to Berkeley Earth's annual report, 88% of the Earth's surface was significantly warmer than average, 7% was of a similar temperature, and only 5% was considerably colder (Berkeley Earth). Based on the map in Figure 1.4, it was concluded that around 8.5% of the Earth's surface set a new warmest record annual average, while no places recorded the coolest average. Scientists expect global temperatures to continue to rise from 1.5 to 2°C , relative to the average from 1850 to 1900, towards the end of the century if no concrete actions are considered (IPCC, 2013).

Global warming ramifications are being felt everywhere. It has disrupted the natural water cycle and led to climate zone shifts in many world regions, causing an expansion of arid climate zones and a contraction of polar climate zones. It has increased the frequency, intensity, and duration of heat waves and droughts. In many areas, the increased land temperature and

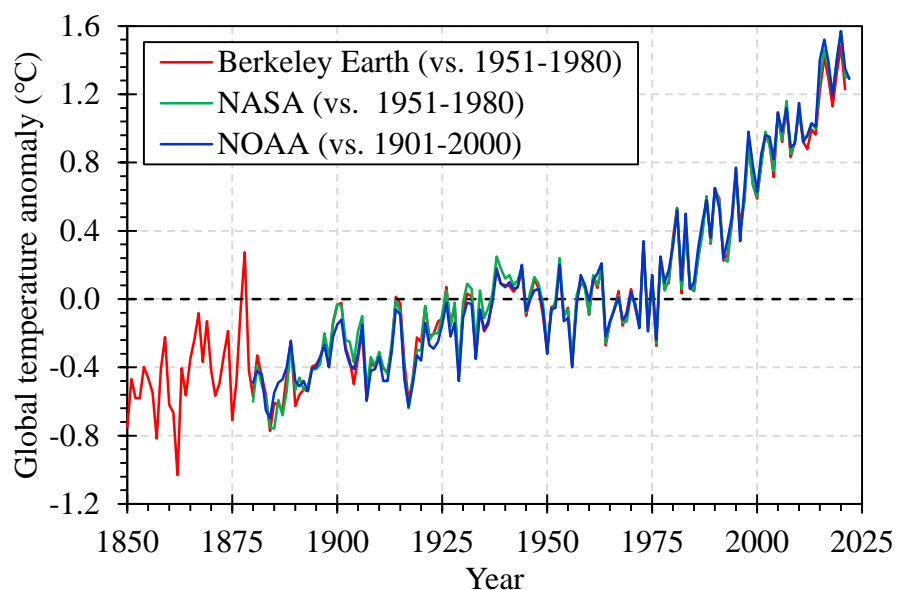


Figure 1.2: Global land average temperature anomalies.

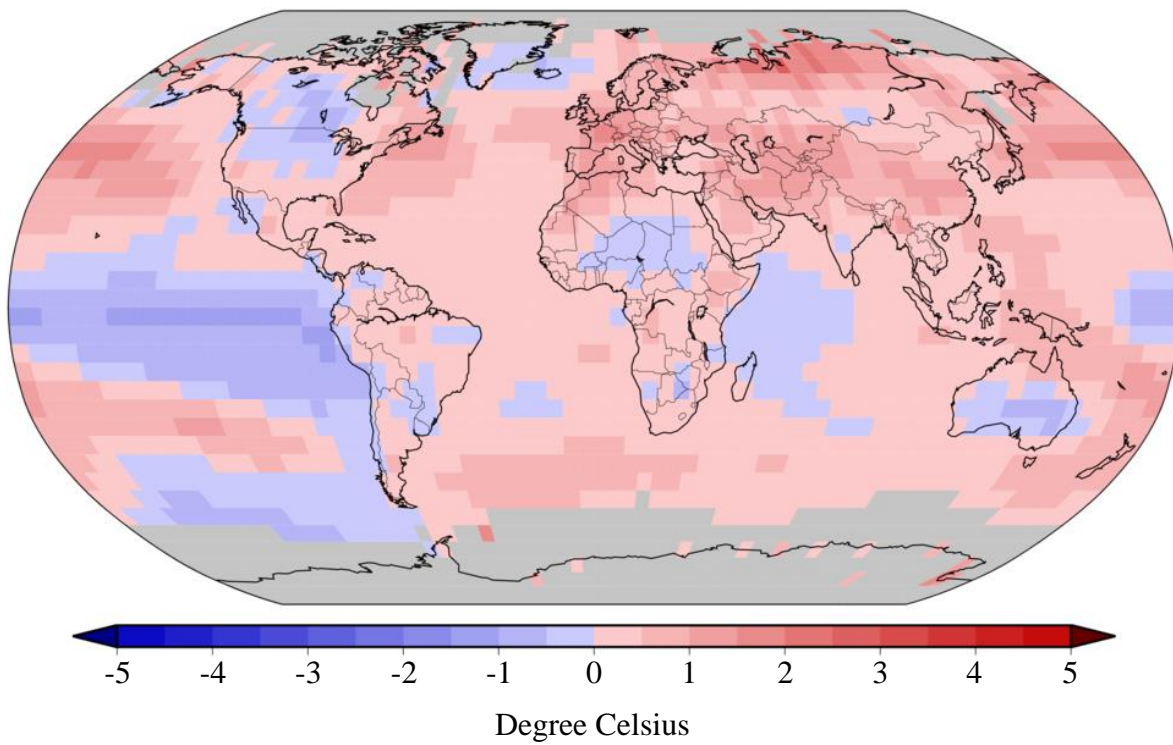


Figure 1.3: Global average Earth's surface temperature anomalies.
 (with respect to a 1991-2020 period)
 [National Centers for Environmental Information]

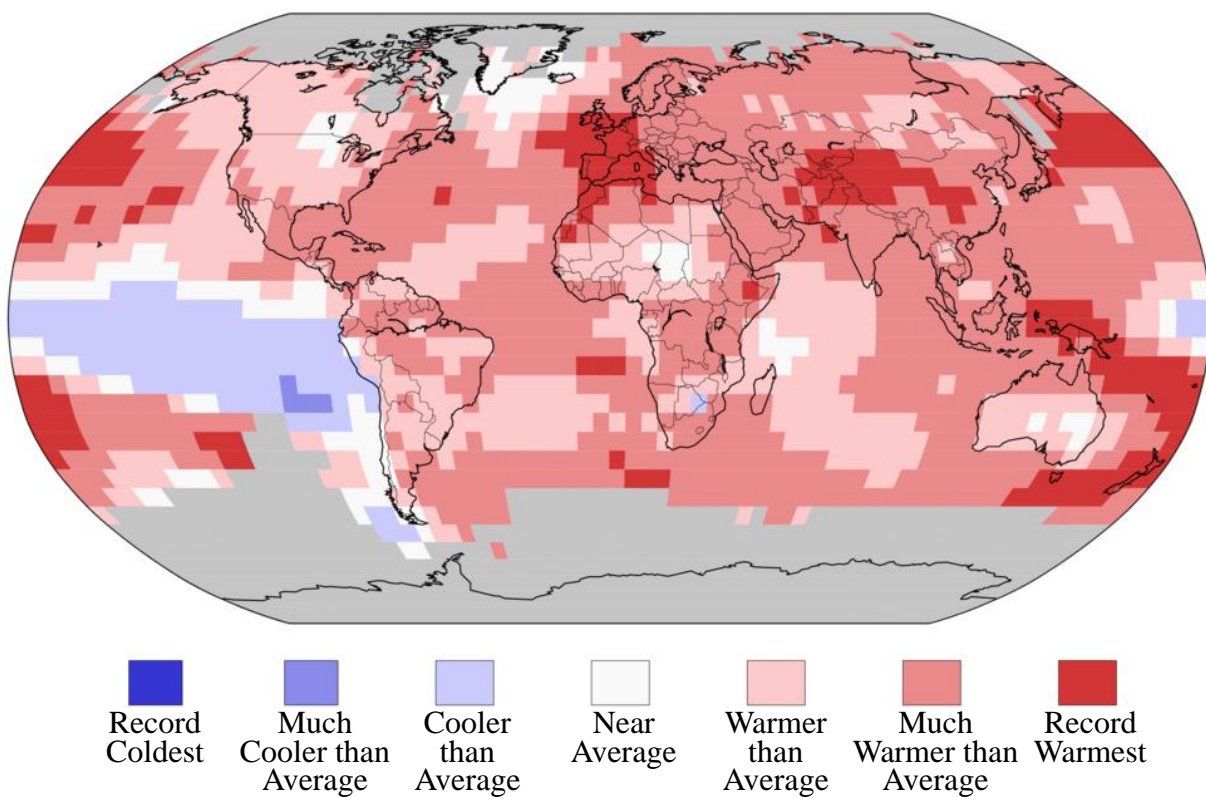


Figure 1.4: Global average Earth's surface temperature percentiles in 2022.
 [National Centers for Environmental Information]

evapotranspiration with decreased precipitation have contributed to water scarcity and desertification. Current levels of warming are associated with moderate risks of such events, while risks are expected to increase simultaneously with a 1.5 and 3°C warming (IPCC, 2019).

1.1.2 Extensive evapotranspiration and Precipitation deficit

Evapotranspiration and precipitation form the two primary processes of water movement in the natural water cycle. Evapotranspiration defines the water rising from open water surfaces, soils, and plants into the atmosphere through evaporation. After water vapor condensates into clouds, water falls to the ground as rain or snow through precipitation. This cycle has been disrupted in recent decades due to several human behaviors and climate change. Warming global temperatures increase the evaporation rate worldwide, which consequently increases precipitation. However, those water processes are not evenly distributed around the world. Some areas have experienced heavy torrential rainfalls, while others have become more prone to droughts.

Figure 1.5 delineates the global average changes in precipitation based on the data adopted from NOAA, where since 1901, an average increase of 1 mm per decade was noticed. However, precipitation patterns and distribution vary worldwide. Some parts have experienced significant precipitation, while others suffer scarcity. The 30-year average annual precipitation rates shown on the world map in Figure 1.6 indicate low precipitation rates, less than 400 mm/year, in the Middle East, North Africa, and significant parts of Asia and North America.

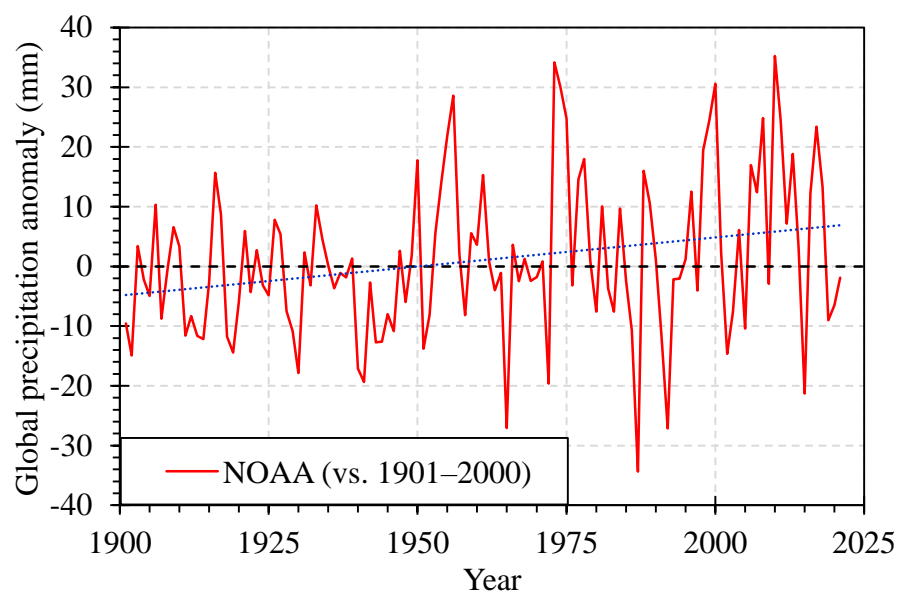


Figure 1.5: Global land average precipitation anomalies. (Blunden and Boyer, 2021)

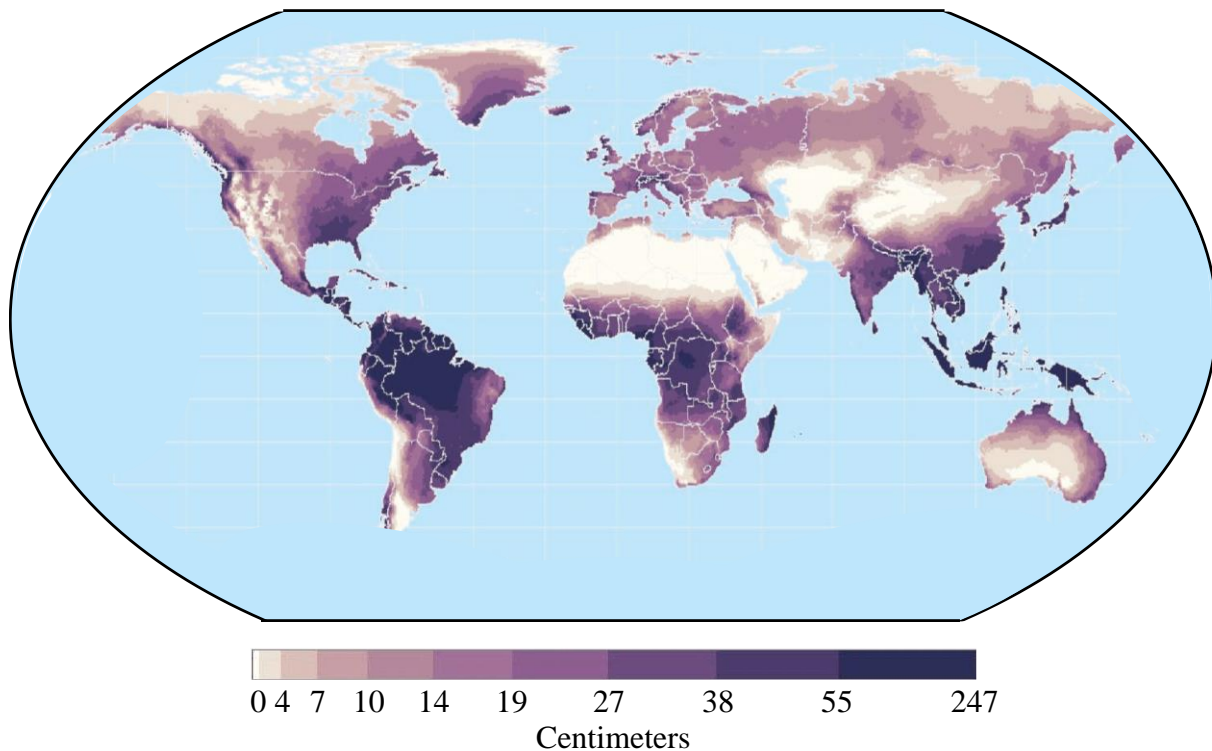


Figure 1.6: Global average annual precipitation from 1960-1990.

[Center for Sustainability and the Global Environment, University of Wisconsin - Madison]

Another evidence of low precipitation can be seen on the map in Figure 1.7, where based on the provided data, many areas worldwide have recorded drier and much drier than their annual average precipitation during 2022. Simultaneously, those areas suffer from high evapotranspiration rates, which have increased water stresses and droughts. The map in Figure 1.8 shows a recent estimation of the global average evapotranspiration rates covering the period of 1970–2000 (Zomer et al., 2022), where the Middle East, North Africa, and other parts of Asia, Australia, and North America are prone to high evapotranspiration that highly exceeds the precipitation rates.

1.1.3 Water scarcity and limited soil moisture

Although water covers 71% of Earth’s surface, only 3% is freshwater, and around 67% is stored in glaciers or unavailable for use. Climate change affects where, when, and how much water is available. Global warming, low precipitation, and high evapotranspiration rates impact water resources. Insufficient freshwater availability or water shortage is divided into physical and economic water scarcity. The latter occurs due to the lack of infrastructure and poor water management. Whistle, the former is an absolute water shortage, which is devastating. Based on the Food and Agriculture Organization (FOA), more than 1.2 billion people are suffering from

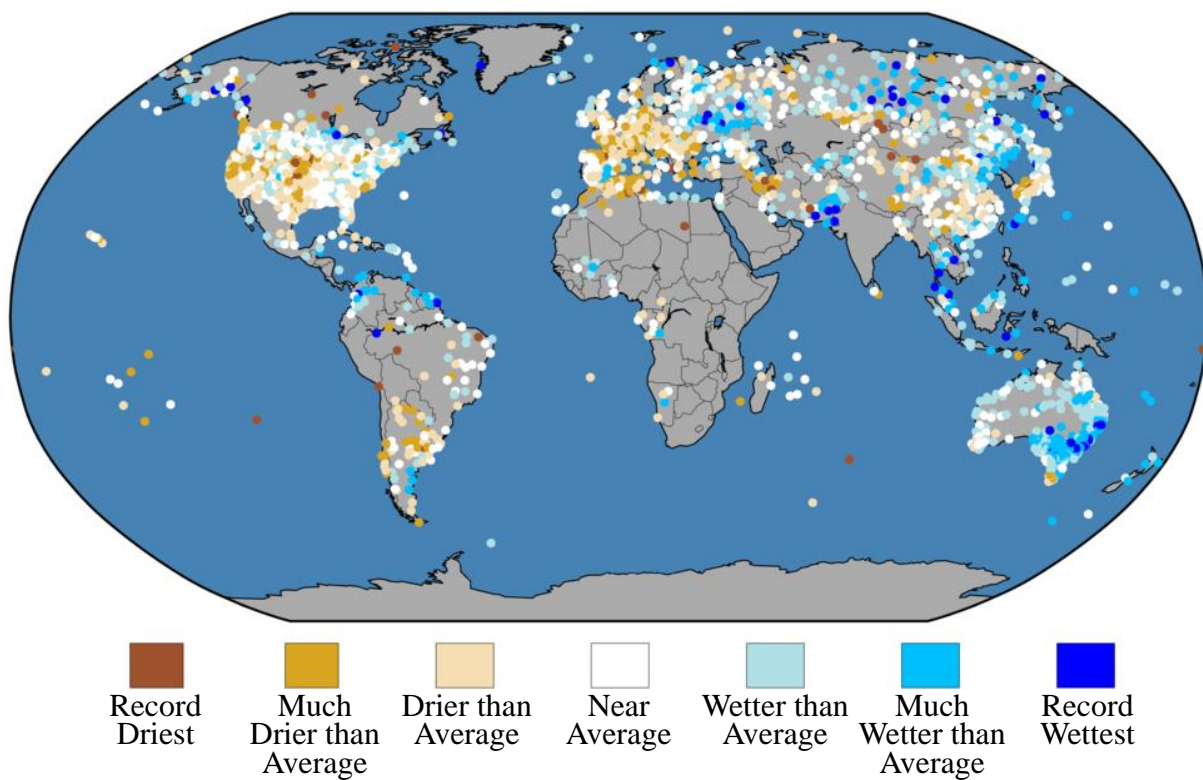


Figure 1.7: Global average Earth's surface precipitation percentiles in 2022.
[National Centers for Environmental Information]

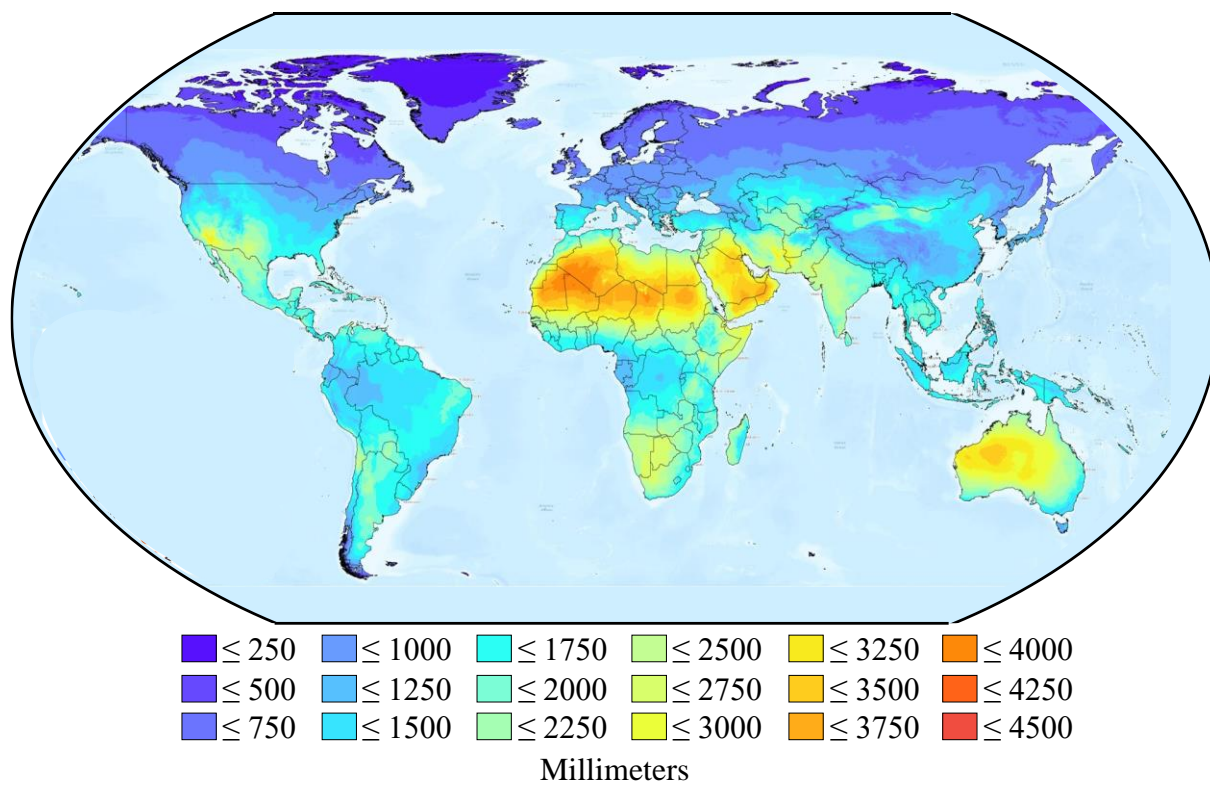


Figure 1.8: Global average annual evapotranspiration from 1970-2000.
[National Centers for Environmental Information]

physical water scarcity, while by 2025, over 3 billion are likely to experience such stresses (FAO, 2007). The water scarcity map in Figure 1.9 shows that all countries in Africa and South America are projected to be physically or economically water-scarce in 2025.

The remaining 29% of the Earth's surface is soil-covered land. Soil is also a natural resource that is highly vulnerable to the current climatic changes. Reduced or erratic rainfall and severe hot weather periods extend soil moisture deficits. Intensified and shorter rainfall events combined with higher evapotranspiration rates lead to increased erosion from water and accelerated runoff, while strong winds reduce soil moisture available for plant growth. Additionally, higher soil surface temperatures increase soil salinization and impair the soil's capacity to retain water. Consequently, such changes in soil moisture seriously impact agricultural productivity, forestry, and ecosystem health.

1.1.4 Droughts

All the severe climatic changes discussed earlier lead to drought, which is one of the most complex and severe climate-related hazards. Droughts are prolonged dry periods lasting from a few weeks to several years. The IPCC (2019) defines droughts as:

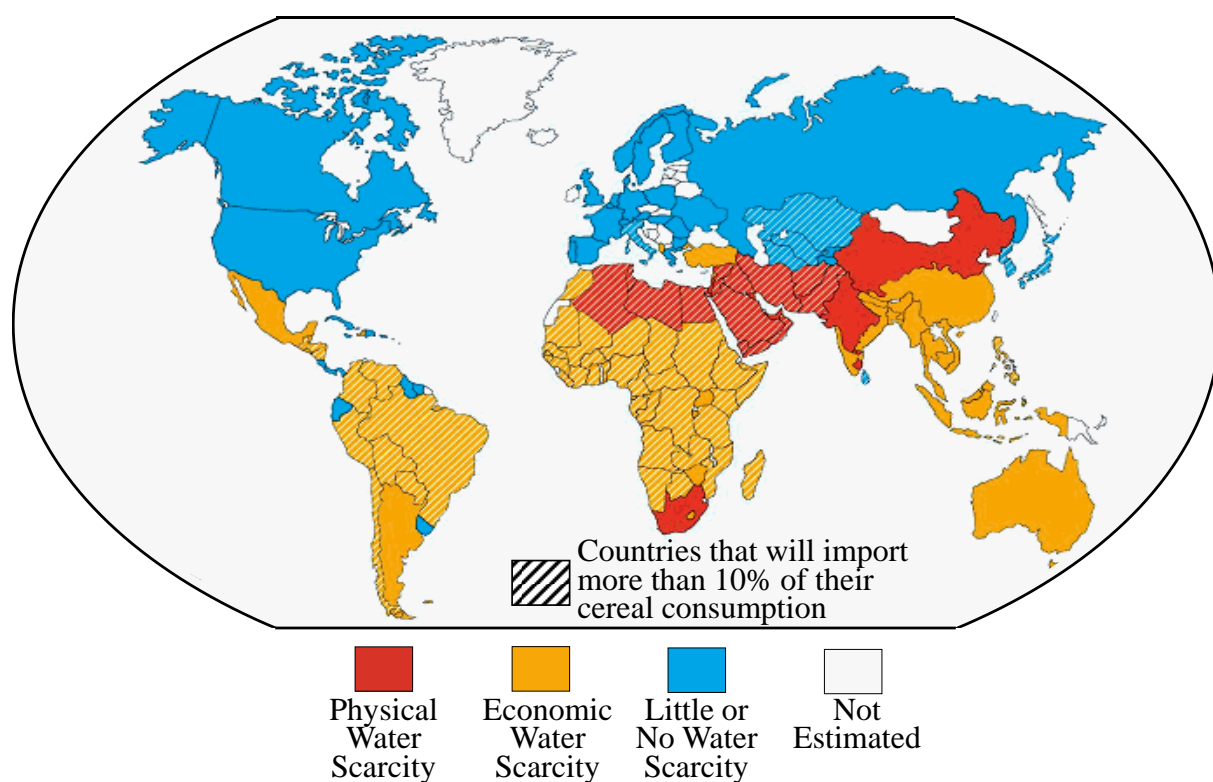


Figure 1.9: Global projected water scarcity in 2025.
[International Water Management Institute (IWMI, 2000)]

“a period of abnormally dry weather long enough to cause a serious hydrological imbalance.”

This phenomenon has occurred throughout history, but its intensity and duration have been exacerbated in recent decades. The World Meteorological Organization (WMO, 2021) reported a 29% increase in droughts since 2000 compared to the previous two decades. While droughts cause water and food shortages, many impacts on populations' health can result in death. From 1970 to 2012, drought caused almost 680 thousand deaths due to severe African droughts (FAO, 2022). Climate change is expected to increase the risk of droughts in many vulnerable regions. The drought projection map shown in Figure 1.10 classifies the lands and their vulnerability to droughts as of 2022. Within the next few decades, 129 countries are expected to experience increased drought exposure due to climate change alone (UNCCD, 2022). Forecasting droughts has been challenging due to the high complexity and the unprecedented interactions between their driving forces. Therefore, mitigation and adaptation strategies are being implemented in several vulnerable areas to increase communities' resilience and ability to cope with droughts.

1.2 Drylands and Desertification

1.2.1 Drylands

Thornthwaite (1948) developed a classification system for climate based on the moisture index, which considers the annual precipitation and potential evapotranspiration. After several years, the United Nations Environment Programme (UNEP, 1992) adopted the concept and produced the Aridity Index (AI) to classify arid regions. The AI is the ratio of the average annual precipitation (P) to potential evapotranspiration (PET). Hyper-arid, arid, semi-arid, and dry sub-humid areas constitute drylands (UNEP, 1992). The map in Figure 1.11 delineates the distribution of drylands worldwide, while their geographic classification based on the AI is indicated in the legend. Drylands cover approximately $46.2 \pm 0.8\%$ of the global land area and are home to around $38.2 \pm 0.6\%$ of its population, comprising more than 3 billion people (IPCC, 2019). The population in drylands is projected to increase about twice as rapidly as in non-drylands, Figure 1.12, reaching 4 billion people by 2050, where about 90% live in developing countries (van der Esch et al., 2017). Scientists have also confirmed that the warming trends over drylands are twice the global average (Lickley and Solomon, 2018). It is anticipated that some temperate drylands are projected to convert to subtropical drylands due to the increased drought frequency and reduced soil moisture availability (Engelbrecht et al., 2015; Schlaepfer

et al., 2017). Water scarcity, droughts, and other climate stresses present an unprecedented threat to drylands with far-reaching environmental, social, and economic consequences.

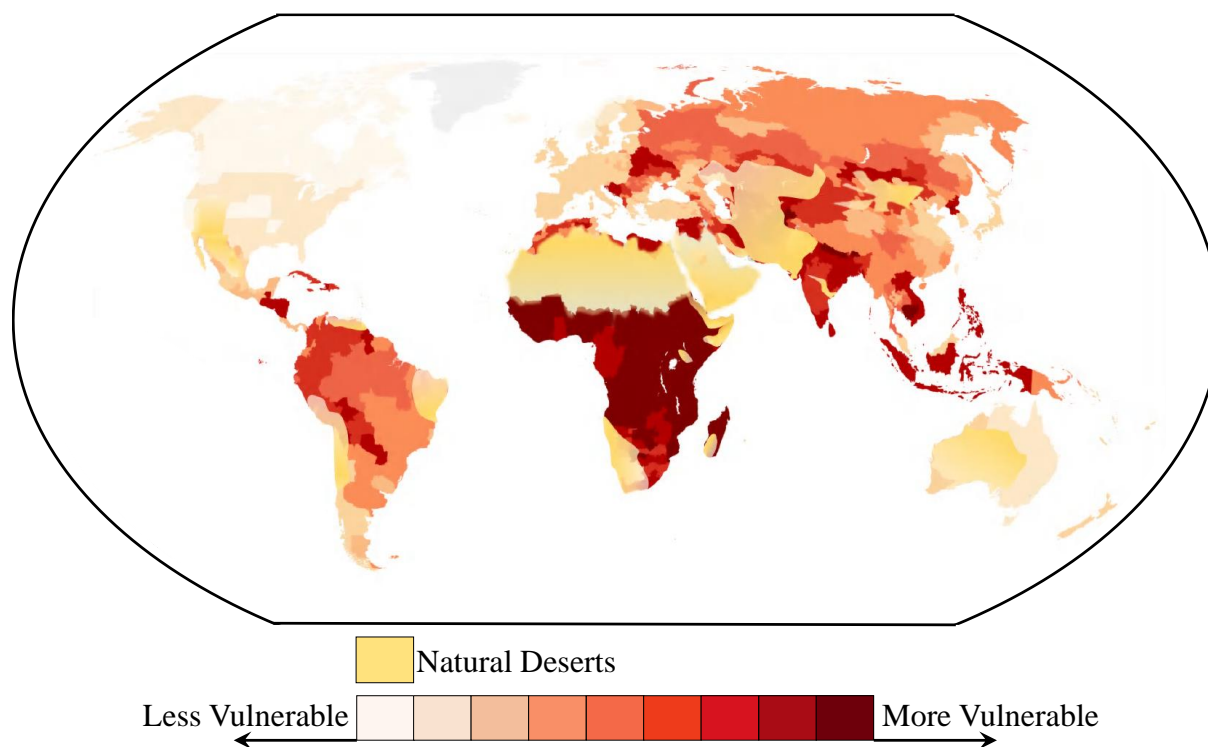


Figure 1.10: Global drought-vulnerability index in 2022. (UNCCD, 2022)

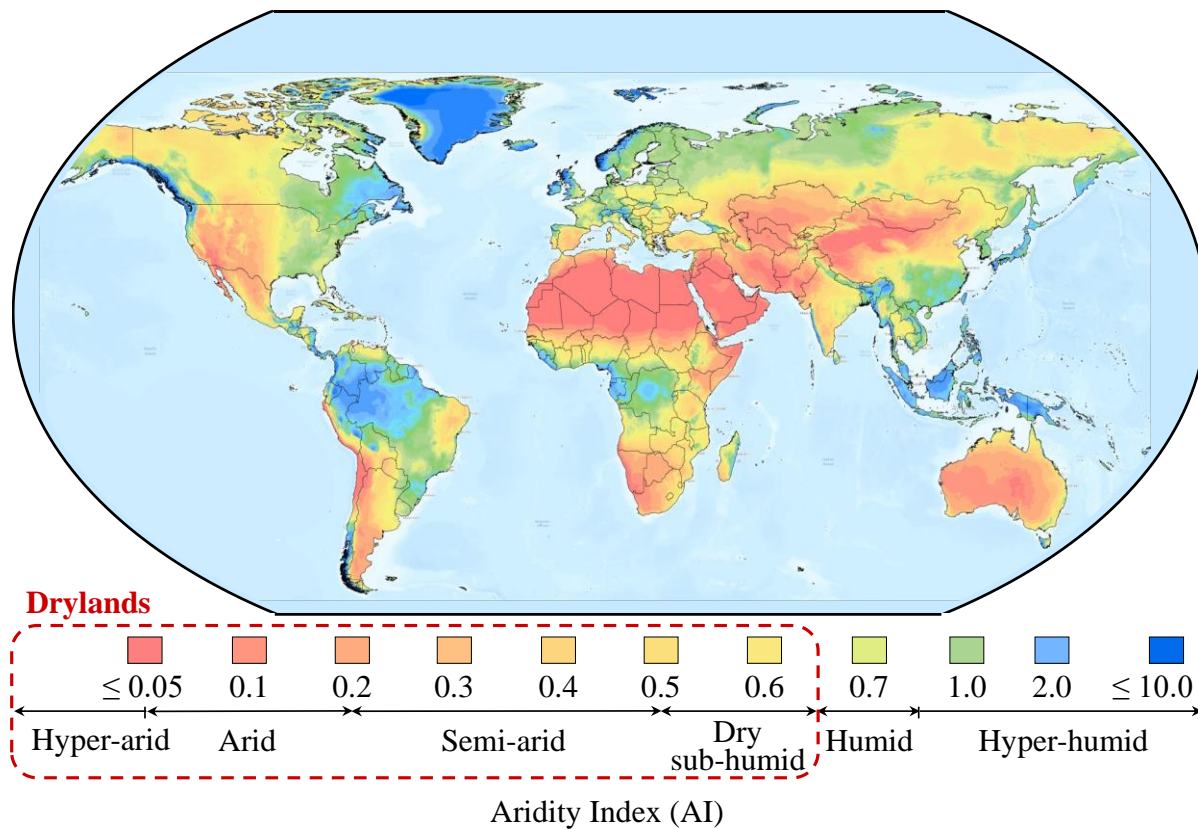


Figure 1.11: Global geographical distribution of drylands. (Zomer et al., 2022)

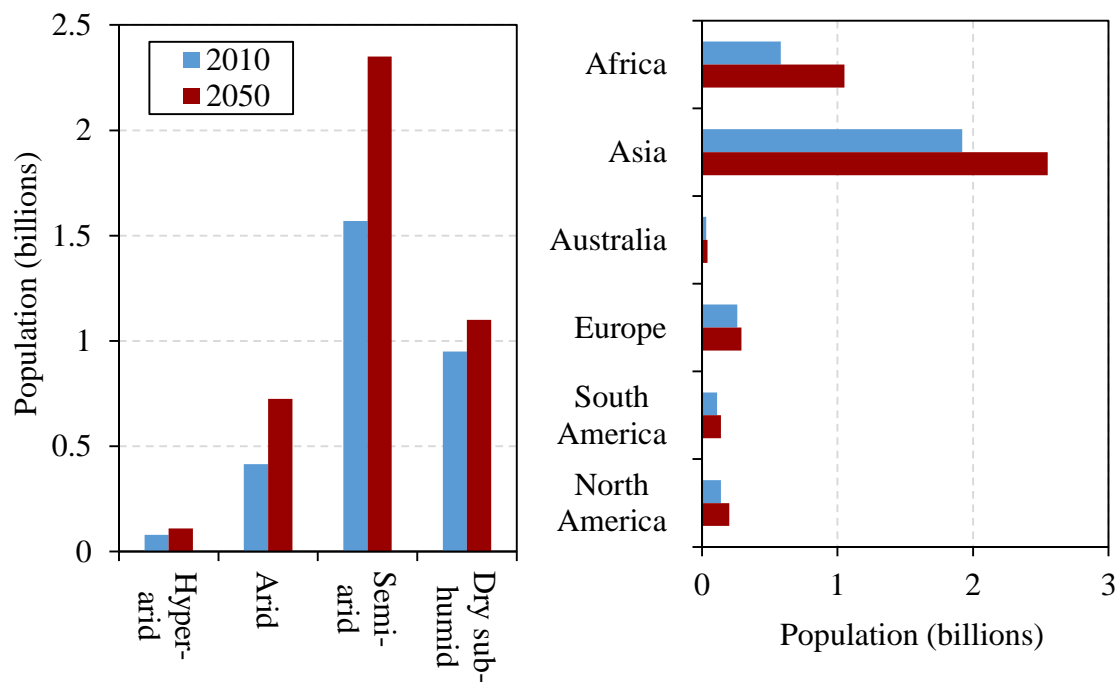


Figure 1.12: Current and projected population in drylands. (van der Esch et al., 2017)

1.2.2 Land degradation and desertification

Land degradation is a negative trend in land conditions, including soil, near-surface air, vegetation, and water. It can be caused by direct or indirect human-induced processes expressed as long-term reduction or loss of biological productivity, ecological integrity, or value to humans. On the other hand, soil degradation refers to a subset of land degradation processes directly affecting soils. Climate change exacerbates the rate and magnitude of several ongoing land degradation processes and introduces new degradation patterns. Human-induced global warming has already caused observed changes in two drivers of land degradation: increased frequency, intensity, and amount of heavy precipitation; and increased heat stress (IPCC, 2019).

The United Nations Convention to Combat Desertification (UNCCD, 1994) reported that any land degradation in arid, semi-arid, and dry sub-humid areas resulting from many factors, including human activities and climatic variations, is called desertification. It includes the reduction or loss of the biological or economic productivity and land integrity resulting from land uses or other processes, such as soil erosion caused by wind or water; deterioration of the physical, chemical, biological, or economic properties of soil; and long-term loss of natural vegetation. Therefore, the difference between land degradation and desertification is not process-based but geographic. Although land degradation can occur anywhere, it is considered desertification when it occurs in drylands. Hyper-arid areas ($AI < 0.05$) are included in drylands

but are excluded from the definition of desertification (UNCCD, 1994). Deserts are geographically located in drylands and vulnerable to climate change, yet they are not considered prone to desertification (IPCC, 2019). The range and intensity of desertification have increased in some drylands over the past several decades. It extended to about $9.2 \pm 0.5\%$ of drylands, affecting about 500 ± 120 million people in 2015 (IPCC, 2019).

Desertification is caused by various factors that change with time and vary by location. Some are direct, and others are indirect. However, all factors interact together causing an increased complexity to the process. The climate is a direct driver for desertification. Particularly, low soil moisture, rainfall patterns, and extensive evaporation rates. Others, such as globalization and changing land-use patterns are indirectly drivers of the desertification phenomenon. Therefore, a single metric cannot be used to characterize desertification, and a single indicator cannot make or map its future projections. However, many efforts are made to predict the land vulnerability to desertification based on some global reclassifications, such as the map shown in Figure 1.13.

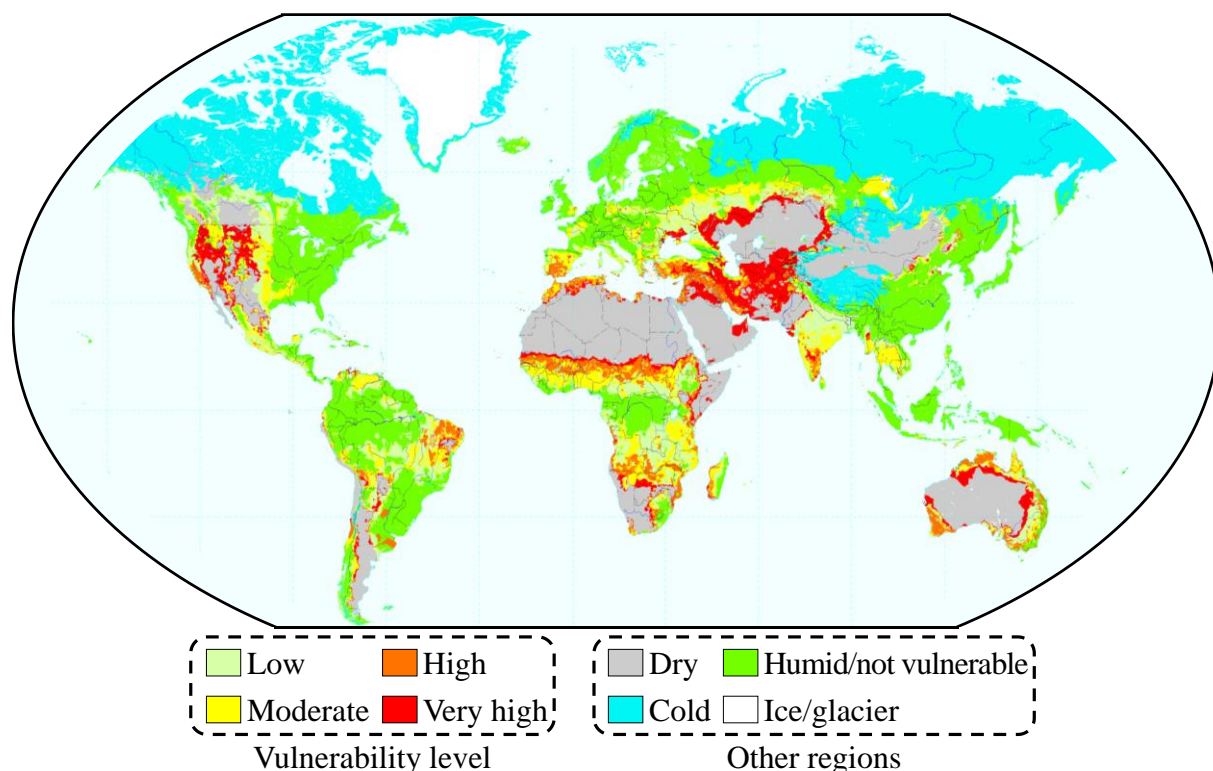


Figure 1.13: Global desertification-vulnerability level based on a reclassification of the global soil climate map and global soil map. (USDA, 1998)

1.2.3 Combating Desertification

Many international institutes and joint researchers highlighted the seriousness of desertification and the importance of drought mitigation. After around 15 years of advocating for land justice and desertification prevention, the United Nations Convention to Combat Desertification (UNCCD), comprised of 197 parties, was established on June 17, 1994. It became the first legally binding international agreement linking environment and development to sustainable land management. The UNCCD efforts aim to promote international cooperation to address the global-scale issues related to desertification that threatens the world, primarily in developing countries. The UNCCD collaborates with other conventions, the Convention on Biological Diversity (CBD) and the United Nations Framework Convention on Climate Change (UNFCCC), to maintain and restore land and soil productivity and mitigate drought effects. The UNCCD was the leading light behind Sustainable Development Goal 15:

“Protect, restore and promote sustainable use of terrestrial ecosystems, sustainably manage forests, combat desertification, and halt and reverse land degradation and halt biodiversity loss.”

Moreover, the UNCCD was the driving force behind one of the most critical initiatives to arrest land degradation, the Land Degradation Neutrality (LDN). The concept was proposed in October 2015 and is defined as:

“a state whereby the amount and quality of land resources, necessary to support ecosystem functions and services and enhance food security, remains stable or increases within specified temporal and spatial scales and ecosystems.”

The LDN aims to avoid further degradation, reduce current degradation, and put efforts into restoring and returning degraded lands to a natural or more productive state. Over the last 25 years, some promising sustainable practices have shown evidence of the recovery and restoration of degraded landscapes in many areas.

The UNCCD and other policymakers have created many rational steps and policies toward preventing and reversing desertification. On the other hand, many efforts are invested in optimizing and implementing projects in drylands to prevent such phenomena from augmenting. According to the 2005 report by the Millennium Ecosystem Assessment (2005), integrated land, and water management and protecting the vegetation cover are critical methods

of desertification prevention. All measures that protect soils from erosion, salinization, and other soil degradation patterns effectively prevent desertification. Therefore, new and natural ways of managing soils and groundwater are urgently required to improve their function and save them from degradation.

1.3 Ground Surface Boundary Fluxes and Water Flow through Soil Profiles

Soil is a vital element and a non-renewable resource on Earth. It is a site of intense activity and home to a vibrant ecosystem. With all the climate changes, water stresses, and droughts, soils become particularly vulnerable to desertification. Concurrently, soils are critical in mitigating climate change, where healthy soils form the second largest carbon sink after the ocean. Therefore, soil prevention is essential for a sustainable future on the planet.

Naturally and specifically in drylands, the near-surface soil or the soil layer extending from the groundwater table to the ground surface is mainly unsaturated. It is widely known as the Vadose Zone or the Unsaturated soil profiles. The water flow through such profiles and the related fluxes are of extra complexity. Unsaturated soils are naturally in transient conditions or under unsteady-state flow, where the water storage continuously changes. The ground surface forms the uppermost boundary with the ambient atmosphere. At times, it is subjected to precipitation or irrigation, where water infiltrates through soil profiles, while at others, water exfiltrates by evaporation from the boundary or through plants' roots. Boundary fluxes are highly dependent on the soil body and related to water movement and storage. Therefore, determining the net moisture flux at the surface and understanding the water flow through profiles is essential for finding solutions to prevent soil degradation in drylands and serving many other applications related to soil mechanics. A summary of the related soil problems is shown in the flowchart of Figure 1.14. For years extensive research has been undertaken in many disciplines, including surface hydrology, climatology, and agriculture, to predict such fluxes. However, with the need to solve soil mechanics issues, methods should be reevaluated, and new models must be proposed to correctly and accurately determine such fluid phenomena from a geotechnical engineering perspective.

Ground surface boundary fluxes are highly complicated processes involving many micro-mechanisms related to water movement through soil profiles. Generally, boundary fluxes are a function of demand, supply, and vegetation cover. Demand reflects the boundary or the

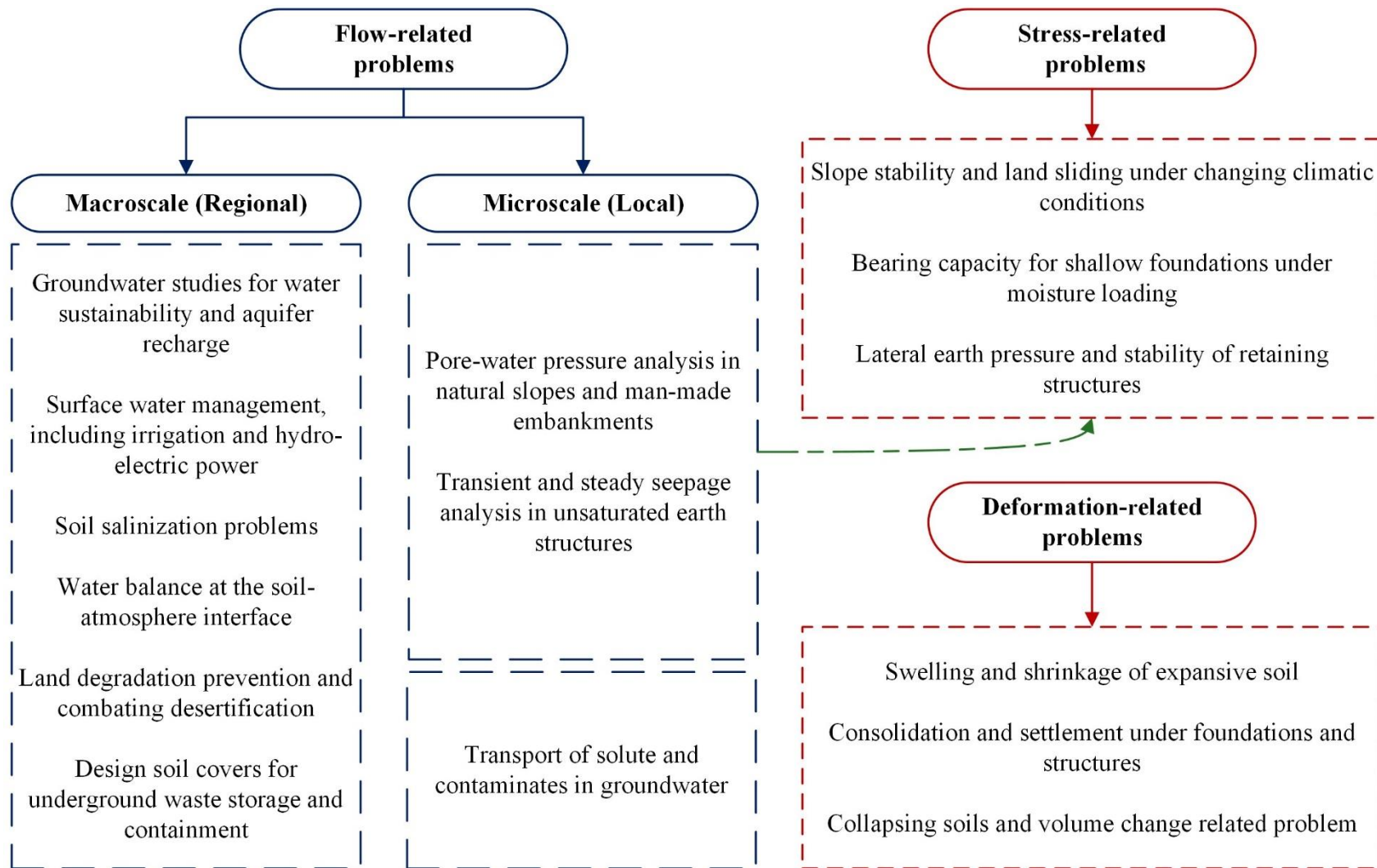


Figure 1.14: Categorized problems that require proper determination of boundary fluxes and water flow through soil profiles.

atmospheric conditions, including temperature, ambient air velocity, relative humidity, and net radiation. The water supply is the soil's ability to transport water. It is a function of the soil pore structure and transport properties, including permeability and retention properties. Finally, the vegetation cover, where the root uptake flux varies significantly depending on the density and type of vegetation. From bare soil surfaces, demand and supply become the dominant parameters. Therefore, water infiltration and evaporation into and out of the soil profile are the main controlling factors of the soil moisture state, responsible for the near-surface pore water pressure variations that control the unsaturated soil stress state.

Water infiltration is relatively well understood and widely discussed in the literature (Eagleson, 1978; J.R. Philip, 1957). Its theory is mechanistic and based on fundamental principles of water flow in porous media (Wilson, 1990). Therefore, a clear rationale for predicting infiltration is available. On the contrary, less knowledge is provided regarding evaporation flux. Its mechanism is unclear, with many ambiguities. Moreover, a suitable evaluation methodology of the evaporation rates from soil profiles is still lacking. Evaporation is a complex multiphase pore-scale process that involves coupled heat and mass transfer. It includes liquid-gas phase change, capillary-induced water flow, and vapor flow through the soil pores. The need for predicting evaporation flux from soil profiles was widely addressed in the literature. Qiu and Prato (1998) mentioned the importance of estimating the amount of water loss to reduce agriculture's evaporation. Many studies highlighted the use of the evaporation flux in designing a soil cover of mine tailings (E.K. Yanful and Choo, 1997), investigating the long-term performance of moisture-retaining soil cover (Yanful et al., 2003), and designing an evapotranspiration cover system for waste containment and mining sites (Cui and Zornberg, 2008). Besides water loss, evaporation from soils also involves the danger of soil salinization. This danger is felt most in drylands where water is scarce and in regions with a high groundwater table (Hillel, 1980). Similarly, predicting the evaporation rates is significantly required to combat desertification in drylands where the frequency and duration of evaporative events highly exceed infiltration. A complete description of the evaporation process and an accurate evaluation of its rate is fundamental to developing natural soil covers to optimize water retention and reduce water losses from soils. Such environmental-friendly solutions prevent soils from degrading, consequently combating desertification.

1.4 Research objectives

This thesis investigates and evaluates the evaporation process from unsaturated soil profiles by tackling the evolving micro-mechanisms occurring at the soil pore level and reflecting them on the macroscale behavior of evaporation. Moreover, this research considers developing natural soil covers to control and suppress evaporation from bare soil profiles in drylands as a step toward combating desertification. Consequently, the specific objectives of the thesis are delineated in Figure 1.15 and can be drawn as follows:

1. To parameterize the soil pore structure through an experimental approach and investigate its influence on the evaporation behavior and the water transport mechanisms that vary between the evaporation stages.
2. To visualize the formation and development of the unsaturated soil layer and its boundaries during evaporation through an experimental approach and investigate their role in the process.
3. To formulate an empirical and theoretical framework to estimate the evaporation rate based on the soil pore structure parametrization and the visualization of the unsaturated layer dynamics.

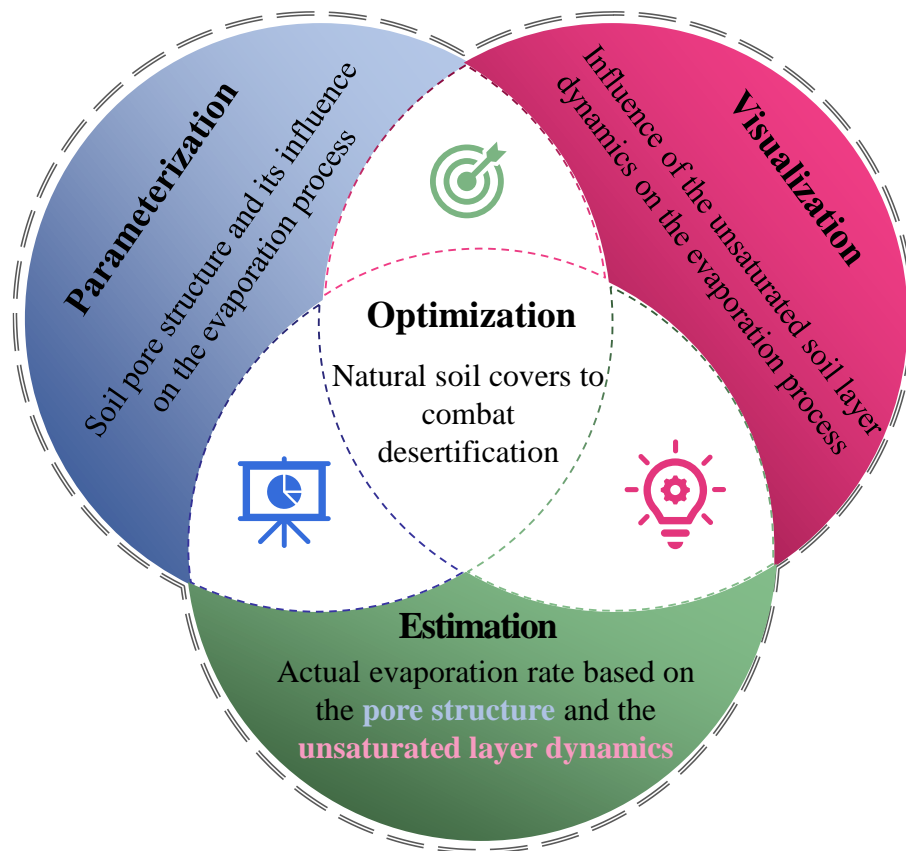


Figure 1.15: Research objectives.

4. To optimize a conceptual framework for a natural soil cover that suppresses evaporation and maximizes water retention in drylands by identifying the role of the relative soil properties between the natural ground and the applied soil cover.

The current research work focuses on the evaporation process from bare soil profiles. This approach does not deny the essential role of the vegetation cover in the process. However, its presence highly increases the complexity. Therefore, a complete understanding of the evaporation dynamics from bare soils allows for a more systematic extension to a research scheme that considers vegetated-surface soil profiles.

1.5 Thesis Framework and Outlines

The thesis is organized into seven chapters, systematically satisfying the current research work's objectives and scope. The thesis's framework is delineated in Figure 1.16, and the outlines of each chapter are briefly described as follows:

Chapter 1 presents the scientific understanding of the primary climatic changes that have caused the world's soils and lands to degrade. It briefly discusses global warming, water scarcity, droughts, and the scales at which it threatens humanity and the ecosystem. It distinguishes between desertification and land degradation and presents facts and statistical records of drylands and their increasing patterns in the past century. Consequently, the necessity to combat desertification is discussed, concluding with the vital role and need to accurately evaluate the ground surface boundary fluxes, mainly the dominant evaporation flux and water flow through soil profiles for many engineering applications. Finally, the proposed goals, objectives, and framework are reported.

Chapter 2 presents a comprehensive literature review of the current research scopes and objectives. It starts with a theoretical explanation of the water balance at the ground surface and the dominance of the upward fluxes in drylands. Consequently, an inclusive view of the potential and actual evaporation fluxes is provided. The micro and macroscale definitions are provided, while the most used models and methods by geotechnical engineers to evaluate the evaporation rates are discussed. The influencing factors of the actual evaporation behavior are delineated, while the importance of bridging the demand at the surface and water supply through the soil profile is reviewed. Moreover, the latest methods used to suppress water evaporation from soil profiles are presented, while the need to propose innovative and practical solutions to combat desertification is discussed. This chapter concludes with the current research's original contributions and expected impacts on the field.

Chapter 3 focuses on understanding the macroscale behavior of the evaporation process and the soil properties' influence, particularly soil texture and relative density, on its behavior. Moreover, the influence of the soil pore structure on the actual evaporation flux and the formation of the unsaturated layer is studied. The evaporation process and soil pore structure are investigated through experimental testing of homogeneous sandy soil profiles under constant atmospheric demand. Accordingly, a robust and comprehensive pore structure-based index is proposed to represent the pore structure variation while its significant influence on evaporation behavior is discussed.

Chapter 4 focuses on investigating the microscale behavior of the evaporation process by studying the evolving mechanisms occurring at the pore level during drying. Accordingly, a simple and effective technique is developed to visualize the unsaturated layer during evaporation. The novel image analysis-based technique considers capturing high-quality images, followed by a series of image analysis operations that enable the detection of the air-dry layer, film region, and their boundaries during Stages 2 and 3. Accordingly, new insights are discussed regarding the spatial and temporal development of the drying front, vaporization plane, and film region. Furthermore, the influence of the pore structure on the unsaturated layer dynamics is further elucidated.

The main focus of Chapter 5 is reflecting the evolving micro-mechanisms at the pore level to the macroscale behavior of the evaporation process. Consequently, a new actual evaporation rate estimation model is proposed based on the pore structure and water transport mechanisms through the unsaturated soil profile. The pore-scale-based estimation model conjugately solves the atmospheric demand and the water supply during evaporation. The theory, assumptions, and empirical-theoretical derivation of the model are thoroughly discussed throughout the chapter. Moreover, its reliability, limitations, and the simplicity of its utilization are presented.

Following the need to develop innovative solutions to combat desertification in drylands, Chapter 6 proposes a new design concept for an environmental-friendly natural soil cover that suppresses water evaporation and maximizes water storage in bare soil profiles. The physics behind the two proposed criteria is thoroughly explained. Moreover, the efficiency and applicability of the design concept in selecting the suitable material and thickness of the natural soil cover are discussed.

Finally, Chapter 7 summarizes the current research work's main conclusions and findings. It delineates the remaining issues to be solved and defines goals for future research

issues and scopes that need to be investigated concerning evaporation and combating desertification.

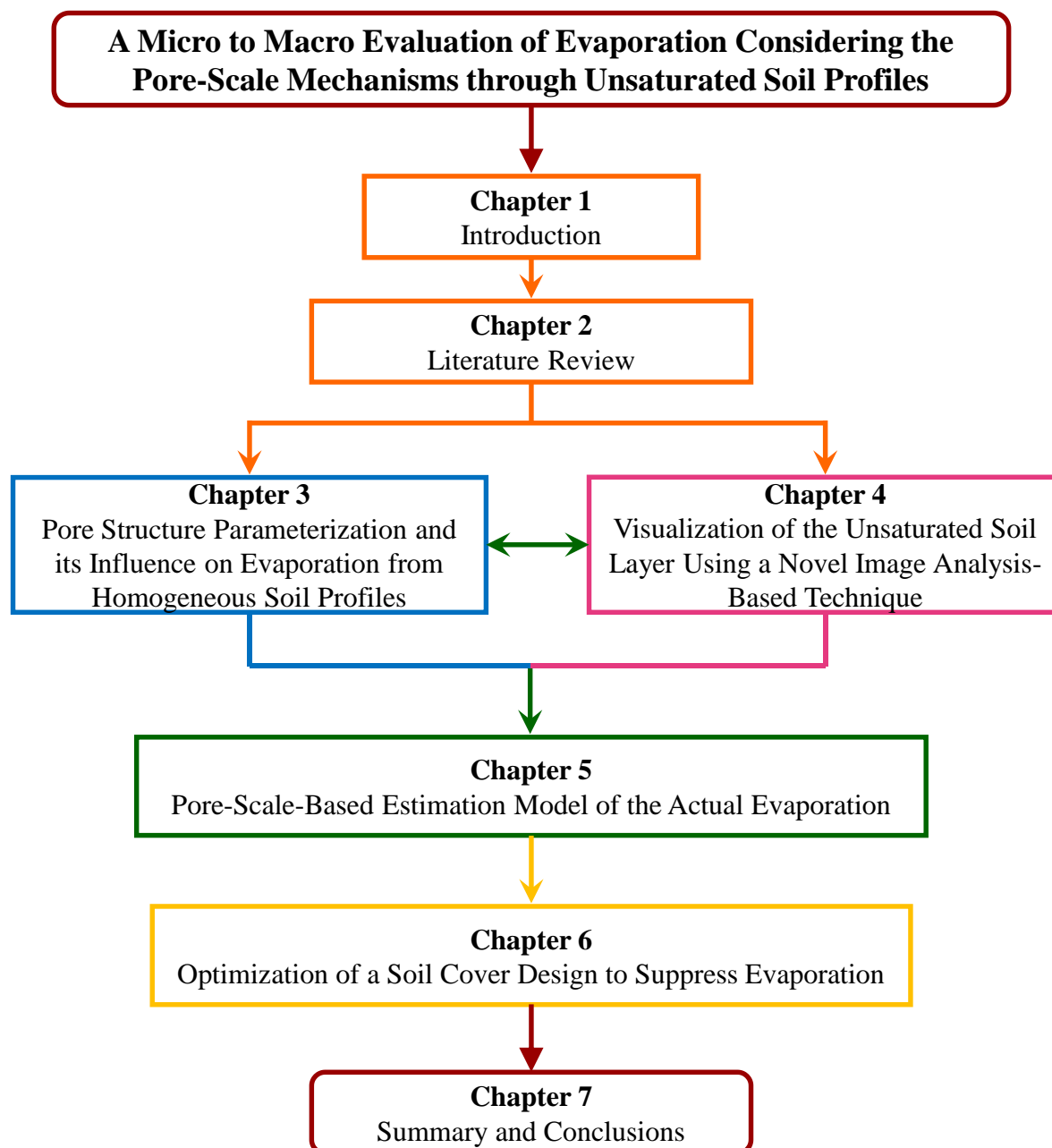


Figure 1.16: Thesis framework and organization.

References

- Blunden, J., Boyer, T., 2021. *State of the Climate in 2020*. *Bull Am Meteorol Soc* 102.
- Cui, Y.J., Zornberg, J.G., 2008. Water balance and evapotranspiration monitoring in geotechnical and geoenvironmental engineering. *Geotechnical and Geological Engineering* 26, 783–798. <https://doi.org/10.1007/s10706-008-9198-z>
- Eagleson, P.S., 1978. Climate, soil, and vegetation: 3. A simplified model of soil moisture movement in the liquid phase. *Water Resour Res* 14, 722–730.
- Engelbrecht, F., Adegoke, J., Bopape, M.J., Naidoo, M., Garland, R., Thatcher, M., Gatebe, C., 2015. Projections of rapidly rising surface temperatures over Africa under low mitigation. *Environmental Research Letters* 10, 085004. <https://doi.org/doi:10.1088/1748-9326/10/8/085004>
- FAO, 2022. *The State of the World's Land and Water Resources for Food and Agriculture – Systems at breaking point*.
- FAO, 2007. *The state of food and agriculture: Paying farmers for environmental services*. [Agricultural Development Economics Division (ESA)].
- Hillel, D., 1980. *Applications of Soil Physics*. Academic Press, Inc., New York. <https://doi.org/10.2307/2403017>
- IPCC, 2019. *An IPCC special report on climate change, desertification, land degradation, sustainable land management, food security, and greenhouse gas fluxes in terrestrial ecosystems*. <https://doi.org/https://doi.org/10.1017/9781009157988.001>
- IPCC, 2013. *Summary for Policymakers*. In: *Climate Change 2013: The Physical Science Basis. Contribution of Working Group I to the Fifth Assessment Report of the Intergovernmental Panel on Climate Change*.
- Lickley, M., Solomon, S., 2018. Drivers, timing and some impacts of global aridity change. *Environ. Res. Lett.* 13, 104010. <https://doi.org/doi:10.1088/1748-9326/aae013>.
- Millennium Ecosystem Assessment, 2005. *Ecosystems and Human Well-being: Desertification Synthesis*.
- Olivier, J.G., Schure, K.M., Peters, J.A.H.W., 2017. Trends in global CO₂ and total greenhouse gas emissions. *PBL Netherlands Environmental Assessment Agency* 5, 1–11.
- Philip, J.R., 1957. The theory of infiltration: 4. Sorptivity and algebraic infiltration equations. *Soil Sci* 84, 257–264.
- Qiu, Z., Prato, T., 1998. Economic Evaluation of Riparian Buffers. *J Am Water Resour Assoc* 34, 877–890.
- Schlaepfer, D.R., Bradford, J.B., Lauenroth, W.K., Munson, S.M., Tietjen, B., Hall, S.A., Jamiyansharav, K., 2017. Climate change reduces extent of temperate drylands and intensifies drought in deep soils. *Nat Commun* 8, 14196.
- Thornthwaite, C.W., 1948. An Approach toward a Rational Classification of Climate. *Geogr Rev* 38, 55–94. <https://doi.org/10.2307/210739>
- UNCCD, 2022. *DROUGHT IN NUMBERS 2022 - restoration for readiness and resilience*.
- UNCCD, 1994. *United Nations Convention to Combat Desertification*. United Nations General Assembly.
- UNEP, 1992. *World Atlas of Desertification*. World atlas of desertification (United Nations environment programme). <https://doi.org/https://doi.org/10.1002/ldr.3400030407>
- van der Esch, S., ten Brink, B., Stehfest, E., Bakkenes, M., Sewell, A., Bouwman, A., Doelman, J., 2017. Exploring future changes in land use and land condition and the impacts on food, water, climate change and biodiversity: scenarios for the UNCCD Global Land Outlook.
- Wilson, G.W., 1990. *Soil Evaporative Fluxes for Geotechnical Engineering Problems (Doctoral Thesis)*. University of Saskatchewan - Saskatoon, Canada.

- WMO, 2021. *Drought Overview [WWW Document]*. https://www.who.int/health-topics/drought#tab=tab_1 Retrieve 23/01/2021. URL <https://www.who.int/health-topics/drought#>
- Yanful, E.K., Choo, L.P., 1997. *Measurement of evaporative fluxes from candidate cover soils. Canadian Geotechnical Journal* 34, 447–459.
- Yanful, E.K., Mousavi, S.M., Yang, M., 2003. *Modeling and measurement of evaporation in moisture-retaining soil covers. Advances in Environmental Research*. [https://doi.org/10.1016/S1093-0191\(02\)00053-9](https://doi.org/10.1016/S1093-0191(02)00053-9)
- Zomer, R.J., Xu, J., Trabucco, A., 2022. *Version 3 of the Global Aridity Index and Potential Evapotranspiration Database. Sci Data* 9, 409.

2

Literature Review

CHAPTER

Fully saturated soil profiles in drylands last shortly after precipitation or irrigation events. Due to high evaporation rates, soil profiles become unsaturated, losing productivity and leaving living organisms without water resources. Under such severe conditions, soils become highly exposed to the risk of degradation and desertification. Developing adaptations and innovative solutions to combat desertification requires accurate prediction and evaluation of the evaporation from unsaturated soil profiles.

The following chapter presents a comprehensive review of the evaporation process and its prediction models and tools used in the literature. It covers the primary evaporation fluxes in geotechnical and geo-environmental engineering. Additionally, it communicates the most common innovative solutions proposed in the past decades to suppress evaporation fluxes. Finally, and based on the literature background, the originality of the present research and its influential contribution to the field are discussed.

2.1 Water Balance at the Ground Surface and Evaporation Fluxes

Net moisture flux at the ground surface was not part of the historical soil mechanics. However, the assessment of the water balance at the site is required to solve many geotechnical engineering problems, including near-surface engineered structures. Therefore, it has become an essential part of unsaturated soil mechanics (Fredlund et al., 2012). The ground surface forms a flux boundary between soil and the atmosphere, as delineated in Figure 2.1. Naturally, water is either entering the ground by Precipitation (P) or leaves through Actual Evaporation (AE) or evapotranspiration (ET). Water may also be shed from the ground surface through Runoff (R). Therefore, the net moisture flux at the ground surface or the net infiltration component (I) can be calculated as follows:

$$I = P - AE - ET - R \quad (2.1)$$

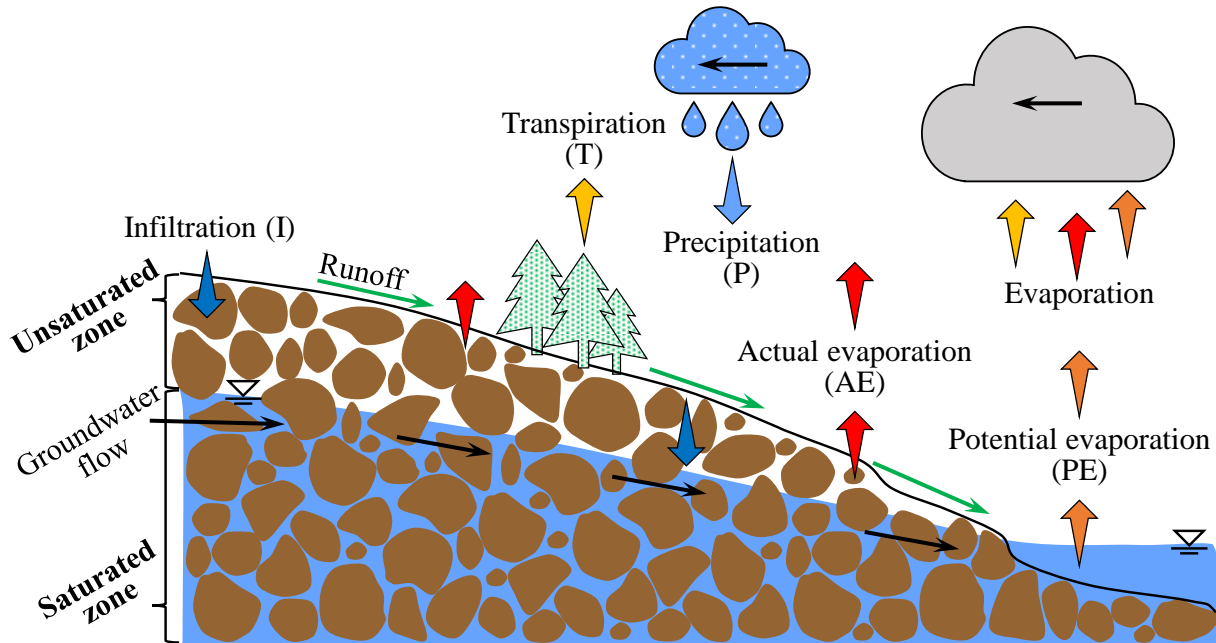


Figure 2.1: Water fluxes at the ground surface.

From a macroscale perspective, evaporation is the process by which water changes its physical state from liquid to vapor and gets lost into the atmosphere. From a microscale perspective, evaporation is the process where the total energy absorbed from the surrounding environment allows the liquid water molecules to overcome the attraction and cohesion forces between them and then detach and escape as vapor to the atmosphere. Evaluating the upward

water movement from the ground surface involves three commonly used terms, as shown in equation 2.1 and Figure 2.1: Potential Evaporation (PE), Actual Evaporation (AE), and Transpiration (T). The literature uses the term evapotranspiration, usually referring to the combination of transpiration and evaporation from the plant and the host soil. Actual evaporation is water evaporation from soil surfaces, while transpiration is water evaporation from plant tissues. Both terms are necessary for quantifying the water balance and are of primary interest in geotechnical engineering. However, before evaluating those terms, the potential evaporation and its controlling factors must be understood. Potential evaporation defines the evaporation from open surfaces of water bodies or saturated ground surfaces. Obtaining the potential evaporation is simpler than actual evaporation, where the latter involves soil's affinity for water, making it smaller in magnitude than the potential evaporation. The potential evaporation can be measured or calculated based on climatic conditions, while the actual evaporation involves more complexity, and predicting it requires many assumptions and approximations. The current research's primary focus is accurately predicting the evaporation rates from bare soil profiles and proposing a natural soil cover for suppressing the evaporation rates. This study is believed to be fundamental for extending to a more comprehensive investigation of the evaporation fluxes from soils and vegetation cover.

2.2 Potential Evaporation Flux

2.2.1 Definition of the potential evaporation

The understanding of the evaporation process has developed significantly since the 1940s, primarily focusing on potential evaporation. Potential evaporation is the amount of water that can evaporate if ample water is available at the ground surface. It is defined by the International Glossary of Hydrology (WMO, 1974):

“The quantity of water vapor which can be emitted by a surface of pure water per unit surface area and unit time under the existing atmosphere conditions.”

For evaporation to occur, there are three required conditions, as described by Hillel (1980), Tran (2013), and Wilson (1990). Firstly, a continuous supply of energy for the latent heat of vaporization. Generally, 80% of the energy required for evaporation comes from the sun as net radiation (Fredlund et al., 2012). Secondly, the aerodynamic function which depends on the vapor pressure gradient between the evaporating surface and its overlaying air, in addition to the profile of turbulent mixing above the evaporating surface. The vapor pressure is proportional to the number of vapor molecules in a unit volume of air and can be interpreted as

a measure of vapor concentration. If the vapor in the air is not removed and an energy source keeps the kinetic energy of the liquid water molecules high enough, evaporation continues until the vapor pressure in the surrounding air reaches a value equal to the vapor pressure at the evaporating surface. Consequently, the air turbulence near the surface becomes the dominant factor, where the air movement stirs the moist air layer adjacent to the soil surface and mixes it with the upper dryer layer. Therefore, the vapor deficit and wind, in the form of mixing term, form the second component contributing to evaporation. Thirdly, water availability at and below the evaporating surface, and in the case of a free water surface, the water supply is related to the depletion of the water body. Therefore, the first two conditions required for evaporation to occur determine the potential evaporation. They are both controlled by micro-meteorological factors, such as long and short-wave radiation, humidity, air temperature, and wind speed.

2.2.2 Direct measurements of potential evaporation

Meteorologists and hydrologists commonly perform direct measurements of evaporation. Since the potential evaporation generally depends on the water availability and the atmospheric demand above its surface, many simple devices were developed to determine the potential evaporation rate at the location of interest. Among those, the atmometers and pan evaporation are the most widely used.

Atmometers

The potential evaporation can be directly measured using the atmometers. They are small paper or porous ceramic evaporating surfaces provided with a continuous water supply. They are either black or white and respond quickly to atmospheric conditions, including radiation, wind speed, and humidity. Atmometers are portable, inexpensive, and can provide a quick indication of potential evaporation. Rosenberg et al. (1983) reported that atmometers reasonably estimate potential evaporation. Nevertheless, they are hypersensitive to wind and radiation, resulting in highly variable results. Figure 2.2 shows an illustration of the atmometers device.

Pan evaporation

The potential evaporation can also be measured directly using one of the most straightforward and widely used standard evaporimeter devices, the evaporation pan. It consists of a shallow water-filled container placed on the ground at a specific location, usually a weather station. The amount of water evaporated daily can be obtained by measuring the water volume per unit area of the pan that must be added to bring the water surface back up to a marked level. The

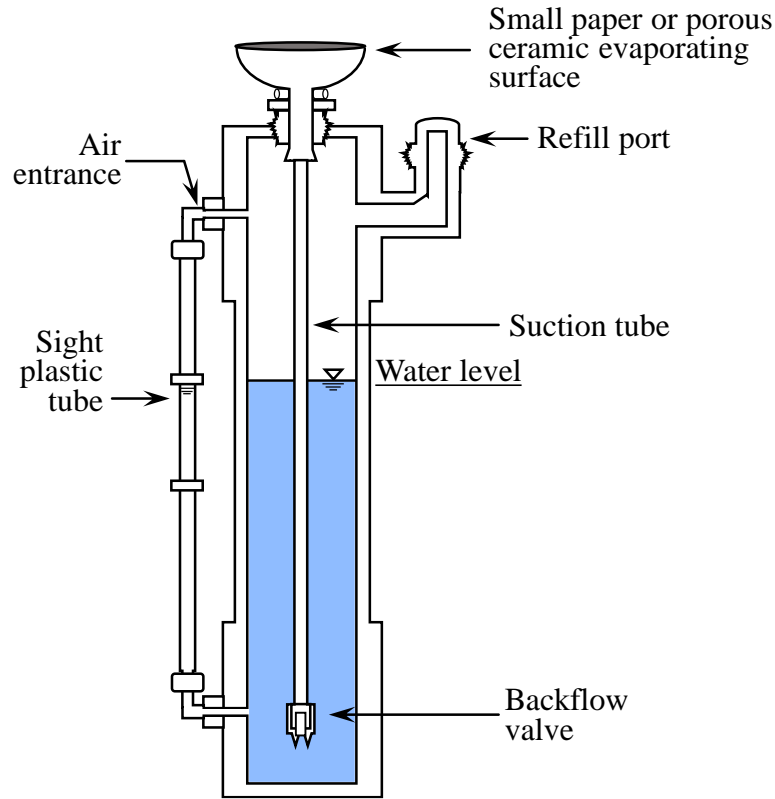


Figure 2.2: Atmometer device. (Altenhofen, 1985)

evaporation pan is subject to the integrated effects of net radiation, wind velocity, temperature, and relative humidity. Those are usually recorded at weather stations along with precipitation events and probably other variables. Figure 2.3 shows the ‘Class A’ pan, a standardized evaporation pan introduced by the U.S. Weather Bureau. A cylindrical container with a depth of 25.4 cm and a diameter of 121.9 cm, accurately leveled at a flat and free from obstructions site (Hillel, 2004).

Numerous researchers utilized the concept of the evaporation pan to conduct model testing in laboratories (Alowaisy and Yasufuku, 2018; Wilson et al., 1994). Generally, such evaporation pans are used to determine the potential evaporation under specific testing conditions while conducting other model testing related to geotechnical, agriculture, or hydrology. Usually, the experimental evaporation pans have an identical surface area and, sometimes, the geometry of the model testing setup. They are installed adjacent to the setup and subjected to similar environmental conditions. They are filled and replenished with water continuously during testing. The potential evaporation rate is usually determined based on the change in mass of the testing pan.

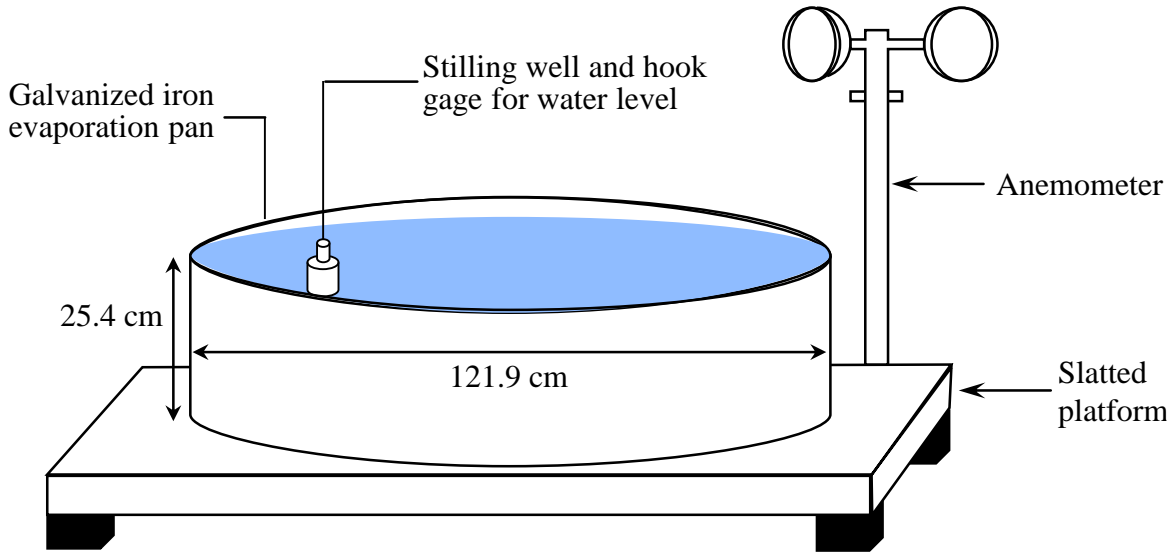


Figure 2.3: Standard U.S. Weather Bureau ‘Class A’ evaporation pan. (Alsumaiei, 2020)

2.2.3 Determination methods of the potential evaporation

Various indirect methods were developed in the literature to determine the potential evaporation rate. The large body of methods is based on empirical and semi-empirical methods developed using different physical concepts. The indirect methods are mainly classified as (1) energy balance methods, (2) mass transfer methods (aerodynamic), and (3) a combination of energy balance and aerodynamic methods. Wilson (1990) differentiated between climatological-based methods and micrometeorological methods. The latter evaluates the potential evaporation rate at a point or within some local area. For geotechnical and geo-environmental engineering applications, climatological-based methods are more acceptable because they require routine climate data, such as relative humidity and average temperature. They combine the effect of many microclimates within a regional scale. Other researchers further classified the climatological-based methods based on input parameters used for determination, including radiation-based methods, temperature-based methods, and other combined methods involving both approaches (Singh and Xu, 1997; Xu and Singh, 2001, 2000). Table 2.1 presents a chronological overview of some methods used in geotechnical engineering to estimate the potential evaporation with their classification indicated. Each of them has its advantages and limitations. This summary is not exhaustive yet shows that many computational equations are available. In the current research, the following equations were selected because of their popularity in the geotechnical and geo-environmental engineering fields, where many of them were later extended for determining the evaporation rate from soil surfaces.

Table 2.1: Determination methods of the potential evaporation

Method and classification	Parameters
<u>Dalton-type equation</u> (Dalton, 1802) <i>Mass transfer, micrometeorological method</i>	
$PE = f(u)(P_v^{\text{sat}} - P_v^{\text{air}}) \quad (2.2)$	f(u) : transmission function, which depends on the mean wind speed and turbulent mixing; P_v^{sat} : Surface saturation vapor pressure; P_v^{air} : Vapor pressure at the near ground surface air.
<u>Bowen Ratio Energy Balance method [BREB]</u> (Bowen, 1926) <i>Energy balance, micrometeorological method</i>	
$PE = \frac{Q_n}{\rho_w L_v (1+R)} \quad (2.3)$	PE : Potential evaporation [m/s]; Q_n : Net radiation [J/m ² . s]; ρ_w : water density [kg/m ³]; L_v : Latent heat of evaporation [J/Kg]; R : Bowen ratio.
<u>Rohwer equation</u> (Rohwer, 1931) <i>Mass transfer, aerodynamic method</i>	
$PE = 0.44(1 + 0.118u)(P_v - P_v^a) \quad (2.4)$	PE : Potential evaporation [mm/day]; u : wind speed [miles/h]; P_v : evaporating surface vapor pressure; P_v^a : vapor pressure above the surface.
<u>Thornthwaite and Holtzman equation</u> (Thornthwaite and Holzman, 1942) <i>Aerodynamic, micrometeorological method</i>	
$PE(x_0, y_0) = C u_2^{0.76} x_0^{0.88} y_0 (P_v - P_v^a) \quad (2.5)$	PE : Potential evaporation [mm/day]; x₀, y₀ : evaporating area [m]; C : constant related to the temperature; u₂ : wind speed at 2 m [miles/day]; P_v : vapor pressure at the surface; P_v^a : vapor pressure above the surface unaffected by evaporation.
<u>Thornthwaite equation</u> (Thornthwaite, 1948) <i>Temperature-based, climatological-based method</i>	
$PE = 1.6 \left(\frac{L}{12} \right) \left(\frac{N}{30} \right) \left(\frac{10T_a}{30} \right)^a \quad (2.6)$	$a = (6.75 \times 10^{-7})I^3 - (7.71 \times 10^{-5})I^2 - (1.79 \times 10^{-2})I - 0.492;$ $I = \sum_{\text{month}=1}^{12} \left(\frac{T_a}{5} \right)^{1.514};$ PE : Potential evaporation [cm/month]; L : Length of daylight [hours]; N : Number of days in the month; T_a : mean monthly air temperature [°C].

Table 2.1 (Continued)

Method and classification	Parameters
Penman equation (Penman, 1948) <i>Combination method: energy balance and mass transfer (aerodynamic), climatological-based method</i>	
$PE = \frac{\Gamma Q_n + \eta E_a}{\Gamma + \eta} \quad (2.7)$	$E_a = 0.35(1 + 0.15W_w)(P_{vsat}^{air} - P_v^{air})$ [m/s]; PE : Potential evaporation [m/s]; Γ : the slope of the saturation vapor pressure; versus temperature curve [mmHg/°F]; Q_n : net radiation at the surface [m/s]; η : psychrometric constant [0.27 mmHg/°F]; W_w : wind speed [km/h]; P_v^{air} : near-surface air vapor pressure.
Blaney and Criddle equation (Blaney and Criddle, 1950) <i>Temperature-based, climatological-based method</i>	
$PE = p(0.457T + 8.13) \quad (2.8)$	PE : Potential evaporation [mm/day]; p : mean annual fraction of day that is in daylight; T : mean daily temperature [°C].
Jensen and Haise equation (Jensen and Haise, 1963) <i>Radiation-based, climatological-based method</i>	
$PE = (0.025T + 0.078) \frac{R_s}{59} \quad (2.9)$	PE : Potential evaporation [mm/day]; T : air temperature [°C]; R_s : incident solar radiation [mm/day].
Penman-Monteith equation (Monteith, 1965) <i>Combination method: energy balance and mass transfer (or aerodynamic), climatological-based method</i>	
$PE = \frac{1}{\lambda} \left[\frac{\Gamma A + \rho_a c_p D / r_a}{\Gamma + \eta(1 + r_s / r_a)} \right] \quad (2.10)$	$A = R_n - G$ [MJ/m ² .day] PE : Potential evaporation [MJ/m ² .day]; Γ, η : same as in Penman (1948) [kPa/°C]; ρ_a : air volume heat capacity [MJ/m ³ °C]; c_p : vapor pressure deficit [kPa]; D : fraction of the day that is in daylight; r_s, r_a : canopy and aerodynamic resistances to vapor transfer [day/m].
Priestley-Taylor equation (Priestley and Taylor, 1972) <i>Energy balance, radiation-based, climatological-based method</i>	
$PE = \alpha \frac{\Gamma}{\Gamma + \eta} (R_n - G) \quad (2.11)$	PE : Potential evaporation [mm/day]; α : empirical constant; Γ, η : same as in Penman (1948); R_n : net radiation [mm/day]; G : soil heat flux [mm/day].

Mass transfer and aerodynamic models

The mass transfer approach has the most profound historical roots as its origin is attributed to Dalton at the turn of the 19th century (Rosenberg et al., 1983; Gray, 1970). The simplest form of the mass transfer method is written as a Dalton-type equation, equation 2.2. Many researchers have proposed ways to determine the transmission function, $f(u)$. It can be evaluated based on the boundary layer mixing theory (Penman, 1948; Rohwer, 1931), which transforms the method into an aerodynamic approach, as in Rohwer equation, equation 2.4. (Thornthwaite and Holzman, 1942) were among the first to propose the aerodynamic approach for evaluating evaporation. The method determines the potential evaporation based on the wind speed and the relative humidity profiles. It is not applied to routine practice due to the high accuracy required when measuring humidity, temperature, and wind speed, as shown in equation 2.5. However, the method retained its appeal because it is physically based on the first principles of classical fluid mechanics (Rosenberg et al., 1983). Thornthwaite (1948), equation 2.6, considers the mean monthly temperature the most stable parameter since it is a function of solar radiation and moisture availability. It is a simple method that does not require sophisticated data and has proven reliable for many applications (Sattler, 1989). One of its limitations is the estimation of evaporation at large-scale areas over at least a month, yet it remained one of the most popular methods. Blaney and Criddle (1950), equation 2.8, used variables of mean daily air temperature and the fraction of the daily sunlight to compute the potential evaporation, while Jensen and Haise (1963), equation 2.9, considered the air temperature and the incident solar radiation.

Energy balance models

Bowen (1926) introduced the ratio between the sensible heat flux (Q_H) and latent heat flux (Q_E) as the Bowen ratio. The ratio was then substituted in the energy balance equation to determine the latent heat flux as in equation 2.3. For many general applications, the Bowen Ratio Energy Balance method (BREB) accurately estimates the potential evaporation rates. However, Rosenberg et al. (1983) and Blad and Rosenberg (1976) reported that under regional sensible heat advection conditions, the BREB method underestimates evaporation. Similarly, Priestley and Taylor (1972) recognized that sensible and latent heat over large-scale surfaces could be accurately described in terms of energy balance alone. The empirical constant, α , in equation 2.11 is considered 1 for a particular case where the profiles of specific humidity and temperature are in equilibrium. However, an average value of 1.26 for well-watered land and open-water surfaces is often used (Rosenberg et al., 1983). The method was confirmed to be reliable in humid areas. However, some studies demonstrate that it needs modification under

conditions of strong advection (Jury and Tanner, 1975; Rosenberg et al., 1983; Shouse et al., 1980).

Combination methods

Penman (1948) was the first researcher to combine the energy balance and aerodynamic method to formulate a potential evaporation determination equation, equation 2.7. It is simple and easy to use, requiring commonly measured weather parameters that incorporate the effect of several important factors, including air temperature, relative humidity, and wind speed, while the heat budget or all net radiation is determined empirically. Linsley et al. (1958) pointed out that Penman's equation overestimates the evaporation rate for low winds and humid conditions and underestimates the evaporation rate for windy and dry conditions. However, it remained the most popular and widely used combination method to determine the potential evaporation from an open surface (Rosenberg et al., 1983). The Penman-Monteith equation (Monteith, 1965) is an enhancement of the original Penman equation and has been widely used in agriculture-related disciplines since it considers the canopy and aerodynamic resistances, as shown in equation 2.10.

2.3 Actual Evaporation Flux

2.3.1 Actual evaporation process and its stages

Throughout the years, the actual evaporation has been of broad interest to researchers and engineers. However, it is a complicated natural process, and understanding its mechanisms has been challenging. Many researchers described the phenomenon based on its macroscale behavior. Many have tried defining its complicated micro-mechanisms in recent decades to reflect on its macroscale behavior. Therefore, the following subsection reviews the actual evaporation macroscale and microscale definitions to contemplate the process's evolution and dynamics.

2.3.1.1 Macroscale: Actual evaporation curve

The actual evaporation defines the rate at which water liquid transforms to vapor from the soil surfaces to the atmosphere. It involves heat and mass (moisture) transfer at the soil-atmosphere boundary and within the soil profile. It was widely discussed in the literature that evaporation from soil profiles occurs at almost the same rate as the potential evaporation when the water supply to the ground surface is unrestricted (Penman, 1948; Priestley and Taylor, 1972). However, the complexity grows as the soil surface begins to dry and becomes unsaturated due

to the limited water supply to the surface (Gray, 1970; Wilson et al., 1994). Similar to potential evaporation, actual evaporation to occur requires three conditions. Firstly, the continuous energy supply at the surface. Secondly, the aerodynamic function which combines the vapor pressure gradient and the turbulent mixing above the soil surface. Both conditions depend on the micrometeorological factors at the boundary and are similar in the potential and actual evaporation process. However, the third condition, water availability, becomes significant when evaporation occurs from soil surfaces. When the soil becomes unsaturated, the water becomes restricted due to capillarity, which is dominant in moist soils, and adsorption, which is dominant in dry soils (J. R. Philip, 1957). Soil holds onto and store water in its pores by the negative pore water pressure or matric suction. With time, delivering water to the surface becomes more challenging because the unsaturated soil's permeability can become extremely low, and matric suction increases. The net result of the competition between the weather-related factors and soil suction causes a reduction in evaporation from potential conditions to the net moisture flux or actual evaporation. This process depends on the soil subsurface conditions, including water content and potential, soil hydraulic properties, and groundwater level (Hillel, 1980). Therefore, the evaporation rate from soils at any time during drying is either equal to the potential evaporation or a function of the soil-moisture distribution, whichever is less (J. R. Philip, 1957).

Two general conditions of water evaporation from bare soil profiles were studied in the literature. One is with the presence of a shallow groundwater table at a constant or variable depth, and the other is with the absence of the water table or when it is too deep to influence evaporation. When the water table is close to the surface, a continuous water flow occurs from the saturated zone through the unsaturated soil to the surface. While this flow is steady, evaporation does not change the soil's moisture content. This steady-state upward flow of water through the unsaturated soil from a water table follows the Darcy-Buckingham law (Buckingham, 1907):

$$q = -K(\theta) \frac{\partial H}{\partial z} = -K(\theta) \left(\frac{\partial h}{\partial z} + 1 \right) \quad (2.12)$$

where q is the steady-state evaporation rate or the water flow per unit time (m/s), h is the pressure head (m), z is the vertical distance from the water table (m), and $K(\theta)$ is the unsaturated hydraulic conductivity function (m/s), a function of θ , the water content. Equation 2.12 considers the soil-water pressure distribution in unsaturated soils where the hydraulic head (H) equals the summation of the matric suction (ψ) and the gravitational head (z). However, steady-state evaporation from bare soil surfaces is not typical, especially in drylands where the groundwater table is deep, and the recharge by precipitation or irrigation is rare. Therefore, the

water loss and the resulting upward flow are transient or unsteady without a groundwater table that can maintain the water connection with the surface. This flow causes the soil to dry and its moisture content to decrease continuously with progressive evaporation. In this case, the flow of water by Darcy-Buckingham is combined with the principles of water conservation in the soil profile to produce the general flow equation, Richards equation (Richards, 1931):

$$\frac{\partial \theta}{\partial t} = \frac{\partial}{\partial z} \left[K(\theta) \frac{\partial \psi}{\partial z} + K(\theta) \right] = \frac{\partial}{\partial z} \left[K(\theta) \frac{\partial \psi}{\partial z} \right] + \frac{\partial K}{\partial z} \quad (2.13)$$

Many researchers, including Fisher (2012), Keen (1914), and Pearce and Smillie (1974), observed that the unsteady-state evaporation process from a fully saturated bare soil surface under a constant atmospheric evaporative demand follows three distinctive stages. The stages mainly differ in duration and actual evaporation rate, which is the amount of water lost in a specific time interval. Figure 2.4 delineates a typical actual evaporation curve as described by many researchers (Hillel, 1980; Wilson, 1990), and the figures indicate the water-air phase distribution at each stage.

The constant rate stage, Stage 1, occurs when the soil is near-saturation and conductive enough to supply water to the evaporating surface to compensate for the evaporative demand. Its rate equals the potential evaporation from a free water surface under the same demand. Therefore, it attains the maximum evaporation rate of the process (Tran, 2013). Stage 1 is governed by the atmospheric conditions (J. R. Philip, 1957), and according to Hillel (1980), it can also be called the weather-controlled stage. In drylands, Stage 1 last only a few hours to a few days after

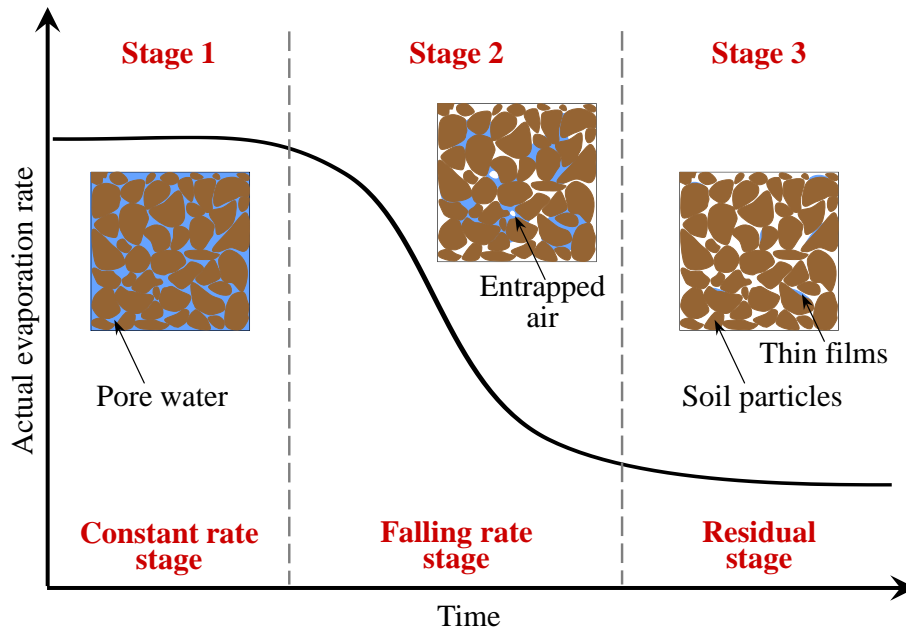


Figure 2.4: Actual evaporation stages and corresponding air-water phase distribution.

precipitation or irrigation events, typically within five days (Rosenberg et al., 1983). Stage 1 evaporation rate remains nearly constant as long as the moisture gradient or water flow toward the surface compensates for the decreasing hydraulic conductivity due to the reduction in the moisture content. At a critical point, the soil surface dries and reaches an air-dry level that equilibrates with the atmosphere. Thus, this limits the moisture gradient to the surface from further increase, resulting in a sharp drop in the evaporation rate announcing the onset of the falling rate stage, Stage 2 (J. R. Philip, 1957). During this stage, the evaporation rate decreases progressively below the potential evaporation rate, and it becomes limited and controlled by the soil profile's ability to supply water to the evaporation zone. Therefore, water supply becomes governed by conditions within the soil medium (J. R. Philip, 1957). Accordingly, Stage 2 can also be called the soil profile-controlled stage (Hillel, 1980). The evaporation rate continues decreasing until it converges gradually to a low value, announcing the residual stage, Stage 3. This stage can persist at a nearly constant low rate for many days, weeks, or months. During Stage 3, the soil profile becomes sufficiently desiccated, resulting in a discontinuous liquid phase. Therefore, the evaporation continues through vapor diffusion to the surface. Stage 3 is often called the vapor diffusion stage since the evaporation rate is controlled by the soil's vapor diffusivity (Hillel, 1980). Philip (1957) concluded that this stage is sensitive to the heat flow and the molecular adsorptive forces between the soil particles.

2.3.1.2 Microscale: Unsaturated layer and water transport mechanisms

The evaporation process from bare soil profiles was extensively discussed from a phenomenological point of view, as was reviewed in the previous subsection. However, such approaches neglect the detailed physics at the pore scale level and how these emerging microscale mechanisms affect the macroscale behavior of the evaporation process. The qualitative understanding of the pore mechanisms controlling the evaporation from soils has been known for over a century. Buckingham (1907) postulated the role of the capillary flow along 'films' in sustaining high evaporation rates and the consequent rate reduction after the breakup of such "water films." Similarly, Sherwood (1929) has identified two mechanisms responsible for reducing the evaporation rate during Stage 2. One is the limited vapor diffusion across a 'surface air film' at the boundary, and another is the resistance due to the internal flow in the porous medium. However, notable breakthroughs have thrived in the past few decades. Technological innovations, including pore-scale modeling (Prat, 2002), Pore network studies (Yiotis et al., 2005), direct X-ray tomography (Shokri et al., 2010a), and neutron radiography

(Shokri et al., 2008), allowed soil scientists and researchers to improve the microscale knowledge, where new insights were offered on the physics involving in the evaporation process at the pore scale level.

Consequently, another classification of the evaporation stages was defined based on the pore scale models. Three-dimensional (3D) invasion percolation model, Le Bray and Prat (1999) and Yiotis et al. (2006) related the evaporation stages to the phase distribution in the soil profile. The concept was further extended to predict the dynamics of the unsaturated soil layer and to study the dominant water transport mechanism during each stage. Figure 2.5 delineates a typical actual evaporation curve, with schematic diagrams explaining the soil profile configuration at each evaporation stage, as was defined by many researchers (Lehmann et al., 2008; Or et al., 2013; Shokri et al., 2009).

Generally, water loss during evaporation from fully saturated bare soil surfaces induces an air invasion into emptied soil pores (Or et al., 2013). This early evaporation stage is called the ‘initial drying period’ in the 3D invasion percolation model. It defines the preliminary drying once the water content at the soil surface starts decreasing. Due to weaker capillary forces holding the water in larger pores at the soil surface, water filling larger pores starts getting lost preferentially while the gas phase invades with a pressure value called the air-entry value

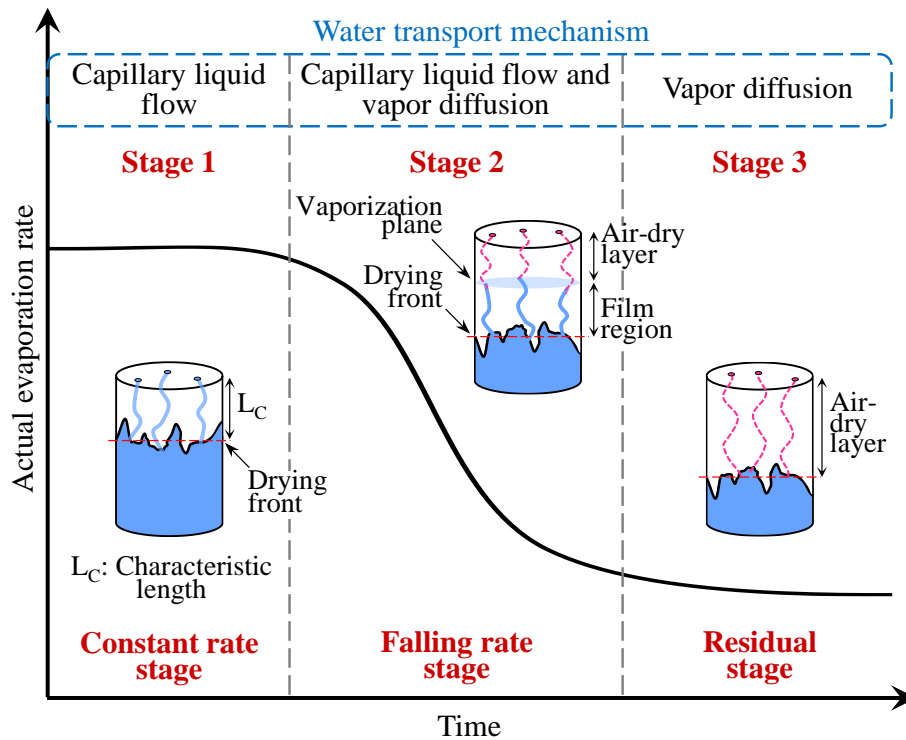


Figure 2.5: Actual evaporation stages and unsaturated layer configuration.

(AEV). The receding water in the larger pores forms a dynamic interface between the saturated and partially air-filled pores, known as the drying front (Lehmann et al., 2008). Simultaneously, the water menisci in the smaller pores persist at the soil surface. The capillary pressure difference between larger pores at the drying front and smaller pores at the surface induces liquid water flow toward the surface (Scherer, 1990). Yiotis et al. (2001) referred to this flow process as ‘capillary pumping,’ which keeps the drying front hydraulically connected to the soil surface. The liquid-filled pores that hydraulically connect the drying front to the evaporating surface, the soil surface at this stage, form the so-called film region (Yiotis et al., 2003). With the film region connected to the surface, the soil profile can sufficiently supply water by capillarity and satisfy the atmospheric demand, which keeps the actual evaporation almost constant and sustained at a high rate. Stage 1, the constant rate stage, is called the “Spanning liquid cluster evaporation regime,” where water flows from the interior through a network of liquid-filled pores (Yiotis et al., 2006).

The capillary flow within the film region during Stage 1 is subjected to a force balance between capillarity, gravitational and viscous forces. This liquid flow remains attainable as long as the capillary driving forces are more significant than gravitational and viscous forces. Lehmann et al. (2008) adopted the simplified hydraulically interacting pair of capillaries (Scherer, 1990) to conceptualize this phenomenon at a microscale level, as described in Figure 2.6 (a). Consequently, the concept was generalized for soil, represented by its hydraulic functions at the macroscale level, defined in Figure 2.6 (b). Lehmann et al. (2008) proposed the gravity-limiting length (L_G), the maximum vertical distance over which liquid-filled pores connect the drying front to the surface and sustain direct evaporation at the surface, and the viscous length (L_V) over which viscous dissipation becomes limiting combining the effects of hydraulic conducting cross-section and evaporation rate. Both lengths are expressed as equivalent distances between the evaporating surface and the drying front position at the end of Stage 1 and are dependent on the width of the soil pore size distribution. The conceptual and parametric representation of the characteristic length (L_C) that involves L_G and L_V marks the end of Stage 1 and the transition to a slower and diffusion-limited Stage 2.

Lehmann et al. (2008) explained that the width of the pore size distribution of a soil profile is often deduced from the drying Soil Water Characteristic Curve (SWCC), shown in Figure 2.7, where the van Genuchten (1980) fitting model was used to parameterize the SWCC as follows:

$$\Theta = \frac{\theta - \theta_r}{\theta_s - \theta_r} \quad (2.14)$$

$$\Theta = \frac{1}{[1 + (-\alpha h)^n]^m} \quad (2.15)$$

$$m = 1 - \frac{1}{n} \quad (2.16)$$

where h is the pressure head, Θ is the normalized water content, θ is the volumetric water content, while θ_s and θ_r are the saturated and residual volumetric water content. α , n , and m are van Genuchten fitting parameters. α is mathematically expressed as the inverse of the air-entry pressure. n is a function of the pore size distribution and reflects the slope of the SWCC, while m is related to the symmetry of the SWCC sigmoidal curve shape. Lehmann et al. (2008) elucidated that the capillary pressure at the drying front remains at the air-entry value (h_b) equivalent to the air-entry value of the drying SWCC (AEV). On the other hand, the air phase starts invading the smaller pores attained at the soil surface with a critical capillary pressure (h_r) equivalent to the pressure at the residual water saturation of the SWCC. Based on that, the maximum range of hydraulically connected water-filled pores can be deduced from the shape

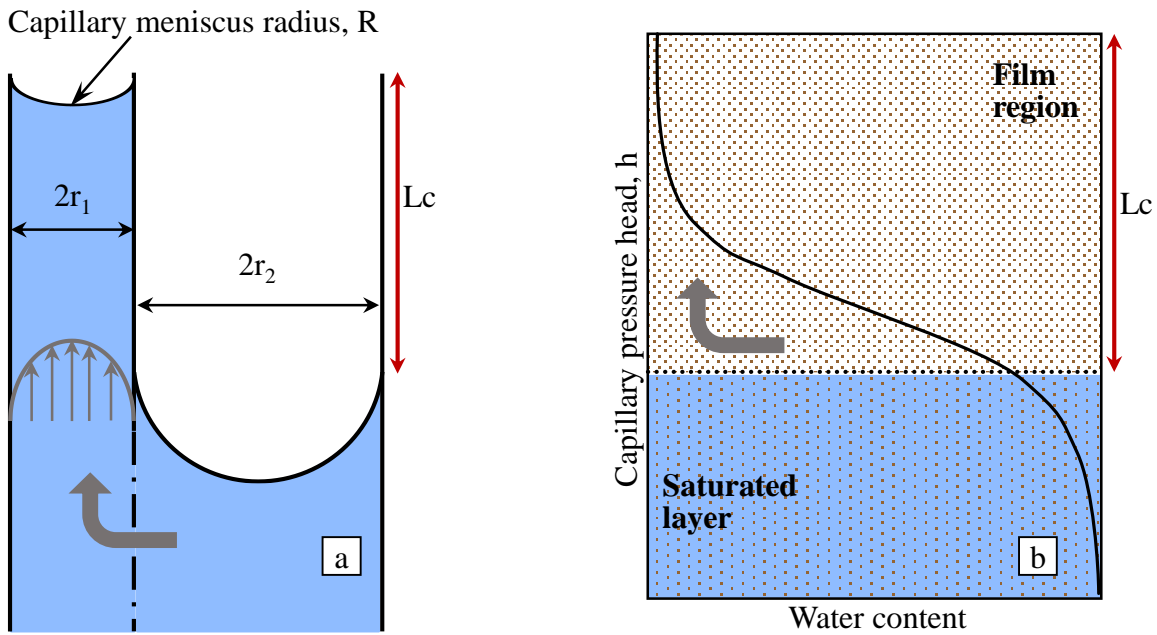


Figure 2.6: L_c and Stage 1 conceptualization: (a) simplified hydraulically interacting pair of capillaries. (b) homogeneous soil profile. (Lehmann et al., 2008)

of the SWCC or by the linearization between these two characteristic pressures, as shown in Figure 2.8. Therefore, the characteristic length of a soil profile can be determined as follows (Lehmann et al., 2008):

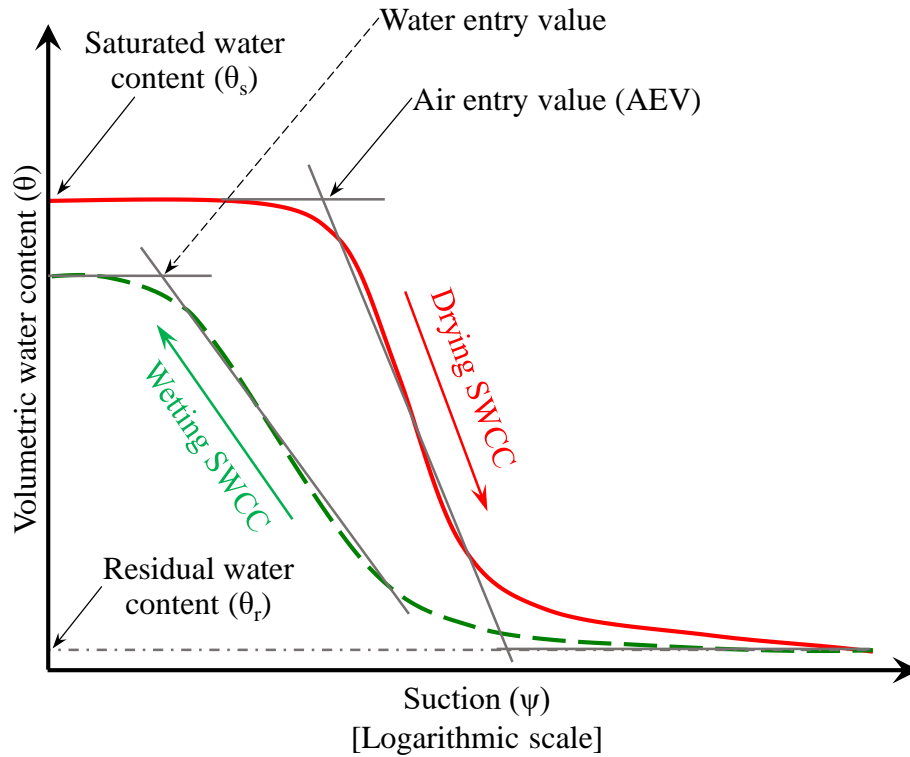


Figure 2.7: Typical initial drying and main wetting SWCCs.

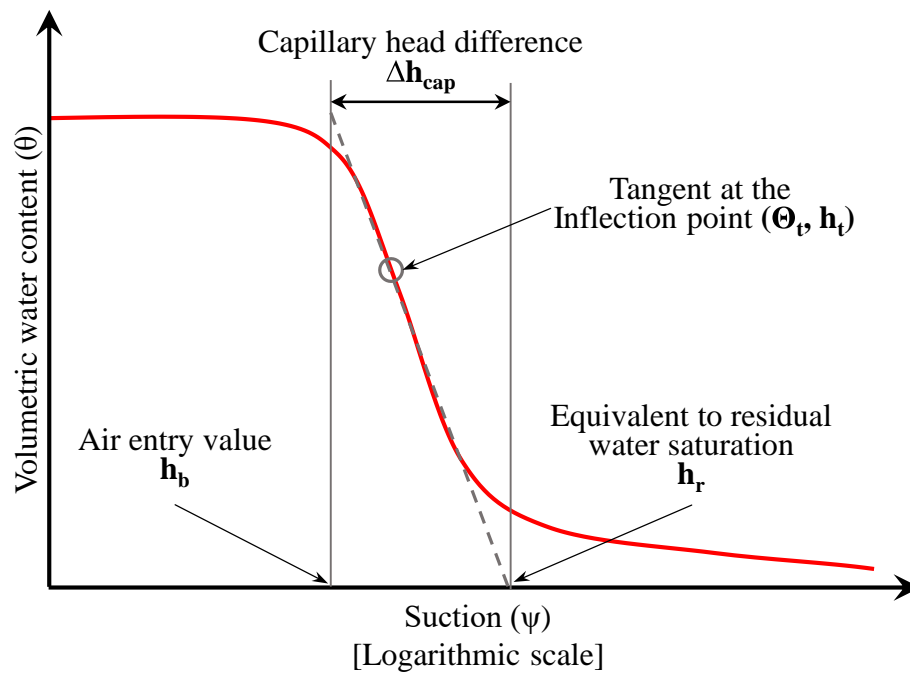


Figure 2.8: Linearization of the drying SWCC to determine L_C . (Lehmann et al., 2008)

$$L_C = \frac{2\sigma}{\rho g} \left(\frac{1}{r_1} - \frac{1}{r_2} \right) \quad (2.17)$$

where σ is the water-air surface tension, ρ is the water density, g is the gravitational acceleration, r_1 is the smallest drainable pore, and r_2 is the largest drainable pore, which can be calculated as follows:

$$r_1 = \frac{2\sigma}{\rho g (h_b + \Delta h_{cap})} \quad (2.18)$$

$$r_2 = \frac{2\sigma}{\rho g} \alpha \quad (2.19)$$

$$\Delta h_{cap} = h_{min} - h_b = \frac{1}{\alpha (n-1)} \left(\frac{2n-1}{n} \right)^{\frac{2n-1}{n}} \left(\frac{n-1}{n} \right)^{\frac{1-n}{n}} \quad (2.20)$$

$$h_b = \frac{1}{\alpha} \left(\frac{n-1}{n} \right)^{\frac{1-2n}{n}} - \Delta h_{cap} \quad (2.21)$$

$$L_V = \frac{L_G}{1 + \frac{e_o}{K(\theta)}} \quad (2.22)$$

where Δh_{cap} is the capillary head difference, e_o is the evaporation rate, and $K(\theta)$ is the unsaturated hydraulic conductivity function. For low evaporation rates with a nearly hydrostatic profile, the distribution of the liquid phase above the drying front is described by the soil water characteristics and the range of hydraulically connected pores. Therefore, Δh_{cap} determines the depth of the drying front at the end of Stage 1, where $L_C = L_G$ and the viscous losses become negligible. The concept of L_C was extended to predict the end of Stage 1 for double and multi-layered soil profiles (Shokri et al., 2010b). A double-layered soil profile's composite characteristic length (L_{Comp}) can be determined using the algorithm shown in Figure 2.9.

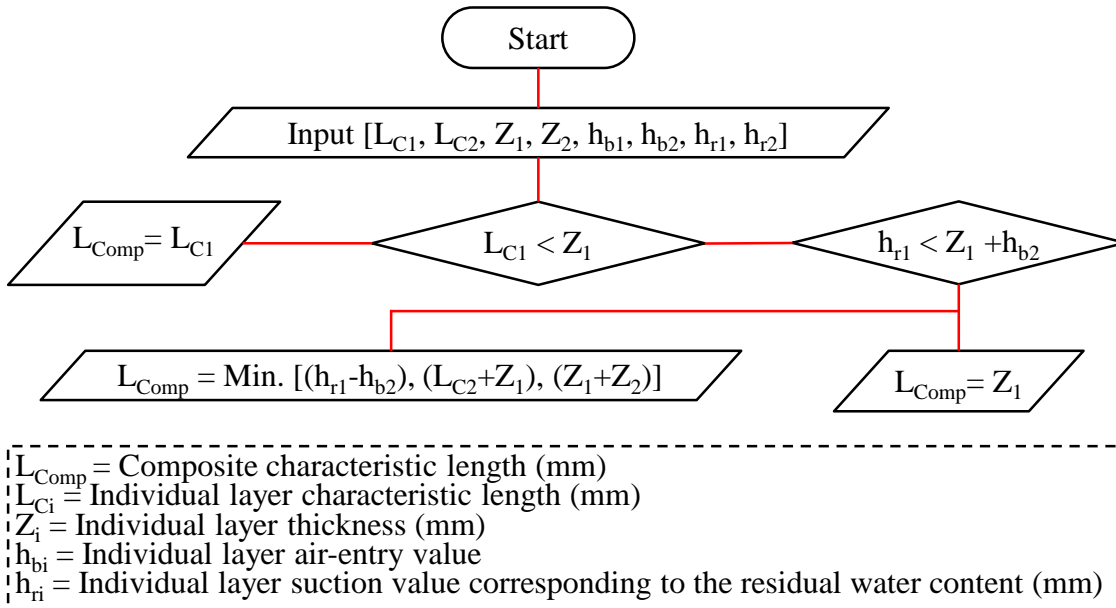


Figure 2.9: Determination of L_{Comp} for double-layered soil profiles. (Shokri et al., 2010b)

Following the disruption of the hydraulic continuity between the drying front (L_C) and the surface at the end of Stage 1, the last menisci at the soil surface recede into the soil profile. Consequently, a new vaporization plane is formed below the soil surface, at which water diffuses as vapor through the air-dry layer to the surface and from there into the atmosphere (Shokri and Salvucci, 2011; Yamanaka et al., 1997). The slowly receding vaporization plane remains hydraulically connected to the drying front below via capillary-induced liquid flow through the film region. Figure 2.10 shows a schematic diagram of a soil saturation profile during Stage 2, indicating the unsaturated layer configuration and the dominant water transport mechanism. The transition into a less sufficient water supply transport mechanism (vapor diffusion) and the gradual increase in the length of the diffusion pathways from the receding vaporization plane to the surface result in a continuous decrease in the evaporation rate during Stage 2 (Or et al., 2013). Therefore, the falling rate stage (Stage 2) is also called the “Disconnected liquid cluster evaporation regime,” where it is mainly dominated by the dissolution of liquid clusters close to the surface Yiotis et al. (2006). Stage 2 is followed by a diffusion-dependent Stage 3, the residual stage. A little was discussed in the literature regarding Stage 3. However, based on Yiotis et al. (2006), it is also called the “Receding front regime,” where the soil profile is left with a dry surface, and a receding front is distinguished.

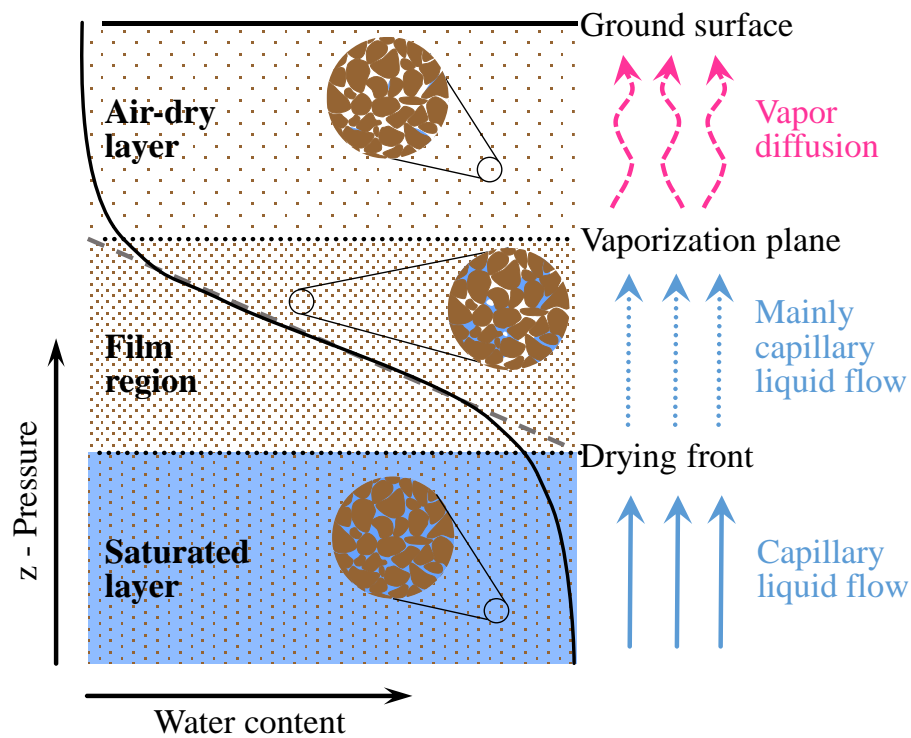


Figure 2.10: Schematic diagram of a soil saturation profile during Stage 2.

Notwithstanding the efforts to predict the end of Stage 2 and the onset of Stage 3, a comprehensive study analyzing the drying front and vaporization plane dynamics and considering the interaction between them is still lacking in the literature. Investigating the unsaturated layer and its boundaries during Stage 2 and Stage 3 allows the accurate prediction of their evaporation rates, which is promising for many geotechnical engineering applications.

2.3.2 Factors influencing the actual evaporation behavior

Evaporation from soils is a complicated phenomenon that involves water transport as liquid and vapor through the soil profile and at the surface. Due to the two fluid phases involved in the process, Van Brakel (1980) highlighted the complexity of the factors that influence the process. With the absence of vegetation cover, the influencing factors can be divided into two categories, external factors representing the demand at the surface and internal factors representing the supply from within the soil profile.

External influencing factors

A continuous energy supply and aerodynamic function at the soil surface are the first two conditions required for evaporation to occur. Both depend on the micro-meteorological conditions at the soil surface and represent the external factors influencing the evaporation process and its behavior. The literature has extensively studied the effect and combined effect of the external factors on the process, including solar radiation or absorbed energy (Heck et al., 2020), temperature or emitted energy (Gilliland, 1938), relative humidity (Teng et al., 2014), and wind speed (Davarzani et al., 2014).

Generally, solar radiation increases the soil surface temperature, thus, providing water molecules at the surface with more energy. Under such conditions, water molecules' kinetic energy increases, allowing them to evaporate as vapor into the adjacent air boundary layer. However, Wang (2006) concluded that at low wind speeds (< 2 m/s), the net radiation influence tends to be minimal due to insufficient air mixing. Kondo et al. (1992) and Yamanaka et al. (1997) confirmed that the evaporation rate increases with the increase of the wind speed being more sensitive during Stage 1 when the soil is still moist. However, at the onset of Stage 2, the soil resistance becomes much larger than the aerodynamic resistance at the surface, making the evaporation rate less sensitive to wind speed. The aerodynamic resistance describes the restriction for water vapor to diffuse from the soil surface into the adjacent air surrounding the surface. The concept became helpful in explaining the evaporation phenomenon when the topsoil moisture recedes (Aluwihare and Watanabe, 2003; Kondo et al., 1990a).

Moreover, the vapor pressure deficit between the soil surface and surrounding air becomes the evaporation flux driving force. Once the vapor concentration at the soil surface reaches equilibrium with the adjacent air, the air turbulence near the surface becomes the dominant factor, where the air movement stirs the moist air layer adjacent to the soil surface and mixes it with the upper dryer layers (Hillel, 1980). The vapor deficit is a function of the relative humidity, where Kayyal (1995) confirmed that high relative humidity corresponds to a lower initial constant evaporation rate and shorter duration of Stage 1, while the influence tends to be minimal during Stage 2.

Internal influencing factors

Water availability is the third condition required for evaporation to occur, and from soil profiles, it is a function of the soil's ability to supply water to the surface. Water supply depends on the soil properties and represents the internal factors influencing the evaporation process and its behavior. The internal factors are summarized in the soil's physical and hydrological properties. Several studies investigated the influence of the retention properties, suction gradient (Wilson et al., 1997), hydraulic conductivity (Wilson et al., 1994), saturated and residual volumetric water contents, soil texture (Lehmann et al., 2018), void ratio, soil temperature (Ernest K. Yanful and Choo, 1997), among others.

Wilson (1990) concluded that the soil texture significantly affects evaporation, especially at the onset of Stage 2, where for coarse-grained soils such as sand, the evaporation rate drops suddenly at the onset of Stage 2, while a prolonged gradual declination occurs from clayey soils. Hillel and van Bavel (1976) reported that fine-grained soils exhibit longer durations of Stage 1, resulting in higher cumulative water loss. Yanful and Choo (1997) and Wilson (1990) experimentally studied the behavior of the soil temperature during drying. It was concluded that under constant atmospheric demand at the surface, soil temperature decreases during the early stages of evaporation, attaining the coolest temperature at the soil surface. However, the temperature increases, exceeding its initial value at later evaporation stages, and the coolest point transfers to a depth below the soil surface. Wilson et al. (1994) explained that the temperature behavior is related to the heat sink provided by evaporation, where energy is required for the latent heat of vaporization at the evaporating surface, whether it is the soil surface during Stage 1 or extended front below the surface at later stages.

Soil suction is another property controlled by water content and soil properties. Wilson et al. (1997) concluded that the actual evaporation rate depends on the total suction at the soil

surface. From thin soil layers, it was observed that the evaporation rate drops at a soil suction value of around 3000 kPa and continues decreasing as the suction increases. It was explained that this behavior is related to the reduction in the relative humidity, causing a reduction in the absolute vapor pressure at the surface. However, when considering water flow through the soil profile and investigating the evaporation from soil columns, the results showed that the evaporation rate and relative humidity drop at two distinct suction values, which suggests that another mechanism is involved (Fredlund et al., 2015; Tran et al., 2016; Wilson, 1990). Moreover, Wilson et al. (1997) concluded that the evaporative fluxes from unsaturated soil surfaces at high suction values are less than those of saturated surfaces, which can be essential for geotechnical applications.

Mosthaf et al. (2014) studied the influence of porosity and other hydrological properties, including intrinsic permeability, thermal conductivity, temperature, capillary pressure, and relative permeability, on the evaporation process and the transition between Stages 1 and 2. The results concluded that higher porosity leads to lower effective thermal conductivity during Stage 1, therefore, a lower saturation vapor pressure at the surface. This results in lower evaporation rates and extended durations of Stage 1. On the contrary, during Stage 2, higher porosity results in higher evaporation rates due to larger pore space and effective diffusivity through the soil profile. Additionally, Wilson et al. (1994) concluded that increasing the saturated hydraulic conductivity extends Stage 1 while not influencing Stage 3, which is considered reasonable since Stage 3 is a diffusion-dependent stage.

Lehmann et al. (2018, 2008) mentioned the importance of the width of the pore size distribution in detecting the evaporation stages. It was concluded that wider pore size distribution extends the hydraulically connected pores from the drying front to the surface (L_c), resulting in a more prolonged Stage 1. In summary, the internal influencing factors are intercorrelated and complicated due to the two fluid phases of water, transporting through the liquid capillary and vapor diffusion within the tortuous structure of the soil profile. Many researchers highlighted the importance of studying the influence of the pore structure on the actual evaporation process. Notwithstanding the efforts to clarify its influence, a robust and comprehensive study is still lacking in the literature.

2.3.3 Direct measurement of the actual evaporation

Several devices and experimental setups were developed to directly measure the actual evaporation rate in-situ and in laboratories. Lysimeters and micro-lysimeters are widely accepted as in-situ testing devices. The thin soil section drying test and the drying soil column

test are widely used to investigate the actual evaporation in laboratories. While the atmospheric demand in the field is recorded continuously, several setups were developed to monitor the atmospheric conditions during experimental testing to further investigate the evaporation mechanism. The literature covers wind tunnels, environmental chambers, and climate control apparatus.

In-situ testing

Lysimeters have been used for hundreds of years to study crop water balance and evaluate evapotranspiration (FOA, 1982). They are the most direct method used to determine the field's evaporation rates and have been used by many researchers in recent years (Assouline et al., 2013; Dijkema et al., 2018; Heck et al., 2020). Lysimeters are large tanks defining a specific boundary of soil. They are installed or constructed in the field such that their surface is continuous with the natural ground and their soil mass is vertically and horizontally isolated from the surrounding natural soil. During testing, the precipitation rate is measured, runoff equals zero, and deep drainage is either measured or permitted. Therefore, the net change in mass is considered due to evaporation. There are two types of lysimeters: weighting and non-weighting, also known as floating lysimeters. The weighing lysimeter is installed on load cells and allows measuring the actual evaporation directly through the mass change due to water loss by evaporation. Figure 2.11 delineates a weighing lysimeter used by Fayer et al. (1997). However, the non-weighting lysimeter determines evaporation by calculating the water budget. Lysimeters vary in diameter from 1 to 6 m and from 1.6 m to several meters in depth. Small-size lysimeters are remolded as the natural ground stratigraphy in a drum and installed in the ground. On the other hand, large-size lysimeters are constructed after evacuating the natural ground, while a vertical seal is installed around the perimeter of the isolated profile of the natural soil. Gray (1970) and Rosenberg et al. (1983) state that carefully constructed and installed lysimeters assimilate well within natural evaporation fields.

The lysimeter was used in some studies for experimental testing. For instance, (Yamanaka et al., 1997) studied the influence of surface resistance over a weighing lysimeter while attaching its top to a wind tunnel. The lysimeter was instrumented with soil moisture sensors, thermometers, tensiometers (to measure the soil suction), heat probes, an inner soil hygrometer, and many other valuable devices. However, it is considered expensive and requires ample space in the laboratory, while other experimental alternatives exist.

Micro-lysimeters were introduced in the past few decades for the in-situ determination of evaporation rates and were used by many researchers (Boast and Robertson, 1982; Liu et al., 2002). They are usually constructed on load cells in the field and can be instrumented with other devices, such as the Time Domain Reflectometry probes (TDRs) or moisture sensors (Wythers et al., 1999). The micro-lysimeters are smaller than the regular ones, usually less than 1 m in diameter and depth. They are constructed by inserting a thin-walled cylinder into the ground. It is then removed with the sampled soil and sealed from the bottom. Finally, the well-sealed cylinder is installed in the same borehole over preinstalled load cells (Daamen and Simmonds, 1996; Uclés et al., 2013).

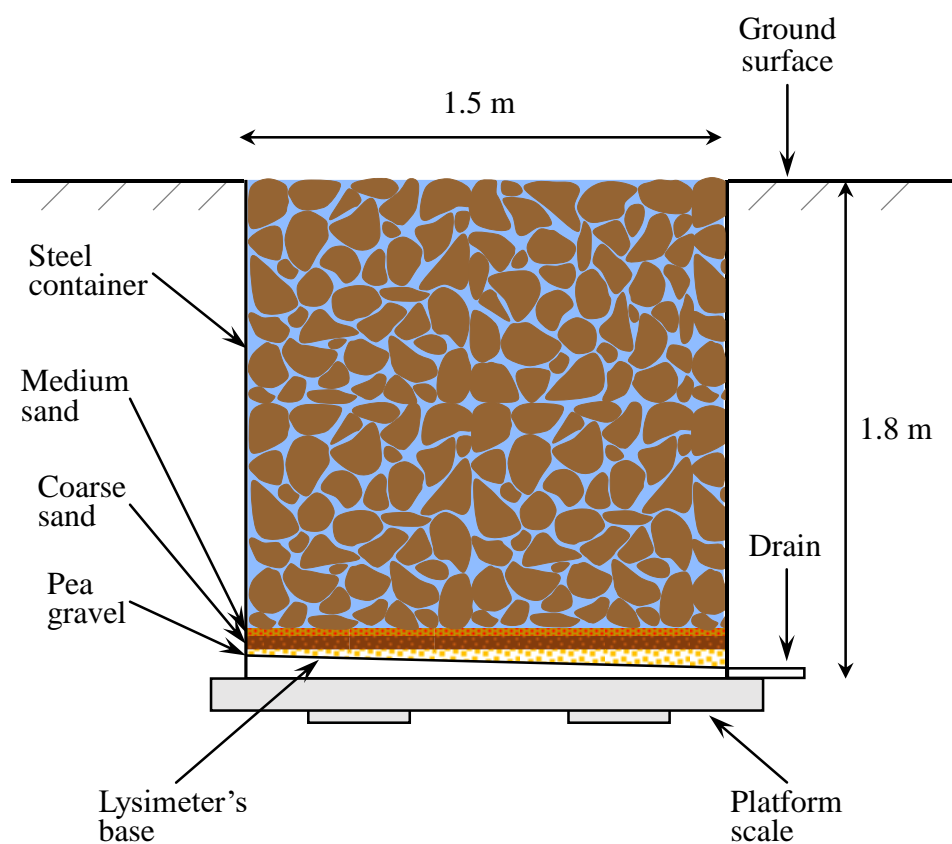


Figure 2.11: Weighing lysimeter test. (Fayer et al., 1997)

Experimental testing

For experimental investigation of the evaporation process, the thin soil section drying test, also known as the thin soil layer pan test, was widely adopted in the literature (Kondo et al., 1990a; Wilson et al., 1997). The test is usually conducted in a pan mounted on a weighing balance. The evaporation rate is measured based on the net change of the soil's mass from a fully saturated to a completely air-dry state. Figure 2.12 delineates the thin soil layer testing setup used by Wilson et al. (1997). The thin layer is prepared by uniformly dusting the soil in layers

onto the pan using a hand-held sieve until the required thickness is satisfied. The dry soil layers are then wetted to saturation using a fine uniform mist of distilled water. The pan's dimensions and soil layer thickness vary based on the study's objective. Generally, the soil layer thickness varies between 0.2 to 50 mm to minimize the water flow influence through the soil profile beneath the surface. Therefore, the thin soil layer drying test is used to study the actual evaporation as a soil-atmosphere boundary flux and a surface phenomenon. However, Kondo et al. (1990) addressed the necessity of considering water transport from deep soil layers to the surface when predicting the surface soil moisture with time, which cannot be satisfied using the evaporation pan.

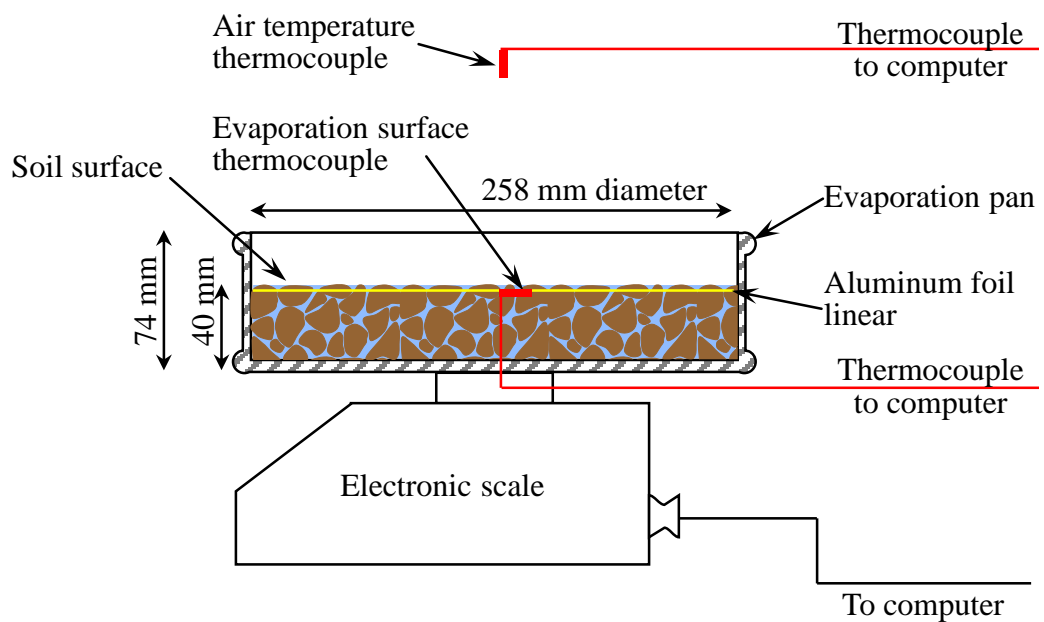


Figure 2.12: Thin soil section drying test. (Wilson et al., 1997)

Drying soil column tests have been used for over three centuries to study soil hydrological properties (De la Hire, 1703). More recently, soil columns have been used to evaluate transport models, mobility of contaminants in soil, and for investigating evapotranspiration (Lewis and Sjöström, 2010). Drying soil columns are discrete blocks of soil located outdoors or in a laboratory. They allow measuring the evaporation rate by weighing the soil column over time. It is used to reproduce the conditions encountered in the unsaturated zone and allows the control of a one-dimensional evaporation flow while maintaining the initial and boundary conditions during testing. Column tests are divided into two broad categories according to the method of construction: monolithic and packed columns. The monolithic columns use undisturbed soils sampled from the field (Strock and Cassel, 2001), while the

packed columns are prepared in the laboratory. Packed columns were utilized by numerous researchers, including Lehmann et al. (2008) and Alowaisy and Yasufuku (2018), while Wilson et al. (1994) setup is delineated in Figure 2.13. The main goal of packing is to produce a homogeneous soil column with a bulk density like naturally observed ones while avoiding the formation of stratifying layers or preferential flow pathways that can bias the testing results. The packing technique also varies based on the tested soil; dry or damp packing (Plummer et al., 2004), slurry packing (Powelson and Mills, 1998), and other less common techniques that involve wetting and drying cycles to assist compaction (Bowman, 1988). However, the selection of the construction methodology and column's material and dimensions highly depends on the study's objective and significantly impacts the results. Another advantage of the soil column tests is the ability to instrument the column with various sensors and instruments to extract information concurrently during drying. The instrumentations can be invasive and non-invasive. The invasive include TDRs, thermometers, pore water pressure gages,

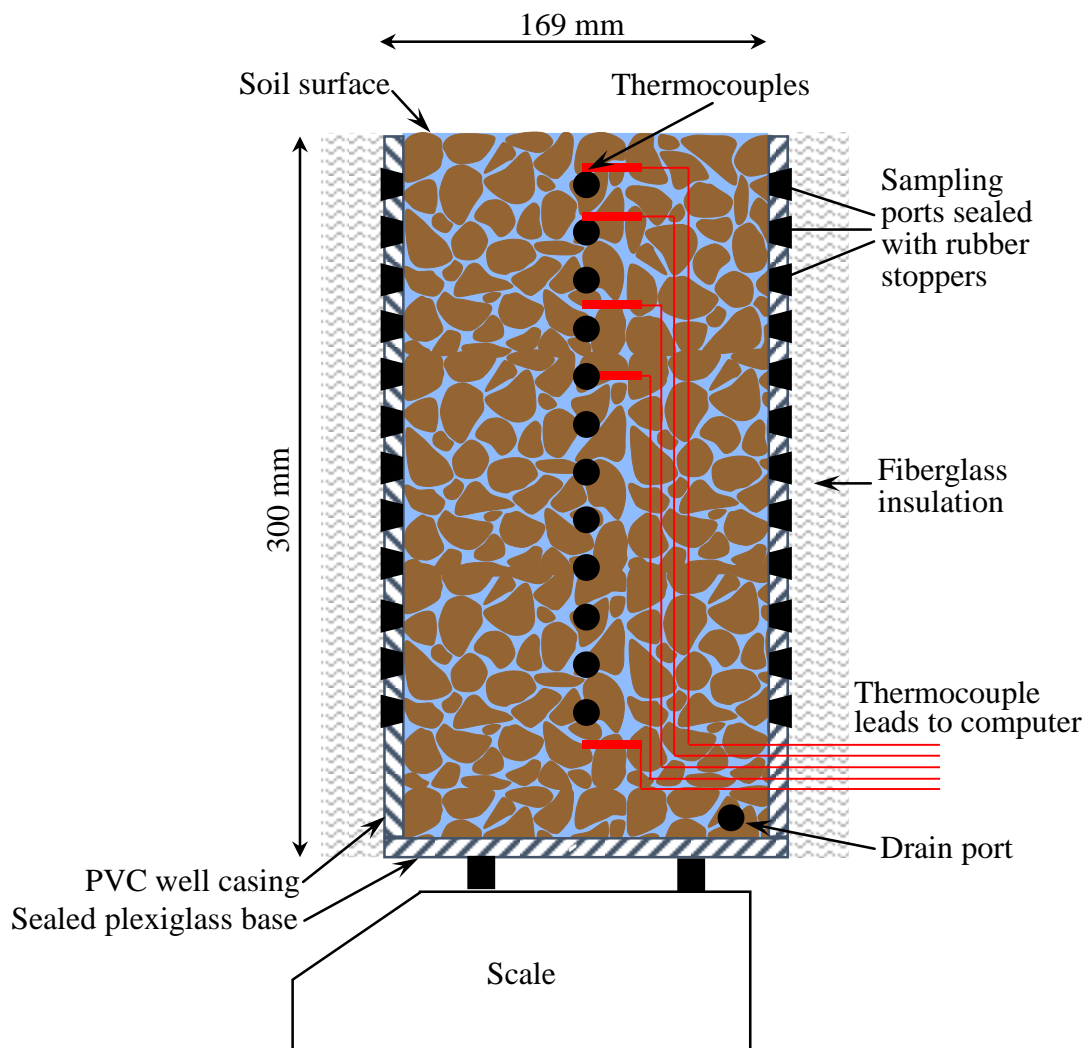


Figure 2.13: Drying soil column test. (Wilson et al., 1994)

tensiometers, or sampling ports to extract pore water, while the non-invasive include spectroscopy, microscopy, and X-ray. Despite the years of experience utilizing the soil columns, no standardization of experimental methods has occurred. However, the literature reviews the best practices in conducting soil column experiments to ensure better reproducibility of the experimental results (Crestana and Manoel Pedro Vaz, 1998; Lewis and Sjöström, 2010; Oliviera et al., 1996).

Experimental apparatuses for atmospheric demand control

Several experimental setups were developed in the literature to control and monitor the atmospheric conditions while conducting pan-drying tests and soil columns. The wind tunnel is a commonly used apparatus (Davarzani et al., 2014; Shahraeeni et al., 2012; Yamanaka et al., 1997). It allows the investigation of evaporation under controlled wind velocity. Additionally, the apparatus can be modified to control air temperature, relative humidity, and radiation supply (Yamanaka et al., 2004, 1997). Generally, a wind tunnel is composed of a fan chamber where a fan is mounted to control the wind speed. The wind then passes to an airflow reducer or an extension chamber followed by airflow straighteners. Both facilitate air transition from the fan chamber to the testing chamber to which the soil column or pan is attached. The design and dimensions of the apparatus vary based on the soil column or pan and the study's objective.

Another atmospheric demand-controlled setup is the environmental chamber. The fast air circulation box (Kohsiek, 1981; van de Griend and Owe, 1994), ventilated chamber (Mohamed et al., 2000), open chamber (Aluwihare and Watanabe, 2003), and environmental chamber (Cui et al., 2013; Song et al., 2013) are examples of the evaporation chambers that were developed and utilized for evaporation tests. The environmental chambers determine the evaporation rate based on the inlet and outlet absolute humidity variation. They are prepared by partially filling a tank of specific dimensions with soil, usually between 0.3 and 1.3 m³ in volume. The chamber is then connected with several climatic controlling devices, such as a compressed air source and heating source, and instrumented with various sensors for data recording at the inlet, outlet, and within the chamber. Following the concept of the environmental chamber, Yanful and Choo (1997) conducted several drying soil column tests instrumented with various sensors while placing them in an atmospheric-controlled environmental chamber. However, each soil column was mounted on a digital balance where the actual evaporation rate was determined based on the net change in the column's mass.

Teng et al. (2014) developed the climate control apparatus, which consists of two interconnected parts: the environmental chamber and the evaporation chamber. The environmental chamber comprises a resistive heater, freezer, humidifier, and dehumidifier. They operate alternatively to maintain a designated temperature and relative humidity. An air blender inside the environmental chamber continuously mixes the air. A fan installed at the outlet of the environmental chamber monitors the instantaneous wind speed. Moreover, the air blender and the fan circulate the blended air into the evaporation chamber. The evaporation chamber can be attached directly to a drying soil column or to a small chamber to conduct a thin soil section drying test or potential evaporation pan test. Generally, the evaporation rate is determined based on the saturated soil mass difference, while the column or the attached chamber can be instrumented with other sensors to extract more information during testing. During prolonged testing, the apparatus confirmed reliability in maintaining the wind speed, relative humidity, and temperature. Additionally, it is considered a full-featured apparatus that can be used and easily modified to conduct several evaporation and fluid transport model tests.

2.3.4 Determination methods of the actual evaporation

Determining the evaporation rate from soils has proven to be one of the most complex analyses associated with unsaturated soil mechanics. Numerous methods were proposed in the literature. Most of them consider the evaporation process as a soil-atmosphere boundary flux. They generally determine the evaporation rate from the soil surface based on the atmospheric demand and the influence of the soil surface hydrological properties. However, recently evaluating the actual evaporation based on the dynamics of the unsaturated soil below the surface has been inaugurated.

In the current research, the indirect determination methods of the actual evaporation are classified into three groups: (1) Soil-atmosphere boundary models; (2) Surface resistance-based models adopting the relative humidity adjustment approach; (3) Pore-scale and dominant water transport mechanism-based models. Various other methods to determine the actual evaporation rate were developed. The threshold formulation methods, for instance, depend on water supply and demand at the surface (Aluwihare and Watanabe, 2003). Such methods adopt the concept proposed by (Hillel (1982):

“The actual evaporation rate is determined either by external evaporativity or by the soils own ability to deliver water, whichever is the lesser (and hence the limiting factors).”

Moreover, surface resistance models adopting the soil suction adjustment approach were also developed. They consider the residual suction conditions at the surface as a function of the actual evaporation rate (Fredlund et al., 2015). Additionally, many researchers modeled the actual evaporation by numerically and analytically solving coupled heat and water flow in unsaturated soils, such as Darcy-Buckingham and Richard's equations, equations 2.12 and 2.13, respectively (Kamai and Assouline, 2018; Sadeghi et al., 2012; Teng et al., 2016). However, solving one or more nonlinear partial differential equations is highly complex and requires several initial and boundary conditions. Therefore, the solutions of such methods are applicable under specific assumptions and conditions and reveal little about the evaporation mechanism (Teng et al., 2019).

In the following subsection, however, the most popular methods during the past several decades in geotechnical and geo-environmental engineering applications are presented chronologically. Besides, the derivation concept is concretely discussed. This summary is rather exhaustive yet shows that many computational equations are available. Each has its advantages, limitations, and application.

Soil-atmosphere boundary models based on the relation with the potential evaporation

Among the most famous methods are those modified from the Potential Evaporation (PE) determination models, summarized in Table 2.2. Wilson (1990) and Wilson et al. (1994) proposed that the Penman (1948) equation (equation 2.7) for PE can be modified and then used to calculate the Actual Evaporation (AE). The modified equation, known as the Wilson-Penman equation, equation 2.23, considers the difference in temperature, relative humidity, and, therefore, vapor pressure between the soil surface and the overlying air. Since it is a modification of Penman (1948) equation, it is considered a combination method of energy balance and mass transfer at the soil surface. The second method, equation 2.24, is based on thermodynamic consideration and assumes different temperature conditions at and above the soil surface. It is referred to as the limiting function equation for the actual evaporation. Through thin soil section drying tests, Wilson et al. (1997) found a strong relationship between the actual evaporation rate and total suction, independent of soil texture, drying time, and water content. Therefore, a simple equation for calculating actual evaporation based on scaling the relative humidity equation for air was proposed. The equation forms a "Limiting Function" between zero and potential evaporation depending on the vapor pressure at the soil surface. The third method is the empirical, experimental function, equation 2.25, developed based on

Table 2.2: Soil-atmosphere boundary models for the determination of the actual evaporation

Method	Parameters
<u>Modified-Penman or Wilson-Penman equation</u> (Wilson, 1990)	
$AE = \frac{\Gamma Q_n + \eta E_a}{\Gamma + \eta A} \quad (2.23)$	$E_a = 0.35(1 + 0.15 W_w) P_{vsat}^{air} (B - A)$ [m/s]; $A = 1/RH$ $B = 1/RH_{air}$; AE : Actual evaporation; Γ : the slope of the saturation vapor pressure; versus temperature curve [mmHg/°F]; Q_n : net radiation at the surface [m/s]; η : psychrometric constant [0.27 mmHg/°F]; W_w : wind speed [km/h]; P_v^{air} : near-surface air vapor pressure; RH : relative humidity at the surface; RH_{air} : relative humidity of the air.
<u>Limiting function</u> (Wilson et al., 1994)	
$AE = PE \left[\frac{P_v - P_v^{air}}{P_{vsat} - P_v^{air}} \right]$ $= PE \left[\frac{RH - (P_{vsat}^{air}/P_{vsat}) RH_{air}}{1 - (P_{vsat}^{air}/P_{vsat}) RH_{air}} \right] \quad (2.24)$	AE : Actual evaporation; PE : Potential evaporation; P_v : soil vapor pressure; P_{vsat} : surface saturation vapor pressure; P_v^{air} : vapor pressure at the near ground surface air; P_{vsat}^{air} : saturation vapor pressure at the near ground surface air; RH : relative humidity at the surface; RH_{air} : relative humidity of the air.
<u>Empirical experimental function</u> (Wilson et al., 1997)	
$\frac{AE}{PE} = \exp \left(\frac{-\Psi g \omega_w}{\zeta (1 - RH_{air}) \gamma_w R (T + 273.15)} \right) \quad (2.25)$	AE : actual evaporation; PE : potential evaporation; T : temperature at the soil surface; Ψ : total suction at the soil surface; ζ : a dimensional empirical parameter with a suggested value of 0.7 R : universal gas constant g : gravity acceleration; ω_w : molecular weight of water; RH_{air} : relative humidity of the air.

experimental results of thin soil section drying tests. A single unique curve for sand, silt, and clayey soil was found between the total suction at the soil surface and the ratio of Actual Evaporation to Potential Evaporation (AE/PE). Consequently, an equation that matched the experimental data with a proper fit was proposed, while the thermodynamic equilibrium relationship between relative humidity and total suction was applied (Edlefsen and Anderson, 1943). Therefore, if the suction value at the soil surface is known, the AE/PE can be simply estimated from equation 2.25. However, among the limitations of equations 2.24 and 2.25 is that they were only verified for thin-layer soils.

The three proposed methods mainly differ in the assumptions related to determining air and soil temperatures. Differences between the soil surface and air temperatures give rise to various “coupled” and “uncoupled” moisture and heat flow formulations. Due to the surface cooling effect associated with evaporation, studies highlighted the importance of utilizing the methods by solving heat and moisture partial differential equations to represent the physical evaporation processes (Fredlund et al., 2012). Therefore, the term coupled refers to the calculation of the actual evaporation by solving the moisture flow partial differential equation simultaneously with the heat flow partial differential equation. If an assumption is made regarding the relationship between soil and air temperature, or a closed-form empirical relationship is used to designate the relationship; the analysis for AE reduces to the solution of the moisture partial differential equation only, forming the uncoupled analysis. Therefore, the three models relating AE to PE (equations 2.23 to 2.25) and the possibility of using a coupled or uncoupled solution give rise to six procedures for assessing AE. Fredlund et al. (2011) summarize the possible solutions for the proposed procedures and outline the flow of utilizing the developed soil-atmospheric models implemented into the SoilCover (MEND, 1993) and SVFlux computer code (Fredlund, 2001) to solve the procedures.

Surface resistance-based models adopting the relative humidity adjustment approach

Generally, the surface resistance-based models have parametrized the bare soil surface resistance to evaporation, assuming that evaporation occurs at the soil surface or within soil pores at the surface (Kondo et al., 1990). When the near-surface soil is moist, and its pores are yet partially wet, evaporation is conceptualized in two processes following the schematic diagram shown in Figure 2.14 (a). In the first process, water vapor is transported by molecular diffusion from the water surface in the pore space to the land surface; thus, evaporation is restricted by the surface resistance, r_s . In the second process, water vapor is carried from the

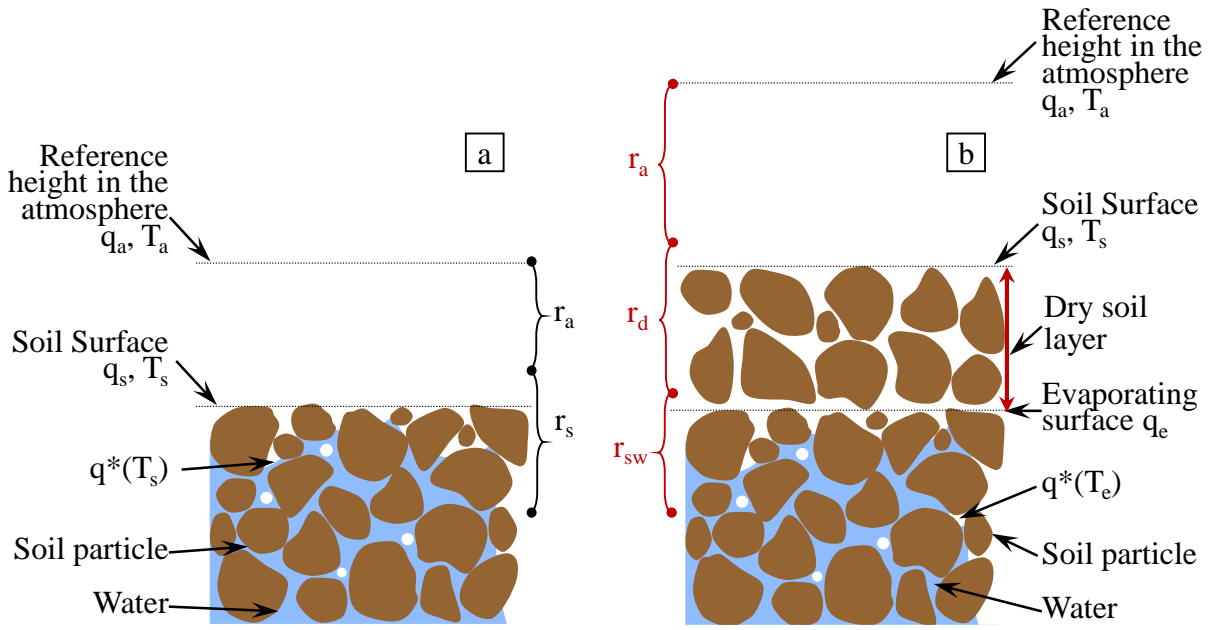


Figure 2.14: Resistances associated with evaporation when the top soil layer is (a) moist and (b) dry. (Aluwihare and Watanabe, 2003)

land surface into the atmosphere by laminar or turbulent flow, while the aerodynamic resistance, r_a , is imposed. Accordingly, two methods are used to determine the actual evaporation; α and β methods. The α method is expressed between the soil surface and a reference height in the atmosphere involving r_a , as in Kondo et al. (1990) and Mahfouf and Noilhan (1991):

$$AE = \frac{\rho_a}{r_a} (\alpha q^*(T_s) - q_a) \quad (2.26)$$

where $q^*(T_s)$ is the saturated specific humidity at the surface temperature T_s defined as the solution of the surface energy balance, ρ_a is the air density, and q_a is the relative humidity at a reference height in the atmosphere. Consequently, the coefficient α represents the relative humidity at the soil surface. It has been parameterized as a function of the surface volumetric water content, θ , as shown in equations 2.30 to 2.32, summarized in Table 2.3. Additionally, its value often starts decreasing below the field capacity, θ_{fc} , defined in equation 2.32 as the volumetric water content corresponding to a hydraulic conductivity of 0.1 mm/day. On the other hand, the β method describes the whole evaporation process from the water surface in the pore space to the atmosphere involving r_a and r_s :

$$AE = \frac{\rho_a}{r_a} \beta (h_r q^*(T_s) - q_a) \quad (2.27)$$

$$\beta = \frac{r_a}{r_a + r_s} \quad (2.28)$$

where h_r is the relative humidity of the air adjacent to a flat free-water surface in the pore space, and from thermodynamic reasoning, it is expressed as follows:

$$h_r = \exp\left(\frac{g\psi}{RT_s}\right) \quad (2.29)$$

where g is the acceleration of gravity, ψ is suction at the soil surface, and R is the gas constant for water vapor. Table 2.3 summarizes some expressions for the moisture availability parameter, β , equations 2.33 to 2.38. Considering h_r equals 1 in equations 2.33 and 2.34 rather than calculating it from equation 2.29 tends to overestimate AE. In contrast, equation 2.36 seems to be the most comprehensive β method. However, it requires knowledge of the relationship between ψ and θ and some reliable parameterization of r_s for a broad range of soil textures (Mahfouf and Noilhan, 1991).

Table 2.3: Surface-resistance-based methods for the determination of the actual evaporation

α method (equation 2.26)	β method (equation 2.27 and 2.28)
Barton (1979)	Deardorff (1977)
$\alpha = \min\left(1, \frac{1.8\theta}{\theta + 30}\right)$	(2.30) $\beta = \min\left(1, \frac{1.8\theta}{0.75\theta_{sat}}\right)$ $h_r = 1$ (2.33)
Yasuda and Toya (1981)	Sun (1982)
$\alpha = \min\left(1, \frac{1.8\theta}{0.7\theta + 0.4}\right)$	(2.31) $r_s = 3.5 \left(\frac{\theta_{sat}}{\theta}\right)^{2.3} + 33.5$ $h_r = 1$ (2.34)
Noilhan and Planton (1989)	Passerat de Silans (1986)
$\alpha = \begin{cases} \theta < \theta_{fc}, \frac{1}{2} \left[1 - \cos\left(\frac{\theta}{\theta_{fc}} \frac{\pi}{2}\right)\right] \\ \theta \geq \theta_{fc}, 1 \end{cases}$	(2.32) $r_s = 3.81 \times 10^4 \exp\left(-13.515 \frac{\theta}{\theta_{fc}}\right)$ $h_r = 1$ (2.35)
<u>Parameters</u>	Camillo and Gurney (1986) Dorman and Sellers (1989)
α : coefficient representing the soil surface relative humidity	$r_s = 4140(\theta_{sat} - \theta) - 805$ $h_r = \text{equation 2.29}$ (2.36)
β : moisture availability parameter	Kondo et al. (1990)
r_s : surface resistance	$r_s = \frac{216 (\theta_{sat} - \theta)^{10}}{D_{atm}}$ $D_{atm} = 0.229 \times 10^{-4} (T_s / 273.16)^{1.75}$ (2.37)
h_r : relative humidity of the air adjacent to a flat free-water surface in the pore space	van de Griend and Owe (1994)
θ : surface volumetric water content	$r_s = 10 \times e^{0.3563(15 - \theta)}$ (2.38)
θ_{sat} : saturated water content	
θ_{fc} : field capacity	

As time passes during evaporation, when the water in the small pores is evaporated, a dry layer is formed. Therefore, water starts evaporating from the bottom of the dry soil layer rather than the surface (Hillel, 1971; Yamanaka et al., 1997). Following the concept of surface resistance, Aluwihare and Watanabe (2003) explained that at that point, the evaporation from the soil consists of three processes, as delineated in Figure 2.14 (b). In the first process, water vapor is transported from the water surface in the soil pore to the bottom pores of the dry soil layer, while the second and the third are similar to the first and second processes when the soil surface is moist. Based on that, r_{sw} and r_d were proposed. r_{sw} is the resistance imposed on vapor flux while traveling from the pore of the wet soil layer to the bottom pores of the dry soil layer, while r_d is the resistance imposed on vapor flux in the dry soil layer. Consequently, the evaporation rate through the three processes from the dry soil layer can be calculated as follows (Aluwihare and Watanabe, 2003):

$$AE = \rho_a \frac{q^*(T_e) - h_a q_a^*(T_a)}{r_{sw} + r_d + r_a} \quad (2.29)$$

where h_a and T_a are the relative humidity and temperature of the air at a reference height in the atmosphere, $q_a^*(T_a)$ is the saturated specific humidity at the air temperature T_a , while $q^*(T_e)$ is the saturated specific humidity at the evaporative surface temperature T_e .

Pore-scale and dominant water transport mechanism-based models

Despite the numerous actual evaporation determination methods proposed in the literature, the process is often determined from an atmospheric point of view. However, in the past few decades, researchers attempted to predict the actual evaporation from pore-scale based on the internal transport mechanisms. Shahraeeni et al. (2012) proposed a pore-scale model for vapor exchange across a boundary layer above the soil surface. The model extended the fundamental solution of Suzuki and Maeda (1968) by including pores of different sizes and a diminishing vapor flux from menisci invading pores and receding into the soil. It considers diffusion fluxes from discrete pores while the porous surface gradually dries. It also assumes that the energy input is constant, while Stage 1 is defined by the presence of the vaporization plane at the soil surface. Besides capillary pore invasion, Shahraeeni et al. (2012) solved for force balance at the pore menisci and considered the capillary flow supplying water to the surface during Stage 1. Such a model could capture evaporation dynamics for different airflow velocities. However, the absolute drying rates after the transition to Stage 2 were underestimated. The discrepancy was attributed to an incomplete description of the unsaturated layer dynamics during Stage 2 and the vapor transport through the formed air-dry layer.

Shokri et al. (2009) conducted soil drying column tests with dyed water to study the unsaturated layer dynamics and water transport mechanisms during Stage 2. A formation of a growing band marked by dye deposition below the surface of the column was observed. The thickness of the dyed layer increased gradually with time, marking the development of an overlaying dry surface layer as postulated in Yamanaka et al. (1998, 1997) and Saravanapavan and Salvucci (2000). Based on that, Shokri et al. (2009) concluded that vapor diffusion and capillary flow occur in series during Stage 2, where liquid flows from the drying front to the vaporization plane formed below the surface and continues as vapor diffusion to the surface. Shokri et al. (2009) utilized the experimental data to calculate the diffusive flux from the vaporization plane using Fick's law. It was concluded that despite vapor diffusion and capillary flow occurring during Stage 2, using Fick's law of diffusion under specific assumptions would be sufficient for approximating vapor transport through the air-dry layer.

In the literature, just a few models were proposed to determine the actual evaporation rate based on the dominant transport mechanisms. This is ascribed to the complexity of the process and the related difficulties in studying its micro-mechanics. Nonetheless, since the evaporation process comprises several micro-scale mechanisms, such innovative models form a promising step towards accurately predicting the evaporation rates. Therefore, a full-scale model that considers the dominant micro-mechanisms within the unsaturated soil layer and the atmospheric demand is essential for many applications, including controlling and suppressing evaporation from soils in the field.

2.4 Suppressing Evaporation and Maximizing Water Retention in Soil Profiles

Water evaporation must be suppressed from soil profiles to maintain the soil's moisture status at a favorable stage for biodiversity, crop growth, and soil productivity. Hillel (2004) stated that the evaporation flux from the soil surfaces could be modified in three alternative or complementary ways. Firstly, by controlling the energy supply to the soil surface. This can be satisfied by modifying the albedo, the light fraction reflected by the surface, or altering the soil color or structure, or by shading the surface. Secondly, reducing the potential gradient, or the force driving water upward through the soil profile. This can be applied by lowering the water table or warming the surface to set up a downward-acting thermal gradient. Thirdly, by decreasing the conductivity or diffusivity of the soil profile, particularly of the surface zone, through tillage, soil conditioning, or incorporating organic matter into the topsoil. Throughout

the years, several solutions have been proposed and utilized for evaporation suppression from profiles. However, the choice of means for reducing evaporation depends on which stage of the process is of interest. For instance, the meteorological factors at the soil surface highly influence the behavior and the evaporation rate during Stage 1. On the other hand, Stage 2 is controlled by the internal water supply to the surface, which is a function of the soil's hydrological properties.

Covering or mulching is one of the most used methods for suppressing evaporation from soil profiles. Mulching the surface with vapor barriers or reflective materials can reduce the intensity of the external factors acting on the surface (Hanks, 2012). Therefore, surface treatment by mulching can interrupt the heat and mass transfer with the atmosphere, consequently retarding evaporation during Stage 1. Mulches are made of different materials, such as sawdust, manure, straw, leaves, crop residue, paper, and plastic sheets (Lal, 1991). Each is used to reduce the effect of a specific meteorological factor. Some types are applied to lower water vapor pressure at the surface (Jones, 2018), while others control the surface temperature. Vegetative mulch with a sufficient thickness was confirmed effective in reducing evaporation since its light color reflects most of the incident radiations. Gravel mulching is also common in water conservation, as it enhances infiltration, simultaneously suppresses evaporation, and reduces soil erosion.

During Stage 2, however, the effect of surface treatments tends to be slight. Alternatively, reducing the evaporation rate and eventual water loss depends on decreasing the soil profile's diffusivity or conductivity. Deep tillage is a technique used to change the variation of diffusivity with the soil profile's water content. This changes the water flow rate supplied to the soil surface underneath for evaporation. Tillage operations generally result in soil opening up, changes in its structure, loosening of tilled soil, and soil compaction immediately below the tilled layer (Lal and Shukla, 2021). The opening of the topsoil enhances the evaporation from the tilled soil layer. However, the compaction of layers underneath and the diffusivity reduction obstruct water's upward transmission and subsequently limit water availability and evaporation. Generally, water loss from deep irrigation is less than from shallow ones, where Stage 1 persists most of the time. Therefore, new water application methods, such as drip or trickle irrigation and the self-watering system (Liu et al., 2018), concentrate water in a particular area below the surface while maintaining the greater part of the surface dry. Such solutions reduce the direct evaporation of soil moisture significantly.

Many researchers have recently investigated and analyzed the impact of utilizing natural soil cover to suppress evaporation from soil profiles (Assouline et al., 2014; Huang et al., 2013; Yanful et al., 2003; Yang and Yanful, 2002; Zhou et al., 2008). A key element of such soil covers is the application of a soil layer with a contrasting texture over the original ground to minimize net percolation, therefore maximizing water storage. Alowaisy and Yasufuku (2018) and Assouline et al. (2014) concluded that adding a thin soil layer that has different properties from the underlying natural ground is a simple means of controlling evaporation losses. Additionally, adding a coarser material reduces the evaporation losses due to the preferential invasion of the larger pores by the gas phase within the coarse material. On the other hand, adding finer soil can either increase or reduce the evaporation losses depending on the thickness of the applied layer. Based on a field study, Zhou et al. (2008) concluded that natural covers significantly inhibit soil water evaporation, and their thickness is essential in improving their influence.

Despite the innovation in these new and simple techniques, a robust design criterion or a utilization standard of a soil cover is still lacking in the literature. Proposing such techniques requires an accurate prediction and understanding of the micro-mechanisms of the evaporation process from homogeneous soil profiles, consequently extending the investigation to a layered soil profile (Alowaisy and Yasufuku, 2018; Shokri et al., 2010b). Reducing water evaporation and maximizing its retention in soil profiles has been of broad and current interest. It is essential for soil prevention and recovery from degradation and desertification. Comprehensive and innovative solutions in this field are pivotal for numerous geotechnical, geo-environmental, and agricultural engineering applications.

2.5 Research Original Contributions Relative to the Literature

The literature review provided in this chapter indicates that a comprehensive actual evaporation determination model that considers the atmospheric demand and water supply through the unsaturated soil profiles is still lacking. Moreover, a design or utilization standard for natural soil cover to suppress evaporation is not available for application by geotechnical and geo-environmental engineers. Accordingly, the original contributions of the current research are drawn as follows:

1. Propose a comprehensive index that reflects the pore structure variations and considers the factors affecting the capillary and diffusion flow during the evaporation stages. The Pore

Size Distribution Index (I_{PSD}) correlates well with the evaporation measures and is systematically determined from the soil water retention properties. It is a robust index used to propose an actual evaporation estimation model and is expected to contribute to the water movement through unsaturated soil profiles.

2. Develop a new experimental technique to visualize the dynamics of the unsaturated layer during drying. The novel image-analysis-based technique captures high-quality images and applies robust image-analysis operations that enable tracing the drying front and vaporization plane. The proposed technique was confirmed reliable and definite, where the extracted micro-dynamics of the vaporization plane were utilized to propose an actual evaporation estimation model. Moreover, the simple technique is believed to improve the research related to water movement and solute transport through porous mediums.
3. Propose a semi-empirical model to evaluate the evaporation rates from unsaturated soil profiles. The pore-scale-based estimation model considers the atmospheric demand and water supply capabilities through the soil profile. It utilizes Fick's law and the dynamics of the vaporization plane as a function of the proposed I_{PSD} to accurately predict the evaporation rates during the evaporation stages. The comprehensive model is reliable and can be efficiently utilized for many engineering applications.
4. Proposes a novel design concept for an environmental-friendly natural soil cover to suppress evaporation rates and increase water storage in soil profiles. The simple design concept considers the soil cover's retention properties relative to the original soil ground and the textural contrast boundary between them. Through two design criteria, the design concept can optimize a soil cover with appropriate soil material and thickness to ensure maximum water retention within the target zone of the natural soil ground.

References

- Alowaisy, A., Yasufuku, N., 2018. *Characteristics of the second stage of evaporation and water redistribution through double layered sandy soil profiles*. *Lowland Technology International* 20, 273–284.
- Alsumaiei, A.A., 2020. *Utility of artificial neural networks in modeling pan evaporation in hyper-arid climates*. *Water (Basel)* 12, 1508.
- Altenhofen, J., 1985. *A modified atmometer for on-farm ET determination*, in: *National Conference on Advances in Evapotranspiration*. pp. 16–17.
- Aluwihare, S., Watanabe, K., 2003. *Measurement of Evaporation on Bare Soil and Estimating Surface Resistance*. *Journal of Environmental Engineering* 129, 1157–1168. [https://doi.org/10.1061/\(ASCE\)0733-9372\(2003\)129:12\(1157\)](https://doi.org/10.1061/(ASCE)0733-9372(2003)129:12(1157))

- Assouline, S., Narkis, K., Gherabli, R., Lefort, P., Prat, M., 2014. Analysis of the impact of surface layer properties on evaporation from porous systems using column experiments and modified definition of characteristic length. *Water Resour Res* 50, 3933–3955. <https://doi.org/10.1002/2013WR014489>
- Assouline, S., Tyler, S.W., Selker, J.S., Lunati, I., Higgins, C.W., Parlange, M.B., 2013. Evaporation from a shallow water table: Diurnal dynamics of water and heat at the surface of drying sand. *Water Resour Res* 49, 4022–4034. <https://doi.org/10.1002/wrcr.20293>
- Barton, I.J., 1979. A parameterization of the evaporation from nonsaturated surfaces. *Journal of Applied Meteorology* 18, 43–47. [https://doi.org/10.1175/1520-0450\(1979\)018<0043:APOTEF>2.0.CO;2](https://doi.org/10.1175/1520-0450(1979)018<0043:APOTEF>2.0.CO;2)
- Blad, B.L., Rosenberg, N.J., 1976. Evaluation of resistance and mass transport evapotranspiration models requiring canopy temperature data. *Agron J* 68, 764–769.
- Blaney, H.F., Criddle, W.D., 1950. Determining water requirements in irrigated areas from climatological irrigation data, US Department of Agriculture, Soil Conservation Service. Washington, D.C.
- Boast, C.W., Robertson, T.M., 1982. A “Micro-Lysimeter” Method for Determining Evaporation from Bare Soil: Description and Laboratory Evaluation. *Soil Science Society of America Journal* 46, 689–696. <https://doi.org/10.2136/sssaj1982.03615995004600040005x>
- Bowen, I.S., 1926. The ratio of heat losses by conduction and by evaporation from any water surface. *Physical review* 27, 779–787.
- Bowman, B.T., 1988. Mobility and Persistence of Metolachlor and Aldicarb in Field Lysimeters. *J Environ Qual* 17, 689–694. <https://doi.org/10.2134/jeq1988.00472425001700040028x>
- Buckingham, E., 1907. Studies on the movement of soil moisture. U.S. Department of Agriculture, Bureau of Soils, Washington, DC. 38.
- Camillo, P.J., Gurney, R.J., 1986. A resistance parameter for bare-soil evaporation models. *Soil Sci* 141, 95–105. <https://doi.org/10.1097/00010694-198602000-00001>
- Crestana, S., Manoel Pedro Vaz, C., 1998. Non-invasive instrumentation opportunities for characterizing soil porous systems. *Soil Tillage Res* 47, 19–26. [https://doi.org/10.1016/S0167-1987\(98\)00068-3](https://doi.org/10.1016/S0167-1987(98)00068-3)
- Cui, Y.J., Ta, A.N., Hemmati, S., Tang, A.M., Gatmiri, B., 2013. Experimental and numerical investigation of soil-atmosphere interaction. *Eng Geol* 165, 20–28. <https://doi.org/10.1016/j.enggeo.2012.03.018>
- Daamen, C.C., Simmonds, L.P., 1996. Measurement of evaporation from bare soil and its estimation using surface resistance. *Water Resour Res* 32, 1393–1402. <https://doi.org/10.1029/96WR00268>
- Dalton, J., 1802. Experimental essays, on the constitution of mixed gases; on the force of steam or vapour from water and other liquids in different temperatures, both in a Torricellian vacuum and in air; on evaporation; and on the expansion of elastic fluids by heat.
- Davarzani, H., Smits, K., Tolene, R.M., Illangasekare, T., 2014. Study of the effect of wind speed on evaporation from soil through integrated modeling of the atmospheric boundary layer and shallow subsurface. *Water Resour Res* 50, 661–680. <https://doi.org/10.1002/2013WR013952>
- Deardorff, J.W., 1977. A Parameterization of Ground-Surface Moisture Content for Use in Atmospheric Prediction Models. *Journal of Applied Meteorology* 16, 1182–1185. [https://doi.org/10.1175/1520-0450\(1977\)016<1182:apogsm>2.0.co;2](https://doi.org/10.1175/1520-0450(1977)016<1182:apogsm>2.0.co;2)
- De la Hire, P., 1703. Sur l’origine des rivières, in: *L’Academie Royale Des Sciences*. Paris, pp. 1–6.

- Dijkema, J., Koonce, J.E., Shillito, R.M., Ghezzehei, T.A., Berli, M., van der Ploeg, M.J., van Genuchten, M.Th., 2018. Water Distribution in an Arid Zone Soil: Numerical Analysis of Data from a Large Weighing Lysimeter. *Vadose Zone Journal* 17, 1–17. <https://doi.org/10.2136/vzj2017.01.0035>
- Dorman, J.L., Sellers, P.J., 1989. A global climatology of albedo, roughness length and stomatal resistance for atmospheric general circulation models as represented by the simple biosphere model (SiB). *J Appl Meteorol Climatol* 28, 833–855.
- Edlefsen, N.E., Anderson, A.B.C., 1943. Thermodynamics of soil moisture. *Hilgardia* 15, 31–298. <https://doi.org/DOI:10.3733/hilg.v15n02p031>.
- Fayer, M.J., Gee, G.W., Reynolds, T.D., Morris, R.C., 1997. Hydrologic model tests for landfill covers using field data, in: *Proceedings Landfill Capping in the Semi-Arid West: Problems, Perspectives, and Solutions*. Environmental Science and Research Foundation, Idaho Falls, ID. pp. 53–68.
- Fisher, D.K., 2012. Simple weighing lysimeters for measuring evapotranspiration and developing crop coefficients. *International Journal of Agricultural and Biological Engineering* 5, 35–43. <https://doi.org/10.3965/j.ijabe.20120503.00?>
- FOA, 1982. Lysimeters. FAO Irrigation and Drainage Paper, 39. Food and Agriculture Organization of the United Nations.
- Fredlund, D.G., Rahardjo, H., Fredlund, M.D., 2012. *Unsaturated Soil Mechanics in Engineering Practice*. John Wiley & Sons, Inc., Hoboken, New Jersey.
- Fredlund, M.D., 2001. *SVFlux Manual*. SoilVision Systems, Saskatoon, SK.
- Fredlund, M.D., Zhang, J.M., Tran, D., Fredlund, D.G., 2015. Classification of Actual Evaporation Models 1–15.
- Fredlund, M.D., Zhang, J.M., Tran, D., Fredlund, D.G., 2011. Coupling Heat and Moisture Flow for the Computation of Actual Evaporation. *Proceedings of the Canadian Geotechnical Conference and Fifth Pan-American Conference*, Toronto, Ont 2–6.
- Gilliland, E.R., 1938. Fundamentals of drying techniques. *Ind Eng Chem* 30, 506–514. <https://doi.org/10.1080/07373938908916595>
- Gray, D.M., 1970. *Handbook on the principles of hydrology*.
- Hanks, R.J., 2012. *Applied Soil Physics: Soil Water and Temperature Applications, Second Edi.* ed. Springer Science & Business Media.
- Heck, K., Coltman, E., Schneider, J., Helmig, R., 2020. Influence of Radiation on Evaporation Rates: A Numerical Analysis. *Water Resour Res* 56. <https://doi.org/10.1029/2020WR027332>
- Hillel, D., 2004. *Introduction to environmental soil physics*, Elsevier Science.
- Hillel, D., 1982. *Introduction to Soil Physics*. Academic Press, Inc. <https://doi.org/10.2136/vzj2006.0013br>
- Hillel, D., 1980. *Applications of Soil Physics*. Academic Press, Inc., New York. <https://doi.org/10.2307/2403017>
- Hillel, D., 1971. *Soil and Water, Physical Principles and Processes*. Academic Press, Inc., New York.
- Hillel, D., van Bavel, H.M., 1976. Simulation of Profile Water Storage as Related to Soil Hydraulic Properties. *Soil Science Society of America Journal* 40, 807–815. <https://doi.org/10.2136/sssaj1976.03615995004000060009x>
- Huang, M., Bruch, P.G., Barbour, S.L., 2013. Evaporation and Water Redistribution in Layered Unsaturated Soil Profiles. *Vadose Zone Journal* 12, vzj2012.0108. <https://doi.org/10.2136/vzj2012.0108>

- Jensen, M.E., Haise, H.R., 1963. Estimating evapotranspiration from solar radiation. *Journal of the Irrigation and Drainage Division* 89, 15–41.
- Jones, F.E., 2018. *Evaporation of water with emphasis on applications and measurements*. CRC Press.
- Jury, W.A., Tanner, C.B., 1975. Advection modification of the Priestley and Taylor evapotranspiration formula. *Agron J* 67, 840–842. <https://doi.org/10.2134/agronj1975.00021962006700060031x>
- Kamai, T., Assouline, S., 2018. Evaporation From Deep Aquifers in Arid Regions: Analytical Model for Combined Liquid and Vapor Water Fluxes. *Water Resour Res* 54, 4805–4822. <https://doi.org/10.1029/2018WR023030>
- Kayyal, M.K., 1995. Effect of the moisture evaporative stages on the development of shrinkage cracks in soils, in: *UNSAT'95 : International Conference on Unsaturated Soils*. pp. 373–380.
- Keen, B.A., 1914. The evaporation of water from soil. *J Agric Sci* 6, 456–475. <https://doi.org/10.1017/S0021859600002288>
- Kohsiek, W., 1981. Rapid circulation chamber for measuring bulk stomatal resistance. *Journal of Applied Meteorology, American Meteorological Society* 20, 42–52.
- Kondo, J., Saigusa, N., Sato, T., 1992. A Model and Experimental Study of Evaporation from Bare-Soil Surfaces. *Journal of Applied Meteorology* 31, 304–312. [https://doi.org/10.1175/1520-0450\(1992\)031<0304:AMAESO>2.0.CO;2](https://doi.org/10.1175/1520-0450(1992)031<0304:AMAESO>2.0.CO;2)
- Kondo, J., Saigusa, N., Sato, T., 1990. A Parameterization of Evaporation from Bare Soil Surfaces. *J Appl Meteorol Climatol* 29, 385–389. [https://doi.org/10.1175/1520-0450\(1990\)029<0385:APOEFB>2.0.CO;2](https://doi.org/10.1175/1520-0450(1990)029<0385:APOEFB>2.0.CO;2)
- Lal, R., 1991. Soil structure and sustainability. *Journal of Sustainable Agriculture* 1, 67–92. https://doi.org/10.1300/J064v01n04_06
- Lal, R., Shukla, M.K., 2021. *Principles of Soil Physics, Principles of Soil Physics*. <https://doi.org/10.4324/9780203021231-20>
- Le Bray, Y., Prat, M., 1999. Three-dimensional pore network simulation of drying in capillary porous media. *Int J Heat Mass Transf* 42, 4207–4224. [https://doi.org/10.1016/S0017-9310\(99\)00006-X](https://doi.org/10.1016/S0017-9310(99)00006-X)
- Lehmann, P., Assouline, S., Or, D., 2008. Characteristic lengths affecting evaporative drying of porous media. *Phys Rev E Stat Nonlin Soft Matter Phys* 77, 1–16. <https://doi.org/10.1103/PhysRevE.77.056309>
- Lehmann, P., Merlin, O., Gentine, P., Or, D., 2018. Soil Texture Effects on Surface Resistance to Bare-Soil Evaporation. *Geophys Res Lett* 45, 10,398–10,405. <https://doi.org/10.1029/2018GL078803>
- Lewis, J., Sjöström, J., 2010. Optimizing the experimental design of soil columns in saturated and unsaturated transport experiments. *J Contam Hydrol* 115, 1–13. <https://doi.org/10.1016/j.jconhyd.2010.04.001>
- Linsley, R.K., Kohler, M.A., Paulhus, J.L.H., 1958. *Hydrology for engineers*, McGraw-Hill Book Company. [https://doi.org/10.1016/0022-1694\(84\)90195-1](https://doi.org/10.1016/0022-1694(84)90195-1)
- Liu, C., Zhang, X., Zhang, Y., 2002. Determination of daily evaporation and evapotranspiration of winter wheat and maize by large-scale weighing lysimeter and micro-lysimeter. *Agric For Meteorol* 111, 109–120. [https://doi.org/10.1016/S0168-1923\(02\)00015-1](https://doi.org/10.1016/S0168-1923(02)00015-1)
- Liu, Q., Yasufuku, N., Omine, K., 2018. Self-watering system for arid area: A method to combat desertification. *Soils and Foundations* 58, 838–852. <https://doi.org/10.1016/j.sandf.2018.03.013>
- Mahfouf, J.F., Noilhan, J., 1991. Comparative study of various formulations of Evaporation from Bare Soil Using In Situ Data. *Journal of Applied Meteorology* 30, 1354–1365.

- MEND, 1993. *SoilCover, User's Manual for an Evaporative Flux Model*. University of Saskatchewan, Saskatoon, SK.
- Mohamed, A.A., Sasaki, T., Watanabe, K., 2000. Solute Transport through Unsaturated Soil due to Evaporation. *Journal of Environmental Engineering* 126, 842–848. [https://doi.org/doi:10.1061/\(ASCE\)0733-9372\(2000\)126:9\(842\)](https://doi.org/doi:10.1061/(ASCE)0733-9372(2000)126:9(842))
- Monteith, J.L., 1965. Evaporation and environment. *Symp Soc Exp Biol* 19, 205–234.
- Mosthaf, K., Helmig, R., Or, D., 2014. Modeling and analysis of evaporation processes from porous media on the REV scale. *Water Resour Res* 50, 1059–1079. <https://doi.org/10.1002/2013WR014442>
- Noilhan, J., Planton, S., 1989. A simple parameterization of land surface processes for meteorological models. *Mon Weather Rev* 117, 536–549.
- Oliviera, I.B., Demond, A.H., Salehzadeh, A., 1996. Packing of Sands for the Production of Homogeneous Porous Media. *Soil Science Society of America Journal. Division S-1—Soil Physic* 60, 49–53. <https://doi.org/10.2136/sssaj1996.03615995006000010010x>
- Or, D., Lehmann, P., Shahraeeni, E., Shokri, N., 2013. Advances in Soil Evaporation Physics-A Review. *Vadose Zone Journal* 12, vzj2012.0163. <https://doi.org/10.2136/vzj2012.0163>
- Passerat de Silans, A., 1986. *Transferts de masse et de chaleur dans un sol stratifié soumis à une excitation atmosphérique naturelle: comparaison: modèles-expérience (Doctoral Thesis)*. The Grenoble Institute of Technology.
- Pearce, E.I.F., Smillie, A.C., 1974. An investigation of possible changes in keratins accompanying injury-induced hair follicle mineralization. *Calcif Tissue Res* 15, 133–141. <https://doi.org/10.1007/BF02059051>
- Penman, H.L., 1948. Natural evaporation from open water, bare soil and grass, in: *Proceedings of the Royal Society of London. Series A, Mathematical and Physical Sciences*. pp. 120–145. <https://doi.org/10.1098/rspa.1948.0037>
- Philip, J.R., 1957. Evaporation, and moisture and heat fields in the soil. *Journal of Meteorology* 14, 354–366.
- Plummer, M.A., Hull, L.C., Fox, D.T., 2004. Transport of Carbon-14 in a Large Unsaturated Soil Column. *Vadose Zone Journal* 3, 109–121. <https://doi.org/10.2113/3.1.109>
- Powelson, D.K., Mills, A.L., 1998. Transport of *Escherichia coli* in Sand Columns with Constant and Changing Water Contents. *J Environ Qual* 30, 238–245. <https://doi.org/10.2134/jeq2001.301238x>
- Prat, M., 2002. Recent advances in pore-scale models for drying of porous media. *Chemical Engineering Journal* 86, 153–164. [https://doi.org/10.1016/S1385-8947\(01\)00283-2](https://doi.org/10.1016/S1385-8947(01)00283-2)
- Priestley, C.H.B., Taylor, R.J., 1972. On the Assessment of Surface Heat Flux and Evaporation Using Large-Scale Parameters. *Mon Weather Rev* 100, 81–92. [https://doi.org/10.1175/1520-0493\(1972\)100<0081:otaosh>2.3.co;2](https://doi.org/10.1175/1520-0493(1972)100<0081:otaosh>2.3.co;2)
- Richards, L.A., 1931. Capillary conduction of liquids through porous mediums. *J Appl Phys* 1, 318–333. <https://doi.org/10.1063/1.1745010>
- Rohwer, C., 1931. *Evaporation from free water surfaces*. US Department of Agriculture.
- Rosenberg, N.J., Blad, B.L., Verma, S.B., 1983. *Microclimate: The Biological Environment*. John Wiley and Sons, Inc., Canada.
- Sadeghi, M., Shokri, N., Jones, S.B., 2012. A novel analytical solution to steady-state evaporation from porous media. *Water Resour Res* 48. <https://doi.org/10.1029/2012WR012060>

- Saravanapavan, T., Salvucci, G.D., 2000. Analysis of rate-limiting processes in soil evaporation with implications for soil resistance models. *Adv Water Resour* 23, 493–502. [https://doi.org/10.1016/S0309-1708\(99\)00045-7](https://doi.org/10.1016/S0309-1708(99)00045-7)
- Sattler, P., 1989. *Modelling Vertical Ground Movements Using Surface Climatic Flux (Masters Thesis)*. University of Saskatchewan, Saskatoon, Canada.
- Scherer, G.W., 1990. Theory of Drying. *Journal of the American Ceramic Society* 73, 3–14. <https://doi.org/10.1111/j.1151-2916.1990.tb05082.x>
- Shahraeeni, E., Lehmann, P., Or, D., 2012. Coupling of evaporative fluxes from drying porous surfaces with air boundary layer: Characteristics of evaporation from discrete pores. *Water Resour Res* 48, 1–15. <https://doi.org/10.1029/2012WR011857>
- Sherwood T.K., 1929. The Drying of Solids - II. *Ind Eng Chem* 21, 976–980.
- Shokri, N., Lehmann, P., Or, D., 2010a. Liquid-phase continuity and solute concentration dynamics during evaporation from porous media: Pore-scale processes near vaporization surface. *Phys Rev E Stat Nonlin Soft Matter Phys* 81, 1–7. <https://doi.org/10.1103/PhysRevE.81.046308>
- Shokri, N., Lehmann, P., Or, D., 2010b. Evaporation from layered porous media. *J Geophys Res Solid Earth* 115, 1–12. <https://doi.org/10.1029/2009JB006743>
- Shokri, N., Lehmann, P., Or, D., 2009. Critical evaluation of enhancement factors for vapor transport through unsaturated porous media. *Water Resour Res* 45, 1–9. <https://doi.org/10.1029/2009WR007769>
- Shokri, N., Lehmann, P., Vontobel, P., Or, D., 2008. Drying front and water content dynamics during evaporation from sand delineated by neutron radiography. *Water Resour Res* 44, 1–11. <https://doi.org/10.1029/2007WR006385>
- Shokri, N., Salvucci, G.D., 2011. Evaporation from Porous Media in the Presence of a Water Table. *Vadose Zone Journal*. <https://doi.org/10.2136/vzj2011.0027>
- Shouse, P., Jury, W.A., Stolzy, L.H., 1980. Use of Deterministic and Empirical Models to Predict Potential Evapotranspiration in an Advective Environment. *Agron J* 72, 994–998. <https://doi.org/10.2134/agronj1980.00021962007200060031x>
- Singh, V.P., Xu, C.Y., 1997. Evaluation and generalization of 13 mass-transfer equations for determining free water evaporation. *Hydrol Process* 11, 311–323. [https://doi.org/10.1002/\(SICI\)1099-1085\(19970315\)11:3<311::AID-HYP446>3.0.CO;2-Y](https://doi.org/10.1002/(SICI)1099-1085(19970315)11:3<311::AID-HYP446>3.0.CO;2-Y)
- Song, W.K., Cui, Y.J., Tang, A.M., Ding, W.Q., 2013. Development of a Large-Scale Environmental Chamber for Investigating Soil Water Evaporation. *Geotechnical Testing Journal* 36. <https://doi.org/10.1520/GTJ20120142>
- Strock, J.S., Cassel, D.K., 2001. Developing and testing a system for studying unsaturated solute transport on undisturbed soil blocks. *J Soil Water Conserv* 56, 112–119.
- Sun, S.F., 1982. *Moisture and heat transport in a soil layer forced by atmospheric conditions (Masters Thesis)*. University of Connecticut.
- Suzuki, M., Maeda, S., 1968. On the mechanism of drying of granular beds: Mass Transfer from Discontinuous Source. *Journal of Chemical Engineering of Japan* 1, 26–31. <https://doi.org/10.1252/jcej.1.26>
- Teng, J., Yasufuku, N., Liu, Q., Liu, S., 2014. Experimental evaluation and parameterization of evaporation from soil surface. *Natural Hazards* 73, 1405–1418. <https://doi.org/10.1007/s11069-014-1138-z>

- Teng, J., Yasufuku, N., Zhang, S., He, Y., 2016. Modelling water content redistribution during evaporation from sandy soil in the presence of water table. *Comput Geotech* 75, 210–224. <https://doi.org/10.1016/j.compgeo.2016.02.009>
- Teng, J., Zhang, X., Zhang, S., Zhao, C., Sheng, D., 2019. An analytical model for evaporation from unsaturated soil. *Comput Geotech* 108, 107–116. <https://doi.org/10.1016/j.compgeo.2018.12.005>
- Thornthwaite, C.W., 1948. An Approach toward a Rational Classification of Climate. *Geogr Rev* 38, 55–94. <https://doi.org/10.2307/210739>
- Thornthwaite, C.W., Holzman, B., 1942. Measurement of evaporation from land and water surfaces, 817th ed. US Department of Agriculture.
- Tran, D.T.Q., 2013. Re-visitation of actual evaporation theories. University of Alberta - Edmonton, Canada.
- Tran, D.T.Q., Fredlund, D.G., Chan, D.H., 2016. Improvements to the calculation of actual evaporation from bare soil surfaces. *Canadian Geotechnical Journal* 53, 118–133. <https://doi.org/10.1139/cgj-2014-0512>
- Uclés, O., Villagarcía, L., Cantón, Y., Domingo, F., 2013. Microlysimeter station for long term non-rainfall water input and evaporation studies. *Agric For Meteorol* 182–183, 13–20. <https://doi.org/10.1016/j.agrformet.2013.07.017>
- Van Brakel, J., 1980. Mass transfer in convective drying, in: *Advances in Drying*. Hemisphere Publishing Corporation, Washington, New York, pp. 217–267.
- van de Griend, A.A., Owe, M., 1994. Bare soil surface resistance to evaporation by vapor diffusion under semiarid conditions. *Water Resour Res* 30, 181–188. <https://doi.org/10.1029/93WR02747>
- van Genuchten, M.Th., 1980. A Closed-form Equation for Predicting the Hydraulic Conductivity of Unsaturated Soils. *Soil Science Society of America Journal* 44, 892–898. <https://doi.org/10.2136/sssaj1980.03615995004400050002x>
- Wang, W.Z., 2006. Wind tunnel experiments on bare soil evaporation (Masters Thesis). National Central University.
- Wilson, G.W., 1990. Soil Evaporative Fluxes for Geotechnical Engineering Problems (Doctoral Thesis). University of Saskatchewan - Saskatoon, Canada.
- Wilson, G.W., Fredlund, D.G., Barbour, S.L., 1997. The effect of soil suction on evaporative fluxes from soil surfaces. *Canadian Geotechnical Journal* 34, 145–155. <https://doi.org/10.1139/t96-078>
- Wilson, G.W., Fredlund, D.G., Barbour, S.L., 1994. Coupled soil-atmosphere modelling for soil evaporation. *Canadian Geotechnical Journal* 31, 151–161. <https://doi.org/10.1139/t94-021>
- WMO, 1974. International glossary of hydrology. World Meteorological Organization Report, 393.
- Wythers, K.R., Lauenroth, W.K., Paruelo, J.M., 1999. Bare-Soil Evaporation Under Semiarid Field Conditions. *Soil Science Society of America Journal* 63, 1341–1349. <https://doi.org/10.2136/sssaj1999.6351341x>
- Xu, C.Y., Singh, V.P., 2001. Evaluation and generalization of temperature-based methods for calculating evaporation. *Hydrol Process* 15, 305–319. <https://doi.org/10.1002/hyp.119>
- Xu, C.Y., Singh, V.P., 2000. Evaluation and generalization of radiation-based methods for calculating evaporation. *Hydrol Process* 14, 339–349. <https://doi.org/10.1002/hyp.119>
- Yamanaka, T., Inoue, M., Kaihotsu, I., 2004. Effects of gravel mulch on water vapor transfer above and below the soil surface. *Agric Water Manag* 67, 145–155. <https://doi.org/10.1016/j.agwat.2004.01.002>

- Yamanaka, T., Takeda, A., Shimada, J., 1998. Evaporation beneath the soil surface: some observational evidence and numerical experiments. *Hydrol Process* 12, 2193–2203. [https://doi.org/10.1002/\(SICI\)1099-1085\(19981030\)12:13/14<2193::AID-HYP729>3.0.CO;2-P](https://doi.org/10.1002/(SICI)1099-1085(19981030)12:13/14<2193::AID-HYP729>3.0.CO;2-P)
- Yamanaka, T., Takeda, A., Sugita, F., 1997. A modified surface-resistance approach for representing bare-soil evaporation: Wind tunnel experiments under various atmospheric conditions. *Water Resour Res* 33, 2117–2128. <https://doi.org/10.1029/97WR01639>
- Yanful, E.K., Choo, L.P., 1997. Measurement of evaporative fluxes from candidate cover soils. *Canadian Geotechnical Journal* 34, 447–459. <https://doi.org/10.1139/97-002>
- Yanful, E.K., Mousavi, S.M., Yang, M., 2003. Modeling and measurement of evaporation in moisture-retaining soil covers. *Advances in Environmental Research*. [https://doi.org/10.1016/S1093-0191\(02\)00053-9](https://doi.org/10.1016/S1093-0191(02)00053-9)
- Yang, M., Yanful, E.K., 2002. Water balance during evaporation and drainage in cover soils under different water table conditions. *Advances in Environmental Research* 6, 505–521. [https://doi.org/10.1016/S1093-0191\(01\)00077-6](https://doi.org/10.1016/S1093-0191(01)00077-6)
- Yasuda, N., Toya, T., 1981. Evaporation from non-saturated surface and surface moisture availability. Title. *Papers in Meteorology and Geophysics* 32, 89–98.
- Yiotis, A.G., Boudouvis, A.G., Stubos, A.K., Tsimpanogiannis, I.N., Yortsos, Y.C., 2003. Effect of liquid films on the isothermal drying of porous media. *Phys Rev E Stat Phys Plasmas Fluids Relat Interdiscip Topics* 68, 4. <https://doi.org/10.1103/PhysRevE.68.037303>
- Yiotis, A.G., Stubos, A.K., Boudouvis, A.G., Tsimpanogiannis, I.N., Yortsos, Y.C., 2005. Pore-network modeling of isothermal drying in porous media. *Transp Porous Media* 58, 63–86. <https://doi.org/10.1007/s11242-004-5470-8>
- Yiotis, A.G., Stubos, A.K., Boudouvis, A.G., Yortsos, Y.C., 2001. A 2-D pore-network model of the drying of single-component liquids in porous media. *Adv Water Resour* 24, 439–460. [https://doi.org/10.1016/S0309-1708\(00\)00066-X](https://doi.org/10.1016/S0309-1708(00)00066-X)
- Yiotis, A.G., Tsimpanogiannis, I.N., Stubos, A.K., Yortsos, Y.C., 2006. Pore-network study of the characteristic periods in the drying of porous materials. *J Colloid Interface Sci* 297, 738–748. <https://doi.org/10.1016/j.jcis.2005.11.043>
- Zhou, H., Li, S., Sun, S., Xu, X., Lei, J., Liu, S., Du, W., Yan, Z., Wang, Y., 2008. Effects of natural covers on soil evaporation of the shelterbelt along the Tarim Desert Highway. *Chinese Science Bulletin* 53, 137–145. <https://doi.org/10.1007/s11434-008-6016-1>

3

CHAPTER

Pore Structure Parameterization and its Influence on Evaporation from Homogeneous Soil Profiles

3.1 Introduction

Evaporation from soil profiles is the predominant flux in drylands. It is a highly dynamic process that varies considerably in space and time, reflecting the interplay between the atmospheric conditions (energy input, air temperature, and relative humidity) and the internal water flow processes (capillary liquid flow and vapor diffusion). The process is divided into three stages from a fully saturated bare soil profile. Each stage has a unique behavior, evaporation rate, and influencing factors, generally due to the variation in the dominant water transport mechanism at each stage, Figure 2.5.

During Stage 1, water is supplied to the surface by capillary liquid flow, where water directly gets lost into the atmosphere. Therefore, Stage 1's evaporation rate is relatively high and influenced by the adjacent atmospheric conditions. Nevertheless, recent studies confirmed that Stage 1 is governed by the extent of the hydraulically connected region from the drying front to the surface. This region is also known as the film region or the unsaturated layer

dominated by capillary flow. Lehmann et al. (2008) proposed the characteristic length (L_c) to represent this maximum water-filled connected pores which can be reflected from the width of the pore size distribution. In arid and semi-arid areas characterized by parched weather, Stage 1 lasts for short durations after irrigation or rainfall events. However, Stages 2 and 3 are more complicated and believed to be dominant in drylands. Nonetheless, little is known about the micro-mechanisms involved in those stages compared to Stage 1. The literature has confirmed that Stages 2 and 3 are diffusion-dependent stages, where water transports by vapor diffusion from a receding vaporization plane through an air-dry layer formed at the top of the profile. Consequently, Stage 2 and 3 evaporation flux is governed by the soil's ability to supply water through its tortuously structured body which is reflected by the profile's properties.

In early works, the evaporation process was approached from a phenomenological point of view, focusing mainly on the actual evaporation rate and considering the evaporation as a boundary flux at the surface. However, such approaches neglect the detailed physics within the soil profile and how those emerging microscale mechanisms affect the macroscale behavior of the evaporation process. On the other hand, the literature has thoroughly investigated the influence of internal and external influencing factors on the evaporation stages and their behavior. At the same time, many researchers highlighted the importance of the pore structure on evaporation. However, an extensive study on the pore structure's influence on the process is still lacking.

Based on that, in the following chapter, the influence of the soil pore structure on the actual evaporation flux and the formation of the unsaturated layer is studied. The evaporation process and soil pore structure are investigated through experimental testing of homogeneous sandy soil profiles under constant atmospheric demand. Accordingly, a simple yet robust pore structure-based index is proposed. The index comprehensively represents the variation in the pore structure and other soil properties and strongly correlates with the evaporation process. Furthermore, new insights related to the evaporation rate during the falling rate stage, Stage 2, and its unsaturated layer are presented. Consequently, the importance and contribution of Stage 2 to the evaporation process is elucidated.

3.2 Materials

Major climate components in soil formation are precipitation, evapotranspiration, and temperature. The temperature in drylands is usually high. However, the diurnal variation is generally wide. Similarly, the deserts are characterized by wide diurnal and seasonal

temperature fluctuations. This behavior is caused due to the rapid heat escape from dry air. The repeated fluctuations of gaining and losing heat have a destructive effect on the exposed rock surfaces. Consequently, rocks experience severe weathering due to expansions and contractions, resulting in ultimate disintegration. Large areas of shattered rocks and rubbles are formed, where most of them are either dust or sand. Dust is originated from solidified clay or volcanic deposits, whereas sand generates from the fragmentation of harder granite, limestone, and sandstone. Smalley and Vita-Finzi (1968) mentioned that stresses produced by temperature changes could break rocks that are not below a critical size of about 0.5 mm, marking sand-sized particles.

Osman (2018) mentioned that natural vegetation types in drylands and deserts have short growing seasons, low growth rates and biomass production, and meager organic matter supply. Moreover, drylands soils have a variety of parent materials, including predominantly desert sands, dunes, aeolian sands, and loess. Under such conditions and climate components, rocks and minerals satisfactorily undergo physical weathering in dryland environments. However, biogeochemical weathering is limited due to moisture scarcity. Therefore, drylands soils tend to become coarse-textured soils such as sand, loamy sand, and sandy loam, with minor formation of clayey soils.

Accordingly, silica sand was adopted for testing in the present study. Silica sand is resistant to volume change associated with moisture content variation. Thus, the shrinkage and cracking effects are assumed to be negligible. Moreover, the mother material was unified in this study, while two other soil properties were varied, gradation and relative density, which allows deducing the pore size distribution directly from the matric suction and excluding the influence of the osmotic suction. Therefore, seven distinct soil textures were varied, while three relative densities were considered. The influence of soil gradation and relative density on evaporation was investigated. Consequently, a new pore index was proposed, and its influence on the process was studied.

The commercial names of the samples are K-7, K-6, K-5, K-4, K-2, and K-3.6, a mixture of K-3 and K-6 soils with a 1:1 ratio by mass. Their particle size distribution curves are delineated in Figure 3.1. The particle size distribution test was conducted using the sieve analysis according to the Japanese Geotechnical Society standard JGS 0131-2009. However, the fine fraction particle size distribution was analyzed using a laser diffraction-particle size analyzer. The soil profiles were compacted at 90%, 80%, and 70% relative density. Therefore, ten soil profiles identifying unique pore structures were used for the evaporation tests. A

summary of the physical and hydrological properties of the tested profiles is shown in Table 3.1. The soils' specific gravity (G_s) was determined according to the JGS 0111-2009, while the dry density was found based on the minimum and maximum dry density, following the JGS 0161-2009. Based on the soils' physical properties, all soils are classified as Sand [S] except for the K-7, which is classified as Sand with Fine fraction [S-F] according to the JGS soil classification of geomaterials, JGS 0051-2009. Additionally, the saturated hydraulic conductivity (k_s) was determined for some profiles following the JGS standard for permeability of saturated soils, JGS 0311-2009, while others were estimated using the physically-based Kozeny-Carman equation (Carman, 1956; Kozeny, 1927).

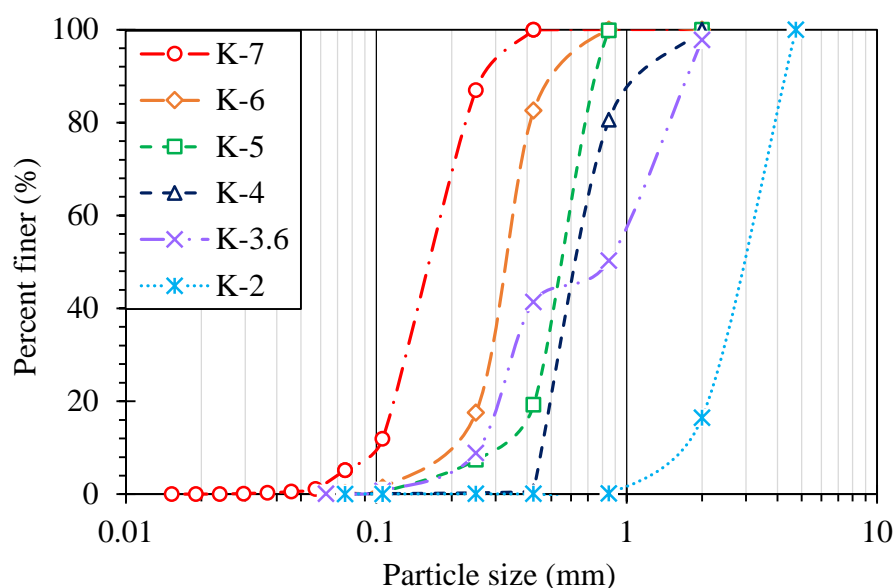


Figure 3.1: Particle size distribution curves.

The Soil Water Characteristic Curves (SWCCs) and the Hydraulic Conductivity Functions (HCFs) were determined using the Continuous Pressurization Method (CPM) developed by Alowaisy et al. (2020, 2019). The CPM allows for a continuous, direct, and accurate determination of the SWCC and HCF in a relatively short time. Utilizing the axis-translation technique, the CPM involves pressurizing the sample at a constant rate while instantly measuring the developing pore water pressure using a micro-tensiometer installed at the center of the sample. In this study, the evaporation process was investigated from initially fully saturated soil profiles, where the water development and redistribution are believed to follow the main drying SWCCs at which the contact angle is constant (Zhou, 2013). Therefore, the SWCC hysteresis and variation in the contact angle were not considered. The obtained

Table 3.1: Soil profiles' physical and hydrological properties

		K-7	K-6	K-5				K-4		K-3.6	K-2
Relative Density	Dr (%)	80	80	90	80	70	90	80	70	80	80
Physical properties											
Specific gravity	G _s	2.65	2.64		2.65			2.65		2.64	2.62
Effective size	D ₁₀ (mm)	0.10	0.20		0.31			0.47		0.26	1.72
Fine fraction	(%)	5.14	0.20		0.20			0.11		0.13	0.06
Soil Classification		S-F	S		S			S		S	S
Dry density	ρ _d (g/cm ³)	1.48	1.50	1.54	1.50	1.47	1.54	1.51	1.48	1.69	1.43
Void ratio	e	0.79	0.75	0.72	0.76	0.80	0.71	0.75	0.79	0.56	0.84
Porosity	ϕ	0.44	0.43	0.42	0.43	0.45	0.42	0.43	0.44	0.36	0.46
Hydrological properties											
Saturated hydraulic conductivity	k _s (cm/s)	0.01	0.05*	0.22	0.10	0.15	0.26	0.20	0.26	0.04*	4.55*
Saturated volumetric water content	θ _s	0.44	0.47	0.43	0.47	0.48	0.45	0.46	0.47	0.39	0.46**
Residual volumetric water content	θ _r	0.03	0.06	0.05	0.06	0.08	0.05	0.06	0.04	1.00×10 ⁻¹⁰	1.00×10 ^{-10**}
Van Genuchten model fitting parameters	α (cm ⁻¹)	0.02	0.03	0.05	0.05	0.05	0.09	0.08	0.07	0.03	0.35**
	n	5.47	5.01	10.01	6.91	6.96	24.89	14.12	11.78	3.83	9.78**
Characteristic Length	L _C (cm)	26.99	14.49	4.31	6.35	7.38	0.95	1.97	2.66	22.42	0.64**

*k_s were estimated using Kozeny-Carman equation (Carman, 1956; Kozeny, 1927)

**SWCC was estimated using Kitasako model (Sako and Kitamura, 2006)

drying SWCCs, elucidated in Figure 3.2, were fitted using the Van Genuchten (VG) model and following equations 2.14 to 2.16 (van Genuchten, 1980). Besides, the quasi-state model was used to determine the HCF using a single micro-tensiometer installed at the center of the sample in the CPM apparatus under a transient state (Alowaisy et al., 2022). Figure 3.3 delineates the HCFs of the profiles prepared at 80% relative density. Exceptionally, testing the K-2 profile using the CPM was challenging due to the difficulty in maintaining the fully saturated initial conditions during sample preparation. Therefore, the drying SWCC was estimated using the

Kitasako model (Sako and Kitamura, 2006), which statistically determines the SWCC based on the particle size distribution. It must be noted that the adopted sandy soil in the current study is highly resistant to drying-induced volume change. Thus, the density and void ratio is assumed to be constant during the SWCC determination, and that was confirmed experimentally by monitoring the samples' surfaces when utilizing the CPM.

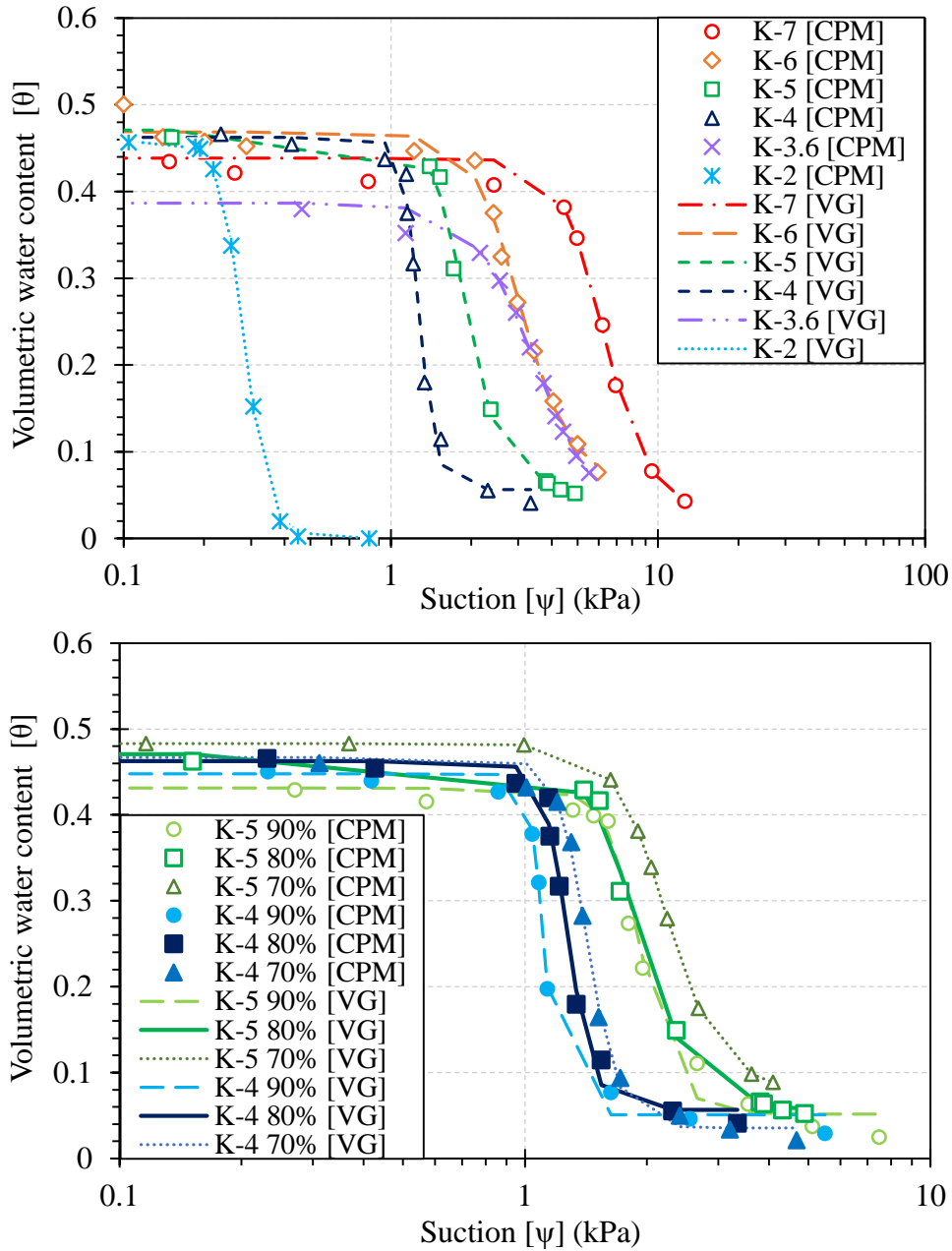


Figure 3.2: Drying soil water characteristic curves.

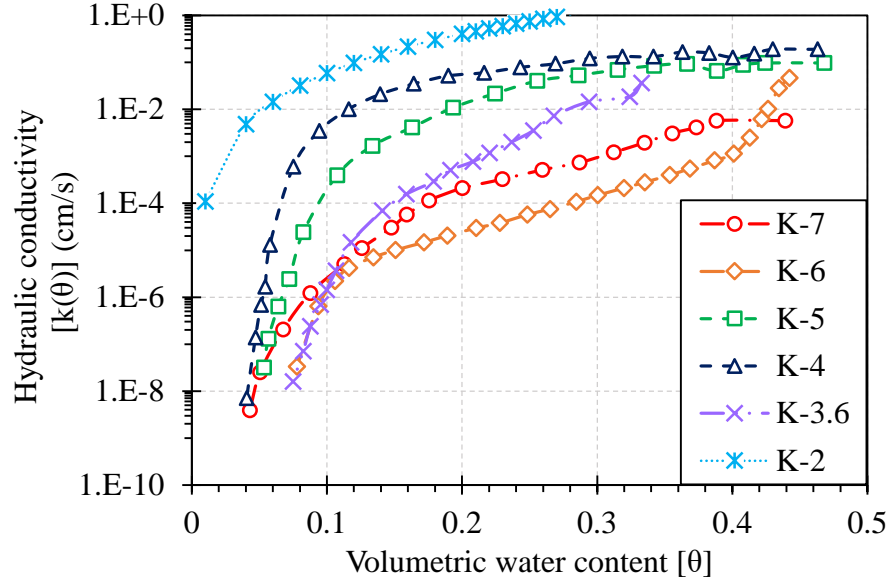


Figure 3.3: Hydraulic conductivity functions.

The current study investigates the evaporation stages from fully saturated soil profiles. Therefore, the L_C for the tested profiles was determined following Lehmann et al. (2008) to ensure capturing the whole process. The L_C was used as a guide for estimating the soil profile length and designing the experimental setup. Additionally, it was used in the analysis when tracing the unsaturated layer during drying. The L_C , extensively explained in Chapter 2, indicates the drying front depth within the unsaturated layer at the end of Stage 1. Physically, it defines the maximum capillary pressure attained between the smallest and largest pores at the surface and drying front, respectively. It is determined by linearizing the drying SWCC of each soil profile, using equations 2.17 to 2.21.

3.3 Methodology and Experimental Considerations

Drying soil column tests were adopted in the present study to investigate the influence of internal factors and soil pore structure on evaporation. The influence of the external factors was eliminated by maintaining the atmospheric demand at the evaporating surface. An exhaustive review of the experimental setup, soil preparation technique, and testing conditions is discussed in this section.

3.3.1 Experimental setup

The utilized experimental setup in the present study considers repeatability, reliability, and accuracy in determining the actual evaporation flux during drying under unified atmospheric conditions. Figure 3.4 delineates the experimental setup, and the adjoining table explains the

Unit	No.	Component	Functions and remarks
Climate control	1	Environmental chamber	Transparent acrylic cylindrical chamber (50 cm diameter, 30 cm height), maintains the atmospheric conditions.
	2	Control panel	Includes the switch key and other controlling keys and digital display of the thermo-hygrometer sensor.
	3	Air blender	Continuously mixes the air inside the environmental chamber and supports its movement through the air pipes.
	4	Freezer	Cools down and heats the air inside the environmental chamber, automatically operate in an alternative mode to maintain the designated temperature.
	5	Heater	
	6	Dehumidifier	Decreases and increases the humidity of the air inside the environmental chamber, automatically operate in an alternative mode to maintain the designated humidity.
	7	Ultrasonic humidifier	
	8	Fan	Monitors the instantaneous wind speed and circulates the air between the chambers.
	9	Thermo-hygrometer	Records and monitors the temperature and humidity in the environmental and evaporation chamber.
	10	Switch	Controls the wind speed at the outlet of the environmental chamber.
	11	Evaporation chamber	Transparent acrylic rectangular chamber (40×20×15 cm), allows evaporation under controlled demand.
	12	Wind speed sensor	Records the wind speed in the evaporation chamber. (± 0.1 m/s resolution)
Evaporation testing	13	Soil column	Transparent acrylic cylindrical column (10 cm diameter, 50 cm height), includes the tested soil profiles.
	14	Column's base	Acrylic base consists of a valve and porous stone disk to distribute water during saturation uniformly.
	15	Valve	Function as a water inlet for the up-flow saturation.
Control and acquisition	16	Digital balance	Continuously measures the change in the soil column's mass. (31 kg capacity and ± 1 g resolution)
	17	TDRs	Time Domain Reflectometry probes, indirectly measure the water content of the soil profile.
	18	Sensors' data logger	Continuously records data from the climate control unit, while the data is saved directly through a computer application.
	19	Computer	
	20	Weighing data logger	Continuously records data from the digital balance, while the data is retrieved directly from a computer.
	21	TDRs data logger	Continuously records data from the TDRs while the data is retrieved through a computer application.

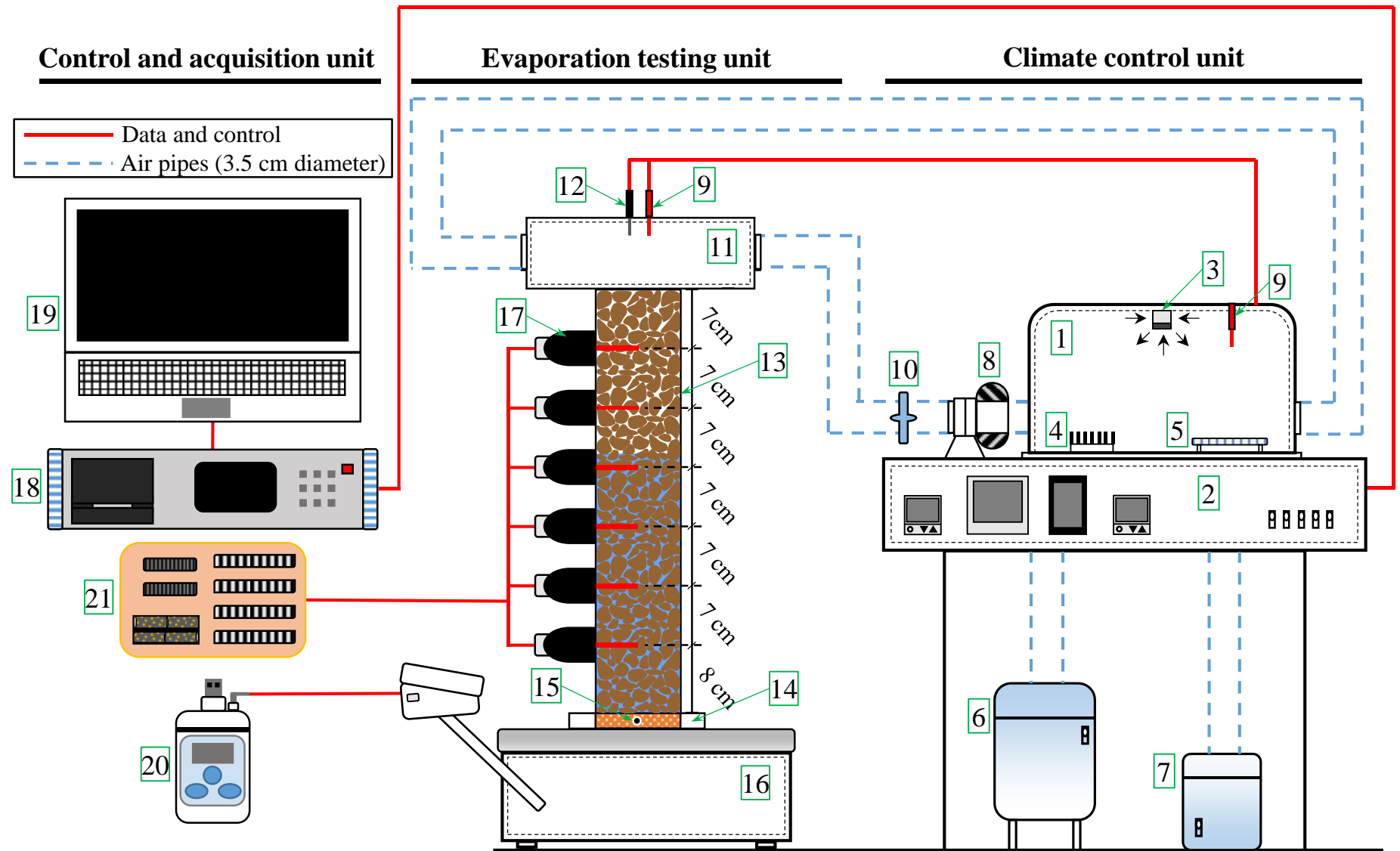


Figure 3.4: Experimental setup of the drying soil column test.

deployed instrumentations. The experimental setup comprises three main units: the climate control unit, the evaporation testing unit, and the control and acquisition unit.

The climate control unit involves the Climate Control Apparatus (CCA) developed by Teng et al. (2014). It unifies and maintains a constant and steady atmospheric demand during testing. The apparatus is reliable in controlling the temperature, relative humidity, and wind speed during prolonged testing. The heater versus freezer, and the ultrasonic humidifier versus dehumidifier, automatically operate in an alternative mode to maintain the designated temperature and relative humidity in the environmental chamber. The well-sealed environmental chamber is a 50 cm in diameter and 30 cm in height cylindrical chamber made of transparent acrylic material. It is instrumented with a thermo-hygrometer and an air blender that continuously mixes the inner air. A fan installed at the environmental chamber outlet monitors the instantaneous wind speed and circulates the air to the evaporation chamber. The well-sealed evaporation chamber is a 40×20×15 cm rectangular-shaped chamber made of transparent acrylic material. It is connected to the environmental chamber with an inlet and outlet 3.5 cm in diameter plastic pipes. The evaporation chamber is instrumented with a thermo-hygrometer and a wind speed sensor that serves as feedback for the control panel to operate the devices alternatively in the environmental chamber and maintain the designated atmospheric conditions.

The evaporation chamber is attached directly to the top of the tested soil column in the evaporation testing unit. A one-dimensional evaporation flow is facilitated at the soil's top surface through the evaporation chamber. A 50 cm height transparent acrylic cylindrical column is selected to adjust with the L_c of the tested profiles. The used column is 10 cm in diameter with a wall thickness of 1 cm. During saturation, a valve is installed at the column's base to function as a water inlet. The valve is connected directly to a porous stone disk to distribute the water into the soil profile uniformly. The base is appropriately sealed to avoid leakage during preparation and testing.

The climate control apparatus sensors are connected to a logger and computer for the control and acquisition unit to continuously record atmospheric conditions during testing. Moreover, the column is mounted on a digital balance, 31 kg capacity, and ± 1 g resolution. It is connected to a weighting data logger to determine the water loss amount and calculate the evaporation rate. The column is instrumented with Time Domain Reflectometry probes (TDRs) through drilled ports. They are connected to a data logger that records the data and indirectly measures the water content through the entire profile during the testing period.

3.3.2 Soil column preparation

Various soil placements and packing methods were reported in the literature. The dry or damp packing method is widely used for sandy soil flow movement experiments (Alowaisy and Yasufuku, 2018; Hrapovic et al., 2005). This method allows packing dry soils in the column at a specific density, then saturating the column to the designated degree of saturation. This study adopts the dry packing method to maintain a uniform porosity throughout the entire soil profile corresponding to each profile's relative density and dry density. Additionally, a specific saturation technique is applied on the compacted profiles from dry conditions to ensure fully saturated initial conditions and avoid any related ambiguities.

At first, the amount of oven-dry soil required to fill the column was calculated based on the soil's physical properties for each profile. A single filter paper layer was placed above the porous stone disk, as illustrated in Figure 3.5. The filter paper prevents soil losses or blockage of the porous stone's grooves. Additionally, it allows uniform soil saturation and reduces the influence of the preferential water flow. The soils were then loaded in separate layers of 7 and 8 cm. Each layer was mechanically compacted until it satisfied the required relative density, confirmed by its thickness marked on the column. A metal pestle and hammer were used for soil compaction to obtain consistent and uniform density throughout the column. At each layer, the soil surface was lightly scarified after compaction to ensure hydraulic connectivity between layers and avoid the formation of preferential flow pathways. Meanwhile, the TDRs were installed carefully during soil placement at each designated drilled port. The ports were sealed properly using cold silicone sealant to prevent leakage during saturation and testing. The TDRs measure the soil water content based on the travel time of a high-frequency electromagnetic pulse through the soil, while the travel time is used to calculate the soil permittivity (dielectric constant). Therefore, the TDRs' positions, shown in Figures 3.4 and 3.5, were selected based on their reading coverage range to avoid disruption or overlapping between the TDRs, ensuring the whole profile's degree of saturation is recorded.

Deaerated water was used to saturate the soil profiles. The water was prepared for at least a day before it was used for saturation. At first, a deaerator tank was filled with distilled water and connected to a vacuum pump at 80 kPa to allow the removal of dissolved gases. Initially, the up-flow saturation technique was applied, which favors the displacement of air bubbles in the soil pores. The deaerator tank was connected to the soil column through the inlet valve installed at the base. A head difference between the deaerator tank and the soil column allows the water to propagate into the soil profile. Once the water reached the soil surface, a

vacuum chamber was attached to the top of the soil profile, where the chamber and the connected deaerator tank were connected to the vacuum pump for an additional 80 kPa vacuum at the column's top and bottom. This technique eliminates the entrapped air bubbles and ensures the soil profile is fully saturated. The TDRs' readings were then checked to confirm the column's initial fully saturated conditions.

Finally, the column was detached from the water deaerator tank, while the top vacuum chamber was removed. Meanwhile, the climate control apparatus was set at the designated temperature and relative humidity. Consequently, the soil column was mounted on the digital balance while the evaporation chamber was carefully attached and sealed to its top. Before starting the test, the balance and all sensors were confirmed to be connected to their data loggers and computer.

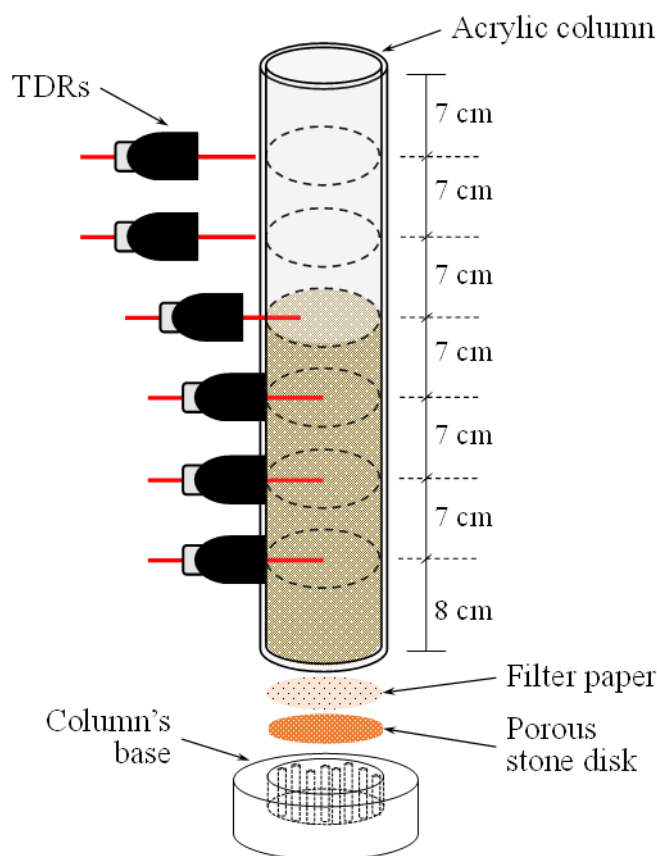


Figure 3.5: Drying soil column preparation and compaction method.

3.3.3 Testing procedure and boundary conditions

The ten homogeneous sandy soil drying column tests were conducted individually. The columns were initially fully saturated while evaporation was allowed through the topsoil surface. The atmospheric evaporative demand at the surface was unified in order to exclusively investigate the influence of the pore structure and water supply on the process. Therefore, the temperature, relative humidity, and wind speed were maintained and continuously recorded during testing.

According to Shahraeeni et al. (2012), for relatively high evaporative demand (typically > 5 mm/day), even during Stage 1, when the capillary flows are not limiting, and evaporation occurs at the surface, the actual evaporation rates constantly decrease. It was explained by Schlünder (1988) that it is a phenomenon attributed to the limitations on vapor exchange between the drying surface and the air boundary above. Therefore, in the current study, a low atmospheric demand was adopted for testing to detect the three distinct evaporation stages, at which the Stage 1 evaporation rate is relatively high and constant. Consequently, an average temperature of $28.4 \pm 1.2^\circ\text{C}$, relative humidity of $47.4 \pm 2.4\%$, and wind speed of 2.0 ± 0.2 m/s were confirmed 5 cm above the soil surface for all the tested profiles during the entire testing duration. Figure 3.6 shows the average and fluctuation range of the atmospheric conditions of each tested soil profile. Additionally, Figure 3.7 delineates the fluctuations of the atmospheric conditions during the prolonged testing of the K-7 profile.

The potential evaporation rate was calculated based on the prevailing atmospheric conditions. Two empirical methods were used to estimate the potential evaporation. The Thornthwaite equation, equation 2.6, which considers the evaporation as the only boundary flux (Thornthwaite, 1948), and the Blaney and Criddle equation, in its form that considers the temperature, wind speed, and the minimum relative humidity for estimating the potential evaporation (Yates and Strzepek, 1994). It was found that under the applied testing conditions, the potential evaporation equals 4.5 ± 0.6 and 5.1 ± 0.4 mm/day, according to Thornthwaite and Blaney, and Criddle, respectively. Both methods resulted in low atmospheric demand. The result was confirmed experimentally, where the average actual evaporation rate attained during Stage 1 in all the tested profiles was equal to 3.7 ± 0.5 mm/day.

The atmospheric conditions, amount of water loss from the soil profiles, and the water content across the profiles' depth were recorded at a 2-minute interval during the whole testing period. Testing was shut down once the actual evaporation rate converged to a low and constant value, announcing the onset of the residual stage, Stage 3.

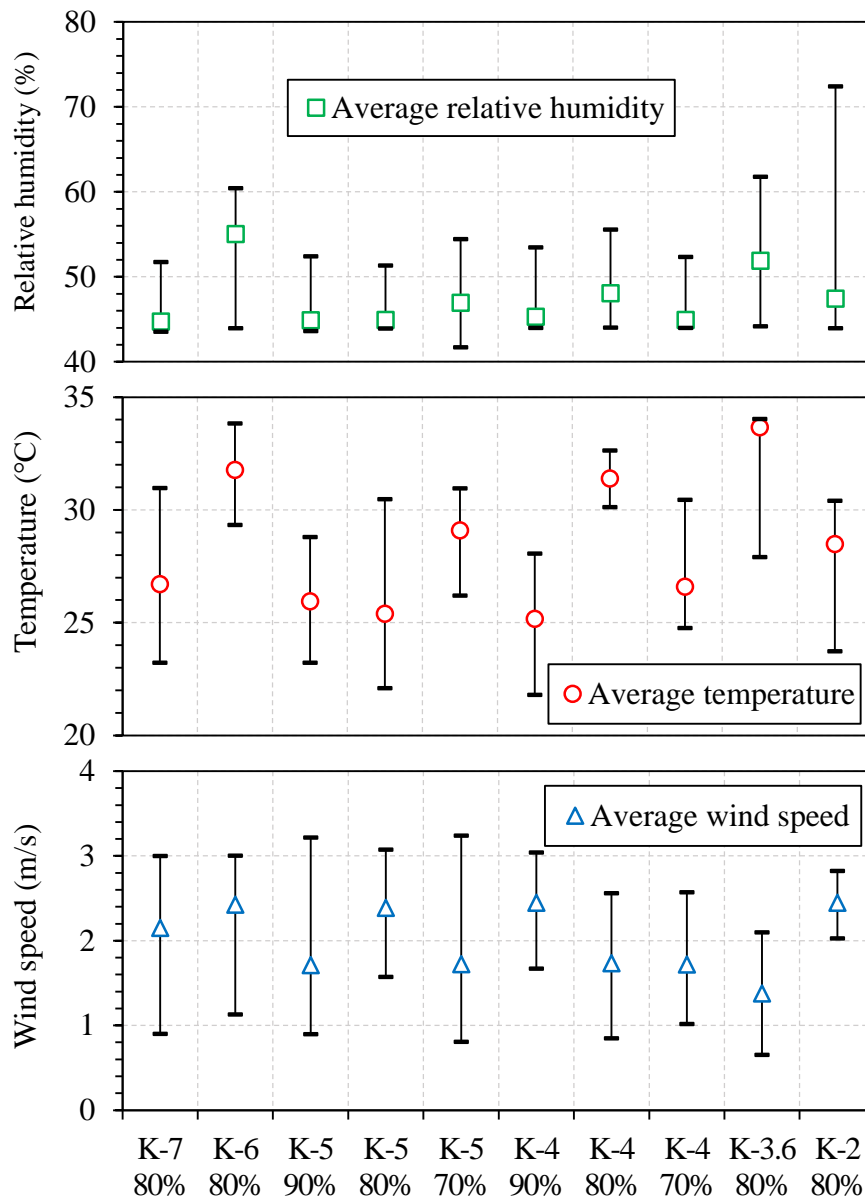


Figure 3.6: Average atmospheric conditions of the tested profiles.

3.4 Actual Evaporation and its Stages

The actual evaporation rate during drying was determined experimentally using the data recorded by the digital balance. The Actual Evaporation rate (AE) is the amount of water loss per unit area in a specific time (mm/day). The normalized actual evaporation curves were used to study the evaporation process and determine its stages for easier comparison between the tested profiles. The normalized actual evaporation rate (NAE) was obtained individually for

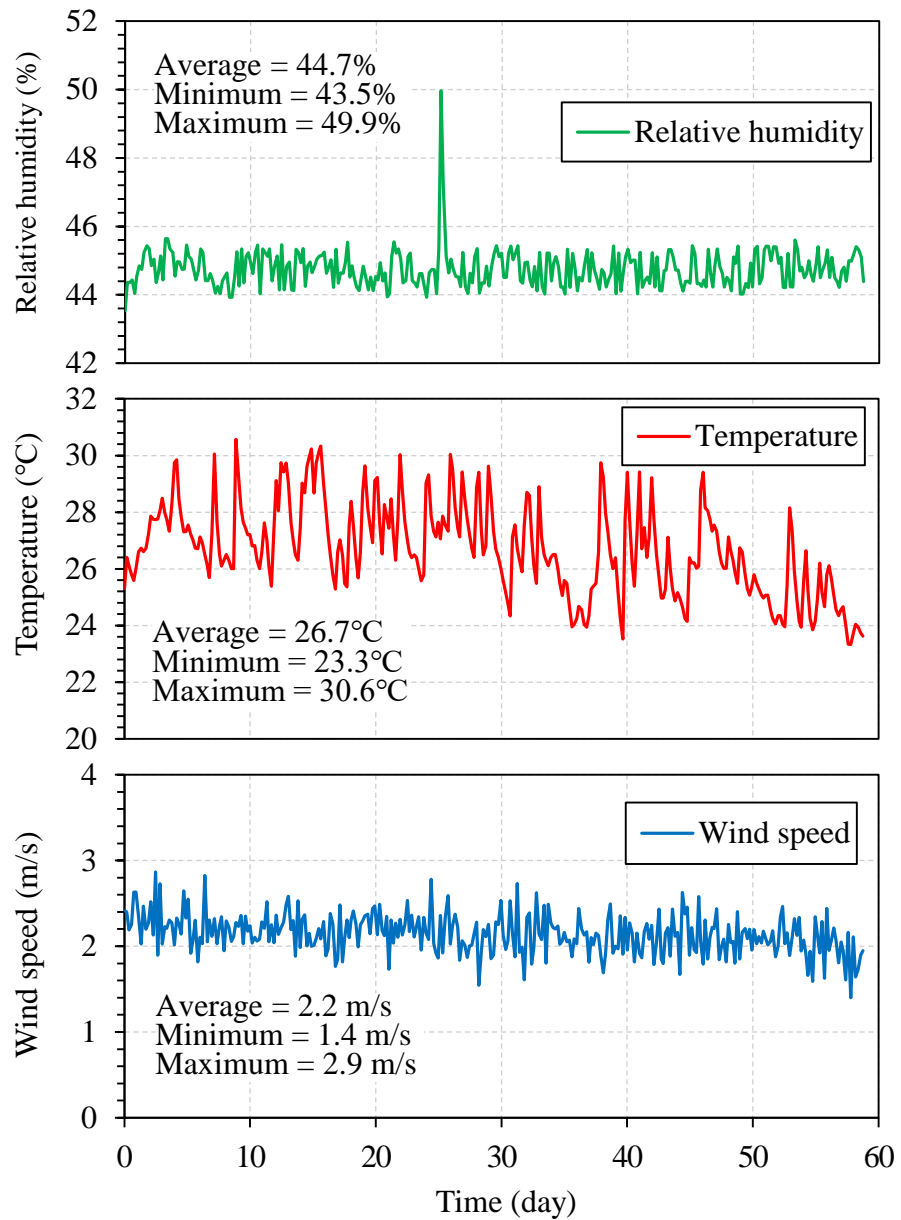


Figure 3.7: Fluctuations of the atmospheric conditions during testing the K-7 profile.

each profile by dividing the actual evaporation rate at any time during drying over the constant actual evaporation rate attained during Stage 1 ($AE_{\text{Stage 1}}$).

The following section discusses the influence of soil texture and relative density on evaporation behavior. The variation between the stages' durations for each profile is also presented. Hence, the tested profiles are divided into two groups: the soil texture group with the profiles of different textures and compacted at 80% relative humidity, and the relative density group comprised of K-5 and K-4 profiles, compacted at 90%, 80%, and 70% relative density.

3.4.1 Influence of soil texture

Figure 3.8 delineates the normalized actual evaporation rates with the elapsed time for the six profiles of the soil texture group. Additionally, the actual evaporation rate during Stage 1 and the duration of Stages 1 and 2 are summarized in the adjoining table. It must be noted that the number of days is rounded to the nearest integer. Generally, the duration of the whole evaporation process varied among the adopted textures. It can be observed that coarser soil textures reached Stage 3 faster, which results in less evaporated water during Stages 1 and 2. Lehmann et al. (2008) concluded that the duration of Stage 1 is related to the extent of the hydraulically connected region from the receding drying front to the surface, defined by the L_C . This agrees well with the obtained results, where Stage 1 was more extended for finer soil profiles when L_C was comparatively deeper. K-2 had the shortest Stage 1, and its L_C was the shallowest. On the contrary, K-7 had the longest Stage 1, and its L_C was the deepest.

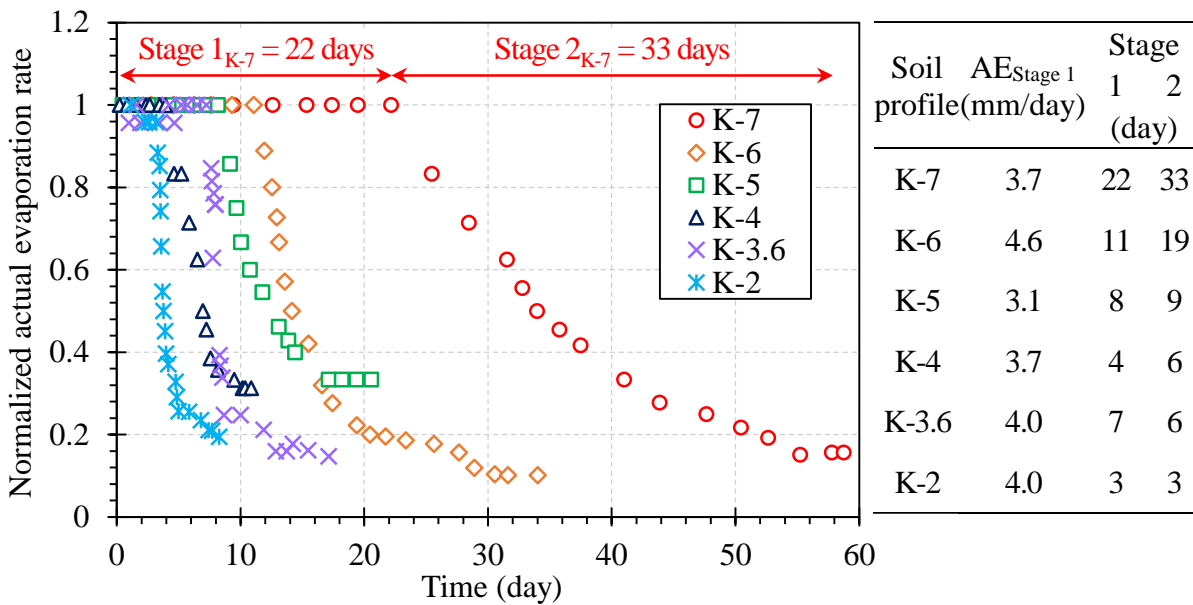


Figure 3.8: Normalized actual evaporation curves – Influence of soil texture.

Similarly, it was observed that Stage 2 is more extended for finer soil profiles, contributing to more water loss from the profile. This results in the longest Stage 2 attained by the K-7 profile, while Stage 2 lasted for a couple of days in the K-2 profile. Despite the differences in the duration of Stages 1 and 2 for different soil profiles, the duration of Stage 2 tends to be longer than Stage 1 for all the soil profiles.

It was noticed that the reduction slope of the normalized actual evaporation rate during Stage 2 differs between the profiles. In the interest of comparison, the evaporation reduction rate was assumed to be linear, as shown by the lines delineated at each evaporation curve in Figure 3.9. Consequently, its slope or the normalized actual evaporation reduction rate (ΔNAE) was found and summarized in the adjoined table. K-7 profile exhibited the gentlest slope of reduction during Stage 2, while the slope tends to become steeper for coarser soil profiles. The actual evaporation reduction rate (ΔAE) was also calculated and confirmed to have the same pattern as ΔNAE . The acceleration of actual evaporation reduction increases for coarser soil profiles. This behavior is believed to be related to the unsaturated layer formation and dynamics during Stage 2, which is discussed later in this chapter.

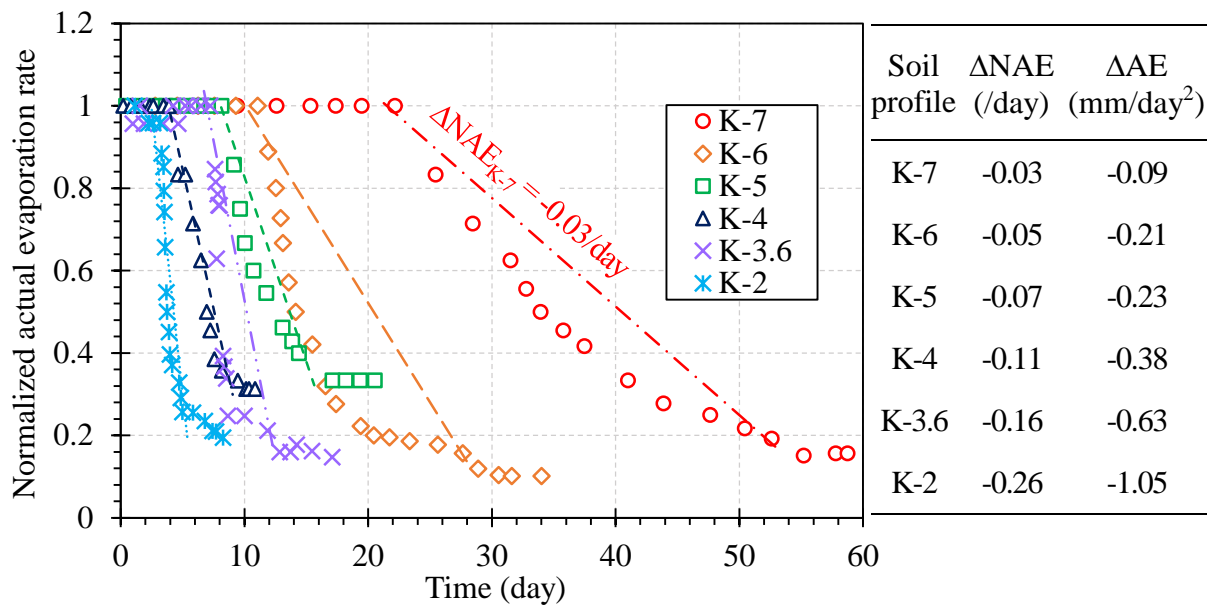


Figure 3.9: Normalized actual evaporation reduction rate during Stage 2.

Once the actual evaporation converges to a low and almost constant rate, diffusion-dependent Stage 3 is reached. Each soil profile was observed to have a different residual rate during Stage 3. K-7 and K-6 profiles showed the lowest residual evaporation rate during Stage 3, resulting in less water loss during this extended stage. The K-3.6 and K-2 profiles follow, while K-5 and K-4 profiles attain a comparatively high residual rate. Generally, vapor diffusion through the formed air-dry layer is dominant and highly dependent on the vaporization plane depth during Stage 3. Based on the results, it can be postulated that the vaporization plane depth for finer soil profiles is pinned into deeper layers compared to coarser profiles resulting in a

slower water supply to the surface and lower residual evaporation rates. Further analysis and discussion concerning the vaporization plane are presented in the following chapters.

3.4.2 Influence of relative density

Figure 3.10 delineates the normalized actual evaporation rates with the elapsed time for K-5 and K-4 profiles, compacted at 90%, 80%, and 70% relative density, the relative density group. Additionally, the actual evaporation rate during Stage 1 and the duration of Stages 1 and 2 are summarized in the adjoining table. It must be noted that the number of days is rounded to the nearest integer. It was noticed that the evaporation process extended almost similarly for each soil texture. Despite the relative density, Stage 1 ended within the first ten days and five days for the K-5 and K-4 profiles, respectively. However, Stage 2 tends to be slightly shorter for denser soil profiles, with an average deviation of less than two days.

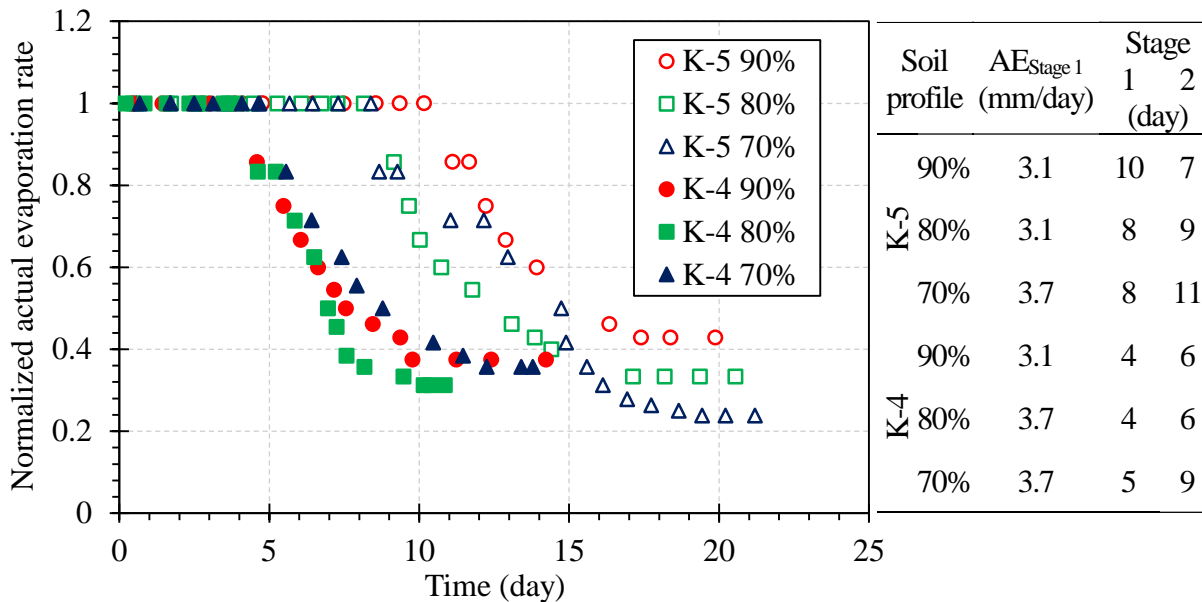


Figure 3.10: Normalized actual evaporation curves – Influence of relative density.

The normalized actual evaporation reduction rate during Stage 2 was studied for the tested profiles. The K-5 profile exhibited an average slope of $-0.07 \pm 0.004/\text{day}$, equivalent to an actual evaporation reduction rate of $-0.24 \pm 0.01 \text{ mm/day}^2$, while the K-4 showed an average of $-0.1 \pm 0.02/\text{day}$, equivalent to $-0.31 \pm 0.05 \text{ mm/day}^2$ actual evaporation reduction rate. Based on the results, it must be concluded that the relative density has a remarkably low influence on evaporation from poorly-graded sandy soil profiles.

3.5 Water Redistribution and Unsaturated Layer Formation

Investigating the evaporation flux and the influence of the water supply on the process requires a thorough understanding of the saturation profile development and the formation of the unsaturated layer during drying. Therefore, this section discusses the amount of evaporated water from the soil profile and the water redistribution profiles during drying.

The cumulative evaporated water from the soil profiles recorded using the digital balance was plotted with time for each soil profile. The slope of the curve indicates the actual evaporation rate at each stage. Based on that and the stages' durations extracted from the actual evaporation curves, the amount of water lost during each stage was determined. Additionally, the TDRs readings were utilized to depict the water restitution profile of each tested column. Six different times were selected during drying, considering the inflection points on the evaporation curves in Figure 3.8. Chronologically, starting with the onset and middle of Stage 1, followed by the onset, middle, and end of Stage 2, and finally, 12 hours from the onset of Stage 3.

The soil texture and relative density influence the water loss, and the unsaturated layer formation is investigated. Hence, the same groups are used for discussion: the soil texture group with the profiles of different textures and compacted at 80% relative humidity, and the relative density group comprised of K-5 and K-4 profiles, compacted at 90%, 80%, and 70% relative density. Furthermore, new insights about the unsaturated layer and its relation with the actual evaporation rate are discussed.

3.5.1 Influence of soil texture

Figure 3.11 delineates the relationship between the cumulative evaporated water with the elapsed time for the six profiles of the soil texture group. The evaporation stages are also marked on each curve, and the amount of water loss is summarized in the adjoining table. At the early stages of evaporation, the slope was nearly linear, corresponding to the constant rate stage. Once the slope changes, representing the decreasing actual evaporation rate, a concaved-down curve is formed, announcing Stage 2. The curves showed that the cumulative evaporated water from the K-7 profile during the process was remarkably higher than the other profiles, followed by the K-6 profile. The K-3.6 and K-5 profiles lost almost the same amount of water, followed by K-4 and K-2. Generally, the K-7 profile lost around three times more water than the K-5 and around seven times more than the K-2 profile.

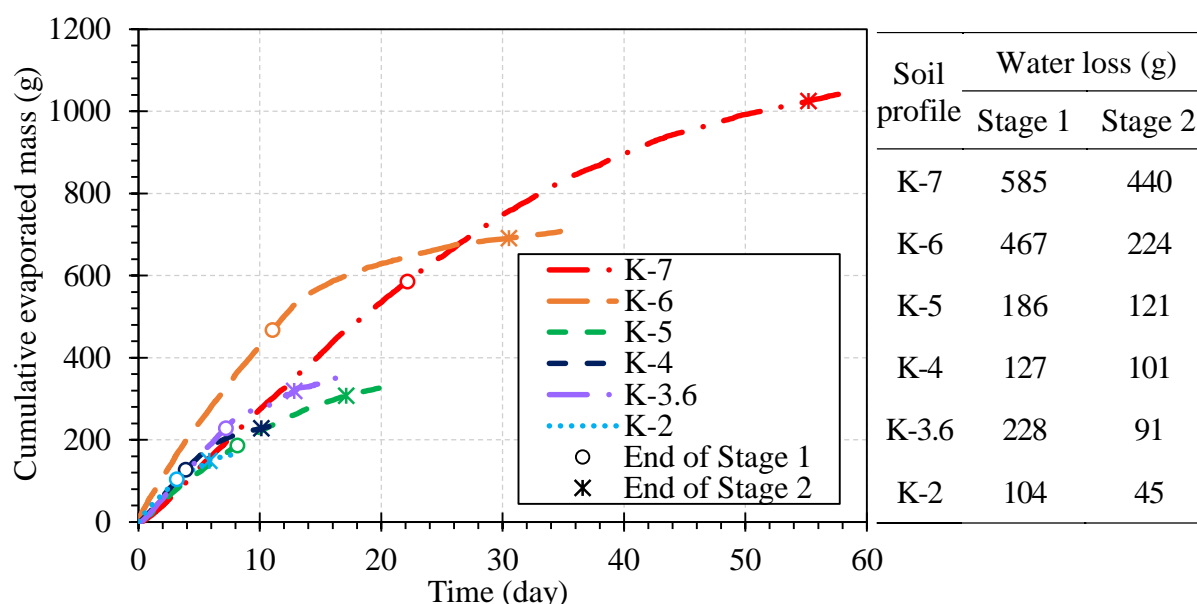


Figure 3.11: Cumulative evaporated water mass – Influence of soil texture.

Similarly, during Stages 1 and 2 individually, K-7 lost more water than the other profiles. This significantly larger amount of evaporated water from the K-7 column might be attributed to the relatively long time required to reach the residual stage, as discussed in Figure 3.8. In particular, during Stage 2, K-7 maintained relatively higher evaporation rates for a longer time, which can be confirmed by the reduction slope of the actual evaporation rate. Despite the differences in the amount of water loss during Stages 1 and 2 for different soil profiles, the evaporated water during Stage 2 tends to be less than that evaporated during Stage 1 for all the soil profiles. This is attributed to the high evaporation rates during Stage 1 compared to Stage 2.

Figure 3.12 depicts the water redistribution profiles for the texture group soil profiles. It was confirmed that the columns achieved fully saturated conditions before starting the tests (Onset of Stage 1). At the top of the soil profile, the air phase started invading larger pores at the surface, and consequently, the drying front started receding into deeper layers. The saturation reduction at the profile's top within the middle of Stage 1 (red circle dashed lines) indicates the drying front, the boundary between the saturated and the unsaturated layers. The drying front propagated to different depths and times for each profile. At the end of testing (blue triangle dotted lines), the drying front propagated to the bottom layer in the K-7 and K-6 profiles, to around the middle of K-5 and K-3.6 profiles, while it stayed within the top 14 cm in the K-4 profile. On the other hand, the unsaturated layer of the K-2 profile could not be observed since it is formed within the top 7 cm layer where the data could not be recorded. Consequently, the

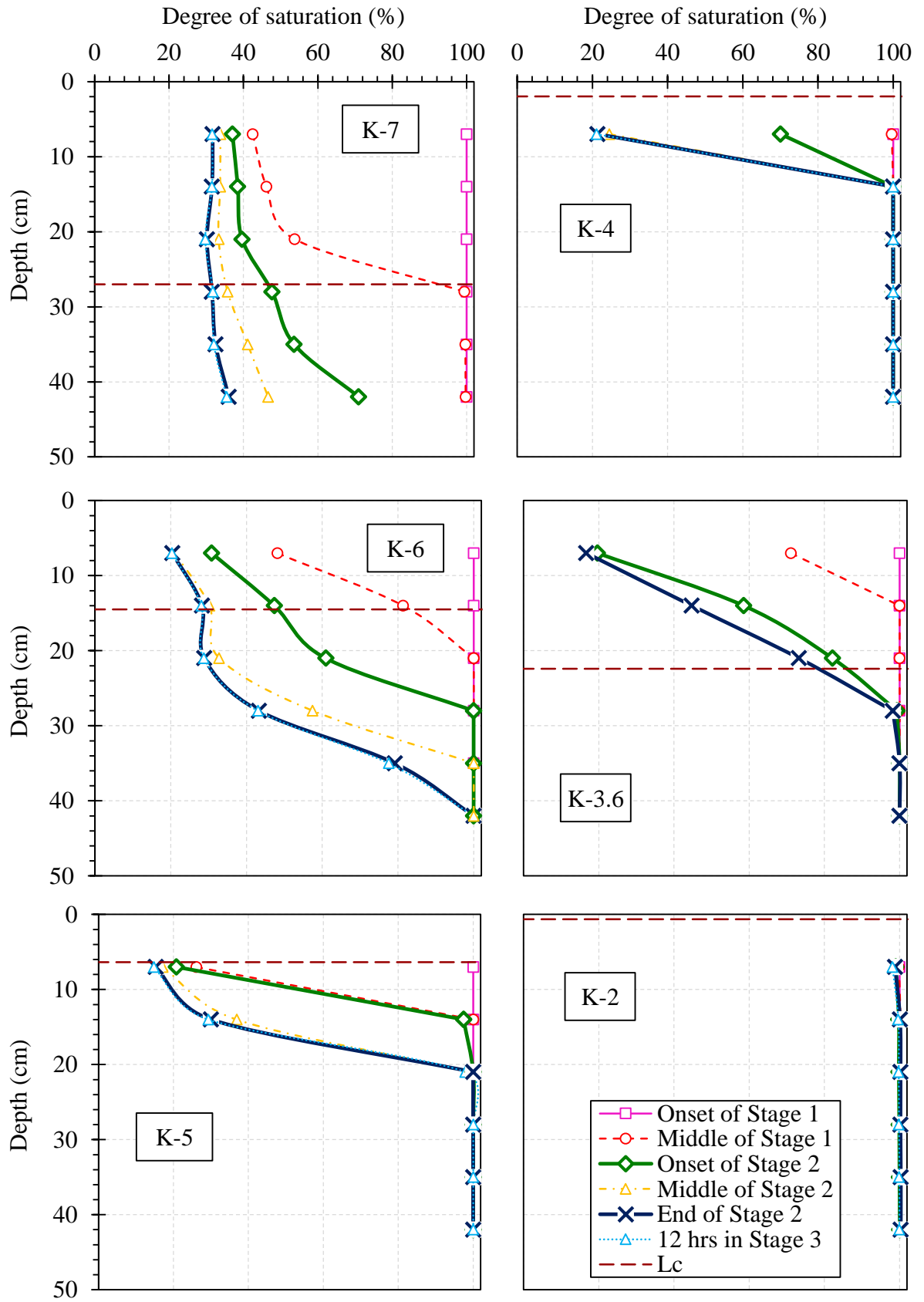


Figure 3.12: Water redistribution profiles during evaporation - Influence of soil texture.

unsaturated layer comprised around 85% of the K-7 and K-6 profiles, around 50% of the K-5 and K-3.6 profiles, and less than 25% of the K-4 and K-2 profiles. It was observed that for deeply propagating drying front profiles, a significant unsaturated soil layer almost reached the residual degree of saturation towards the end of the test, while others retained a significant amount of water in their pores. Based on the results, it must be concluded that the soil texture significantly influences the amount of water loss and thickness of the unsaturated layer during drying, whereas finer soils tend to lose more water keeping the soil profile in a severe unsaturated condition.

Drying front during Stage 1

The determined L_C of each profile is delineated with the horizontal dashed line in Figure 3.12. By definition, the L_C determines the drying front depth at the end of Stage 1. However, the boundary between the saturated and unsaturated layer at the end of Stage 1 (green rhombus solid lines) was deeper than the calculated L_C for all profiles. It must be noted that once the drying front reaches the L_C , the water transport mechanism changes from capillary during Stage 1 to vapor diffusion through an air-dry layer to the soil surface during Stage 2. At that point, the summation of the vapor diffused from all the active pores at the drying front might have compensated for the reduction in the supply efficiency associated with the change in the transport mechanism under the imposed low atmospheric demand. Consequently, the actual evaporation at the beginning of Stage 2 might have persisted at a high rate, equal to that of Stage 1. As a result, the indicated onset of Stage 2, found in Figure 3.8, delineates an inflection point on the actual evaporation curve, but it does not necessarily represent the change in the transport mechanism; therefore, it does not mark the actual commencement of Stage 2.

Drying front and unsaturated layer during Stage 2

The drying front or the boundary between the saturated and unsaturated layer at the onset and end of Stage 2 persisted at the same depth in K-4 and K-3.6. It persisted between 28 and 42 cm in the K-6 profile and between 14 and 21 cm in the K-5 profile. On the other hand, it reached the base of the column in the K-7 profile. This behavior results in maintaining or slightly increasing the thickness of the unsaturated layer during Stage 2, comprised of a capillary dominant film region topped with a diffusion-dominant air-dry layer. However, a significant reduction in the unsaturated layer's degree of saturation was noticed. Such observation suggests that during Stage 1, water evaporates from larger pores within the hydraulically connected film region. On the other hand, during Stage 2, once the smallest meniscus breaks and starts receding

from the soil surface, water gets lost from the smaller pores within the same unsaturated layer rather than the larger pores within the saturated bottom layer. Ultimately, this significantly reduces the unsaturated layer's degree of saturation while causing only a slight change in its thickness.

Vaporization plane during Stage 2

The reduction of the unsaturated layer's saturation during Stage 2 to almost a residual value suggests that the vaporization plane is formed below the soil surface. Consequently, the water starts transporting through the air-dry layer to the surface as vapor. Figure 3.12 shows that the degree of saturation recedes at different rates between the samples. This behavior reflects the receding rate of the vaporization plane during Stage 2.

According to Fick's law, the diffusion rate (J) is directly proportional to the concentration gradient with respect to the diffusion distance ($\partial c / \partial L$). This relation is mathematically delineated as follows:

$$J = -D \frac{\partial c}{\partial L} \quad (3.1)$$

where D is the soil's vapor diffusion coefficient or the diffusivity, and the negative sign indicates that the movement direction is opposite the concentration gradient. Assuming the validity of Fick's law through the air-dry layer under steady-state conditions, the receding rate of the diffusion distance (ΔVP), here the vaporization plane, is inversely proportional to the diffusion rate change (ΔNAE), which is the actual evaporation reduction rate during Stage 2. ΔVP was traced from the water redistribution profiles, where the vaporization plane is considered the boundary between the air-dry layer and the film region, and its location was determined as the point at which the degree of saturation reaches the residual, indicating the top dry layer. Consequently, the vaporization plane depth change during Stage 2 was determined for each soil profile, and its relationship with the normalized evaporation reduction rate in Figure 3.9 was studied considering the negative sign in Fick's law. Despite the simplicity and the associated errors with the determination method of ΔVP , the results in Figure 3.13 show a good correlation between the change in the normalized actual evaporation rate and the vaporization plane receding rate during Stage 2. Accordingly, a lower receding rate of the vaporization plane during Stage 2 corresponds to a lower reduction of the actual evaporation rate, resulting in gentler slopes of the evaporation curve during Stage 2.

Notwithstanding the slight changes in the vaporization plane depth under low atmospheric demand, it highly influences the evaporation behavior during Stage 2. Based on

the results, it must be concluded that the vapor diffusion is dominant during Stage 2, and the evaporation rate mainly depends on the diffusion distance from the vaporization plane to the surface under unified atmospheric demand. Due to the importance of the vaporization plane and the unsaturated layer's dynamics, especially during the complicated Stage 2, a new technique is required to accurately trace the unsaturated layer dynamics through any soil profile.

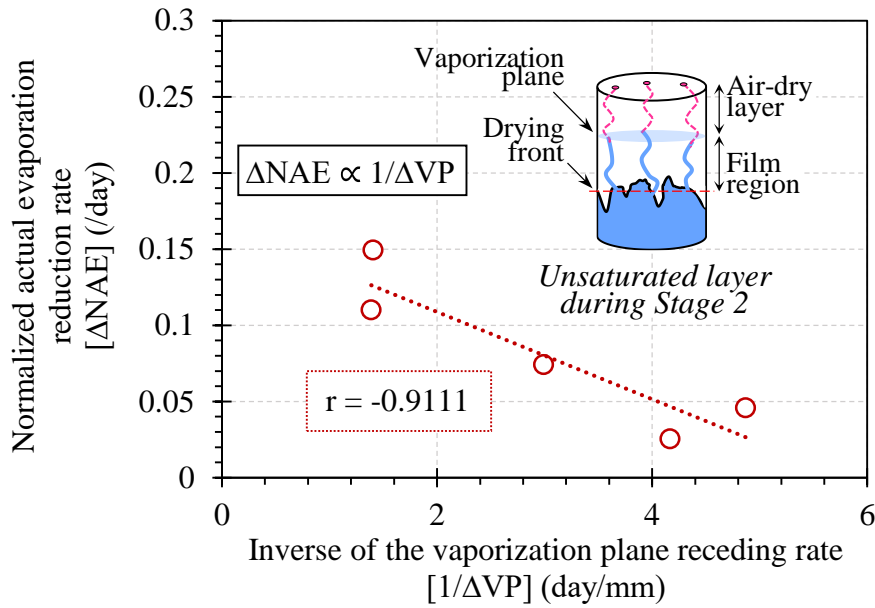


Figure 3.13: Relationship between the normalized actual evaporation reduction rate and vaporization plane during Stage 2.

Another explanation of the gentle slopes during Stage 2 can be drawn from Shahraeeni et al. (2012). It was reported that the decrease in the surface water content during drying increases the dry region between the water-filled pores that persisted at the surface, denoted as the active pores. The diffusion through the viscous sublayer at the surface increases from an isolated pore while the total evaporation from the entire surface decreases. Those nonlinear vapor fluxes strongly depend on the absolute size of the active pore. For a soil profile comprised of small pores, the evaporation rate per pore and its growth rate is higher than that of a profile with larger pores. Ultimately, its actual evaporation reduction rate is relatively smaller. In this study, the pores comprising the K-7 profile, shown in the next section, are relatively smaller than the other profiles. Therefore, the pores' evaporation growth rate is the highest for K-7, which partially compensates for the increase in the diffusion distance, resulting in the gentlest actual evaporation reduction slope during Stage 2.

Vaporization plane during Stage 3

During Stage 2, vapor diffuses through the formed air-dry layer at the top of the soil profile. The diffusion distance with the tortuous nature of the pore passages makes the actual path even longer than the apparent straight depth, which highly affects the diffusion rate (Hillel, 2004). Therefore, the diffusion distance becomes the main factor suppressing the actual evaporation rate announcing the onset of Stage 3. For the adopted samples, the unsaturated layer reached the bottom of the column in the K-7 and K-6 profiles during Stage 3, allowing the vapor to diffuse through a relatively thicker air-dry layer. This behavior explains the relatively lower residual evaporation rate of these profiles marked in Stage 3 than the other profiles (Figure 3.8).

The high dependency of the evaporation during Stage 3 on the diffusion depth was also reported by Shahraeeni et al. (2012). It was concluded that when the active pores reach a minimum density at the surface and the total evaporation from the entire pores decreases to a specific level, the relative evaporation rate per pore and the total surface's efficiency become almost similar, despite the absolute size of the pores that comprise the soil sample. Consequently, vapor supply from deeper layers becomes governing.

3.5.2 Influence of relative density

Figure 3.14 delineates the relationship between the cumulative evaporated water with the elapsed time for the K-5 and K-4 profiles, compacted at 90%, 80%, and 70% relative density, the relative density group. The evaporation stages are also marked on each curve, and the amount of water loss is summarized in the adjoining table. It was noticed that the cumulative evaporated water slightly differs for each soil texture. Similar results were observed during Stage 2, where varying the relative density between 70-90% results in a $\pm 20\%$ and $\pm 15\%$ difference in water loss for K-5 and K-4 samples, respectively. Additionally, water loss during Stage 2 tends to be comparatively less for denser soil profiles.

Figure 3.15 depicts the water redistribution profiles for the same tested soils. It must be noted that the material adopted in this study is highly resistant to volume change. Thus, the void ratio is assumed to be invariant during testing and was confirmed experimentally by monitoring the samples' surfaces. It was observed that despite the relative density, the unsaturated layer at the end of testing formed around 56% (21-28 cm) and 42% (14-21 cm) for the K-5 and K-4 groups, respectively. However, at the end of Stage 1 (green rhombus solid lines), different densities developed different water redistribution. On the other hand, at the end of Stage 2 (navy cross solid lines), the profile exhibited similar patterns, yet the thickness and

severity of the unsaturated layers were almost invariant despite the relative density. Therefore, it must be concluded that the relative density has a low influence on the amount of evaporated water and its distribution, especially during Stage 2.

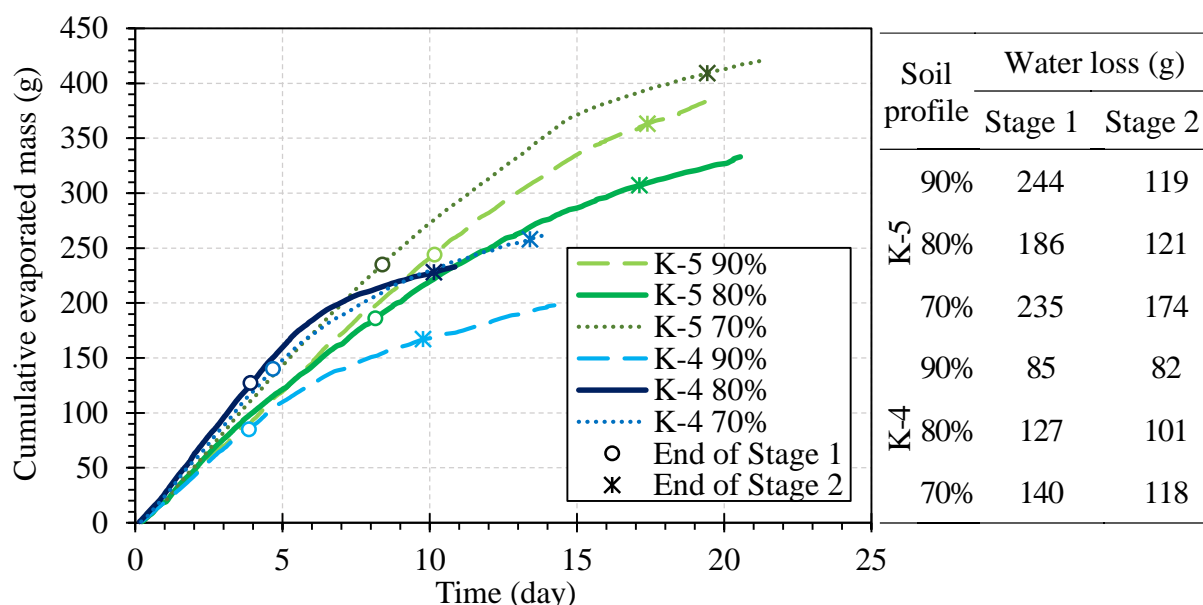


Figure 3.14: Cumulative evaporated water mass – Influence of relative density.

Similar observations concerning the unsaturated layer were confirmed for the K-5 and K-4 profiles. The determined L_c was shallower than the experimentally determined saturated-unsaturated boundary at the end of Stage 1. Likewise, the unsaturated layer formed during Stages 1 and 2 maintained similar unsaturated layer thickness. However, it experienced an average reduction of 20% and 30% in its degree of saturation for the K-5 and K-4 profiles, respectively.

3.6 Significance of the Falling Rate Stage (Stage 2)

Based on the experimental results, it was concluded that the relative density has a remarkably low influence on the evaporation process and Stage 2 for sandy soil profiles. However, varying the soil texture resulted in various soil drying behaviors. Therefore, the effective particle size (D_{10}) for each soil profile was used to further elaborate on the influence of the soil texture on the evaporation process. D_{10} was chosen to represent the soil texture as it is considered an excellent measure to estimate the hydraulic conductivity and drainage through the soil profiles (Das, 2010). Figure 3.16 indicates the relationship between D_{10} and the duration and evaporated water during Stages 1 and 2. The results demonstrate that coarser sandy soil profiles,

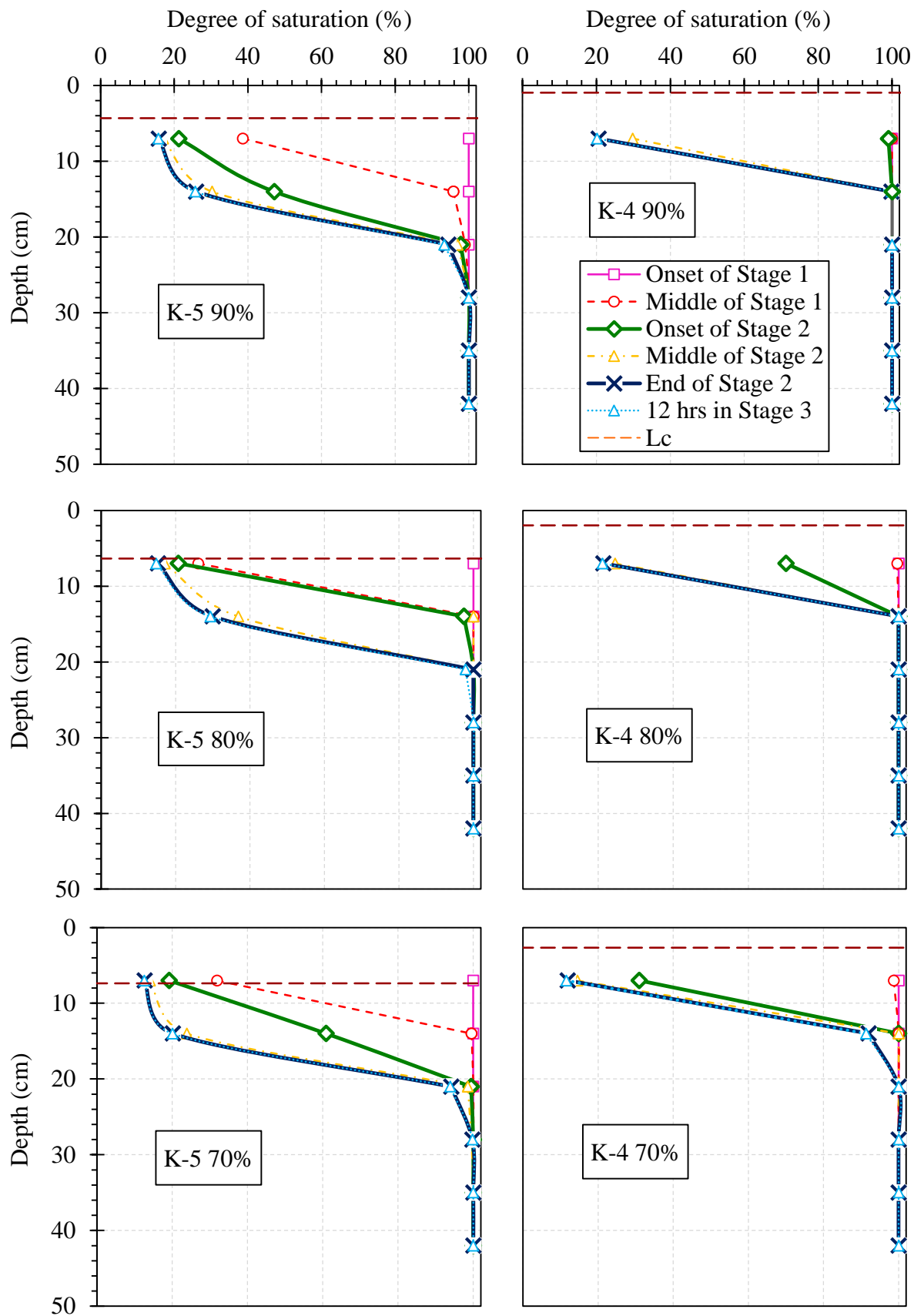


Figure 3.15: Water redistribution profiles during evaporation - Influence of relative density.

characterized by a larger effective particle size, are associated with shorter stages resulting in less evaporated water from the soil profiles. Both Stages 1 and 2 showed the same pattern of their relationship with D_{10} , confirming the soil texture's significant influence on the evaporation process. Generally, D_{10} can be considered a reliable index to define Stage 1 since water mainly transports by capillarity through water-filled pores to the evaporation surface. However, Stage 2 is a more complex process that involves vapor diffusion transport through the air-dry layer besides the capillary water transport. Additionally, D_{10} exclusively reflects the particle size, neglecting the particle shape, soil tortuosity, voids structure, and other related soil properties. Therefore, a more comprehensive and robust microscale index is required to adequately represent the soil properties, despite their influence on the evaporation behavior. Consequently, such an index can represent the evaporation stages and their transport mechanisms. Besides, it can be a supplementary parameter for enhancing the evaporation-predicting models to accurately predict the evaporation rates and water losses.

The pie charts in Figure 3.16 delineate the contribution of each stage to the evaporation process. The percentage presents the average ratio between the duration and water loss of each stage to the total of the evaporation process, while the total is assumed as the summation of

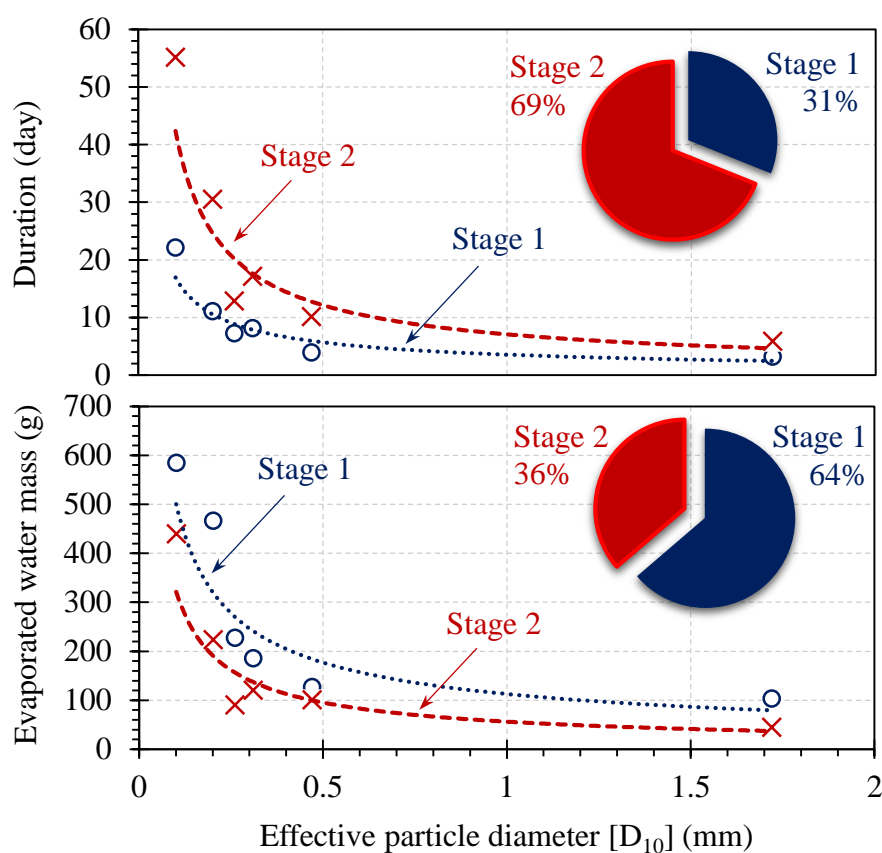


Figure 3.16: Significance of Stage 2.

Stages 1 and 2. From the charts, it must be concluded that under low atmospheric demand and despite the soil properties, Stage 2 persists longer than Stage 1. However, the amount of water loss during Stage 1 is more significant than that of Stage 2. This result is associated with the availability of water at the soil surface supported through the sufficient water supply from the drying front by capillary liquid flow during Stage 1. On the other hand, forming the air-dry layer at the onset of Stage 2 drives the transition to a less sufficient water transport mechanism causing the evaporation rates to reduce. Evaporation by vapor diffusion through the tortuous structure of the soil pores limits the amount of water transported to the surface and, therefore, less water lost to evaporation.

Due to the intense solar radiation and dry atmospheric conditions, hyper-arid, arid, and semi-arid regions are characterized by high potential evaporation rates. In rare short-time precipitation events, most water evaporates rapidly and sometimes faster than water infiltration into the soil. These conditions accelerate the time required to reach Stage 2, making Stage 1 even shorter or practically eliminating its existence. Therefore, a thick air-dry layer, between 5 and 50 cm, is predominantly present in the topsoil. Consequently, the actual evaporation rates become significantly hindered by the water supply from the subsurface, controlled by the rate of vapor diffusion through the air-dry layer. Therefore, it can be concluded that in drylands, Stage 2 is dominant and responsible for most of the water loss in the field. Therefore, more consideration and attention are required to understand the Stage 2 mechanism from sandy soil profiles, which are abundant in arid and semi-arid regions. Investigating the factors that influence Stage 2 behavior is essential to effectively mitigate droughts and water loss and find innovative solutions for desertification in drylands.

3.7 Pore Structure and Evaporation Stages

From a phenomenological point of view, most existing studies investigated the influence of atmospheric conditions and macroscale soil properties on evaporation behavior. Furthermore, most of the proposed actual evaporation models are based on atmospheric conditions (Monteith, 1965; Wilson et al., 1997). Few have considered the influence of the soil surface properties, such as the surface resistance and surface water availability (Fredlund et al., 2011; Kondo et al., 1990). Nonetheless, evaporation from soil profiles is an integrated process comprised of a group of micro-mechanisms that need to be simplified, investigated, and reflected in a macroscale evaluation of the evaporation rates. Therefore, focusing on a single macroscale index to reflect the water supply during evaporation might not be efficient. Instead, a comprehensive and robust microscale index is required to represent the soil profile's properties and reflect the micro-

mechanisms of the evaporation process. This section proposes a new index inferred from the soil pore structure and correlates well with the involved micro-mechanisms of the evaporation process. A detailed explanation of the pore structure determination and parameterization is presented.

3.7.1 Pore structure and pore size distribution

Generally, the pore space is the portion of the soil's volume not occupied by or isolated by solid material. It affects and is affected by almost everything that occurs within the soil body; water and air movement, fluids transport and their chemical reactions, the residence of roots, biota, and many others. By convention, pore space is a single, contiguous space within the soil body, composed of tortuous fluid pathways, variably constricted, and usually highly connected. However, in soil science and hydrology, the pore space is often considered in terms of individual pores to quantify its essential characteristics (Nimmo, 2004).

The literature defined a particularly useful conceptualization of the pore space as a collection of channels through which fluid can flow. The effective width of such channels varies along their length. The pore body is the relatively wide portion, also called the belly or waist; the pore opening is the relatively narrow portion that separates the pore body, also called the neck or throat. In a medium dominated by textural pore space, like sandy soils, pore bodies are the intergranular spaces that typically have smaller dimensions than the adjacent particles. An effective radius usually specifies pore sizes equal to the radius of curvature of the air-water interface occurring at the pore body or neck. Capillarity is related to the matric pressure at which sudden water emptying or filling of the pore, also known as the Haines Jumps.

The pores and the microstructure of the soil profiles are generally represented by the Pore Size Distribution (PSD). It describes the relative abundance of each pore size in a representative soil volume. The literature used two standard methods to determine the PSD: the image-based technique and the effective capillary size-based technique. The image-based technique can directly determine the PSD using tomographic imaging or three-dimensional analysis. However, these techniques can be tedious since enough pores must be analyzed for adequate statistical analysis. On the contrary, the effective capillary size-based technique infers the PSD indirectly from the fluid behavior in an unsaturated soil profile utilizing the mercury intrusion porosimetry or the Soil Water Characteristic Curves (SWCC). This method is the most commonly used due to its simplicity and reliability in determining the PSD. Based on the pore size definition and the capillary theory, it is assumed that the suction value at which a specific pore empties or fills corresponds to the diameter of the pore's opening (SWCC) or body

(mercury intrusion porosimetry). Nimmo (2013) reported that different techniques result in different PSD for the same soil. This is associated with the material used, whether it is mercury or water, and what technique is being applied, whether wetting or drying. Generally, in soil environmental applications and for water-based applications, the SWCC is the most common.

The indirect effective capillary size-based technique utilizing the SWCC is selected in the current study to infer the PSD curves in compliance with the pore structure parametrization to investigate the evaporation process. The method converts the desorption path of the SWCC $[\theta(\psi)]$ into an equivalent cumulative PSD curve $[\theta(d)]$, which can then be differentiated with respect to the pore diameter (d) to obtain the PSD curve $[f(d)]$, where θ is the volumetric water content, and ψ is the matric suction. The numerical determination method of the PSD curves used is summarized in the following steps:

1. Based on the Young-Laplace equation, the pore diameters are determined using the drying SWCCs, shown in Figure 3.2. The equation delineates the relationship between the matric suction value at which a pore diameter drains. By assuming a group of ideal cylindrical capillary pores, the equation is outlined as follows:

$$d = \frac{4T_s \cos \alpha}{u_a - u_w} \quad (3.2)$$

where $u_a - u_w$ is the matric suction (kPa), d is the pore diameter (μm), T_s is the water surface tension (0.075 N/m at 25°C), and α is the contact angle, typically assumed zero along the water drying path (Lu and Likos, 2004).

2. The water-filled pore volume per unit solid mass is calculated by dividing the gravimetric water content by the water density:

$$PV = \frac{w_d}{\rho_w} \quad (3.3)$$

where PV is pore volume per unit mass of solid (mL/g), w_d is the gravimetric water content at a specific suction value, and ρ_w is the water unit weight (0.997 g/cm^3 at 25°C).

3. The incremental pore volume (ΔPV) is obtained by subtracting each two consecutive pore volumes as follows:

$$\Delta PV = PV_{i+1} - PV_i \quad (3.4)$$

4. The total pore volume (PV_t) is obtained by summing up the total incremental pore volumes, and it is expressed as follows:

$$PV_t = \sum \Delta PV \quad (3.5)$$

The literature widely discussed the ability to represent the soil particle and void size analysis by the lognormal distribution function (Diamond and Dolch, 1972; Sako and Kitamura, 2006). Statistically, the lognormal distribution is characterized by the location parameter, the shape parameter, and the dispersion of the data around the mean. Each of those parameters can be expressed and calculated as follows (Sako and Kitamura, 2006):

1. The location parameter is defined by the mean of the lognormal distribution (λ):

$$\lambda = \ln \mu - \frac{1}{2} \xi^2 \quad (3.6)$$

2. The shape parameter is represented by the standard deviation of the lognormal distribution (ξ):

$$\xi^2 = \ln \left\{ 1 + \left(\frac{\sigma}{\mu} \right)^2 \right\} \quad (3.7)$$

3. The dispersion of the data around the mean is expressed with the lognormal distribution Coefficient of Variation (CV):

$$CV = \frac{\xi}{\lambda} \quad (3.8)$$

where λ and ξ are the lognormal distribution curve's mean and standard deviation, respectively, while μ and σ are the mean value and the standard deviation of the sample; here, the pore diameters, respectively.

Consequently, the PSD of the tested soil profiles was determined following the abovementioned steps, from 1 to 4. Figure 3.17 delineates the PSD curves of all the tested profiles, plotted in different groups based on the pore diameter range for a better analogy and a broader overview. The plots indicate the relative abundance of each pore diameter based on the pore volume per unit mass. The scatter plots delineate the PSD inferred from the measured SWCC, shown in Figure 3.2, while the smooth lines in Figure 3.17 represent their fitted lognormal distribution functions (logn). The results show that the PSD changes by varying the soil texture and the relative density. The curves differ in the mean and median diameter, the pore diameters' range, and the diameters' dispersion around the mean. The variations are more apparent by varying the soil texture, where finer sand, K-7, covers smaller pore diameters with higher frequency while coarser sand, K-2, covers a broader range of diameters. Despite the relatively lower variations between the soil profiles compacted at different relative densities, slight differences can be noticed in the diameter range in the K-5 profiles and the mode (the highest peak of the distribution) in the K-4 profiles.

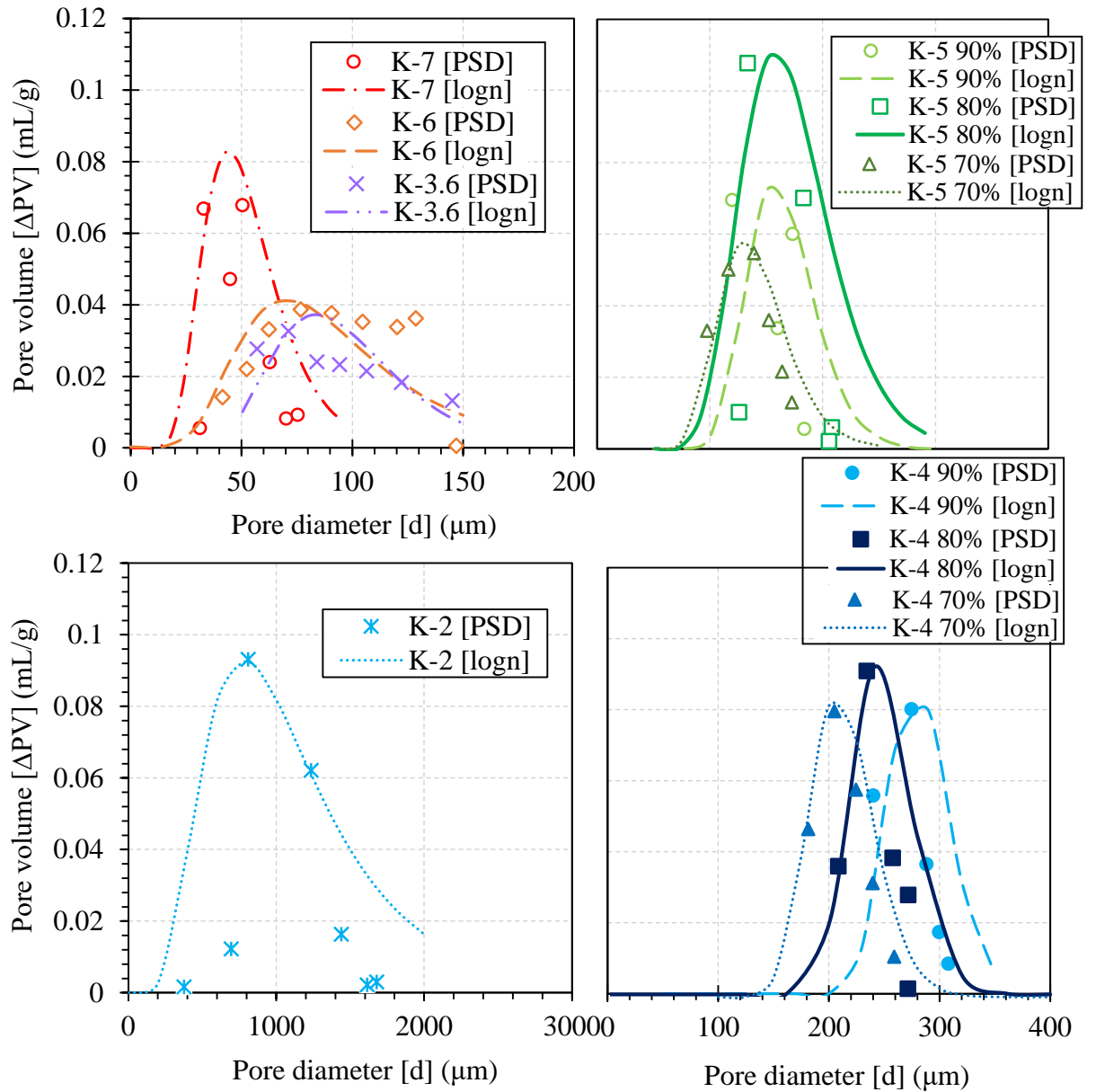


Figure 3.17: Pore size distribution curves and lognormal distribution fitting.

Consequently, it must be concluded that any slight change in the soil profile's properties influences the soil pore space. However, those variations could not be detected based on one macroscale parameter. Therefore, it is essential to parameterize an index based on the pore size distribution that reflects the variations of the pore structure associated with the changes in the macro-properties of the soil profile.

3.7.2 Pore Size Distribution Index (I_{PSD})

3.7.2.1 Concept

Two main points were considered for developing a parameterization framework for the soil pore structure. Firstly, an inclusive representation of the soil's macro and micro-properties.

Secondly, a comprehensive depiction of the macro and micro-mechanisms involved during evaporation. Consequently, the pore structure represented statistically by the pore size distribution curve was combined with the physical water transport mechanisms, liquid capillary, and vapor diffusion in a new Pore Size Distribution Index (I_{PSD}) and is formulated as follows:

$$I_{PSD} = \left(\frac{1}{d_1} - \frac{1}{d_2} \right) \times CV \quad (3.9)$$

- I_{PSD} is the Pore Size Distribution Index ($1/\mu\text{m}$).
- $\left(\frac{1}{d_1} - \frac{1}{d_2} \right)$ is the width of the pore size distribution ($1/\mu\text{m}$), reflecting the capillary liquid flow.
- CV is the Coefficient of Variation of the PSD lognormal fitting, reflecting vapor diffusion.

The proposed index comprises two parameters, each having a statistical and physical meaning. During Stage 1, water flows by capillary liquid flow through the film region extended from the drying front to the surface. Lehmann et al. (2008) concluded that the extent of Stage 1 depends on the maximum capillary pressure difference forms between the largest (d_2) and smallest (d_1) capillaries rather than the mean pore size. d_1 and d_2 can be inferred from the PSD, corresponding to the residual and air-entry suction values. Consequently, the maximum capillary drive, expressed as $(1/d_1 - 1/d_2)$, was adopted as the first parameter of the proposed index resembling the film region and its capillary flow. $(1/d_1 - 1/d_2)$ physically represents the width of the PSD and statistically reflects the range of the pore diameters present in a soil profile. On the other hand, during Stages 2 and 3, water flows by vapor diffusion through the formed air-dry layer extended from the vaporization plane to the surface. Consequently, the vapor diffusion zone is represented using the lognormal coefficient of variation (CV), which physically describes the relative frequency of the diffusion pathways within the air-dry layer and statistically represents the dispersion of the data around the mean pore diameter. Multiplying these two parameters resulted in a comprehensive and robust index representing the variations in soil properties and water transport mechanisms. The newly proposed index is fundamental for many problems related to evaporation and water movement in unsaturated soils.

3.7.2.2 *Determination method*

The I_{PSD} can be systematically and efficiently determined, requiring simple information related to the properties of the soil profile. The flowchart shown in Figure 3.18 illustrates the I_{PSD} determination process. The process starts with the drying SWCC, then inferring the PSD as explained in section 3.7.1, and finalizing by fitting the PSD with the lognormal distribution. The first parameter $(1/d_1 - 1/d_2)$ is then determined from the PSD, while the CV is found from its lognormal distribution.

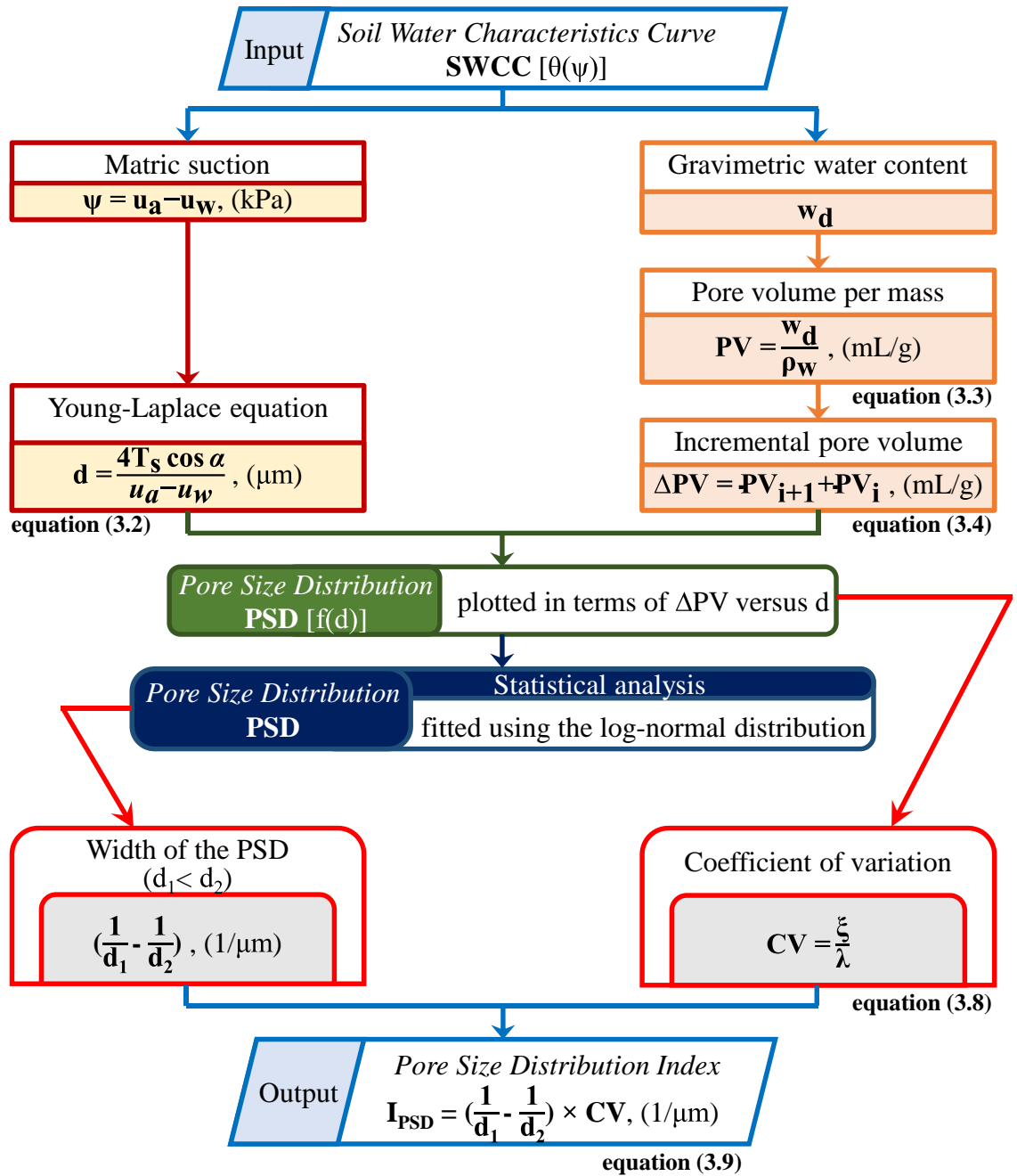


Figure 3.18: Pore Size Distribution Index (I_{PSD}) determination process. [Flowchart]

It must be noted that the SWCC direct determination tools have been progressing rapidly in recent years (Alowaisy et al., 2020). Moreover, in the case of limited laboratory equipment, the SWCC can be indirectly estimated using empirical or statistical approaches that require simple soil properties such as porosity and particle size distribution (Sako and Kitamura, 2006). Therefore, such a simple determination method makes the comprehensive micro-scale index an accessible index for engineers and researchers to utilize in different applications.

3.7.3 Pore Size Distribution Index and Evaporation Stages

Table 3.2 summarizes the PSD and the lognormal distribution parameters for the tested soil profiles, while their I_{PSD} values were determined using equation 3.9. Generally, finer soil profiles tend to have larger I_{PSD} values representing their broader pore size distribution. It must be noted that the PV_t , area under the PSD curve was almost similar in all profiles, with an average of 0.21 ± 0.05 mL/g. However, it might be essential when comparing cohesive and cohesionless soil behavior. The I_{PSD} values were plotted against the duration and amount of evaporated water during Stages 1 and 2, as shown in Figure 3.19 (a) and (b), respectively. It can be observed that the I_{PSD} strongly correlates with both measures of evaporation for both stages, with regression r values greater than 0.75. The positive correlation confirms that sandy

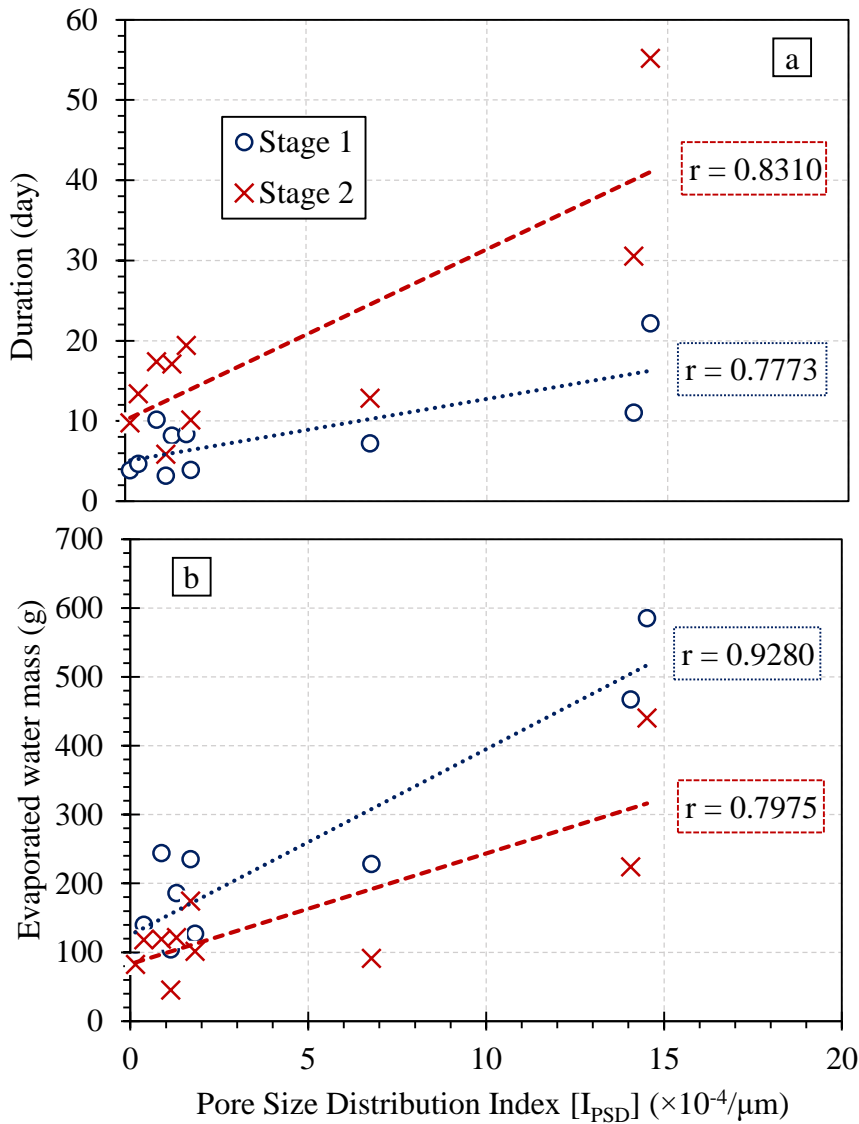


Figure 3.19: Pore Size Distribution Index (I_{PSD}) and evaporation stages.

Table 3.2: Soil profiles' pore structure parameters and Pore Size Distribution Index (I_{PSD})

		K-7	K-6	K-5				K-4		K-3.6	K-2
Relative Density	Dr (%)	80	80	90	80	70	90	80	70	80	80
Pore size distribution											
Largest pore diameter	d ₂ (μm)	75	147	184	207	173	308	271	259	145	1678
Smallest pore diameter	d ₁ (μm)	31	42	120	124	97	240	208	182	57	376
Width of the pore size distribution	$\frac{1}{d_1} - \frac{1}{d_2}$ (1/μm)	0.019	0.017	0.003	0.003	0.004	0.001	0.001	0.002	0.011	0.002
Total pore volume	PV _t (mL/g)	0.23	0.25	0.17	0.20	0.21	0.20	0.20	0.23	0.10	0.32
Lognormal distribution											
Mean	λ (cm/s)	3.91	4.45	5.06	5.11	4.93	5.64	5.17	5.40	4.53	6.94
Standard deviation	ξ	0.30	0.36	0.15	0.21	0.19	0.08	0.83	0.12	0.28	0.38
Coefficient of variation	CV (cm)	0.08	0.08	0.03	0.04	0.04	0.01	0.16	0.02	0.06	0.05
I _{PSD}	(×10 ⁻⁴ /μm)	14.5	14.1	0.9	1.3	1.7	0.1	1.8	0.4	6.8	1.1

soils with larger I_{PSD} exhibit longer durations of the stages and, consequently, more significant amounts of evaporated water.

Finally, it can be concluded that the proposed I_{PSD} comprehensively reflects the pore structure variations associated with the macro-properties of the soil profile, including texture and relative density, and with several micro-scale characteristics, such as the particles and pores shape, uniformity, angularity, tortuosity, and the related conductivity characteristics (hydraulic conductivity and diffusivity). The strong correlation with Stages 1 and 2 indicates that the proposed index captures well the factors affecting the micro-dynamics of fluids corresponding to the capillary and diffusion transport. Such a comprehensive and robust index is fundamental to understanding the integrated micro-mechanisms involved in evaporation. Additionally, it is expected to serve as a principal parameter for accurately estimating the evaporation rates and related water losses. Moreover, it is expected to contribute to water movement research through unsaturated soil profiles.

3.8 Summary and Conclusions

This chapter investigated the influence of the soil pore structure on the evaporation rate and water redistribution during drying. The pore structure was parameterized experimentally by varying the soil profile's texture and relative density. The main conclusions of the chapter can be summarized as follows:

1. The soil texture has a more significant influence on the evaporation process behavior and the water redistribution than the relative density. Finer gradations exhibit relatively longer durations and higher water loss from deeper layers during Stages 1 and 2.
2. Marking the onset of Stage 2 from the actual evaporation curve might not be a reliable practice. The inflection points on the evaporation curve indicate a change in the evaporation rate but do not necessarily represent the change in the transport mechanism between stages.
3. The unsaturated layer thickness is maintained during Stage 2, where water mainly gets lost from the smaller embedded pores rather than the large pores at the drying front. This behavior results in a gradual reduction in the vaporization plane depth, causing an increase in the air-dry layer thickness and the diffusion pathways to the surface.
4. Following Fick's first law of diffusion, it was found that the actual evaporation receding rate correlates well with the vaporization plane receding rate during Stage 2. Consequently, this confirms the dominance of the vapor diffusion during Stage 2 and assures the necessity of investigating the unsaturated layer dynamics during the evaporation process.
5. Under low atmospheric demand, it was confirmed experimentally that Stage 2 comprises more than half of the evaporation process. Therefore, under severe dryland conditions, Stage 2 was concluded to be dominant and responsible for most of the water loss in the field.
6. Finally, a comprehensive and robust index that reflects the pore structure variations and considers the factors affecting the capillary and diffusion flow was proposed. The Pore Size Distribution Index (I_{PSD}) correlated well with the duration and evaporated water during Stages 1 and 2. Generally, sandy soils with larger I_{PSD} exhibit longer stages and more water loss. The proposed index can be systematically determined using only the SWCC. It is expected to serve as a fundamental step toward evaluating the actual evaporation and understanding the unsaturated layer dynamics formed during drying.

References

- Alowaisy, A.M., Yasufuku, N., Ishikura, R., Hatakeyama, M., Kyono, S., 2019. Rapid concurrent measurement of the soil water characteristics curve and the hydraulic conductivity function utilizing the continuous pressurization method. 7th Asia-Pacific Conference on Unsaturated Soils, AP-UNSAT 2019 366–375. <https://doi.org/10.3208/jgssp.v07.059>
- Alowaisy, A., Yasufuku, N., 2018. Characteristics of the second stage of evaporation and water redistribution through double layered sandy soil profiles. *Lowland Technology International* 20, 273–284.
- Alowaisy, A., Yasufuku, N., Ishikura, R., Hatakeyama, M., Kyono, S., 2022. Rapid determination of the unsaturated hydraulic conductivity for sandy soils utilizing the continuous pressurization method, in: *Proc. of the 20th International Conference on Soil Mechanics and Geotechnical Engineering (ICSMGE20)*. pp. 1413–1418.
- Alowaisy, A., Yasufuku, N., Ishikura, R., Hatakeyama, M., Kyono, S., 2020. Continuous pressurization method for a rapid determination of the soil water characteristics curve for remolded and undisturbed cohesionless soils. *Soils and Foundations* 60, 634–647. <https://doi.org/10.1016/j.sandf.2020.03.014>
- Carman, P.C., 1956. Flow of gases through porous media. *Journal of Hydrogeology & Hydrologic Engineering*.
- Das, B.M., 2010. *Principles of Geotechnical Engineering*, 7th ed. Cengage Learning.
- Diamond, S., Dolch, W.L., 1972. Generalized Log-Normal Distribution of Pore Sizes in Hydrated Cement Paste. *Journal of Colloid and Inter/ace ScienC* 38, 234–244.
- Fredlund, M.D., Zhang, J.M., Tran, D., Fredlund, D.G., 2011. Coupling Heat and Moisture Flow for the Computation of Actual Evaporation. *Proceedings of the Canadian Geotechnical Conference and Fifth Pan-American Conference, Toronto, Ont* 2–6.
- Hillel, D., 2004. *Introduction to environmental soil physics*, Elsevier Science.
- Hrapovic, L., Sleep, B.E., Major, D.J., Hood, E.D., 2005. Laboratory study of treatment of trichloroethene by chemical oxidation followed by bioremediation. *Environ Sci Technol* 39, 2888–2897. <https://doi.org/10.1021/es049017y>
- Kondo, J., Saigusa, N., Sato, T., Kondo, J., Saigusa, N., Sato, T., 1990. A Parameterization of Evaporation from Bare Soil Surfaces. *Journal of Applied Meteorology* 29, 385–389. [https://doi.org/10.1175/1520-0450\(1990\)029<0385:APOEFB>2.0.CO;2](https://doi.org/10.1175/1520-0450(1990)029<0385:APOEFB>2.0.CO;2)
- Kozeny, J., 1927. Ueber kapillare leitung der wasser in boden, in: *Proc. Class I*, 136. pp. 271–306.
- Lehmann, P., Assouline, S., Or, D., 2008. Characteristic lengths affecting evaporative drying of porous media. *Phys Rev E Stat Nonlin Soft Matter Phys* 77, 1–16. <https://doi.org/10.1103/PhysRevE.77.056309>
- Lu, N., Likos, W.J., 2004. *Unsaturated Soil Mechanics*. John Wiley & Sons, Inc.
- Monteith, J.L., 1965. Evaporation and environment. *Symp Soc Exp Biol* 19, 205–234.
- Nimmo, J.R., 2013. Porosity and Pore Size Distribution, *Reference Module in Earth Systems and Environmental Sciences*. Published by Elsevier Inc. <https://doi.org/10.1016/b978-0-12-409548-9.05265-9>
- Nimmo, J.R., 2004. Porosity and Pore-Size Distribution. *Encyclopedia of Soils in the Environment* 4, 295–303. <https://doi.org/10.1016/B0-12-348530-4/00404-5>
- Osman, K.T., 2018. Management of soil problems, *Management of Soil Problems*. Springer. <https://doi.org/10.1007/978-3-319-75527-4>
- Sako, K., Kitamura, R., 2006. A Practical Numerical Model for Seepage Behavior of Unsaturated Soil. *Soils and Foundations* 46, 595–604.

- Schlünder, E.U., 1988. On the mechanism of the constant drying rate period and its relevance to diffusion controlled catalytic gas phase reactions. *Chem Eng Sci* 43, 2685–2688. [https://doi.org/10.1016/0009-2509\(88\)80012-5](https://doi.org/10.1016/0009-2509(88)80012-5)
- Shahraeeni, E., Lehmann, P., Or, D., 2012. Coupling of evaporative fluxes from drying porous surfaces with air boundary layer: Characteristics of evaporation from discrete pores. *Water Resour Res* 48, 1–15. <https://doi.org/10.1029/2012WR011857>
- Smalley, I.J., Vita-Finzi, C., 1968. The Formation of Fine Particles in Sandy Deserts and the Nature Of “Desert” Loess. *SEPM Journal of Sedimentary Research* 38, 766–774. <https://doi.org/10.1306/74d71a69-2b21-11d7-8648000102c1865d>
- Teng, J., Yasufuku, N., Liu, Q., Liu, S., 2014. Experimental evaluation and parameterization of evaporation from soil surface. *Natural Hazards* 73, 1405–1418. <https://doi.org/10.1007/s11069-014-1138-z>
- Thornthwaite, C.W., 1948. An Approach toward a Rational Classification of Climate. *Geogr Rev* 38, 55–94. <https://doi.org/10.2307/210739>
- van Genuchten, M.Th., 1980. A Closed-form Equation for Predicting the Hydraulic Conductivity of Unsaturated Soils. *Soil Science Society of America Journal* 44, 892–898. <https://doi.org/10.2136/sssaj1980.03615995004400050002x>
- Wilson, G.W., Fredlund, D.G., Barbour, S.L., 1997. The effect of soil suction on evaporative fluxes from soil surfaces. *Canadian Geotechnical Journal* 34, 145–155. <https://doi.org/10.1139/t96-078>
- Yates, D., Strzepek, K.M., 1994. Potential evapotranspiration methods and their impact on the assessment of river basin runoff under climate change.
- Zhou, A.N., 2013. A contact angle-dependent hysteresis model for soil-water retention behaviour. *Comput Geotech* 49, 36–42. <https://doi.org/10.1016/j.compgeo.2012.10.004>

4

C H A P T E R

Visualization of the Unsaturated Soil Layer Using a Novel Image Analysis-Based Technique

4.1 Introduction

The unsaturated layer formation and development during soil drying play an essential role in the dynamics of the evaporation process. Water loss from soil profiles causes continuous changes in the unsaturated layer configuration. These changes are associated with a change in the water transport mechanism that influences the evaporation rate (Figure 2.5). Chapter 3 discussed the importance of investigating the unsaturated layer dynamics to accurately predict the evaporation rate. Consequently, tracing the unsaturated layer and its boundaries, the drying front and vaporization plane, during drying is highly required.

During Stage 1, the unsaturated layer or the film region is identified with the receding drying front, forming the interface between the fully saturated soil layer and the film region. Mainly water through the film region moves by liquid flow from the drying front to the surface through liquid-filled pores. However, when the liquid continuity with the surface is lost, an air-dry layer is formed, and a vaporization plane appears at a depth below the soil surface.

Consequently, during Stage 2, the unsaturated layer is divided into a film region and an air-dry layer, and the water transport mechanism changes accordingly. The water transports through the film region from the drying front to the vaporization plane by capillary liquid flow and then continues through the air-dry layer, evaporating from the vaporization plane to the surface as vapor diffusion (Shokri et al., 2009). Previous studies have investigated the drying front dynamics during Stage 1. However, little is known about the vaporization plane and its relation with the drying front due to the complexity of the diffusion-dependent Stages 2 and 3 and the lack of advanced techniques.

Several methods were reported in the literature to trace the unsaturated layer during drying, including image analysis, neutron radiography, nuclear magnetic resonance, prediction methods, and other numerical and simulation methods (Assouline et al., 2013; Lehmann et al., 2008; Merz, 2017; Shokri et al., 2008; Shokri and Or, 2011). However, these methods have many limitations, such as the difficulty of taking high-quality images, extracting information related to the dry and saturated layer while neglecting the unsaturated layer, using costly tools not commonly available in geotechnical laboratories, and other sophisticated techniques that require expertise.

Therefore, in the following chapter, a simple and effective technique to visualize the unsaturated layer during the evaporation stages is developed. The technique considers capturing high-quality images, followed by a series of image analysis operations that enable the detection of the air-dry layer, film region, and their boundaries during Stages 2 and 3. The extent of the liquid and vapor pathways is investigated. Accordingly, new insights are discussed regarding the spatial and temporal development of the drying front, vaporization plane, and film region. Furthermore, the influence of the pore structure on the unsaturated layer dynamics is elucidated, while the importance and the potential of considering the newly proposed Pore Size Distribution Index (I_{PSD}) to elaborate on the evaporation process are highlighted.

4.2 Materials

As was thoroughly discussed in Chapter 3 (section 3.2), silica sand is adopted for testing. Through this chapter, three different soil profiles were tested, utilizing three different textures of silica sand compacted at 80% relative density. The commercial names of the samples are K-6, K-4, and K-3.5, a mixture of K-3 and K-5 soils with a 1:1 ratio by mass. Their particle size distribution curves are delineated in Figure 4.1. A summary of the physical and hydrological properties of the tested profiles is shown in Table 4.1. Based on the soils' physical properties

and the JGS soil classification of geomaterials (JGS 0051-2009), all soils are classified as Sand [S]. The Soil Water Characteristic Curves (SWCCs) and the Hydraulic Conductivity Functions (HCFs) are delineated in Figures 4.2 and 4.3, respectively. More details of the soils' physical and hydrological properties determination methods and standards are presented in Chapter 3 (section 3.2).

Table 4.1: Soil profiles' physical and hydrological properties

		K-6	K-4	K-3.5
Relative Density	Dr (%)	80	80	80
Physical properties				
Specific gravity	G _s	2.64	2.65	2.64
Effective size	D ₁₀ (mm)	0.20	0.47	0.43
Fine fraction	(%)	0.20	0.11	0.13
Soil Classification		S	S	S
Dry density	ρ _d (g/cm ³)	1.50	1.51	1.60
Void ratio	e	0.75	0.75	0.65
Porosity	φ	0.43	0.43	0.39
Pore size distribution index	I _{PSD} (×10 ⁻⁴ /μm)	14.1	1.8	11.6
Hydrological properties				
Saturated hydraulic conductivity	k _s (cm/s)	0.05*	0.20	0.14*
Saturated volumetric water content	θ _s	0.47	0.46	0.42
Residual volumetric water content	θ _r	0.06	0.06	0.03
Van Genuchten model fitting parameters	α (cm ⁻¹)	0.03	0.08	0.07
	n	5.01	14.12	5.44
Characteristic Length	L _C (cm)	14.49	1.97	6.73

*k_s were estimated using Kozeny-Carman equation (Carman, 1956; Kozeny, 1927)

The newly proposed Pore Size Distribution Index (I_{PSD}) further elaborates on the pore structure's influence on the evaporation process and the dynamics of the unsaturated layer. The I_{PSD} was determined following the steps in Figure 3.18 and equation 3.9. The pore size distribution curves are delineated in Figure 4.4, while the I_{PSD} values are shown in Table 4.1.

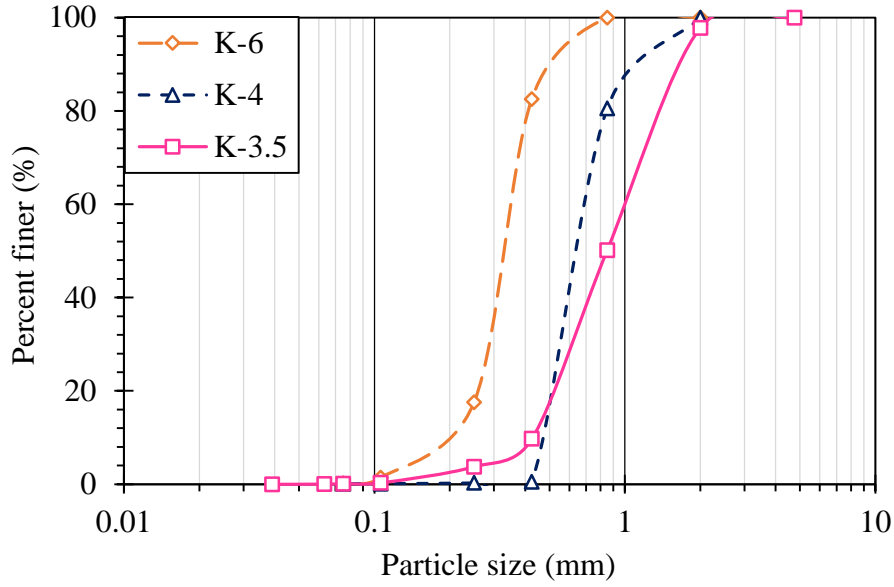


Figure 4.1: Particle size distribution curves.

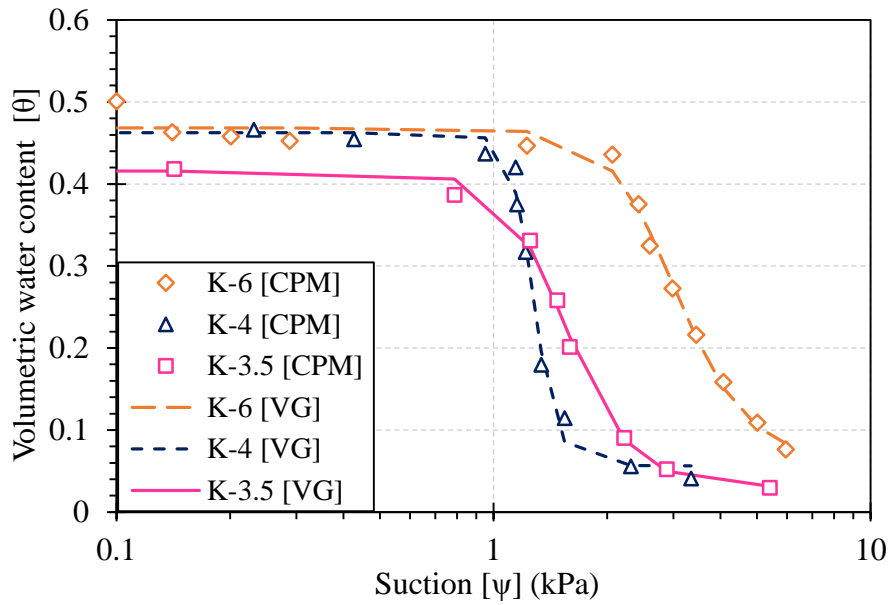


Figure 4.2: Drying soil water characteristic curves.

4.3 Methodology and Experimental Setup Development

The drying soil column tests were adopted to study the evaporation process from soil profiles. The same methodology of Chapter 3 was utilized here. However, tracing the unsaturated soil layer required some modifications to the experimental setup. The developed setup comprises

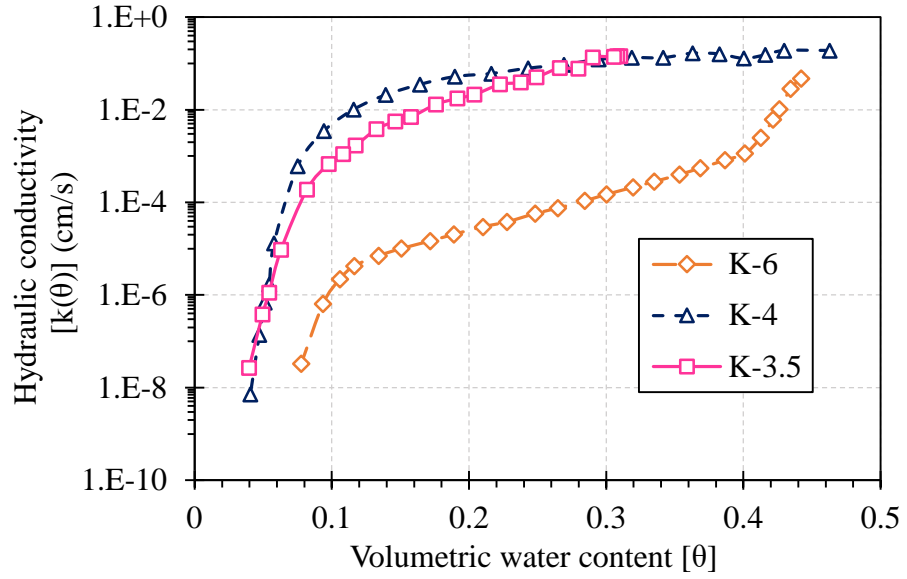


Figure 4.3: Hydraulic conductivity functions.

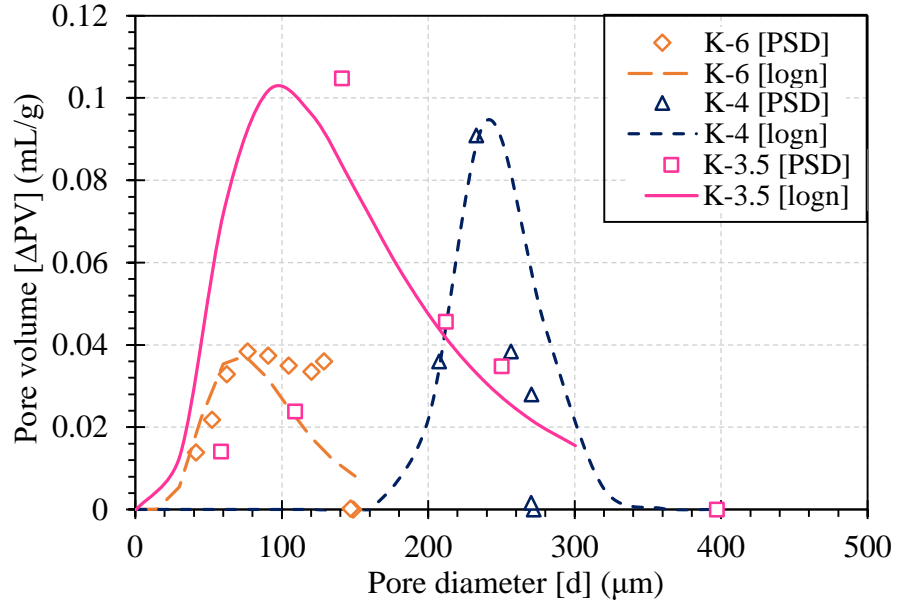


Figure 4.4: Pore size distribution curves and lognormal distribution fitting.

four main units: the climate control unit, the evaporation testing unit, the control and acquisition unit, and the image acquisition unit, as shown in Figure 4.5. Generally, the modifications are limited to the evaporation testing unit while a novel image acquisition unit is added. The following section presents an exhaustive explanation of the improved parts. Moreover, the testing procedure and boundary conditions during testing are discussed.

Unit	No.	Component	Functions and remarks
Climate control	1	Environmental chamber	Transparent acrylic cylindrical chamber (50 cm diameter, 30 cm height), maintains the atmospheric conditions.
	2	Control panel	Includes the switch key and other controlling keys and digital display of the thermo-hygrometer sensor.
	3	Air blender	Continuously mixes the air inside the environmental chamber and supports its movement through the air pipes.
	4	Freezer	Cools down and heats the air inside the environmental chamber and automatically operate in an alternative mode to maintain the designated temperature.
	5	Heater	
	6	Dehumidifier	Decreases and increases the humidity of the air inside the environmental chamber, automatically operating in an alternative mode to maintain the designated humidity.
	7	Ultrasonic humidifier	
	8	Fan	Monitors the instantaneous wind speed and circulates the air between the chambers.
	9	Thermo-hygrometer	Records and monitors the temperature and humidity in the environmental and evaporation chamber.
	10	Switch	Controls the wind speed at the outlet of the environmental chamber.
	11	Evaporation chamber	Transparent acrylic rectangular chamber (40×20×15 cm), allows evaporation under controlled demand.
	12	Wind speed sensor	Records the wind speed in the evaporation chamber (± 0.1 m/s resolution)
Evaporation testing	13	Soil column	Transparent acrylic rectangular column (49 cm ² surface area, 50 cm height) includes the tested soil profile.
	14	Column's base	Acrylic base consists of a valve and porous stone to uniformly distribute the water during saturation.
	15	Valve	Function as a water inlet for the up-flow saturation.
	16	Fully-saturated and	Transparent acrylic rectangular columns (25 cm ² surface area, 50 cm height) used to calibrate the blue color intensity allowing the detection of the fully saturated and air-dry zones in the primary tested column
	17	Dry reference columns	
Control and acquisition	18	TDRs	Time Domain Reflectometry probes, indirectly measure the water content of the soil profile.
	19	Sensors' data logger	Continuously records data from the climate control unit, while the data is saved directly through a computer application.
	20	Computer	
	21	TDRs data logger	Continuously records data from the TDRs while the data is retrieved through a computer application.
Image acquisition	22	Digital camera	High-resolution digital camera mounted on a tripod and placed in front of the evaporation testing unit. Images were captured continuously during testing.
	23	Tripod	
	24	Two soft boxes	Unify the light intensity and spread it without causing harsh reflections on the columns' tracing surfaces.

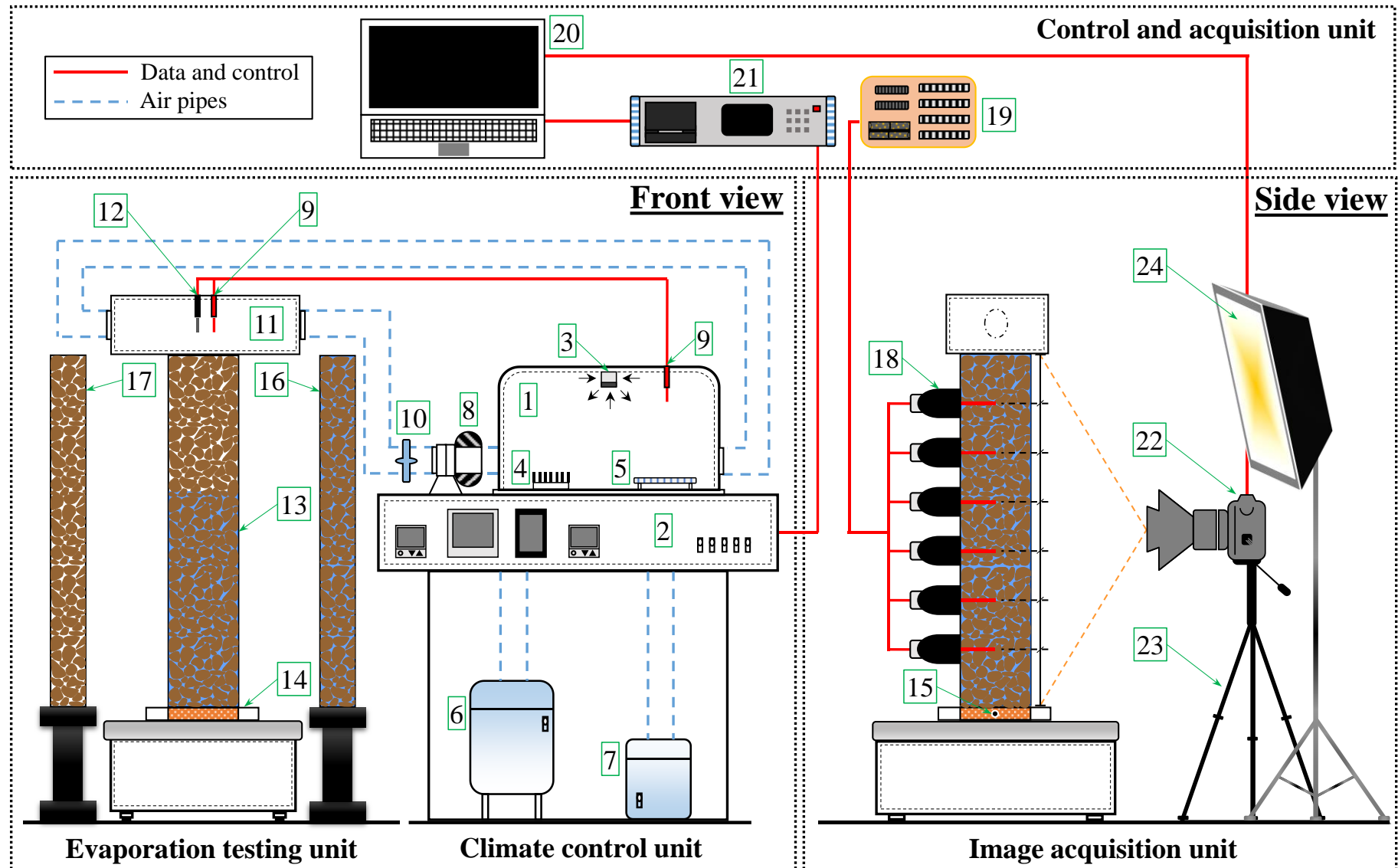


Figure 4.5: Developed experimental setup and image acquisition.

4.3.1 Evaporation testing unit and preparation

The newly proposed technique to trace the unsaturated layer is based on image analysis. Therefore, the main goal of modifying the evaporation testing unit is to ensure capturing high-quality images while conducting soil drying tests. The column used for testing is a transparent acrylic rectangular column, 50 cm in height, 7×7 cm cross-sectional area, and a wall thickness of 2 cm. The column is confirmed to have a flat and well-polished tracing surface with minimal scratches to capture the soil profile exclusively and avoid biased results. Similar to the previously used testing column, a valve is installed at the column's base and connected directly to a porous stone disk to distribute the water into the soil profile uniformly. The column is sealed well from the bottom and all sides to avoid leakage during preparation and testing.

For saturation, a blue dye tracer (brilliant blue) is used to enhance the visual contrast between saturated, unsaturated, and dry layers based on blue color intensity. Generally, a fully saturated profile is dark blue; however, the color starts fading when water evaporates until the soil returns to its original color with hints of blue dots when it dries. The powder dye was dissolved in distilled water at a concentration of 0.2 g/L, which was then prepared in a deaerator tank for saturation. After water evaporation, the dye returns to powder form and does not leave stains on the silica sand particles. This type of blue dye is commonly used in evaporation, infiltration, and fluid transport model testing (Shokri and Or, 2011; Shokri and Salvucci, 2011). Figure 4.6 shows the blue powder dye and its specifications. The soil column compaction and saturation techniques were done following the same steps explained in Chapter 3 (subsection 3.3.2), except for using the blue-dyed deaerated water.

Consequently, two soil reference columns are placed next to the primary tested one to calibrate the blue color intensity during testing: One fully saturated reference column imitating the fully saturated soil layer with a dark blue color, and another fully dry reference column imitating the air-dry soil layer, with the soil original color and hints of blue dots. These columns allow the detection of the fully saturated and air-dry layers in the primary tested column at any time during evaporation. The columns' locations and colors are delineated in Figure 4.5 (Front view) and Figure 4.7. Both reference columns are compacted in transparent acrylic rectangular columns, 50 cm in height, 5×5 cm cross-sectional area, and a wall thickness of 1.5 cm. The reference columns were prepared using the same soil as the primary tested column, with similar soil gradation and dry density, delineated in Table 4.1 for each profile. The fully saturated soil reference column was compacted and saturated as the primary column, where a valve was attached to its bottom to facilitate the up-flow and vacuum saturation (subsection 3.3.2). On the

other hand, the dry reference column was compacted using oven-dry soil previously saturated with blue water, following the same steps as the other columns but skipping saturation. Finally, the reference columns were sealed well from all sides to maintain saturation and color intensity during prolonged testing. The columns' tops were closed using acrylic lids and rubber rings to cease evaporation and keep the blue color intensity constant along the test.

The climate control apparatus sensors were connected to a logger and computer for the control and acquisition unit to continuously record atmospheric conditions during testing. The primary column was instrumented with Time Domain Reflectometry probes (TDRs) through drilled ports. They were connected to a data logger that records the data and indirectly measures the water content through the entire profile during the testing period.

Commercial name	Acid Blue 9
Molecular formula	$C_{37}H_{34}N_2Na_2O_9S_3$
Molecular weight	792.84 g/mol
Physical state (20°C)	Solid-Powder
Appearance	Red to dark red to dark purple powder to crystal
Solubility	Completely soluble in water, alcohol and ether



Figure 4.6: Brilliant blue dye tracer and its specifications.

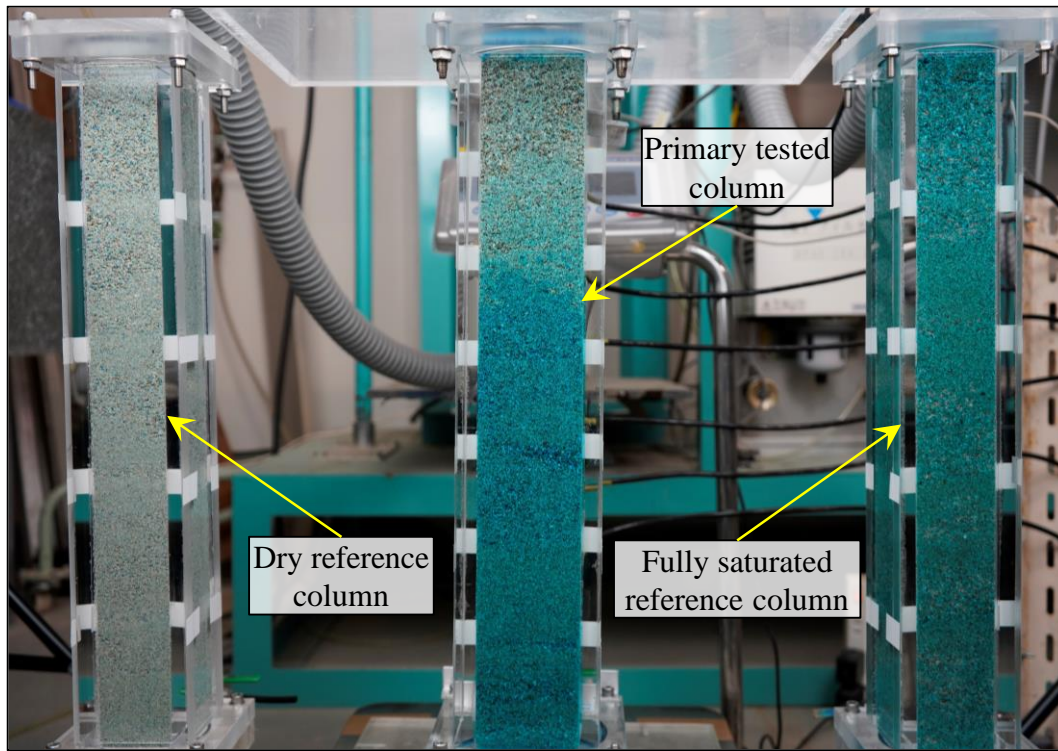


Figure 4.7: Evaporation testing unit. [Picture]

4.3.2 Image acquisition unit

The image acquisition unit, shown in Figure 4.5 (Side view), is a newly developed unit added to the experimental setup to capture high-quality images during the drying column testing. High-quality or high-resolution images are generally characterized by a high concentration of pixels, where more details appear in the image, making it look clear. Moreover, an image's light, color, and composition are essential in reducing noise, blur, and haze, thus increasing quality. Based on that, a high-resolution digital camera and a lighting setup were prepared to satisfy the required elements of a high-quality image.

A high-resolution digital camera was mounted on a tripod and placed in front of the evaporation testing unit. The camera has a resolution of 42 Mega Pixels (MP), where the captured images are created by 7952×5304 pixels. The high-resolution images capture the wide testing unit that includes the primary column and two reference columns while having the ability to crop the primary column exclusively for further analysis. This ensures an overall high-quality image with almost no details lost. The camera was fixed on a tripod during testing facing the primary column. The tripod was adjusted at a height where the camera and the primary column were aligned in the middle and were placed to align precisely with its center. Consequently, the reference columns were placed within the camera's frame at an equal

distance from both sides of the primary column. The camera was then connected to a computer to allow remote image acquisition through a designated application.

A two-point lighting setup was placed at a 45° angle next to the camera, facing the evaporation testing unit. The two light sources were set at the same light intensity through white-shaded softboxes. One of the softboxes is considered the key light that illuminates the columns, while the other is a fill light that helps remove the harsh shadows created by the key light. Besides, utilizing the softboxes assist in unifying the light intensity and spreading it without causing harsh reflections on the columns' tracing surfaces. Figure 4.8 shows a front view of the experimental testing unit and the image acquisition unit, illustrating the two-point lighting setup utilized during testing.

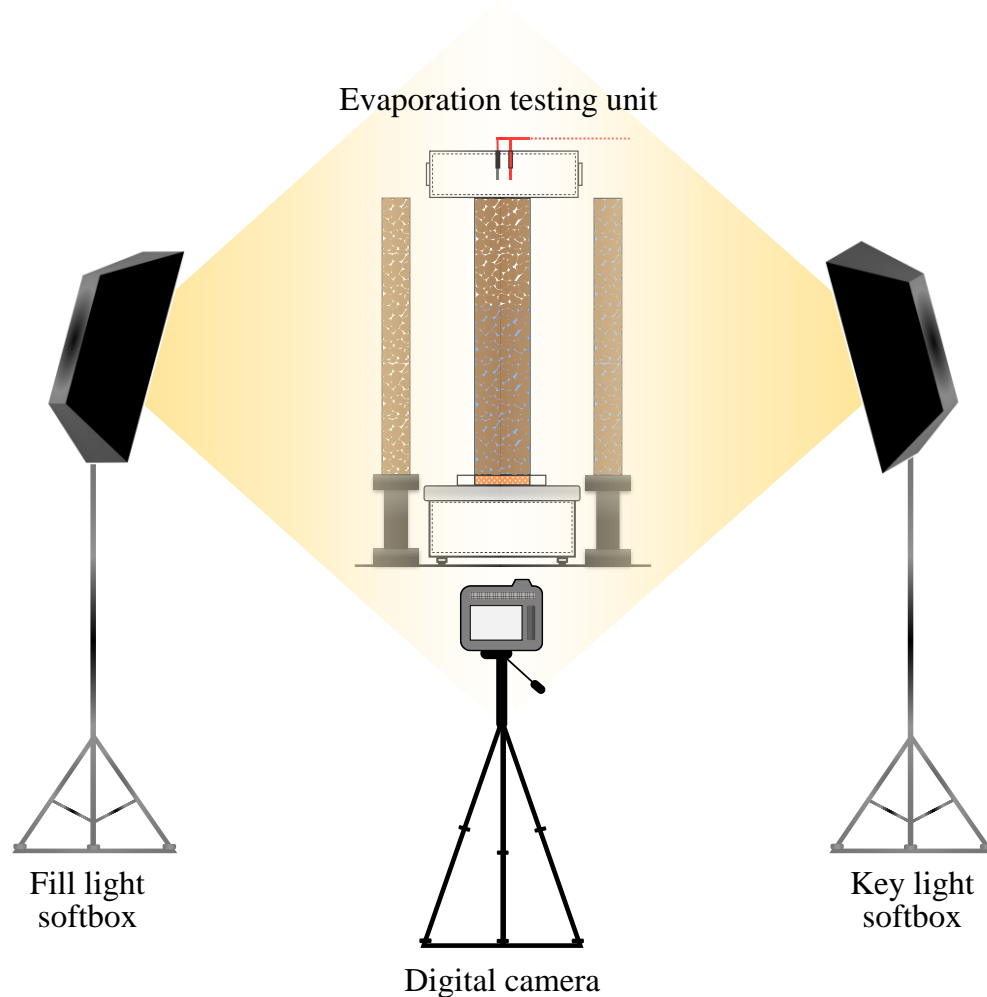


Figure 4.8: Two-point lighting setup.

4.3.3 Testing procedure and boundary conditions

The three homogeneous sandy soil drying column tests were conducted individually. The fully-saturated initial conditions were unified for all tests. One-dimensional evaporation flow was facilitated at the soil's top surface through the evaporation chamber. The atmospheric evaporative demand at the surface was unified in order to exclusively investigate the role of the pore structure and water supply in the process. Therefore, the temperature, relative humidity, and wind speed were maintained and continuously recorded during testing through the climate control unit and the control and acquisition unit.

As explained in Chapter 3 (subsection 3.3.3), low atmospheric demand was adopted for testing. Consequently, an average temperature of $27.2 \pm 1.1^\circ\text{C}$, relative humidity of $44.8 \pm 0.8\%$, and wind speed of 2.3 ± 0.2 m/s were confirmed 5 cm above the soil surface for all the tested profiles during the entire testing duration. Figure 4.9 shows the average and fluctuation range of the atmospheric conditions of each tested soil profile. Accordingly, the potential evaporation rate was calculated based on the prevailing atmospheric conditions. Based on Thornthwaite equation (Thornthwaite, 1948), equation 2.6, and Blaney and Criddle equation (Yates and Strzepek, 1994), the potential evaporation equals 4.8 ± 0.1 and 4.9 ± 0.2 mm/day, respectively. Low atmospheric demand is typically less than 5 mm/day, which confirms testing under a low evaporation rate.

The atmospheric conditions and the water content across the profiles' depth were recorded at a 2-minute interval during the whole testing period. Due to the elongated evaporation process and slow color change at the tracing surface, images were captured once or twice a day. Testing duration varied between the profiles; no specific termination methodology was followed. Due to the low readability of the available digital balances, the actual evaporation rate could not be used to check the beginning of Stage 3. However, each tested profile's characteristic length (L_C) and saturation profiles were used as a guide to ensure the formation of the vaporization plane.

4.4 Image Analysis-Based Technique

4.4.1 Image processing

Image analysis operations were conducted on the acquisition images to detect the unsaturated layer and its boundaries. The flowchart shown in Figure 4.10 illustrates the algorithm followed for image processing, adjoined with the output image of each step.

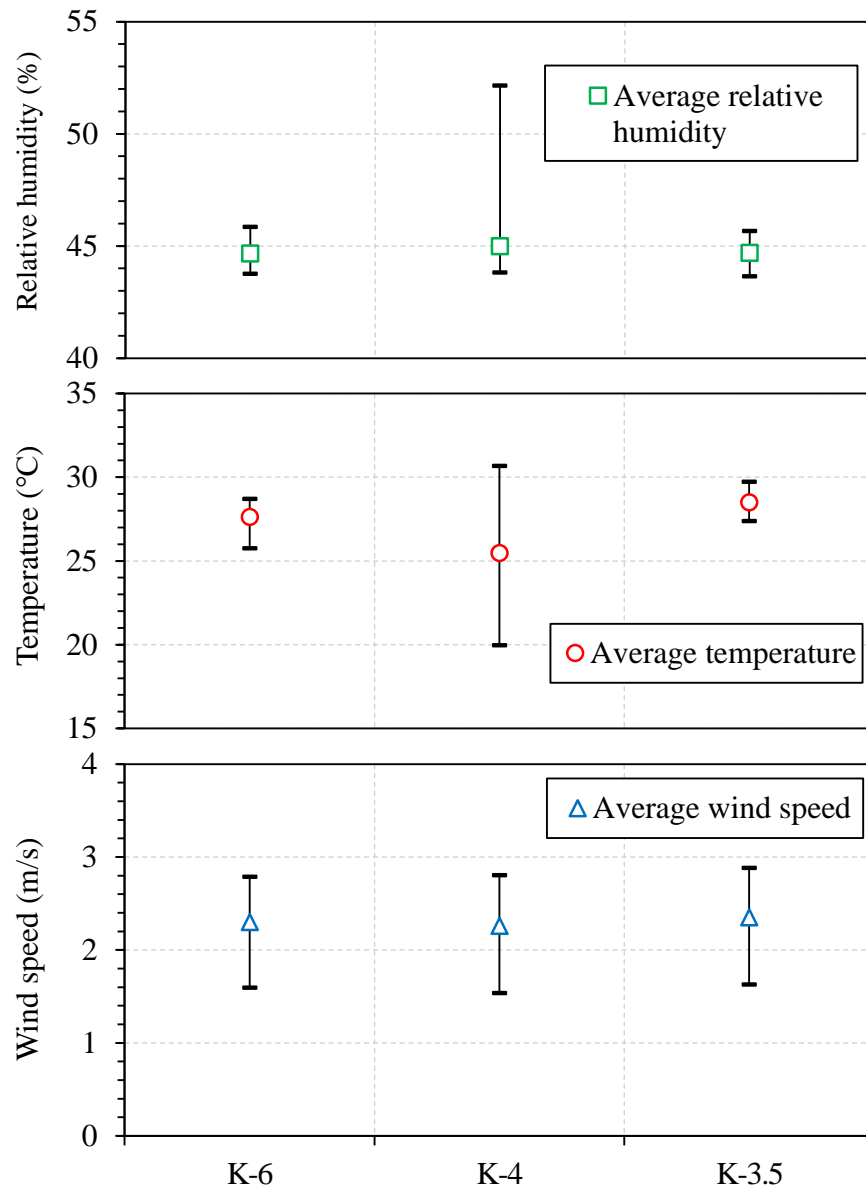


Figure 4.9: Average atmospheric conditions of the tested profiles.

As a first step, the RGB (Red, Green, Blue) acquired images were converted to HSV color space (Hue, Saturation, Value). It must be noted that the RGB and HSV color spaces are two different color models that create a visual representation of any object to facilitate understanding its nature. The RGB is a color model of red, green, and blue mixed to produce a specific color. On the other hand, the HSV color space is a cylindrical color model that remaps the RGB primary colors into dimensions. The Hue specifies the angle of the color on the RGB color circle. A 0° hue results in red, 120° results in green, and 240° results in blue. The saturation controls the amount of color used. A color with full saturation (100% or 1) is the purest color possible, while 0% saturation yields grayscale. The value controls the brightness

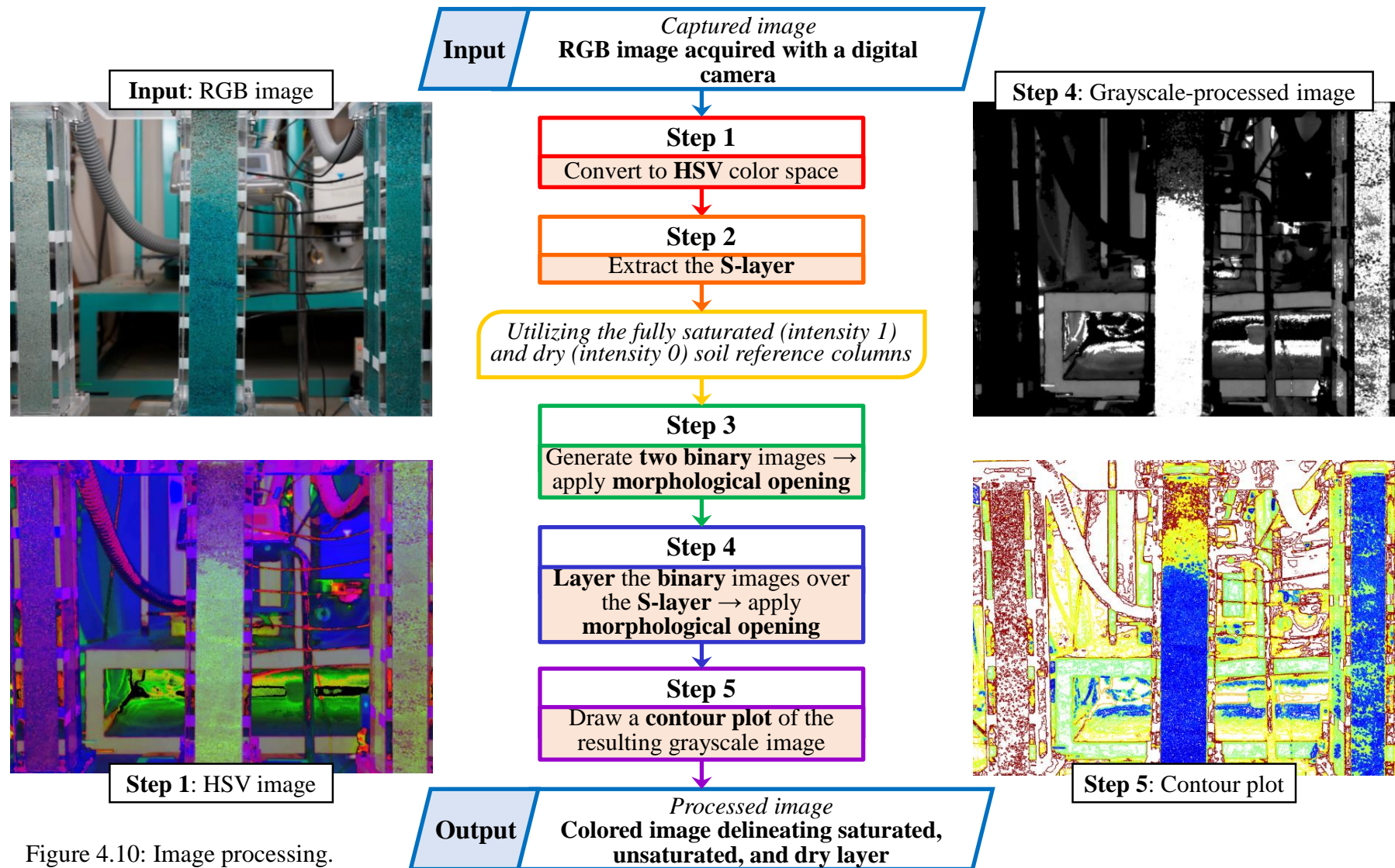


Figure 4.10: Image processing.
[Flowchart]

of the color. A color with 0% brightness is pure black, while a color with 100% brightness has no black mixed into the color.

In the second step, the saturation layer (S-layer) from the HSV color space image, which includes the intensity values from 0 to 1, was extracted for further analysis. The S-layer without the hue or color layer (H-layer) results in an image on grayscale. Therefore, the 1 and 0 peak intensity values were displayed in white and black, respectively, while the in-between values formed different shades of gray. Consequently, utilizing the fully saturated and dry soil reference columns, the average intensity values of the saturated and dry soil were determined, respectively. These intensity values were assigned as threshold values corresponding to the saturated and dry soil layer in the primary tested soil column. It is important to note that each tested soil profile has different intensity values of its saturated and dry layers. This is due to the difference in the soil pore structure and the soil-to-water ratio appearing at the tracing surfaces of the columns. Therefore, under unified lighting, the threshold intensity values are unique for each soil profile and are used to process all its acquisition images. For instance, in the K-3.5 soil profile, all the values > 0.7 were considered saturated soils and designated in white, while the values < 0.1 were considered dry and designated in black. Consequently, the different grey shades were considered unsaturated soil with values between 0.7 and 0.1.

Based on the previous step, the third step starts by generating two different binary images; all ones and all zeros. The all-ones comprises only the white pixels, representing the fully saturated soils, and the other comprises all the black pixels, representing the dry soils. The binary images were carefully improved using morphological opening. Generally, morphological operations process an image based on shape. By applying a specific structuring element, the value of each pixel in the output image is updated according to a comparison of the corresponding pixel in the original image with its neighbors. The morphological opening comprises two consecutive morphological operations, erosion followed by dilation. By performing erosion, the value of the output pixel is the minimum value of all pixels in the neighborhood, while through dilation, the value of the output pixel is the maximum value of all pixels in the neighborhood. It must be noted that the neighborhood takes the shape and size of the chosen structuring element. This operation helps remove small objects and thin lines from an image while preserving the shape and size of larger objects in the image.

In the fourth step, the processed binary images were layered over the original S-layer image to make the saturated and dry zones more visible. Subsequently, an additional morphological opening operation was conducted on the final image. A small structuring

element was applied to avoid essential data loss while refining the boundaries between the saturated, unsaturated, and dry layers.

In the fifth step, a contour plot of the processed grayscale image was drawn to enhance the visualization of the structural outlines (unsaturated layer boundaries) between the different soil layers. The image contouring process was performed with fine lines and different colors to distinguish between the zones. Accordingly, the blue color reflects the saturated soil, the green color delineates the unsaturated soil, and the red color reflects the air-dry layer. Finally, after segmenting the soil layers in the primary tested soil profile based on their saturation, the primary tested soil profile was cropped from each image, and information related to the layers and their boundaries was extracted.

4.4.2 Extracting information from processed images

Figure 4.11 shows a sample of the final processed images from the K-3.5 soil profile after 11 days of testing. Figure 4.11 (a) is the grayscale-processed image, the output of Step 4, while Figure 4.11 (b) is the contouring plot of the grayscale-processed image, the output of Step 5. In both processed images, three layers differing in water content are easily distinguished and are more apparent in the colored contoured plot. The result confirms the ability of the newly

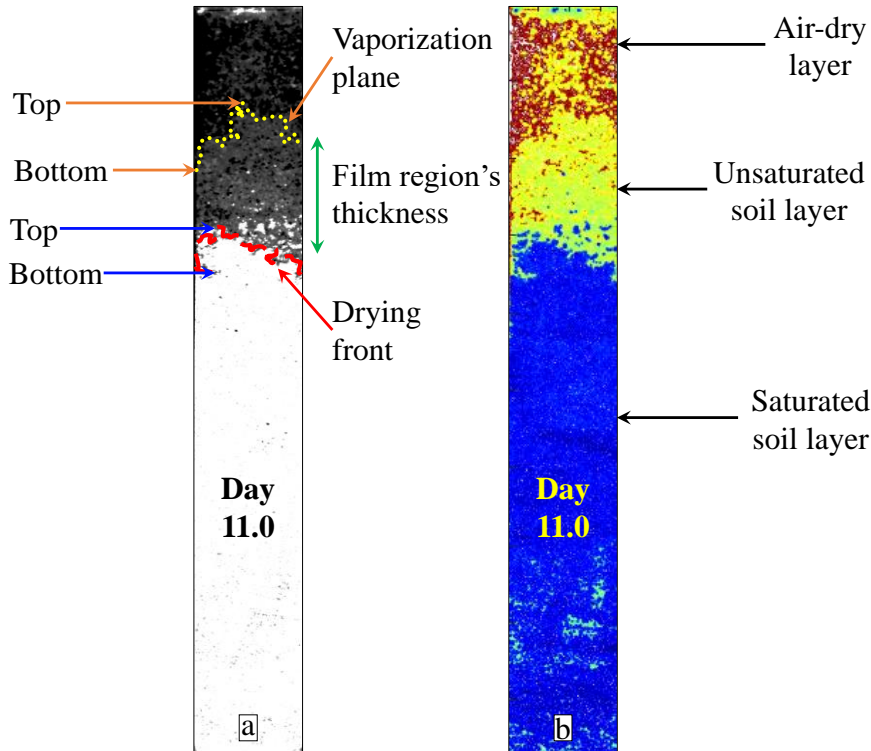


Figure 4.11: Extracting information from the processed images (a) grayscale processed image. (b) corresponding contouring plot.

proposed technique to trace the unsaturated layer during drying, unlike the other existing techniques, which only trace the saturated and dry layers and neglect the unsaturated layer.

Accordingly, information related to the saturated, unsaturated, and dry soil layers is extracted from the processed images. The extracted information is utilized to quantify the dynamics and geometry of the drying front and vaporization plane during evaporation. Therefore, tracing the layers and their boundaries included the following considerations:

1. The blue layer in Figure 4.11 (b) corresponds to the white layer in Figure 4.11 (a), representing the fully saturated zone where pores are filled with liquid water.
2. The green and yellow layer in Figure 4.11 (b) corresponds to the gray layer involving different gray shades in Figure 4.11 (a), representing the unsaturated layer or the film region where some pores are filled with water while others are empty. It must be noted that the yellow color indicates a lower degree of saturation zones while the green highlights higher degrees of saturation. This can be confirmed by the higher density of green color close to the saturated blue zone, while its concentration decreases towards the top.
3. The red layer in Figure 4.11 (b) corresponds to the black layer in Figure 4.11 (a), representing the air-dry layer extending from the surface where the pores are filled with air and the saturation is almost residual. It must be noted that the isolated red patches appearing within the film region are treated as drying patches, gradually forming drying zones.
4. The drying front is the interface between the saturated zone and the film region, the boundary between the blue and green-yellow zones. The drying front is the connected blue line, including the blue patches connected to the saturated zone. Consequently, the blue patches formed within the green-yellow zone are considered isolated wet clusters, not part of the front. This is also shown in Figure 4.11 (a), where the drying front is delineated with a red line.
5. The vaporization plane is the interface between the film region and the air-dry layer, the boundary between the green-yellow and red zones. The vaporization plane is the connected yellow line, including the yellow patches connected to the film region. Consequently, the yellow patches formed within the red zone are considered isolated saturated clusters and not part of the plane. This is also shown in Figure 4.11 (a), where the vaporization plane is delineated with the dotted yellow line.

Accordingly, the geometry of the drying front and vaporization plane are determined based on the extracted information. Firstly, the top and bottom of each boundary are found, in addition to its depth, width, and fluctuation. The top of the interface, whether the drying front

or vaporization plane, is considered its shallowest point, while the bottom is indicated as its deepest point. The determination method of the drying front and vaporization plane's tops and bottoms is explained in Figure 4 (a). Consequently, the depth of the interface is found as the average depth between its top and bottom, while the width of the interface is determined by finding the difference between its top and bottom. Finally, the thickness of the film region was found as the difference between the average depth of the drying front and the vaporization plane during drying.

4.5 Reliability and Accuracy of the Image Analysis-Based Technique

The acquired images during testing were processed as thoroughly discussed in the previous section. Moreover, the TDRs readings were used to plot the water redistribution profile at each processed image. Figures 4.12, 4.13, and 4.14 present groups of processed images for the K-6, K-4, and K-3.5 profiles, respectively. Moreover, each is adjoined with the corresponding water redistribution, where each line in the figures indicates the profile's degree of saturation at the specific time an image was captured.

For the three tested profiles, it can be seen that at the early stages of evaporation, within the first day of testing, the whole soil profile is almost fully-saturated corresponding to a 100% degree of saturation. By definition, once the water starts evaporating at the soil surface, the air phase invades the larger pores at the surface, causing their water level to recede, resulting in the formation of the drying front. It can be seen from the images that the drying front, the boundary between the blue and green-yellow zones, is formed at the top of all the soil profiles within the first couple of days. On the other hand, since the shallowest TDR is installed at a depth of 7 cm from the surface, the degree of saturation at the top layer cannot be determined using the TDRs (Chapter 3, subsection 3.5.1). Therefore, it must be concluded that the newly developed image analysis-based technique can trace the formation of the drying front at shallow depths and even at early stages during drying.

With time, the drying front continues receding into deeper layers in the soil profiles, causing the thickness of the film region, the green-yellow zone, to increase gradually. It must be noted that the film region's color at early evaporation stages differs between soils and with time. Generally, it starts as a connected green zone with hints of yellow and some saturated blue patches. As evaporation continues, the yellow color increases while the blue patches vanish. As explained earlier, the green indicates a higher degree of saturation zones than the yellow

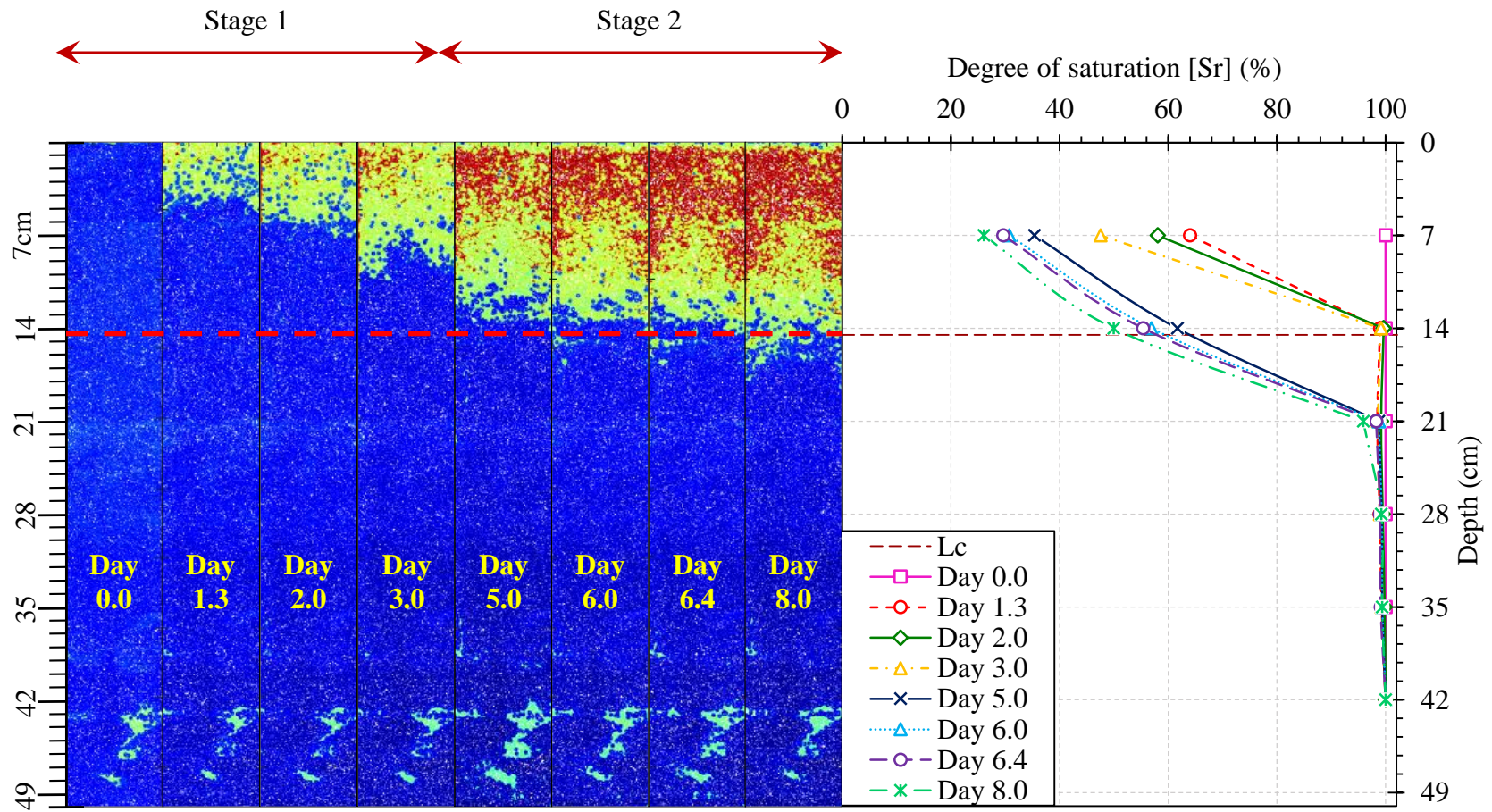


Figure 4.12: K-6 soil profile (a) Processed images. (b) Corresponding water redistribution.

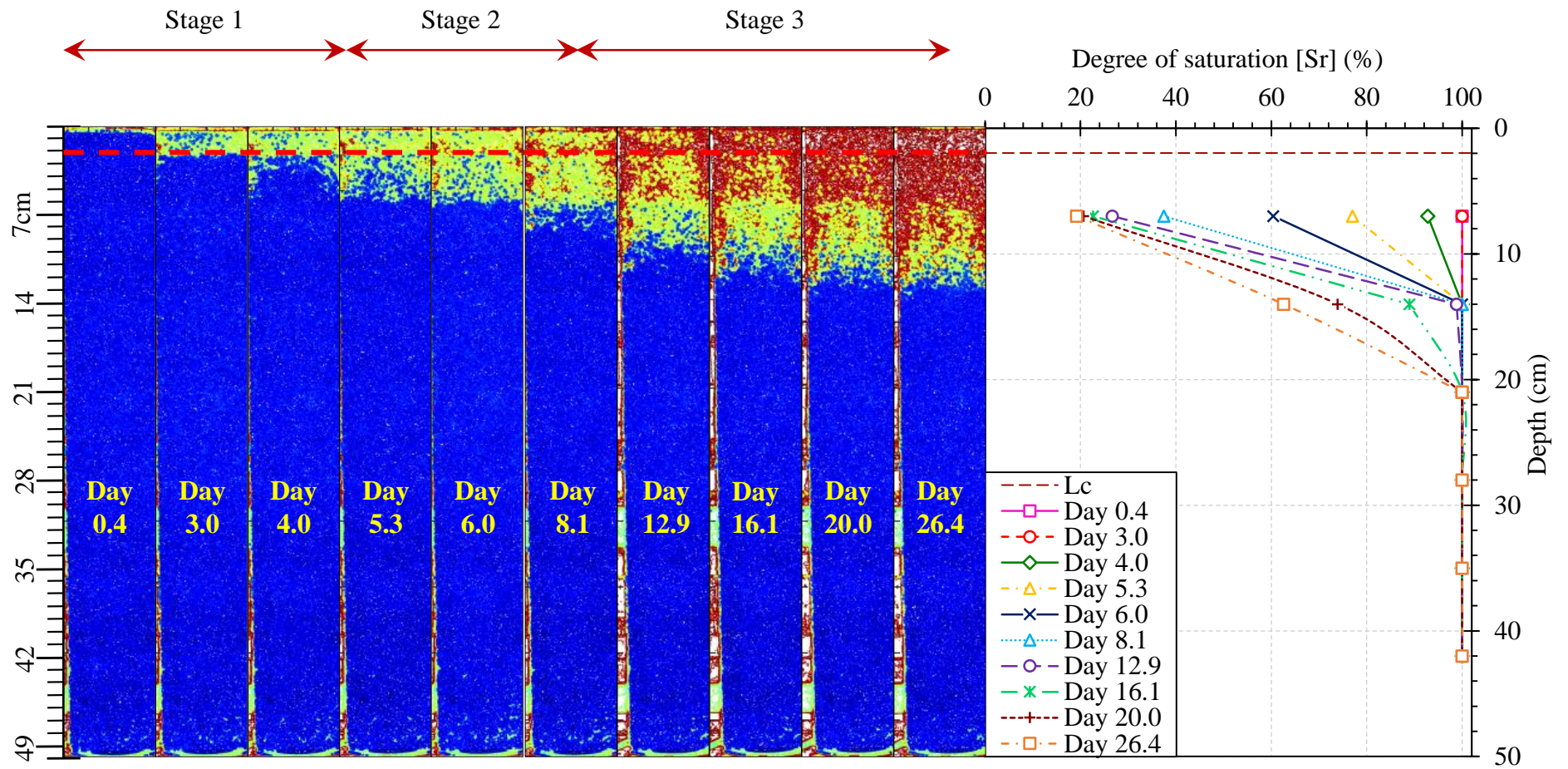


Figure 4.13: K-4 soil profile (a) Processed images. (b) Corresponding water redistribution.

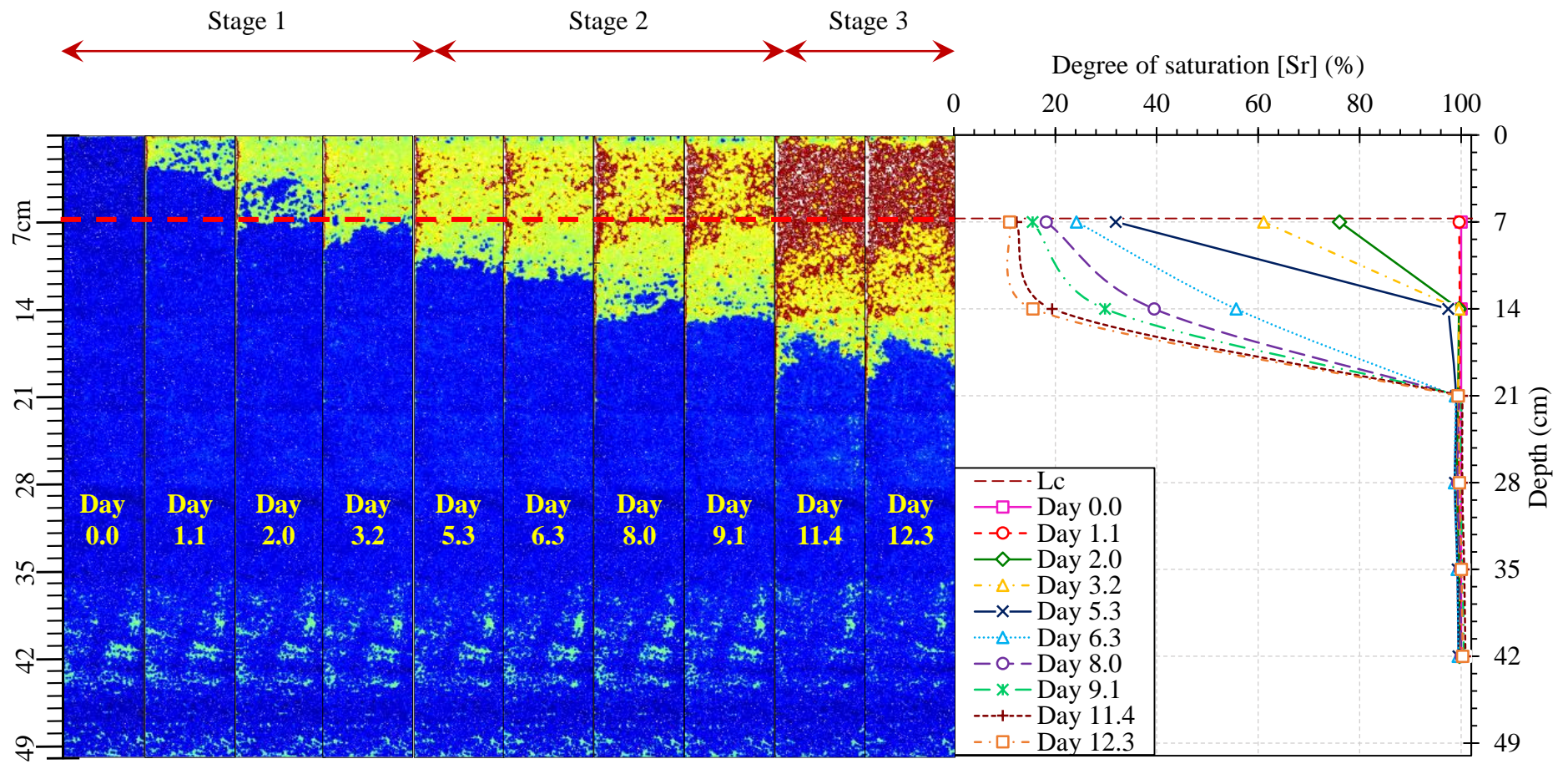


Figure 4.14: K-3.5 soil profile (a) Processed images. (b) Corresponding water redistribution.

ones. This result is attributed to the continuous water loss from the film region's pores and the drying front. The observed color changes due to saturation can be confirmed from the water redistribution profiles, where the degree of saturation continuously decreases with time and with the relocation of the drying front.

As evaporation progresses, dry red patches appear within the film region, generally from the top and continuously propagating downwards. It was also observed that these patches start enlarging and forming a dry red zone, especially once the drying front reaches the L_C . The L_C is indicated with the horizontal dashed red line above the processed images. By definition, once the drying front reaches the depth of the L_C , the smallest pore meniscus persisted at the soil surface retreats forming the vaporization plane and announcing the beginning of Stage 2 of evaporation. This phenomenon can be confirmed by the water redistribution, where the saturation of the top layer becomes closer to the residual with the presence of the dry patches. It is important to note that the processed images delineate the unsaturated layer from an individual tracing surface. However, the water is getting lost from the whole surface area of the tested profile. Therefore, the appearance of the red patches can be considered the beginning of the vaporization plane's formation. This case is particularly noticeable in the soil profiles with shallow L_C , as in the K-4 soil profile, Figure 4.13. The drying front reached the L_C depth between days 3 and 4; while the dry red patches appear in the film region, they do not form a connected dry layer at the current traced surface. However, it is believed that the vaporization plane is formed at the same depth along the thickness of the soil profile in the z-direction.

Subsequently, a continuous increase in the air-dry layer is noticed with continuous water evaporation, where the air-dry layer becomes more continuous with the soil surface. Moreover, the drying front propagation becomes slower, and the saturated green-yellow patches disappear with time. This result indicates that water during Stage 2 gets lost from the vaporization plane and remaining filled pores within the film region rather than the larger pores at the drying front, confirming the hypothesis drawn in Chapter 3 (subsection 3.5.1).

At this stage, once the top layer is dry and the vaporization plane propagates into deeper layers, the evaporation rate becomes slower, announcing the beginning of Stage 3 of evaporation. This observation can be confirmed from the water redistribution, where the soil profile top layer reached the residual degree of saturation.

The results delineated a strong agreement between the processed images and their corresponding saturation profiles for all the tested soil profiles. Therefore, it must be concluded that the newly developed image-analysis-based technique accurately traces the unsaturated

layer during evaporation. It is considered a reliable and definitive technique since the analysis is based on the two unique reference columns for each soil profile, allowing the technique's utilization for broad types of soils. Moreover, the technique proved that it could identify the drying front and the vaporization plane once they are formed in the soil profile.

4.6 Drying Front Dynamics

4.6.1 Spatial development of the drying front

Figures 4.12, 4.13, and 4.14 delineate the drying front's spatial development during the evaporation stages for the K-6, K-4, and K-3.5 soil profiles, respectively. It was observed that the drying front is formed at the early stages of evaporation in all the tested profiles. During Stage 1, the drying front stays connected through liquid-filled pores to the soil surface, where soil sufficiently supplies water due to the capillary pressure difference between larger pores at the drying front and smaller pores at the surface. This phenomenon can be observed from the images during Stage 1 in all the tested profiles. During this stage, the film region comprises liquid clusters between the drying front and the soil surface. Moreover, it is observed that the yellow color of the region increases towards the end of Stage 1, especially in the K-3.5 soil profile, reflecting the reduction in the film region's degree of saturation.

The drying front recedes continuously until it reaches a depth equal to the L_c and is pinned at the L_c for each soil profile on different days. During these days, the dry clusters became more apparent at the top layer of the soil profile. They are promptly enlarged and form the air-dry layer. Consequently, the hydraulic connections with the surface are disrupted, and the vaporization plane is formed, announcing the onset of Stage 2. During this stage, it can be observed that the drying front depth continues receding but more slowly compared to Stage 1 in all the tested profiles. On the contrary, the water continuously evaporates from the remaining liquid clusters within the unsaturated layer, causing the air-dry layer thickness to increase. Consequently, with the beginning of Stage 3, the drying front continues receding, similar to that of Stage 2. This behavior can be observed in K-4 and K-3.5 soil profiles, where no images were acquired during Stage 3 for the K-6 soil profile.

4.6.2 Geometry and temporal development of the drying front

The geometry and dynamics of the drying front were inferred from the processed images for all the tested soil profiles. Figure 4.15 delineates the drying front depth during the evaporation

process. Additionally, its width is marked at each observed point as the shallowest (top) and deepest (bottom) point attained by the drying front (Figure 4.11).

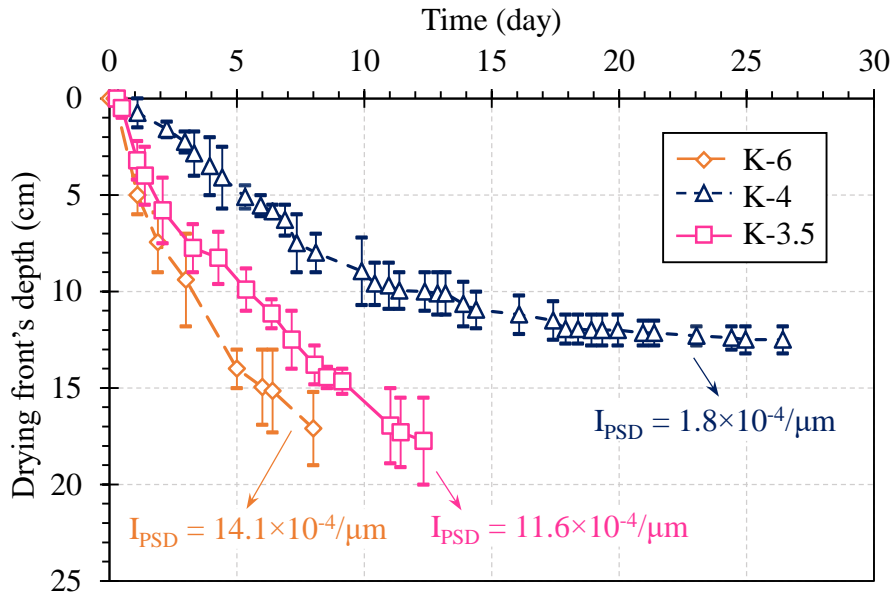


Figure 4.15: Geometry and temporal development of the drying front.

Generally, it was observed that the drying front behavior with time was similar for all the tested profiles. The drying front receding rate tends to be faster during Stage 1, with a slight reduction in its rate with each consecutive stage. This behavior can be observed in the K-4 profile because of the more available data. The difference in the receding rate of the drying front might be attributed to the water transport mechanism at each stage. During Stage 1, the water is directly and sufficiently supplied from the drying front to the surface through capillary liquid flow. Therefore, more and faster water loss at the surface requires more water from the drying front to the surface, causing it to recede faster. In contrast, during Stages 2 and 3, the diffusion pathways through the air-dry layer become deep, and water evaporation becomes less efficient, requiring a longer time for a water unit to evaporate. Moreover, during Stages 2 and 3, the water gets lost from the remaining water clusters within the film regions and air-dry layer.

It was observed that the drying front recedes into deeper layers in the K-6, K-3.5 followed by the K-4 soil profile. This behavior might be highly related to the soil pore structure, where the K-6 has the biggest value of I_{PSD} , followed by K-3.5 and K-4 obtaining the smallest value. Furthermore, the drying front's top and bottom did not always propagate at the same rate. However, its width tends to fluctuate around an average value of 3.41 cm in the K-6, 2.51 cm

in the K-3.5, and 1.81 cm in the K-4 soil profiles. Similarly, the width of the drying front tends to be highly dependent on the pore structure of the soil profile, whereas broader pore size distribution characterized by higher values of I_{PSD} tends to have wider drying fronts. This might be attributed to the localization of the pore diameters within the soil profile. According to the capillary pressure theory, the displaced air-water interface can be pinned in regions with smaller pore diameters, while the bottom of the front might recede to a layer with larger pore diameters.

4.7 Vaporization Plane Dynamics

4.7.1 Spatial development of the vaporization plane

Figures 4.12, 4.13, and 4.14 delineate the vaporization plane's spatial development during Stages 2 and 3 for the K-6, K-4, and K-3.5 soil profiles, respectively. As was explained earlier, once the hydraulic connections with the surface are disrupted, the vaporization plane is formed within the top layers of the soil profiles, announcing the beginning of Stage 2. Consequently, the unsaturated layer is divided into a film region and an air-dry layer, while the water loss mainly occurs from the receding vaporization plane by vapor diffusion through the air-dry layer. This phenomenon can be observed from the images during Stage 2, which started on different days for each soil profile. The vaporization plane continues receding during Stage 2, while the saturated clusters within the air-dry layer continuously shrink, causing a reduction in its degree of saturation. Due to that, the vaporization plane receding rate tends to be slower than the drying front receding rate during Stage 2, which was observed to be slower than its receding rate during Stage 1. This result confirms the continued reduction in the evaporation rate, where water evaporates mainly through the diffusion pathways from the receding vaporization plane supported by the drying front.

An abrupt increase in the vaporization plane depth was observed around days 8 and 11 of the evaporation process from the K-4 and K-3.5 soil profiles, respectively. Simultaneously, a sudden increase in the air-dry layer thickness occurred while the preceding saturated clusters almost vanished. A noticeable decrease in the thickness of the film region accompanied this change. This behavior is believed to be associated with the beginning of Stage 3, where the diffusion pathways from the receding vaporization plane become deeper, leading to an insufficient water supply to the surface.

4.7.2 Geometry and temporal development of the vaporization plane

The geometry and dynamics of the vaporization plane were inferred from the processed images for all the tested soil profiles. Figure 4.16 delineates the vaporization plane depth during Stages 2 and 3. Additionally, its width is marked at each observed point as the shallowest (top) and deepest (bottom) point attained by the vaporization plane (Figure 4.11).

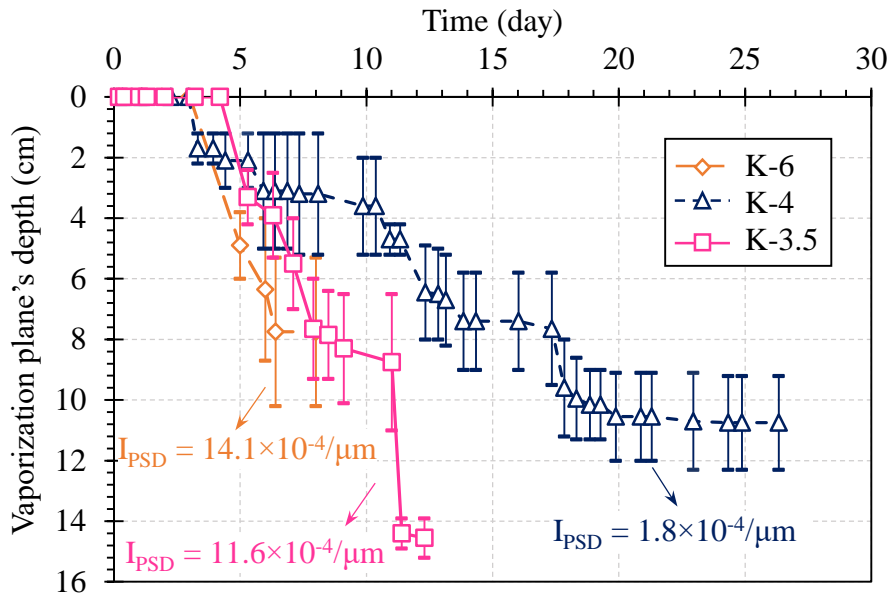


Figure 4.16: Geometry and temporal development of the vaporization plane.

It was observed that the vaporization plane recedes instantly below the surface at the beginning of Stage 2 for all the tested profiles, followed by a continuous increase in its depth. The receding behavior of the vaporization plane during evaporation was quite similar between the profiles. An abrupt reduction in the K-3.5 vaporization plane's depth was observed at the beginning of Stage 3, while a smoother reduction in its depth was noticed at the beginning and during Stage 3 in the K-4 soil profile. The sudden formation of the vaporization plane at the beginning of Stage 2 and the sudden reduction of its depth at the beginning of Stage 3 explain the inflection points of the actual evaporation curve. The formation of the vaporization plane is associated with a change in the water transport mechanism from capillary to vapor diffusion, causing a sudden drop in the evaporation rate. On the other hand, the transition tends to be smoother at the onset of Stage 3, associated with the sudden drop in depth and the longer diffusion pathways rather than a change in the water transport mechanism. The difference in

the plane's sudden drop might be related to the pore structure and where the air-water interface is pinned. The vaporization plane during Stage 3 was pinned in deeper layers for finer soil profiles (K-3.5) compared to K-4, confirming the hypothesis in Chapter 3 (Subsection 3.4.1). It postulated that the vaporization plane depth for finer soil profiles is pinned into deeper layers compared to coarser profiles resulting in a slower water supply to the surface and lower residual evaporation rates during Stage 3.

Similar to the drying front, the vaporization plane in broader pore size distribution profiles, characterized by bigger I_{PSD} , tends to recede into deeper layers relative to the evaporation stage, which highly influences the vaporization plane receding rate. On the other hand, the vaporization plane's top and bottom propagated more constantly during evaporation compared to the drying front. The vaporization plane width tends to fluctuate around an average value of 4.18 cm for the K-6, 3.13 cm for the K-3.5, and 2.82 cm for the K-4 profiles. This result agrees well with the drying front, where broader pore size distribution, characterized by higher values of I_{PSD} , tends to have wider average vaporization plane width. This might be attributed to the localization of the pore diameters within the soil profile.

It must be noted that Chapter 3 (subsection 3.5.1) confirmed that the vaporization plane receding rate plays an essential role in the evaporation process. The change in the normalized actual evaporation rate was found to have a strong correlation with the vaporization plane receding rate during Stage 2. Additionally, it was concluded that vapor diffusion is dominant during this stage, while its evaporation rate mainly depends on the diffusion distance. Accordingly, by distinctly tracing the vaporization plane through the newly developed technique, it was found that the vaporization plane dynamics are highly related to the pore structure of the soil profile. Based on that, more attention is required to investigate the relationship between the vaporization plane dynamics and the pore structure represented by a comprehensive pore index (I_{PSD}). This finding is a fundamental step toward accurately predicting the evaporation rates during diffusion-dependent Stages 2 and 3.

4.8 Film Region Dynamics

Since the drying front and the vaporization plane recede during Stages 2 and 3 of evaporation, investigating the film region is crucial for comprehensively understanding the dynamics. Figure 4.17 delineates the thickness of the film region during the evaporation stages for the three tested soil profiles.

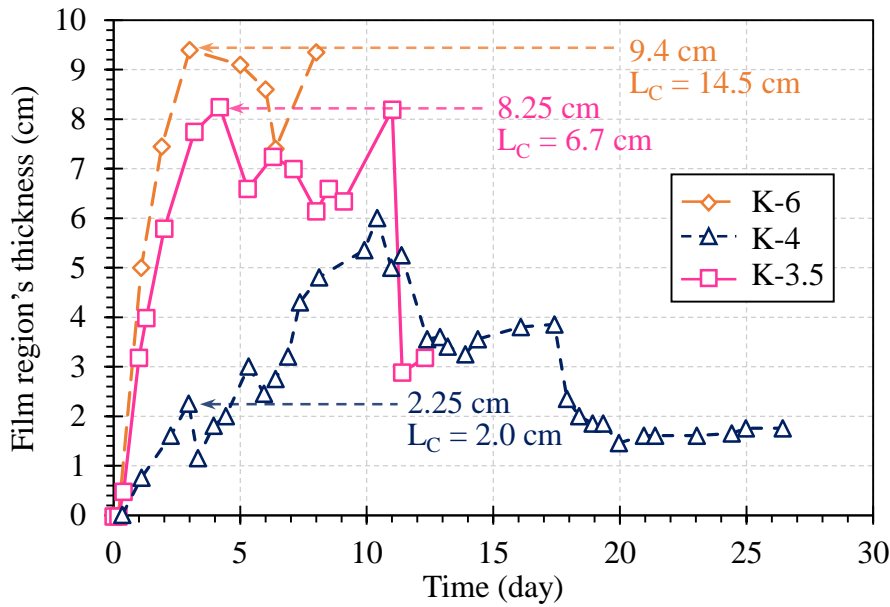


Figure 4.17: Film region dynamics.

By definition, the thickness of the film region during Stage 1 equals the depth of the drying front, where water mainly transports by capillary liquid flow through the unsaturated layer. Therefore, the thickness of the film region at the end of Stage 1 equals the maximum attainable hydrological connection with the surface, defined by the L_C . Nevertheless, once the vaporization plane is formed at the onset of Stage 2, the thickness of the film region gets smaller due to the formation of the air-dry layer. Figure 4.17 shows that in all the tested soil profiles, the film region's thickness increased continuously during Stage 1 until it reached a depth very close to the L_C , as highlighted for each soil profile. Consequently, a slight drop in its thickness was noticed once the vaporization plane was formed, associated with the onset of Stage 2.

The K-6 and K-3.5 film region's thickness slightly fluctuated during Stage 2, yet its thickness did not exceed the maximum thickness attained during Stage 1. However, once the thickness reached the exact value of the L_C , a sudden and remarkable second drop occurred. This drop is believed to be the announcement of Stage 3. On the other hand, in the K-4 profile, the film region thickness increased continuously during Stage 2, followed by a slight drop in thickness and a continuous increase during Stage 3. The film region's thickness extensively exceeded the L_C value, yet, it started receding with the progressing time of Stage 3. Since the film region thickness was found as the difference between the average depth of the drying front and vaporization plane, the film region's thickness slightly differs from the L_C . However, it must be noted that the values are closer in the soil profiles of smaller I_{PSD} .

The film region behavior of the K-4 profile during Stages 2 and 3 is different from the other profiles. This behavior might be related to its pore size distribution. However, more investigations should be conducted to understand the mechanism of its dynamics. Nonetheless, the similar behavior of the K-6 and K-3.5 suggests that each inflection point on the actual evaporation curve might be associated with a significant transition in the film region geometry within the unsaturated soil profile. This result is inconclusive, yet it implies that the film region might have a critical contribution to the evaporation process.

4.9 Summary and conclusions

This chapter investigated the unsaturated layer formation and development during the evaporation process. An image analysis-based technique was developed to facilitate an accurate and reliable tool for tracing the unsaturated layer throughout the evaporation stages. The main conclusions of the chapter can be summarized as follows:

1. The newly developed image-analysis-based technique is confirmed to be reliable and definitive in tracing the unsaturated layer development. The setup included an image acquisition unit to capture high-quality images during testing. Additionally, the two-reference columns prepared next to the primary tested soil column, and the image processing operations allow for accurate and direct detection of the dry, unsaturated, and fully-saturated soil layers and their boundaries.
2. The drying front tends to recede faster during Stage 1, with a slight reduction in its rate with each consecutive stage. This behavior is associated with the sufficient water transport mechanism during Stage 1, where water is directly lost from the surface supported by capillary liquid flow from the drying front. Additionally, the drying front's width is inconsistent, where its top and bottom propagate at different rates during drying.
3. The vaporization plane forms instantly at the onset of Stage 2, followed by a sudden increase in its depth at the onset of Stage 3. This behavior explains the inflection points of the actual evaporation curve where the sudden drop in the evaporation rate at the onset of Stage 2 is associated with the plane's formation followed by a change in the water transport mechanism. On the other hand, the smoother transition between Stages 2 and 3 is caused due to the sudden increase in the length of the diffusion pathways rather than a change in the mechanism.
4. The drying front and vaporization plane depth, receding rate, and width highly depend on the soil pore structure. Both boundaries tend to recede into deeper layers relative to the

- evaporation stage in broader pore size distribution profiles characterized by bigger I_{PSD} . Additionally, the boundaries' average width tends to be more profound in profiles with broader pore size distribution. This finding is fundamental for accurately predicting evaporation rates during diffusion-dependent Stages 2 and 3.
5. The thickness of the film region increased continuously during Stage 1, followed by a slight drop in its thickness once reaching the L_C , associated with the onset of Stage 2. During Stage 2, the thickness slightly fluctuated until reaching a thickness equal to L_C , where a sudden and remarkable second drop in thickness occurred, believed to be the beginning of Stage 3, where the diffusion distance becomes limiting. Further investigations are required to understand the film region dynamics for different soils.

References

- Assouline, S., Tyler, S.W., Selker, J.S., Lunati, I., Higgins, C.W., Parlange, M.B., 2013. Evaporation from a shallow water table: Diurnal dynamics of water and heat at the surface of drying sand. *Water Resour Res* 49, 4022–4034. <https://doi.org/10.1002/wrcr.20293>
- Lehmann, P., Assouline, S., Or, D., 2008. Characteristic lengths affecting evaporative drying of porous media. *Phys Rev E Stat Nonlin Soft Matter Phys* 77, 1–16. <https://doi.org/10.1103/PhysRevE.77.056309>
- Merz, S., 2017. Drying front formation in topmost soil layers as evaporative restraint : non-invasive monitoring by magnetic resonance and numerical simulation (Doctoral thesis). *Schriften des Forschungszentrums Jülich. Reihe Energie und Umwelt / energy and environment ; Rheinischen Friedrich-Wilhelms-Universität.*
- Shokri, N., Lehmann, P., Or, D., 2009. Critical evaluation of enhancement factors for vapor transport through unsaturated porous media. *Water Resour Res* 45, 1–9. <https://doi.org/10.1029/2009WR007769>
- Shokri, N., Lehmann, P., Vontobel, P., Or, D., 2008. Drying front and water content dynamics during evaporation from sand delineated by neutron radiography. *Water Resour Res* 44, 1–11. <https://doi.org/10.1029/2007WR006385>
- Shokri, N., Or, D., 2011. What determines drying rates at the onset of diffusion controlled stage-2 evaporation from porous media? *Water Resour Res* 47, 1–8. <https://doi.org/10.1029/2010WR010284>
- Shokri, N., Salvucci, G.D., 2011. Evaporation from Porous Media in the Presence of a Water Table. *Vadose Zone Journal*. <https://doi.org/10.2136/vzj2011.0027>
- Thorntwaite, C.W., 1948. An Approach toward a Rational Classification of Climate. *Geogr Rev* 38, 55–94. <https://doi.org/10.2307/210739>
- Yates, D., Strzepek, K.M., 1994. Potential evapotranspiration methods and their impact on the assessment of river basin runoff under climate change.

5

CHAPTER

Pore-Scale-Based Estimation Model of the Actual Evaporation

5.1 Introduction

The evaporation process from bare soil profiles was extensively discussed in the literature from a phenomenological point of view. Numerous methods were proposed to determine the evaporation rate from soil profiles based on the atmospheric demand at the surface. Generally, the process was limited to the mechanisms occurring at the surface, considering it as a soil-atmosphere boundary flux. In contrast, the combined transport of liquid water and vapor diffusion within the soil profile, besides the conditions at the boundary, play a significant role in the process. In the past few decades, some studies have shown the importance of the micro-mechanisms occurring within the unsaturated layer at the pore-scale level and their effect on the macroscale behavior of the evaporation process. With recent advanced technologies, soil scientists strived to explain the phenomenon from a microscale perspective. Nevertheless, a comprehensive estimation method of the evaporation rate that considers the emerging water mechanisms through the soil profile is still lacking.

In Chapters 3 and 4, the evaporation process was amply investigated from microscale and pore-level perspectives. It was concluded that the soil pore structure highly influences the evaporation behavior from soil profiles. The pore structure was parameterized in a robust Pore Size Distribution Index (I_{PSD}) that correlated well with the evaporation parameters. Furthermore, the newly proposed index considers the factors affecting water transport mechanisms involved in the process, liquid capillary, and vapor diffusion. The new insights concerning the actual evaporation rate confirmed that its receding rate during Stage 2 is controlled by the vaporization plane receding rate into the soil profile. Additionally, the behavior of the vaporization plane was found to be affected by the soil's I_{PSD} .

For a complete description of the evaporation process and an accurate evaluation of its rate, the atmospheric demand should be solved in conjugation with the water supply and its mechanisms through the unsaturated soil profile. Therefore, the following chapter proposes a new actual evaporation rate estimation model based on the pore structure and the water transport mechanisms through the unsaturated soil profile. The model deploys the new insights from previous chapters related to evaporation, pore structure, and vaporization plane dynamics to estimate the normalized actual evaporation curve of Stages 1 and 2. The proposed semi-empirical model solves the transition from the capillary-driven liquid flow during Stage 1 to the vapor diffusion dominant in Stage 2, resulting in a simple bilinear curve. The chapter thoroughly discusses the theoretical considerations, model derivation, reliability, and limitations.

5.2 Theoretical Considerations

5.2.1 Stage 1: Capillary liquid flow and the characteristic length

During Stage 1, evaporation occurs from smaller pores attained at the soil surface, where the menisci's curvature does not exceed the pore critical invasion pressure. Simultaneously, these pores are supplied by capillary flow from larger pores previously receded and pinned, forming the drying front. The atmospheric demand primarily limits the evaporation rate during Stage 1. However, the capacity of the capillary transport to supply the atmospheric demand is the critical reason for maintaining a high and sometimes constant evaporation rate, as if the soil is virtually saturated (Scherer, 1990). A potentially valuable indicator of these continuous liquid pathways from the receding drying front to the surface is the Characteristic Length (L_C) introduced by Lehmann et al. (2008). The L_C indicates the maximum hydraulically connected distance from

the drying front to the surface that is disrupted due to the interplay between capillary, viscous, and gravitational forces. The L_C is determined by the pore size distribution, equations 2.17 to 2.21, and is used to predict the depth of the drying front at the end of Stage 1.

Shahraeeni et al. (2012) interpreted and proved that under high atmospheric demand (typically > 5 mm/day), even when the capillary flow is still able to supply the atmospheric demand during Stage 1, the evaporation rates from initially saturated surfaces may decrease continuously. This phenomenon is attributed to the limitations on vapor exchange between the drying surface and the viscous sublayer formed by airflow above the surface. In the present study, to allow the detection of the three distinct evaporation stages, the atmospheric conditions were unified at a low demand with an average potential evaporation of 4.8 ± 0.5 mm/day for the tested profiles studied in Chapter 3. Consequently, their average actual evaporation rate during Stage 1 was equal to 3.7 ± 0.5 mm/day, Figures 3.8 and 3.10. It must be noted that this value is slightly lower than the average potential evaporation. Wilson et al. (1994) observed that the soil surfaces were 1°C cooler than water surfaces under the same testing conditions, resulting in a slightly lower saturation vapor pressure at the soil surfaces, hence a slightly lower evaporation rate.

For further investigation of the evaporation process behavior, the K-2 soil profile from Chapter 3 was retested under higher atmospheric demand. Figure 5.1 delineates the normalized actual evaporation rates with the elapsed time for the K-2 soil profile under low (4.0 mm/day) and high (8.4 mm/day) atmospheric demand. The difference in the evaporation behavior due to varying demand is apparent. Stage 1 tends to shorten under high atmospheric conditions, where a twice higher demand reduces its duration to half. Moreover, its evaporation rate decreases continuously, followed by a drop at the beginning of Stage 2. On the other hand, under low demand, the transition between Stages 1 and 2 tends to be sharper and more apparent.

Another experimental evidence confirms the role of evaporative coupling between supply and demand during Stage 1; Figure 5.2 delineates the evaporation depth during drying against the actual evaporation rate. The evaporation depth was determined by dividing the mass lost over the column's cross-sectional area at each specific time. It was observed that while for high atmospheric demand, the evaporation rate decreases with the evaporation depth, it remains constant for low demand until the capillary-driven liquid flow is disrupted and Stage 2 starts. It must be noted that despite the atmospheric conditions, the transition between Stages 1 and 2 occurred at the same evaporation depth, delineated with the blue arrow. This result confirms that the atmospheric demand influences the duration of Stage 1 and its rate, while from a

microscale perspective, the end of Stage 1 is marked by the hydraulic connectivity controlled by the soil pore structure and is mathematically represented by the L_C .

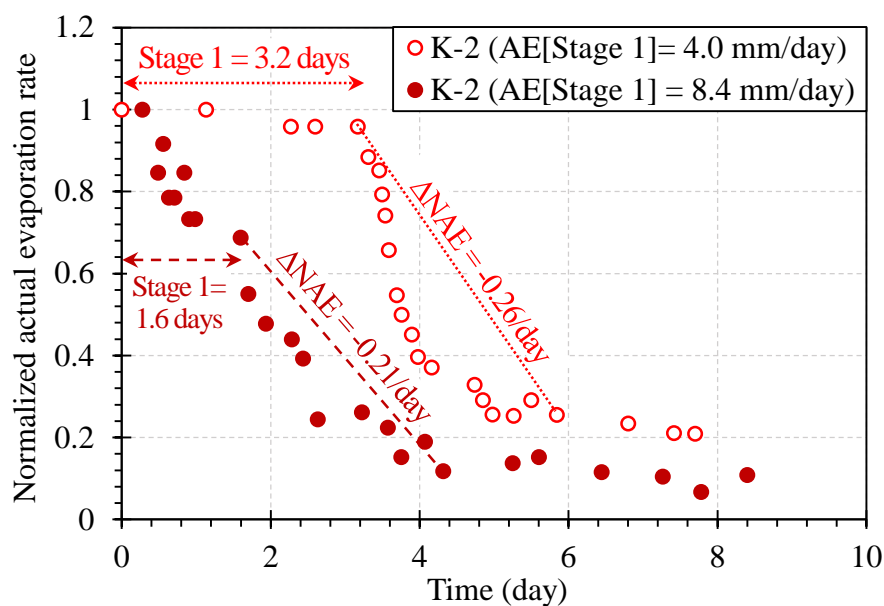


Figure 5.1: Normalized actual evaporation curves – Influence of the atmospheric demand.

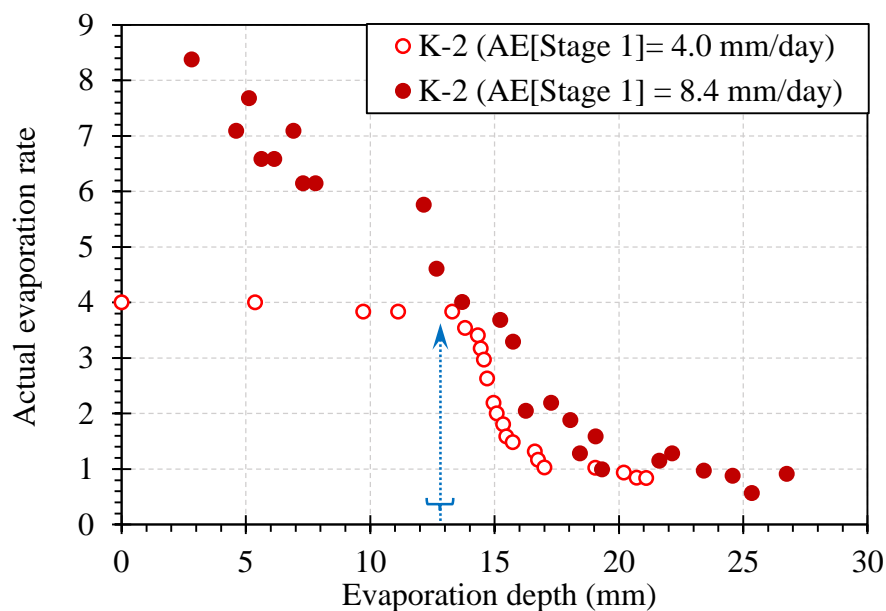


Figure 5.2: Evaporation depth during drying.

5.2.2 Stage 2: Vapor diffusion from a receding vaporization plane

The significant and rapid drop in the evaporation rate at the transition between Stages 1 and 2 is associated with the abrupt change in the water transport mechanism. The continuous liquid flow from the drying front to the surface is disrupted once the smallest pore's meniscus at the surface breaks and the drying front reaches the L_c . Consequently, the liquid menisci recede into the soil profile and form a vaporization plane below the surface, announcing the onset of Stage 2. Following the vanishing of the capillary driving force to the surface, water diffuses as vapor through the overlaying air-dry layer to the surface and then leaves into the atmosphere. However, the slowly receding vaporization plane remains connected to the drying front below via capillary-induced liquid flow, as delineated in the schematic diagram of Figure 2.10. The continuous increase in the diffusion pathways lengths from the receding vaporization plane to the surface results in a gradual decrease of the evaporation rate during Stage 2.

Following Fick's law of diffusion through the air-dry layer, a strong relationship between the normalized actual evaporation rate reduction slope and the vaporization plane receding rate during Stage 2 was found in Chapter 3, as shown in Figure 3.13. It was concluded that a lower receding rate of the vaporization plane during Stage 2 corresponds to a lower reduction in the evaporation rate, resulting in gentler slopes in the evaporation curve. This finding confirmed the dominance of the vapor diffusion during Stage 2. Besides, it assured that the evaporation rate mainly depends on the diffusion distance under unified atmospheric demand. Based on that, the behavior of the actual evaporation receding rate was studied under low and high atmospheric demand from Figure 5.1. Despite the difference in the behavior of Stage 1 and the transition between Stages 1 and 2, it was observed that the atmospheric demand has a relatively low influence on Stage 2. The average duration of Stage 2 for the two profiles was around 2.70 days, with a slight deviation of 0.03 days, while the average normalized actual evaporation rate reduction slope equals -0.24/day with a slight deviation of 0.03/day. Accordingly, it must be concluded that the actual evaporation rate behavior during Stage 2 depends on the soil water supply governed by the soil pore structure. Furthermore, the normalized actual evaporation rate reduction slope is unique for each soil profile with a constant pore structure despite the atmospheric demand and is a function of the vaporization plane receding rate. Consequently, the actual evaporation during Stage 2 can be estimated using Fick's law of diffusion from a receding vaporization plane while considering the soil pore properties.

5.3 Derivation of the Semi-Empirical Evaporation Model

The highly dynamic interactions between the soil pore properties, transport mechanics, and boundary conditions during the evaporation process from soil profiles require an innovative estimation model for the evaporation rate. The newly proposed model utilizes the evaporation dynamics from unsaturated soil profiles to resolve the dominant water transport mechanism at each stage. Additionally, it considers the atmospheric demand at the soil surface and the soil's ability to supply water from its body. The following section presents the assumptions drawn for deriving the pore-scale-based model. Moreover, the derivation flow and the theoretical and empirical utilized formulas are clearly explained.

5.3.1 Model Assumptions

According to the present study's new findings and the theoretical observations elucidated in the previous section, the semi-empirical pore-scale-based model is derived based on the following assumptions:

Stage 1 of evaporation

1. The actual evaporation rate is constant and equal to the potential evaporation rate determined based on the ambient atmospheric conditions at the soil surface.
2. The duration of Stage 1 is dependent on the maximum hydraulic connectivity between the drying front and the surface, represented mathematically by the Characteristic Length (L_C).

Stage 2 of evaporation

3. The actual evaporation rate recedes linearly with time during Stage 2.
4. Water exclusively diffuses as vapor from a receding vaporization plane through the air-dry layer to the surface.
5. Water flows under steady-state conditions through Stage 2's unsaturated profile. The capillary flow continuously supplies water from the drying front to the vaporization plane, which continues by vapor diffusion to the surface. Consequently, the capillary flux through the bottom film region equals the vapor diffusion flux through the air-dry layer.
6. Vapor flux through an air-dry soil layer follows Fick's first law of diffusion. Evaporation occurs under the concentration gradient between the vaporization plane and the adjacent air layer above the surface. Diffusion occurs in a one-dimension under isothermal conditions,

while the concentration gradient (∂C) is assumed constant under unified atmospheric demand within short durations. Similarly, the vapor diffusion coefficient (D) is assumed constant for a homogeneous air-dry layer under constant concentration.

7. The vaporization plane receding rate is a function of the soil pore structure, represented by the Pore Size Distribution Index (I_{PSD}), where the soil pore structure is assumed constant with the moisture content variation.

5.3.2 Fick's law of diffusion to estimate the actual evaporation reduction rate during Stage 2

Fick's law of diffusion (equation 3.1) was adopted to determine the evaporation during Stage 2, as delineated in Figure 5.3. The diffusion flux through a constant area was derived as the evaporation rate change during Stage 2 from a specific diffusion area divided by the potential evaporation. Consequently, the slope of the linear evaporation reduction is found as follows:

$$\frac{\Delta NA E}{A \times \Delta t} = \frac{D \times \partial C \times \left(\frac{1/\Delta VP}{\Delta t}\right)}{PE} \quad (5.1)$$

- $\Delta NA E/\Delta t$ ($1/s.m^2$) is the normalized actual evaporation reduction rate during Stage 2.
- $A=1 m^2$ is the diffusion area assumed unity for one-dimension flux, where the area available for diffusion remains constant with distance.
- D (m^2/s) is the water vapor diffusion coefficient, expressed as the product of the free-air water vapor diffusion coefficient (D_o) and a function of air-filled porosity as follows (Campbell, 1985):

$$D = D_o b \phi^m \quad (5.2)$$

where ϕ is the soil porosity, $b = 0.66$, and $m = 1$ are Penman's constants for dry soils. D_o is the diffusion coefficient at a specific temperature (T) and pressure (P) determined from the following relationship (Campbell, 1985):

$$D_o = D_o(NTP) \times (T/T^0)^n \times (P^0/P) \quad (5.3)$$

where $D_o(NTP)$ is the diffusion coefficient at the Normal Temperature and Pressure (NTP) equal to $2.12 \times 10^{-5} m^2/s$ (Campbell, 1977) at the standard temperature, $T^0 = 273.16 K$ and standard pressure, $P^0 = 101.3 kPa$. The exponent n has a value of 2 for the H_2O and O_2 .

- ∂C (g/m^3) is the driving concentration gradient, found as the difference between the water vapor density at the vaporization plane, assumed saturated (C_{sat}), and the water vapor density 5 cm above the surface (C_∞).

$$\partial C = C_{\text{sat}} - C_{\infty} = C_v \times (1 - RH_{\text{air}}) \quad (5.4)$$

where C_v is the saturation vapor concentration at the vaporization plane, while RH_{air} is the relative humidity of the ambient air 5 cm above the soil surface.

- PE (g/s) is the potential evaporation determined from the atmospheric demand. It must be noted that dividing the determined values by the potential evaporation compensates for the change in the vaporization plane receding rate with the variation in the atmospheric conditions. This step is required since the concentration gradient is assumed constant through the air-dry layer.
- $(1/\Delta VP)/\Delta t$ (1/s.m) is the inverse of the vaporization plane receding rate with time during Stage 2, where VP is the vaporization depth reflecting the diffusion distance to the soil surface. This parameter is thoroughly explained in the following subsection, and it is estimated using the newly proposed empirical formula based on the I_{PSD} (1/ μm) as follows:

$$\frac{1/\Delta VP}{\Delta t} = 0.0478 \times 10^{-4} \times (I_{\text{PSD}}) - 0.95 \times 10^{-4} \quad (5.5)$$

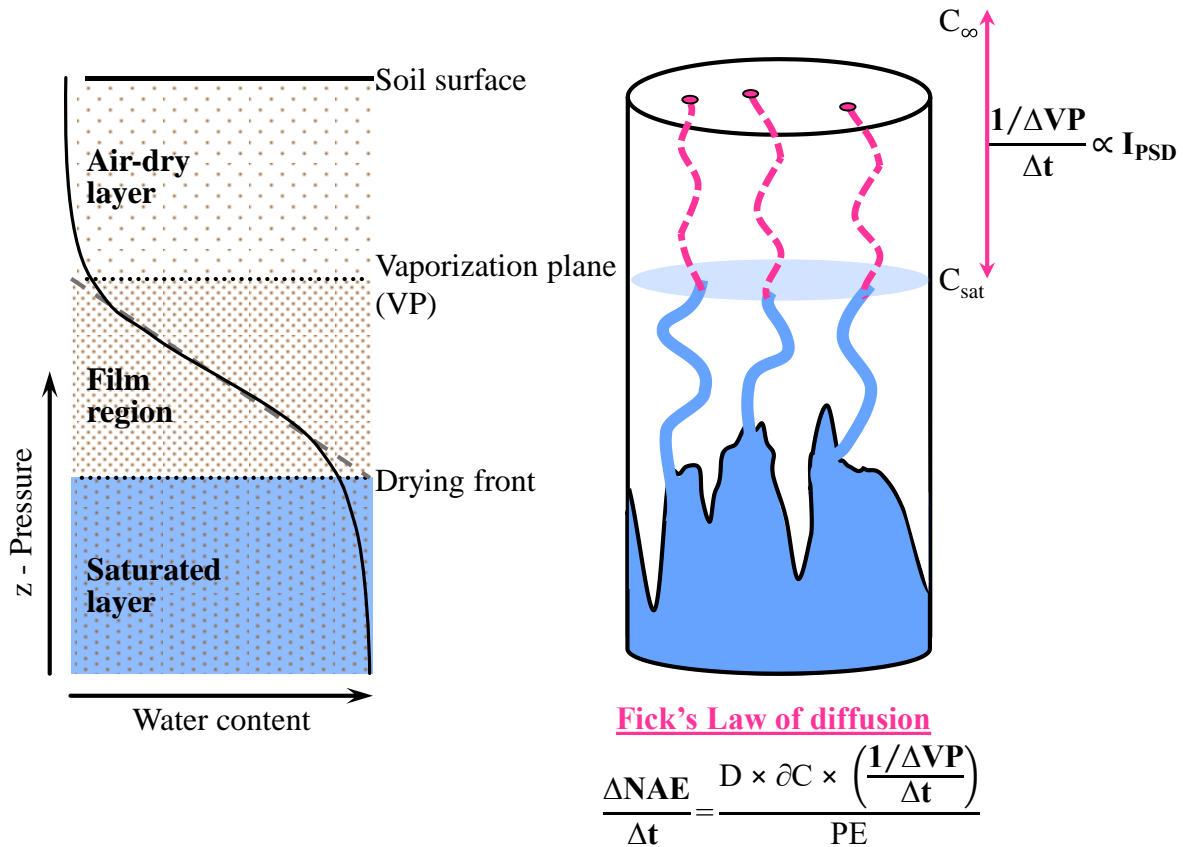


Figure 5.3: Fick's law of diffusion during Stage 2.

5.3.3 Empirical correlation of the vaporization plane receding rate and pore size distribution index

The relationship between the vaporization plane receding rate during Stage 2 and the Pore Size Distribution Index (I_{PSD}) was investigated experimentally using two methods. The first is through the saturation profiles recorded using the Time Domain Reflectometry probes (TDRs). The second method is tracing the vaporization plane from the captured and analyzed images using the newly developed image analysis-based technique (Chapter 4). In the following subsection, both methods are reviewed and compared to show the strong dependency of the vaporization plane receding rate on the I_{PSD} . However, due to the higher accuracy of the newly developed image analysis-based technique, the empirical formula, equation 5.5, extracted from image analysis is adopted in the proposed model.

The data recorded from each TDR was used to delineate the saturation profiles of each tested soil column. Figure 5.4 delineates the change in the degree of saturation with time for three of the soil profiles tested in Chapter 3; K-7, K-6, and K-5. Each line indicates the saturation at different soil profile depths, delineating the TDRs' positions (Figure 3.5). It was assumed that the vaporization plane reaches a specific TDR position once its degree of saturation converges to a constant and low value indicating a residual degree of saturation. In order to find the vaporization plane receding rate during Stage 2, at least two vaporization plane depths at different times during Stage 2 are required. Therefore, the duration of Stage 2 for each soil profile was found from the normalized actual evaporation curve, shown in Figure 3.8, and was identified on the saturation profile. Consequently, two points were selected, and the inverse of the vaporization plane receding rate with time ($(1/\Delta VP)/\Delta t$) was calculated.

Similarly, the data extracted from the processed images in Chapter 4 concerning the vaporization plane was used to determine the vaporization plane receding rate during Stage 2. From Figure 4.16, the inverse of the vaporization plane receding rate with time ($(1/\Delta VP)/\Delta t$) was calculated as an average reduction from its formation at the beginning of Stage 2 until its sudden drop at the beginning of Stage 3 for the K-6, K4, and K-3.6 soil profiles.

The determined $(1/\Delta VP)/\Delta t$ values from both methods were plotted with each soil profile's I_{PSD} value, as delineated in Figure 5.5. Both methods' results confirm the strong correlation between the vaporization plane dynamics that control the evaporation during Stage 2 and the pore structure parameter presented by the I_{PSD} . Based on that, it must be concluded that soil profiles with a broader pore size distribution, characterized by bigger I_{PSD} ,

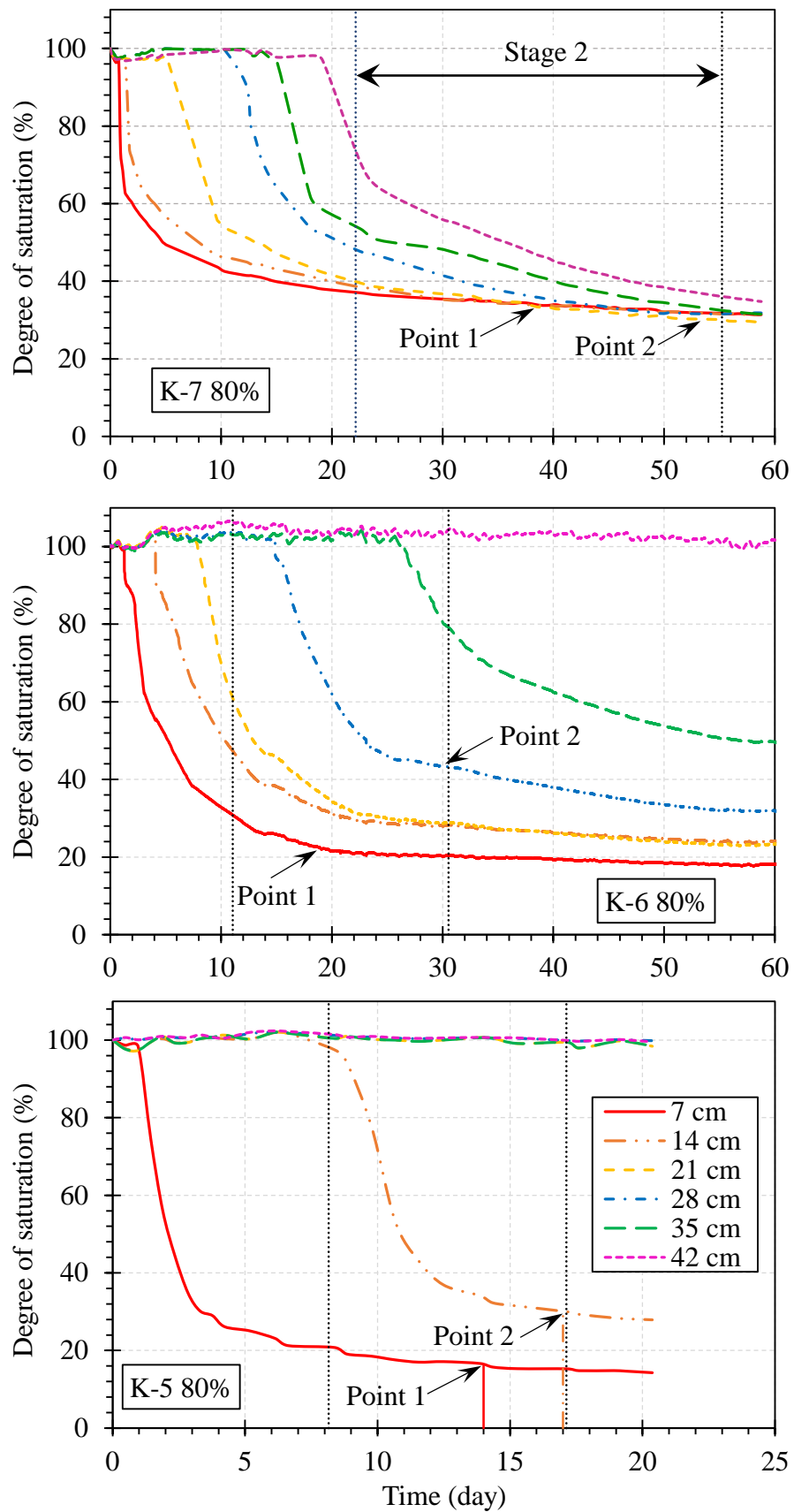


Figure 5.4: Saturation profiles of the soil columns.

tend to have a slower receding rate of the vaporization plane during Stage 2. Moreover, the results confirm the proposed hypothesis of the high dependency and the role of the pore structure on the evaporation process during Stage 2.

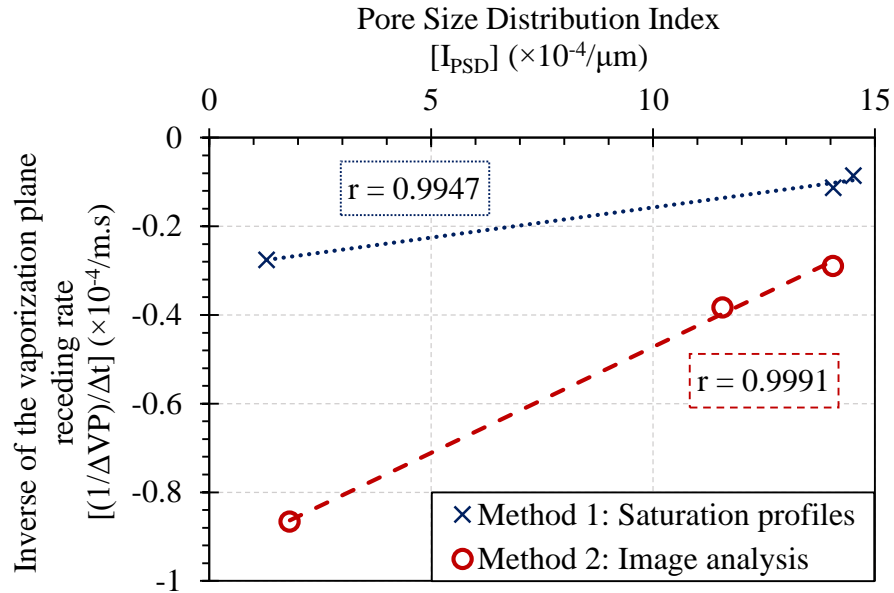


Figure 5.5: Vaporization plane receding rate and I_{PSD} relationship.

Despite the excellent agreement between the two determination methods of the vaporization plane, the image analysis method is believed to be higher in accuracy and more reliable to be considered as a prediction formula of the vaporization plane. The TDRs generally measures the average saturation of a 5 cm soil layer at their installed position, which leads to higher uncertainty in identifying the exact position of the vaporization plane. Besides, the data extracted from the TDRs are discrete information limited to the soil adjacent to their installed positions. Moreover, due to technical limitations of utilizing the TDRs in the drying column testing, including their size and installation difficulty, the vaporization plane could not be traced accurately at the early stages of its formation. Unlike the image analysis-based technique, the vaporization plane formation, dynamics, and geometry were precisely studied through the soil column's tracing surfaces (Chapter 4, section 4.7). Consequently, the newly proposed empirical formula, equation 5.5, was adopted to determine $(1/\Delta VP)/\Delta t$ based on the I_{PSD} , as delineated in Figure 5.6.

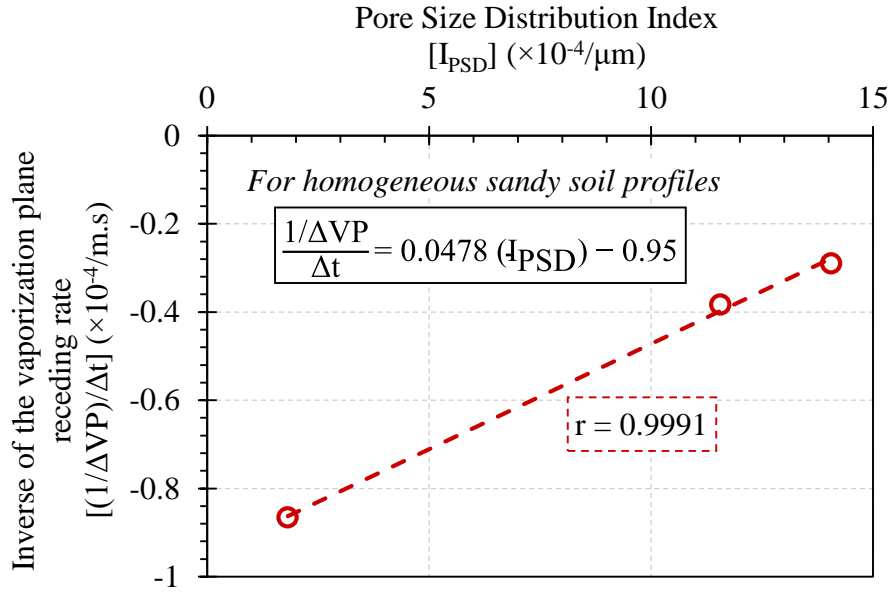


Figure 5.6: Empirical determination of the inverse of the vaporization plane receding rate based on I_{PSD} .

5.3.4 Estimation of the normalized actual evaporation curve

Based on the model assumptions and the determined normalized actual evaporation reduction rate during Stage 2, a soil profile's normalized actual evaporation curve can be estimated as delineated in the schematic diagram of Figure 5.7.

For Stage 1, the evaporation rate is constant and equal to the potential evaporation determined based on the ambient atmospheric conditions at the soil surface. Therefore, the normalized actual evaporation rate during Stage 1 is assumed to be equal to unity ($NAE_{S1} = 1$). The duration of Stage 1 (t_{S1}) is calculated by assuming that Stage 1 ends at the maximum hydraulic connectivity attained between the drying front and the surface, as follows:

$$t_{S1} = \frac{L_C \times \phi}{PE} \quad (5.6)$$

where L_C (mm) is the depth of the drying front at the end of Stage 1, ϕ is the soil porosity assuming that all the water-filled pores in Stage 1's film region are empty, and PE (mm/day) is the potential evaporation rate at which water at the surface is being lost.

Accordingly, the linear equation of the actual evaporation reduction during Stage 2 (NAE_{S2}) is found as follows:

$$NAE_{S2} = \left(\frac{\Delta NAE}{\Delta t} \right) \times t + \left[1 - \left(\frac{\Delta NAE}{\Delta t} \right) \times t_{S1} \right] \quad (5.7)$$

where $\Delta \text{NAE} / \Delta t$ ($1/\text{s.m}^2$) is the reduction slope during Stage 2, and t (s) is anytime during Stage 2. The term $\left[1 - \left(\frac{\Delta \text{NAE}}{\Delta t}\right) \times t_{S1}\right]$ is the intersection of Stage 2's line with the y-axis. It is derived by solving Stage 2's slope considering the point of intersection with the y-axis and another at its intersection with the NAE_{S1} at the end of Stage 1 (t_{S1}).

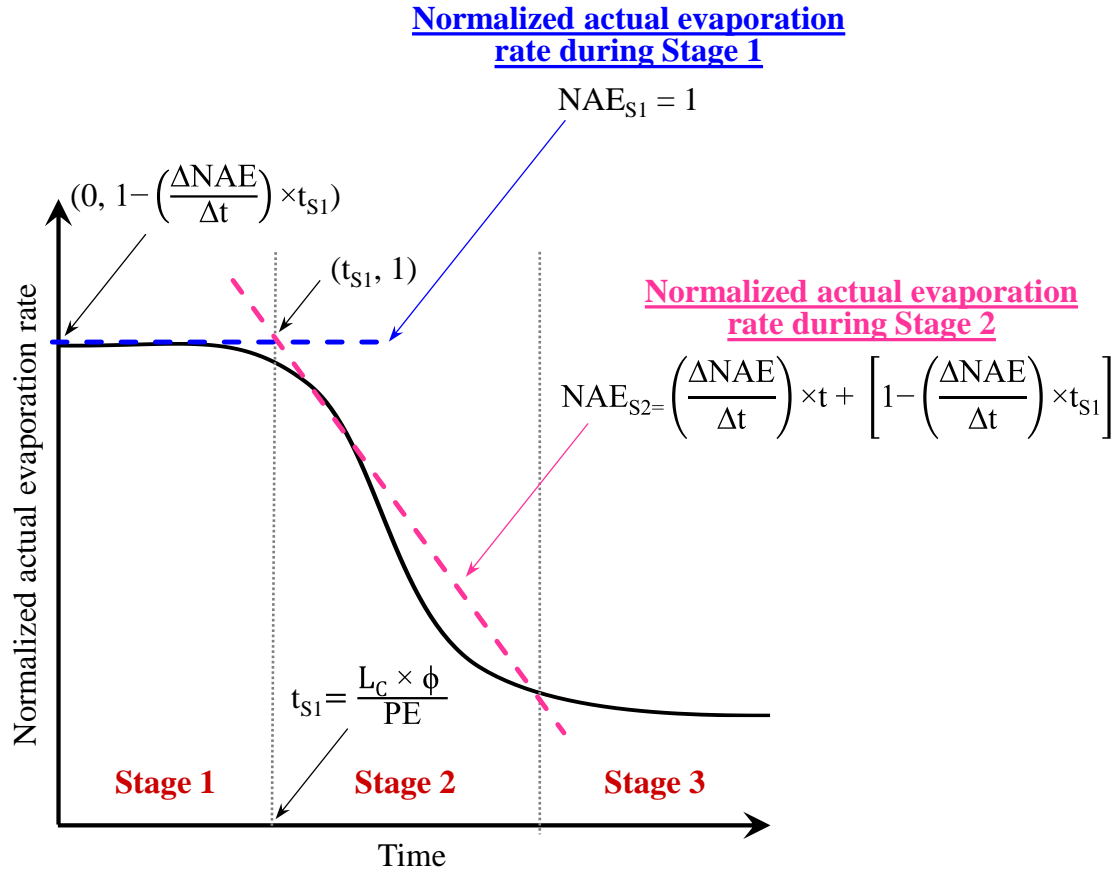


Figure 5.7: Estimation of the normalized actual evaporation curve using the semi-empirical evaporation model.

5.4 Reliability and Limitations of the Pore-Scale-Based Evaporation Model

In the following section, the evaporation curves of all the tested profiles in Chapter 3 were determined using the newly proposed pore-scale-based actual evaporation estimation model. The steps followed for utilizing the model are represented in the flowchart shown in Figure 5.8. The estimated evaporation curves were compared to the experimental results. Consequently, the model's reliability is discussed while its limitations and improvement areas are presented.

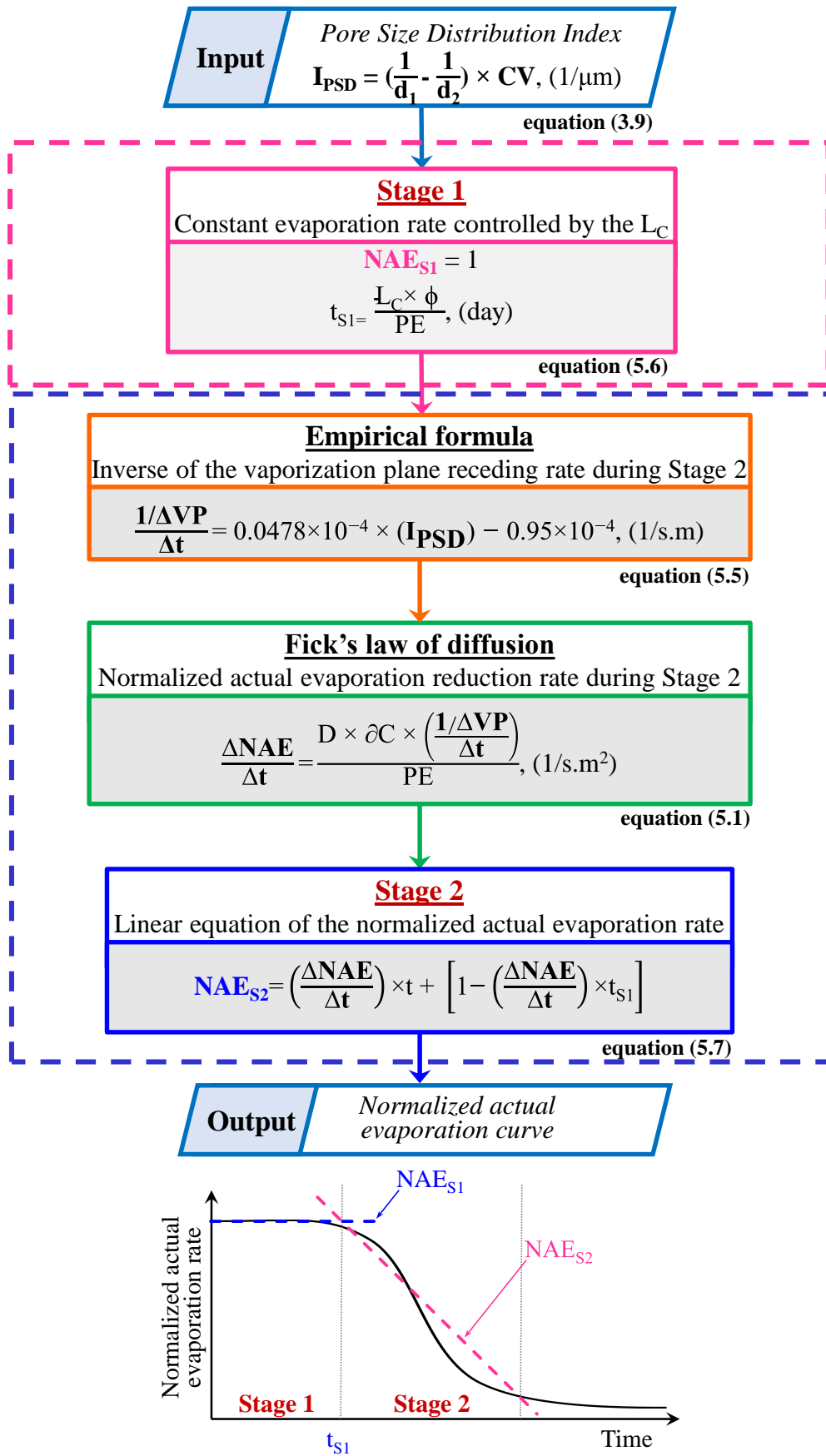


Figure 5.8: Pore-scale-based estimation model of the actual evaporation.
 [Flowchart]

For all the tested profiles, the normalized actual evaporation reduction rate during Stage 2 ($\Delta\text{NAE}/\Delta t$) was determined from equation 5.1. The estimated values were compared with the experimental slopes found in Figure 3.9 to confirm the validity of the proposed method. The experimental and estimated values confirmed that soil profiles with a broader pore size distribution, characterized by bigger I_{PSD} , delineate gentler slopes of their evaporation reduction rate. However, despite the values of the I_{PSD} , it was observed that the average ratio between the experimental and estimated $\Delta\text{NAE}/\Delta t$ values was almost equal to 0.1 ± 0.05 . This discrepancy might be attributed to many factors, including the simplicity of the determination method, the estimation of the air-dry layer's diffusion coefficient, and using the vapor concentration at 5 cm above the soil surface to determine the driving concentration gradient rather than its value directly at the soil surface. Based on that, the estimated $\Delta\text{NAE}/\Delta t$ values were multiplied by the observed average ratio between the experimental and estimated values ($R_{\text{E/E}}$), and the results were delineated as shown in Figure 5.9. It can be observed that most of the points are scattered around the 1:1 line, except for the K-2 soil profile. The slight variation in the K-2 profile is believed to be associated with the difference in determining the Soil Water Characteristics Curve (SWCC) used to deduce the I_{PSD} . In the case of the K-2 soil profile, the SWCC was estimated from the particle size distribution using a statistical model rather than actual measurements in the laboratory (Chapter 3, section 3.2).

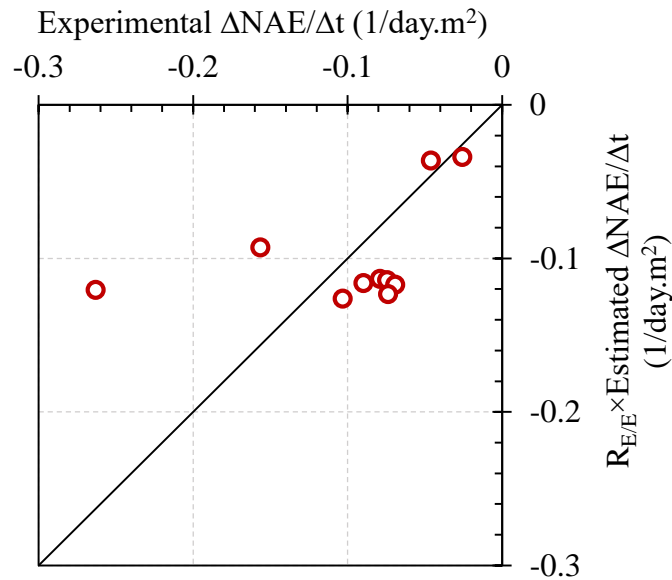


Figure 5.9: Comparison between the estimated and experimental $\Delta\text{NAE}/\Delta t$ of Stage 2.

Accordingly, to evaluate the reliability of the proposed estimation method of the $\Delta\text{NAE}/\Delta t$, the Mean Squared Error (MSE) and the Root Mean Squared Error (RMSE) were performed between the measured, $(\Delta\text{NAE}/\Delta t)_m$ and estimated $(\Delta\text{NAE}/\Delta t)_e$, values as follows:

$$\text{MSE} = \frac{1}{n} \sum_{i=1}^n \left(\left(\frac{\Delta\text{NAE}}{\Delta t} \right)_{m_i} - \left(\frac{\Delta\text{NAE}}{\Delta t} \right)_{e_i} \right)^2 \quad (5.8)$$

$$\text{RMSE} = \sqrt{\frac{1}{n} \sum_{i=1}^n \left(\left(\frac{\Delta\text{NAE}}{\Delta t} \right)_{m_i} - \left(\frac{\Delta\text{NAE}}{\Delta t} \right)_{e_i} \right)^2} \quad (5.9)$$

where n is the number of the tested soil profiles. The proposed estimation model resulted in a deficient error with an MSE of 0.0033 and an RMSE of 0.0577, including the K-2 soil profile. The resulting error proves the accuracy of the proposed semi-empirical model in estimating the normalized evaporation reduction rate during Stage 2 based exclusively on the water supply capabilities and the pore structure of the soil profile.

Consequently, the modified $\Delta\text{NAE}/\Delta t$ values of the tested soil profiles were used, and the steps delineated in the flowchart of Figure 5.8 were followed to determine the normalized actual evaporation curve of the tested soil profiles. The estimated bilinear curves were compared to the experimental results, as shown in Figure 5.10, for the K-7, K-6, K-5, and K-4 compacted at 80% relative density soil profiles. The scatter in the figures delineates the experimental normalized actual evaporation curve, while the black solid line delineates the estimated bilinear model. The results show that the estimated normalized evaporation rate during Stage 2 agrees well with the experimental results. For all the tested profiles, the slope of Stage 2 tends to be close to the experimental results, whether it covers the whole stage as in K-4 or part of the stage as in K-7.

The sudden drop and the inflection point at the actual evaporation rate define the transition between Stages 1 and 2. However, it was observed from the results that the estimated linear evaporation reduction slope does not pass through the experimentally defined beginning and end of Stage 2. For instance, the estimated linear reduction agrees well with the K-7 soil profile, while the duration of Stage 1 is underestimated in the K-5 and K-4 profiles and overestimated in the K-6 profile. This behavior might be related to some limitations in estimating Stage 1 (t_{S1}) and its definition based on the evaporation curve. In the newly proposed model, to determine t_{S1} , it was assumed that the evaporation during Stage 1 occurs under the potential atmospheric demand. Additionally, it was considered that all the pores within the film region of a depth equal to the L_C are emptied at the beginning of Stage 2. However, it was

confirmed by tracing the unsaturated layer during the transition between Stages 1 and 2 in Chapter 4 that the smaller pores persist within the film region during Stage 2, in addition to the isolated liquid clusters present in the unsaturated layer that progressively empty with time. Moreover, it was concluded in Chapter 3 that the inflection points of the evaporation curve indicate a change in the evaporation rate but do not necessarily represent the change in the transport mechanism between stages, which was concluded after observing a discrepancy between the time required to reach the L_C and the duration of Stage 1 deduced directly from the actual evaporation curve.

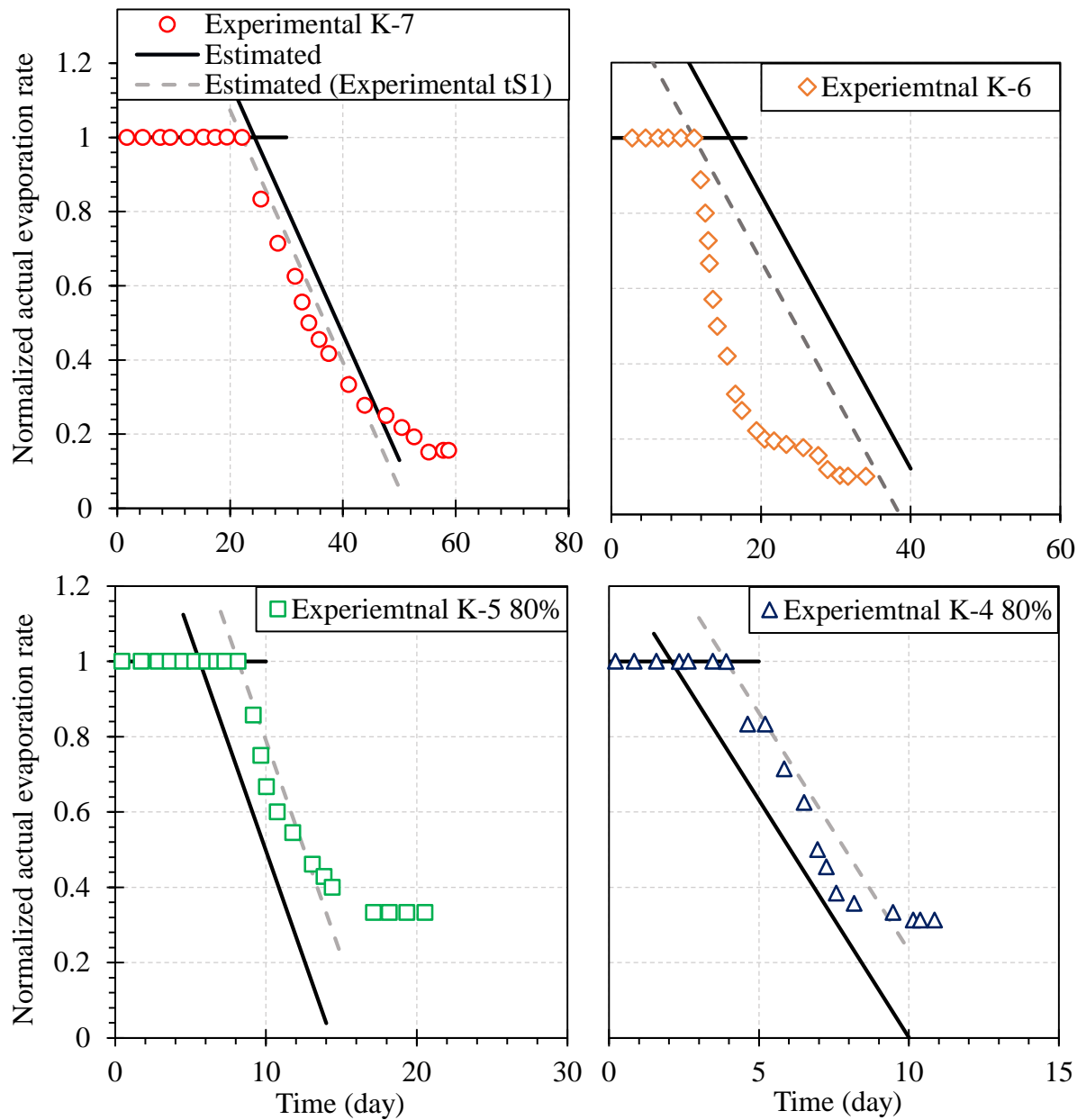


Figure 5.10: Reliability of the pore-scale-based actual evaporation estimation model.

Consequently, to double confirm that the limitation is related to the determination of the t_{s1} , the modified estimated slope ($\Delta NAE/\Delta t$) and the t_{s1} determined directly from the experimental results were plotted with the gray dashed lines, shown in Figure 5.10. It was observed that the linear curve during Stage 2 coincides to a high degree with the experimental data. Therefore, it must be concluded that estimating the $\Delta NAE/\Delta t$ from the empirical I_{PSD} formula is a reliable method for predicting the normalized actual evaporation reduction rate. At the same time, further considerations are required to improve the definition and estimation of Stage 1 duration.

Notwithstanding the substantial agreement of the results, it does not diminish the importance of considering the curve-shaped reduction in the evaporation rate, which can be clearly seen in the K-6 soil profile. Further contemplations to consider the sigmoidal shape of the evaporation curve are highly required for a more accurate prediction of the evaporation rate for sandy soils. For a more generalized model, further considerations must be extended to various soil types, including natural and cohesive soils.

5.5 Summary and Conclusions

This chapter proposed a novel actual evaporation rate estimation model. The pore-scale-based estimation model is simple and comprehensive. It considers the evaporation process's internal and external influencing factors: the atmospheric demand and water supply capabilities. Moreover, it solves the water transport micro-mechanisms dominant during Stages 1 and 2. The semi-empirical model utilizes Fick's law to determine the vapor diffusion flux through the air-dry layer by assuming that the evaporation occurs from a receding vaporization plane. Simultaneously, the receding rate of the vaporization plane is a function of the pore structure, presented by the Pore Size Distribution Index (I_{PSD}), where an empirical formula was derived for homogenous sandy soil profiles under unified atmospheric conditions to predict the receding rate of the vaporization plane.

The newly proposed model was compared with the experimental results and proved reliable in predicting the normalized actual evaporation rate during the dominant Stage 2 of evaporation. Notwithstanding its robustness, the pore-scale-based estimation model requires further considerations and improvements for a more accurate prediction of the evaporation process and a more generalized form to cover natural and cohesive soils.

Finally, it must be concluded that utilizing the pore-scale-based estimation model to accurately predict the evaporation rates requires simple soil properties that can be determined

in any geotechnical laboratory and ambient atmospheric conditions usually recorded at weather stations. The simplicity of the model and its originality in considering the demand and supply distinguish it from other existing models. Therefore, it is believed to be fundamental for many geotechnical engineering applications and common practice in many fields ranging from hydrological and geo-environmental to food science and agricultural engineering.

References

- Campbell, G.S., 1985. Soil Physics with Basic Transport Models for Soil-Plant Systems, Elsevier.*
- Campbell, G.S., 1977. An Introduction to Environmental Biophysics. Springer Verlag, New York.*
- Lehmann, P., Assouline, S., Or, D., 2008. Characteristic lengths affecting evaporative drying of porous media. Phys Rev E Stat Nonlin Soft Matter Phys 77, 1–16. <https://doi.org/10.1103/PhysRevE.77.056309>*
- Scherer, G.W., 1990. Theory of Drying. Journal of the American Ceramic Society 73, 3–14. <https://doi.org/10.1111/j.1151-2916.1990.tb05082.x>*
- Shahraeeni, E., Lehmann, P., Or, D., 2012. Coupling of evaporative fluxes from drying porous surfaces with air boundary layer: Characteristics of evaporation from discrete pores. Water Resour Res 48, 1–15. <https://doi.org/10.1029/2012WR011857>*
- Wilson, G.W., Fredlund, D.G., Barbour, S.L., 1994. Coupled soil-atmosphere modelling for soil evaporation. Canadian Geotechnical Journal 31, 151–161. <https://doi.org/10.1139/t94-021>*

6

CHAPTER

Optimization of a Soil Cover Design to Suppress Evaporation

6.1 Introduction

Suppressing water evaporation from soil profiles and increasing water storage are significant concerns in drylands worldwide. Many geotechnical, geo-environmental, agricultural, and hydrological engineering applications require altering water loss from soil profiles. Maintaining the soil's moisture status at a favorable stage enhances biodiversity, crop growth, and soil productivity. Moreover, it widely contributes to the water management sector. In arid and semi-arid regions with high evaporation rates and hot, dry weather conditions, soil storage efficiency becomes low. Therefore, great attention and improvements are necessary for curtaining water evaporation and increasing retention in soil profiles. Optimizing innovative and environmental-friendly solutions is highly required to prevent soil degradation and combat desertification. Simplified, effective, and economical solutions are essential to ensure applicability in developing countries where 90% of drylands are formed.

The literature adopted many methods to suppress evaporation from soils, as discussed in Chapter 2 (section 2.4). Some considered controlling the energy supply to the soil surface to reduce the water loss during Stage 1. Others considered disturbing the driving forces of water's upward movement or decreasing the conductivity of the soil profile to manage water loss during later stages. Many researchers have recently investigated and analyzed the impact of utilizing natural soil covers to suppress evaporation from soil profiles (Huang et al., 2013; Yanful et al., 2003; Zhou et al., 2008). Alowaisy and Yasufuku (2018) and Assouline et al. (2014) concluded that adding a thin soil layer that has different properties from the underlying natural ground is a simple means of controlling evaporation losses. Willis (1960) studied the evaporation from layered soils with the presence of a water table and concluded that a coarse soil layer below a finer layer has a relatively small effect on water loss. However, Alowaisy and Yasufuku (2018) proved that adding a coarser material reduces the evaporation losses due to the preferential invasion of the larger pores by the gas phase within the coarse material and therefore maintaining high saturation at the natural ground. Kirkham et al. (1967) investigated the effect of the surface sand mulch and the subsurface sand layer in preventing evaporation, where the surface mulch was more effective than the subsurface layer. Unger (1971) placed surface and subsurface gravel layers at different depths to study their influence on evaporation. It was found that the evaporation from soils with gravel at the surface or 5 cm below the surface was slower than from a homogeneous profile. On the other hand, the evaporation was slower from a homogeneous profile compared to the profiles with a gravel layer at 15 and 25 cm below the surface. Benoit and Kirkham (1963) and Corey and Kemper (1968) concluded that gravel mulches effectively suppress evaporation from the natural soil profiles.

Notwithstanding the efforts in utilizing and studying the efficiency of soil covers in suppressing evaporation from bare soil profiles, a comprehensive design criterion of a natural soil cover is still lacking in the literature. Most existing studies focus on utilizing soil covers without considering the role of the relative properties between the cover and the original ground. Moreover, less attention is given to their relation with the textural contrast boundary and efficiency in reducing water losses and evaporation rates. Therefore, the following chapter proposes a robust design concept for a natural soil cover that optimizes water conservation and reduces evaporation from soil profiles. It comprises two criteria: relative retention properties and cover thickness. The criteria are developed and proposed based on the micro-mechanisms and dynamics occurring during evaporation between the soil cover and the natural ground. Consequently, the efficiency of the proposed design concept is confirmed. Besides, new insights related to evaporation from double-layered soil profiles are discussed.

6.2 Evaporation from double-layered soil profiles

Applying soil covers on natural grounds follows the evaporation dynamics of a double-layered soil profile. However, optimizing such covers requires a comprehensive understanding of the homogeneous soil profiles. It enables extending the knowledge to double-layered profiles while considering the influence of the textural contrast boundary, defined as the interface between the two layers that differ in texture. The following section reviews a summary of the recent findings related to the behavior of water evaporation from double-layered soil profiles. Additionally, it presents new insights and findings of the current research that must be considered when extending to a double-layered soil profile.

According to the literature, the evaporation curve from a double-layered soil profile is similar to the actual evaporation curve of a homogeneous soil profile, Figure 2.4. The process is divided into three stages that differ in their actual evaporation rates. However, the textural contrast boundary between the two layers leads to a difference in the unsaturated layer formation and dynamics, resulting in more complicated micro-mechanisms within the composite soil profile during drying. The conceptual definition of the transition between Stages 1 and 2, delineated in Figure 2.6 (Lehmann et al., 2008), was extended to facilitate the prediction of the end of Stage 1 for double and multi-layered soil profiles (Shokri et al., 2010). The composite characteristic length (L_{Comp}) of double-layered soil profiles can be determined using the algorithm shown in Figure 2.9. The L_{Comp} is determined from the intrinsic characteristic lengths of each layer (L_C), layering sequence, and layers thicknesses and reflects the weakest hydraulic link between the drying front and the soil surface. Consequently, Shokri et al. (2010) concluded that the layering sequence and each layer thickness significantly influence the evaporation from layered soil profiles.

The effect of the layering sequence in a two-layer porous media was also investigated by Pillai et al. (2009) using the pore network model. The simulation results showed that the layers' sequence significantly affects the liquid phase distribution patterns and the evaporation rates. It was reported that preferential water loss occurs for a soil layer with small pores overlying a soil layer with large pores. On the other hand, for a reversed sequence, air invades the underlying fine soil layer after invading the top coarse soil layer causing it to dry. Shokri et al. (2010) further investigated the dynamics of a fine-overlying-coarse soil profile utilizing neutron radiography. It was demonstrated that once the drying front recedes into the coarse layer, a rapid and disproportionate water displacement occurs in the coarse layer, which starts ejecting water to the upper fine layer. Consequently, the capillary pressure jump at the fine-

coarse interface induces a transient flow to dissipate and relax the pressure jump. Therefore, the less negative capillary pressure within the coarse layer forms a preferential drying front within the underlying coarse layer that continuously supplies water to the upper fine layer, keeping it saturated. This behavior, called the pumping phenomenon (Shokri et al., 2010), indicates that water distribution and its dynamics through layered soil profiles are significantly different and more complicated than homogeneous soil profiles.

Alowaisy (2019) proposed optimized adaptations for enhancing water conservation capabilities in double-layered soil profiles based on experimental testing. Generally, reducing the duration of evaporation stages results in decreasing water losses and increasing water conservation in soil profiles. Therefore, it was found that utilizing a topsoil layer with a relatively small L_{Comp} accelerates the disruption of the hydraulic connection between the drying front and the surface during Stage 1, thus reducing its duration. Moreover, it was found that shallower textural contrast boundaries significantly decrease the thickness and severity of the unsaturated zone, thus reducing the duration of Stage 2. Finally, it was concluded that regardless of the atmospheric conditions and the layering sequence, coarse-overlying-fine or fine-overlying-coarse soil profiles, the shallower the textural contrast boundary results in higher water conservation capabilities during Stages 1 and 2 for double-layered soil profiles.

The current research postulated many new insights regarding evaporation from homogenous soil profiles. These findings, with the previously discussed literature, serve as a fundamental base when identifying the points of consideration to reduce water losses from double-layered soil profiles. Firstly, it was confirmed that Stage 2 of evaporation dominates in regions with severely dry conditions. Moreover, its diffusion flux was found to be highly dependent on the vaporization plane depth and its receding rate with time. It was also found that the vaporization plane dynamics are a function of the soil pore structure, which was parameterized based on the soil water retention properties. The strong correlation and dependency between the pore structure, water retention properties, and evaporation dynamics propose that evaporation can be suppressed by altering the water retention properties in double-layered soil profiles. Therefore, in the current study, the relative soil properties and the relative thickness are considered.

6.3 Soil Cover Concept and Design Criteria

Despite the complicated evaporation mechanics and water distribution through double-layered soil profiles, proposing a soil cover design criterion requires a direct and simplified way of

tackling the problem. Figure 6.1 delineates a schematic diagram of the practical application and the physical characterization of adopting a soil cover to suppress water evaporation.

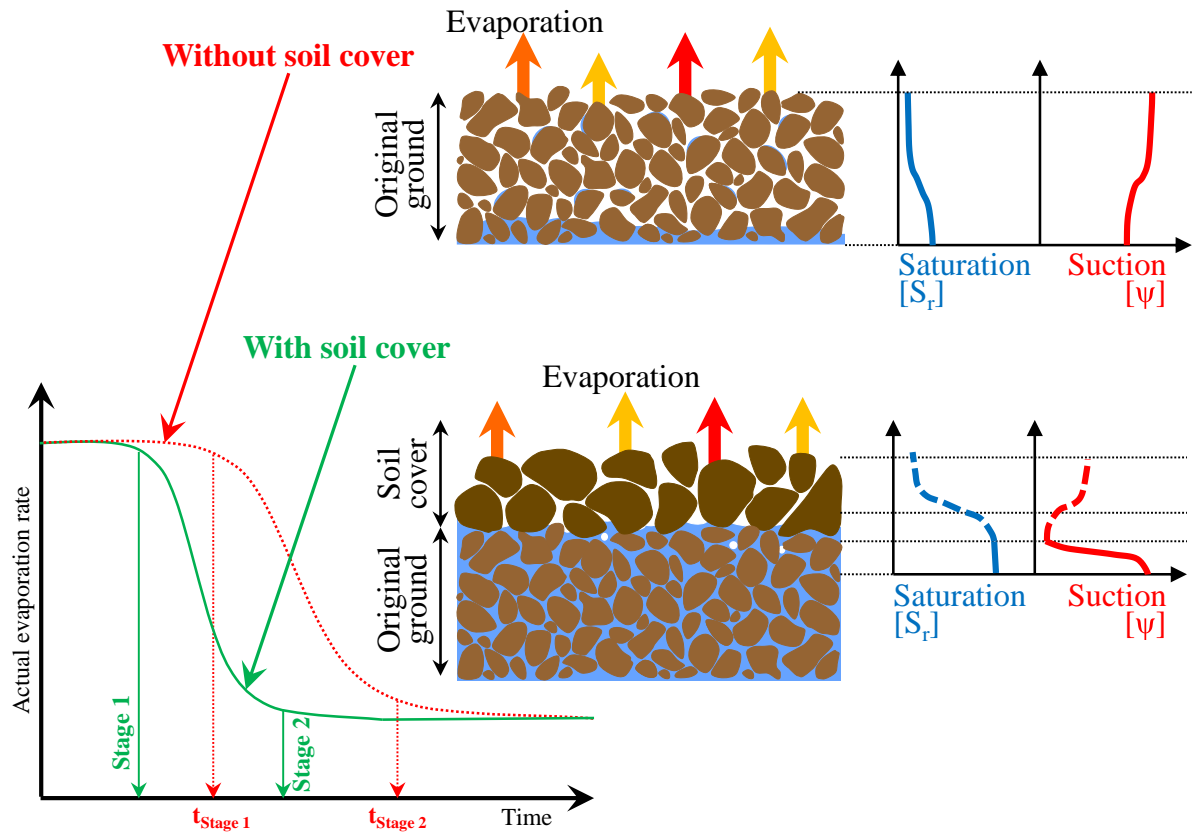


Figure 6.1: Principle of soil covers and their practical application.

The principle of utilizing a soil cover in suppressing evaporation was confirmed experimentally through drying soil column tests. Two tests were conducted under relatively low potential evaporation rates for a soil profile with and without applying a soil cover. The profile without the soil cover is the homogeneous K-6 soil profile tested in Chapter 4, while the double-layered soil profile was conducted utilizing the K-6 sandy soil as the original ground and the K-4 sandy soil as the soil cover. The physical properties used to compact the two soils are presented in Table 4.1. The cumulative evaporated water curves of the two tested soil profiles are delineated in Figure 6.2. The results show the amount of water loss within the first six days of testing. It was observed that the uncovered soil profile tends to lose more water from the beginning of testing compared to the covered soil profile. Moreover, after six days of testing, the profile without a soil cover lost more than double the amount of water from the covered soil profile. This result confirms that adopting a soil cover is a promising practice for suppressing evaporation and water loss from soil profiles. However, investigating and understanding the

science and mechanisms behind such behavior is essential for systematically applying and generalizing the methodology in practice.

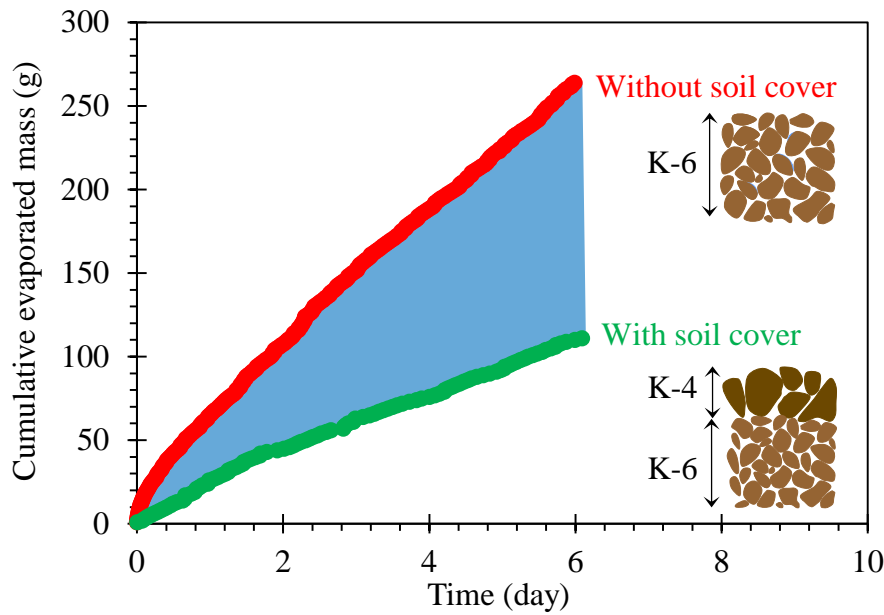


Figure 6.2: Influence of the soil cover on cumulative water losses.

During evaporation from homogenous soil profiles, the top layer dries, causing an increase in its suction pressure. The difference in the suction pressure between the top and bottom layers results in an upward head gradient driving water to the surface. Therefore, redirecting the head gradient downward disrupts the water supply, thus reducing water evaporation. Applying such a concept in the field requires using a suitable soil material for the soil cover relative to the original soil ground. Moreover, based on the literature, approaching the L_{Comp} to the textural contrast boundary between the cover and the ground might result in complicated mechanisms causing more water to evaporate from the original ground. Avoiding such cases requires choosing a suitable material and thickness for the applied soil cover. Consequently, the optimized soil cover design concept proposes two main criteria:

1. C1: relative retention properties; to control the orientation of the head gradient based on the soil retention properties of the cover and the original ground.
2. C2: relative cover thickness; to avoid the arrival of the L_{Comp} to the textural contrast boundary by adjusting the thickness of the soil cover.

By adopting C1 and C2 criteria, a new design concept for a natural soil cover to suppress water evaporation is proposed. The following section presents the design concept and

its efficiency in increasing water retention in soil profiles. Moreover, the determination of the criteria and their utilization are explained thoroughly.

6.3.1 Relative retention properties

Figure 6.3 delineates the interpretation of the relative retention properties, or the C1 criterion. The curves present illustrative Soil Water Characteristic Curves (SWCCs) of the original ground and two soil covers, Cover A and B. Cover A represents a soil material with a retention potential higher than the original ground. In contrast, Cover B represents a soil material with a retention potential lower than the original ground. The Air-Entry Value (AEV) was designated to represent the water retention properties of the soil cover material and the original ground. The AEV is the suction value at which the meniscus of larger pores at the soil surface break due to weaker capillary forces holding the water while the gas phase starts invading the soil profile. Consequently, the C1 criterion corresponding to the relative retention properties is determined as follows:

$$C1 = \frac{AEV_{Cover}}{AEV_{Ground}} \quad (6.1)$$

where AEV_{Cover} is the air-entry value of the cover's soil material, while $AEV_{original}$ is the air-entry value of the original soil ground. It must be noted that the threshold value of the C1 criteria is 1. When $C1 < 1$, the suction head of the soil cover is relatively lower than that of the original ground, which triggers a downward head gradient towards the original ground. Thus, the supply

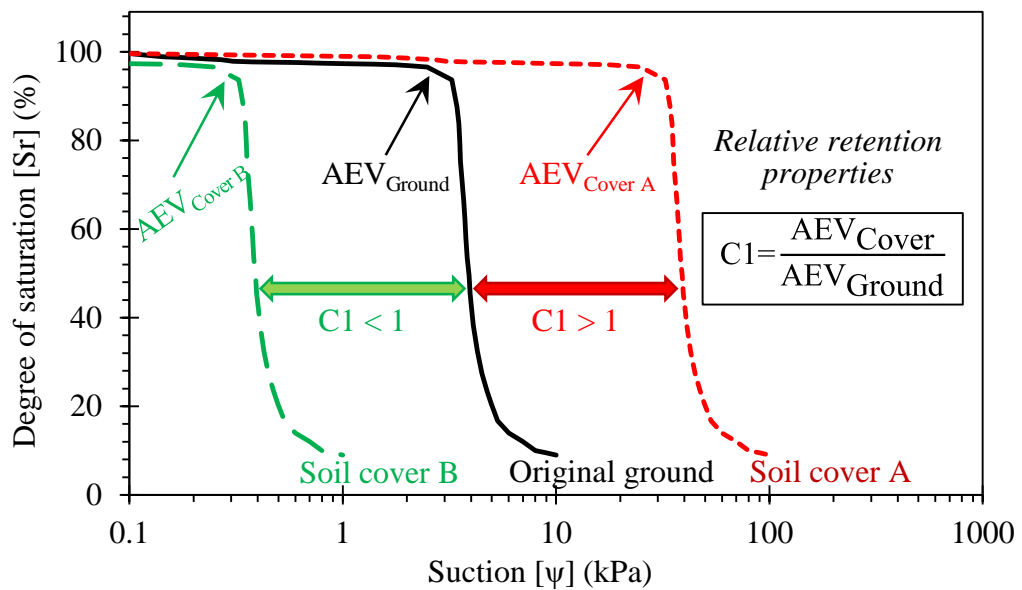


Figure 6.3: Relative retention properties, C1 criterion of the soil cover design.

is disrupted, and water evaporation is limited. On the contrary, when $C1 > 1$, the suction head of the soil cover is relatively higher than the original ground, which augments the upward head gradient causing more water loss to evaporation.

Based on that, it must be concluded that suppressing water evaporation requires predicting the orientation of the head gradient between the applied soil cover and the original soil ground, thus regulating the water supply. This can be achieved by altering the relative retention properties of the soil cover and the original ground by keeping the $C1$ value smaller than 1.

6.3.2 Relative cover thickness

In a double-layered soil profile, the pumping phenomena might occur once the drying front during Stage 1 reaches the textural contrast boundary between the cover and the original ground (Shokri et al., 2010). In such a case, a rapid and disproportionate water displacement occurs from the original soil ground to the cover, causing more water loss from the original ground. Consequently, to avoid the occurrence of the pumping phenomenon, the $C2$ criterion corresponding to the relative cover thickness is proposed as follows:

$$C2 = \frac{L_{Comp}}{Z_{cover}} \quad (6.2)$$

where L_{Comp} is the composite characteristic length of the double-layered profile composed of the soil cover and the original ground, while Z_{cover} is the thickness of the soil cover. Figure 6.4 shows a schematic diagram to interpret the influence of $C2$ on the pumping phenomenon and evaporation process. When $C2 < 1$, the drying front recedes continuously within the applied cover layer at a depth equal to L_{Comp} . Consequently, the evaporation continues from the soil cover without the air phase invading the original ground. On the contrary, when $C2 > 1$, the drying front during Stage 1 recedes below the textural contrast boundary causing preferential capillary water pumping from the original ground to the cover, which increases water losses by evaporation.

Based on that, it must be concluded that suppressing water evaporation requires pinning the drying front within the soil cover to avoid preferential pumping and water losses from the original soil ground. Consequently, this can be achieved by altering the relative cover thickness to the textural contrast boundary by keeping the $C2$ value smaller than 1.

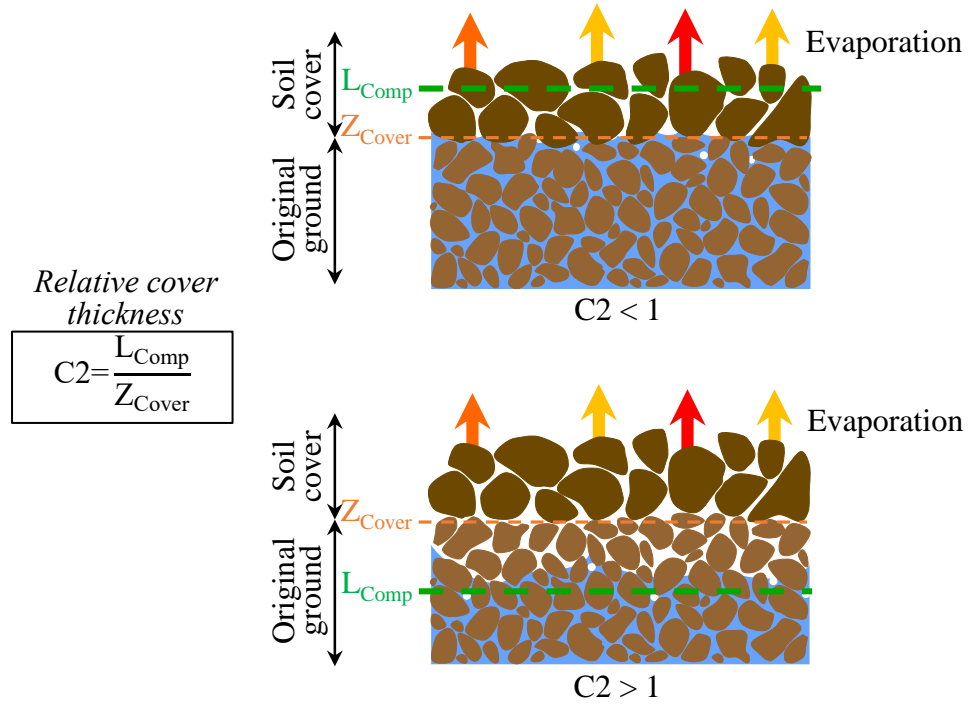


Figure 6.4: Relative cover thickness, C2 criterion of the soil cover design.

6.3.3 Soil cover design and its employment

The two proposed design criteria, C1 and C2, represent the relative properties between the applied soil cover and the original soil ground. These simplified properties can be systematically and efficiently determined, requiring simple information related to the properties of the cover and original ground soil material. The AEV and L_C of the individual layer are deduced from the SWCC of each soil material. Consequently, once the L_{Comp} is determined following Figure 2.9, and the thickness of the soil cover is chosen, the values of C1 and C2 can be found based on equations 6.1 and 6.2.

All the required properties for application are deduced from the SWCC, and as was discussed in Chapter 3, the SWCC direct determination tools have been progressing rapidly in recent years (Alowaisy et al., 2020). Moreover, in the case of limited laboratory equipment, the SWCC can be indirectly estimated using empirical or statistical approaches that require simple soil properties such as porosity and particle size distribution (Sako and Kitamura, 2006). Therefore, such a simple design concept of soil covers makes it a direct and comprehensive tool accessible for engineers to utilize in different applications, especially in combating desertification and water management.

Figure 6.5 illustrates the soil cover design concept, including the C1 and C2 proposed criteria. The threshold values of both criteria, being 1, resulting in four different zones that differ in water retention and storage capabilities. By definition, “Zone I” soil profiles store the highest amount of water, especially within the original soil ground. The storage capabilities deteriorate for the profiles with larger C1 and C2 values. “Zone III” soil profiles sufficiently supply water from the ground to the soil cover due to the formed upward head gradient. Similarly, “Zone II” soil profiles might experience water pumping phenomena, where sufficient capillary water flow supplies water from the original ground to the soil cover during Stage 1. Consequently, “Zone IV” soil profiles are expected to have the highest water losses due to experiencing both the upward gradient and pumping phenomena. Therefore, experimental testing was conducted on double-layered soil profiles to confirm the efficiency of the proposed soil cover design concept, as discussed in the following sections of this chapter.

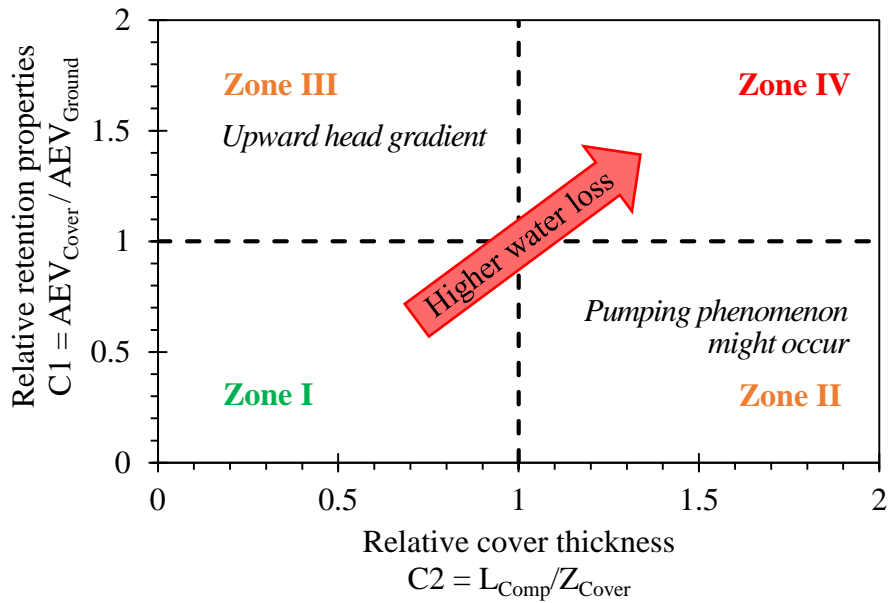


Figure 6.5: The proposed soil cover design concept.

6.4 Materials and Soil Profiles Configurations

As thoroughly discussed in Chapter 3 (section 3.2), sandy soils were adopted for testing in the current research. Besides the silica sand used in studying the evaporation dynamics of homogenous soil profiles, Toyoura sand was used in the following testing scheme of the double-layered profiles. Both soil types resist volume change associated with the moisture content variation. Thus, the shrinkage and cracking effects are assumed to be neglected. Four different

soil textures of silica sand were used, K-7, K-6, K4, K-3, and K-2. Figures 6.6 and 6.7 delineates the particle size distribution curves and the SWCCs of the utilized soil samples, respectively. In order to investigate the influence of the relative soil properties between the soil cover and the original ground on the evaporation process, two patterns of double-layered profiles were tested, fine-overlying-coarse and coarse-overlying-fine soil profiles. Consequently, the Toyoura sand, K-7, and K-6 silica sand were considered fine soil samples (F), while K4, K-3, and K-2 silica sand were considered coarse soil samples (C).

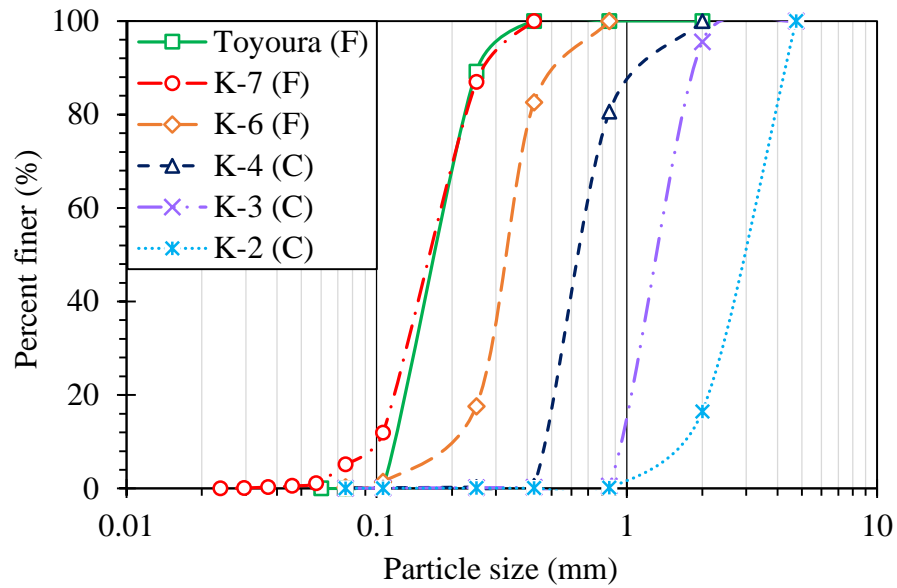


Figure 6.6: Particle size distribution curves.

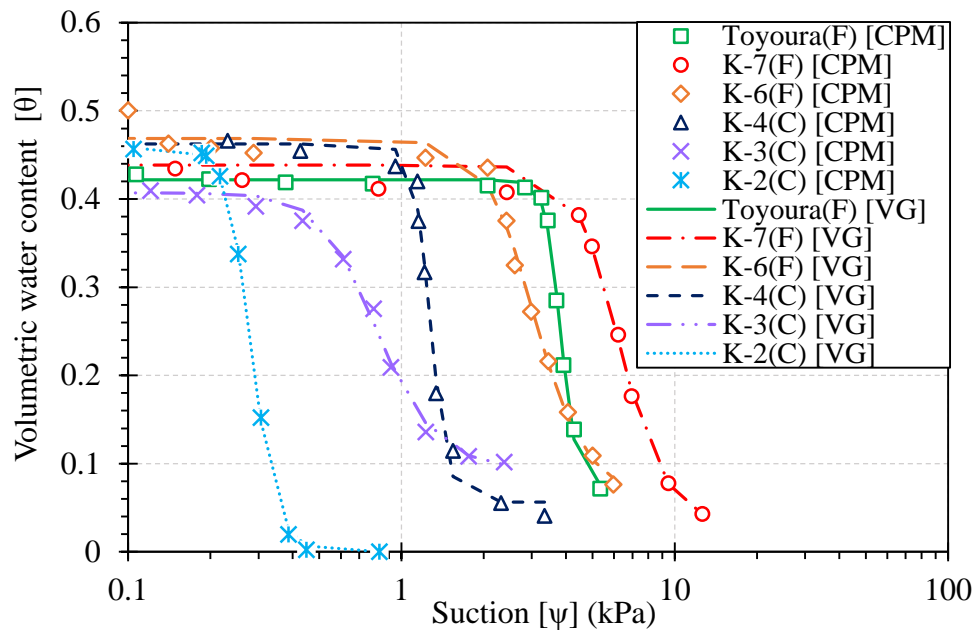


Figure 6.7: Drying soil water characteristic curves.

In the present study, the layers' thicknesses were fixed, while the cover texture was varied to investigate and elaborate on the influence of the relative retention properties and the relative cover thickness. Consequently, six double-layered soil profiles were tested, as delineated in Table 6.1. The original ground was 35 cm thick, topped up with a 15 cm thick soil cover designating the depth of the textural contrast boundary from the soil surface. The tested soil profiles' physical and hydrological properties, the determined L_{Comp} , C1, and C2 criteria, and the zone to which each profile belongs are summarized in Table 6.1 and Figure 6.8.

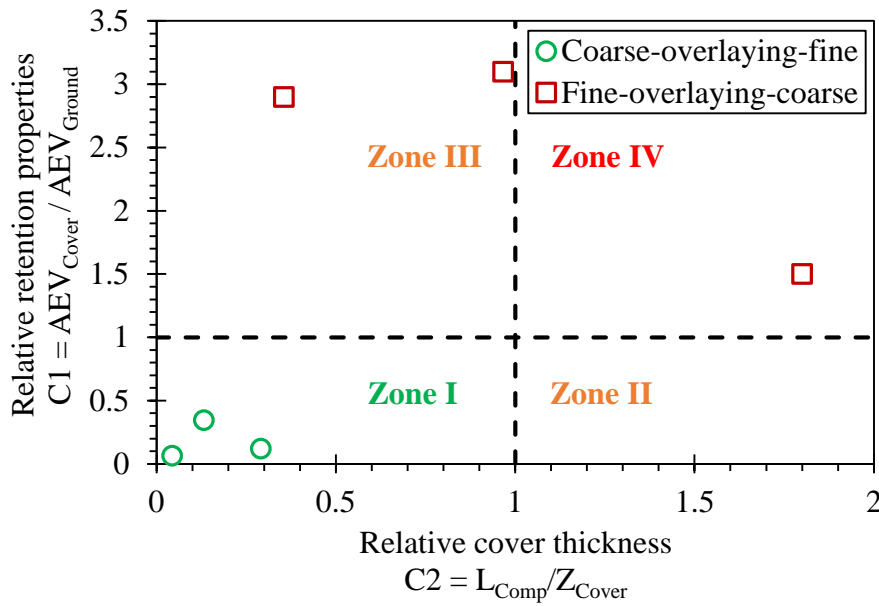


Figure 6.8: Soil cover design concept and the tested double-layered soil profiles.

6.5 Methodology and Experimental Considerations

Drying soil column tests were conducted for double-layered soil profiles to validate the efficiency of the proposed soil cover design concept. The following section presents the utilized experimental setup, soil profile preparation technique, and testing conditions.

6.5.1 Experimental setup

As in the previous chapters, drying column tests were conducted to study the evaporation from double-layered soil profiles. A simple experimental setup was developed to consider repeatability, reliability, and accuracy in determining evaporation and water

redistribution through soil profiles. Figure 6.9 delineates the experimental setup, and the adjoining table explains the deployed instrumentations.

Each group, fine-overlying-coarse, and coarse-overlying-fine soil profiles were tested individually under similar conditions. However, the atmospheric demand varied between the two groups. Consequently, the potential evaporation rate of each group was measured using an evaporation pan placed adjacent to the soil columns and subjected to the same testing conditions. A 250-watt heater lamp and a fan of 1.7 m/s wind speed, were installed above each column to accelerate evaporation. Moreover, a thermo-hygrometer was installed 15 cm above the surfaces to continuously record the temperature and relative humidity within the testing zone.

Table 6.1: Double-layered soil profile's physical and hydrological properties.

Group			Fine-overlying-Coarse			Coarse-overlying-Fine		
Profile name			F-I	F-II	F-III	C-I	C-II	C-III
Soil cover	Soil material		Toyoura	K-7	K-6	K-4	K-3	K-2
	Specific gravity	G _s	2.65	2.65	2.64	2.65	2.63	2.62
	Effective size	D ₁₀ (mm)	0.12	0.10	0.20	0.47	0.96	1.72
	Dry density	ρ _d (g/cm ³)	1.49	1.48	1.44	1.48	1.47	1.40
	Void ratio	e	0.75	0.75	0.79	0.75	0.75	0.84
	Cover thickness	Z _{Cover} (cm)	15	15	15	15	15	15
	Characteristic length	L _C (cm)	5.31	26.99	14.49	1.97	4.35	0.64
Natural soil ground	Soil material		K-4	K-4	K-4	K-7	K-7	K-7
	Specific gravity	G _s	2.65	2.65	2.65	2.65	2.65	2.65
	Effective size	D ₁₀ (mm)	0.47	0.47	0.47	0.10	0.10	0.10
	Dry density	ρ _d (g/cm ³)	1.48	1.48	1.48	1.48	1.48	1.48
	Void ratio	e	0.75	0.75	0.75	0.75	0.75	0.75
	Characteristics length	L _C (cm)	1.97	1.97	1.97	26.99	26.99	26.99
Cover design criteria	Composite characteristic length	L _{Comp} (cm)	5.31	16.97	14.49	1.97	4.35	0.64
	Relative retention properties	C1	3.10	2.90	1.50	0.34	0.12	0.06
	Relative cover thickness	C2	0.35	1.80	0.97	0.13	0.29	0.04
	Proposed soil cover design's zone		III	IV	III	I	I	I

No.	Component	Functions and remarks
1	Soil column	Transparent acrylic cylindrical column (10.4 cm diameter, 50 cm height), includes the tested double-layered soil profiles.
2	Column's base	Acrylic base consists of a valve and porous stone disk to uniformly distribute the water during saturation.
3	Valve	Function as a water inlet for the up-flow saturation.
4	Digital balance	Continuously measures the change in the soil column's mass (31 kg capacity and ± 1 g resolution).
5	EC-5 sensors	Moisture sensors capacitance, indirectly measure the water content of the soil profile.
6	Weighing data logger	Continuously records data from the digital balance, while the data is retrieved directly from a computer.
7	Moisture sensors logger	Continuously records data from EC-5 moisture sensors, while the data is saved directly through a computer application.
8	Heater lamp	Increases the temperature of the ambient air at the top of the soil surface to accelerate the evaporation process, 250-watt heater.
9	Fan	Continuously mixes the air above the soil surface to accelerate the evaporation process, with a wind speed of 1.7 m/s.
10	Thermo-hygrometer	Records the temperature and relative humidity within the testing zone.
11	Pan evaporation	Continuously measures the change in the water pan, which was frequently replenished to keep the water surface at the same level as the soil columns' surfaces. Determine the potential evaporation during testing

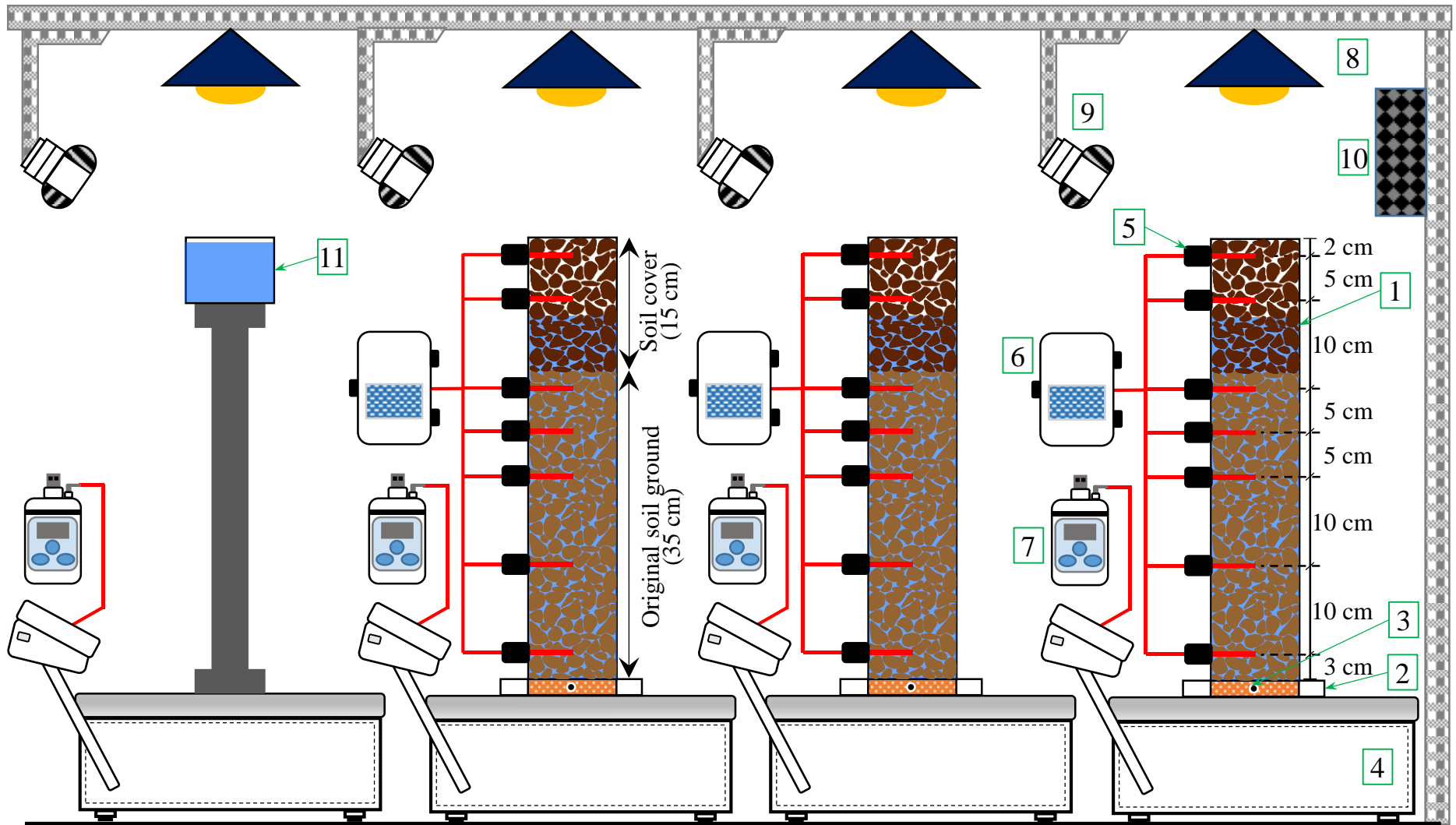


Figure 6.9: Experimental setup of the double-layered drying soil column tests.

A one-dimensional evaporation flow was facilitated at the soil's top surface for the testing columns. A 50 cm height transparent acrylic cylindrical column was selected to adjust with the L_c of the tested profiles and capture the evaporation process. The used columns were 10.4 cm in diameter with a wall thickness of 0.5 cm. A valve was installed at the column's base to function as a water inlet for saturation. The valve was connected directly to a porous stone disk to distribute the water into the soil profile uniformly. The base was appropriately sealed to avoid leakage during preparation and testing.

For data acquisition during drying, the soil columns and the evaporation pan were mounted on a digital balance, 31 kg capacity, and ± 1 g resolution. Each balance was connected to a weighting data logger to determine the water loss and calculate the evaporation rate from each soil profile. The columns were instrumented with EC-5 capacitance or moisture sensors through drilled ports. They were connected to a data logger that recorded the data and indirectly measured the water content through the entire profile during the testing period.

6.5.2 Soil columns preparation

The preparation technique is almost similar to the one explained in Chapter 3. Therefore, the preparation flow is explained, focusing mainly on the additional or different steps while preparing the double-layered profiles.

Similar to the homogenous soil profiles, the dry packing method was adopted to prepare the double-layered soil profiles. The amount of oven-dry soil required to fill each column was calculated based on the soil's physical properties. A single filter paper layer was placed above the porous stone disk, as illustrated in Figure 6.10. The soils were loaded in 3-6 cm separate layers. Each layer was mechanically compacted under unified compacting pressure until it satisfied the required relative density. A metal pestle and hammer were used for compaction, while hydraulic connectivity was ensured between layers by lightly scarifying the surfaces after compaction. Meanwhile, the EC-5 moisture sensors were installed carefully during soil placement at each designated drilled port, and the ports were then sealed properly using cold silicone sealant to prevent leakage during saturation and testing. The EC-5 moisture sensors measure the soil water content based on the charging time of the capacitor's plates and can be installed within 0.5 cm spaces. Therefore, the EC-5 sensors' positions, shown in Figures 6.9 and 6.10, are concentrated within the soil cover and around the textural contrast boundary to carefully investigate the micro-mechanisms and dynamics occurring at the boundary.

For saturation, the up-flow saturation technique was used to displace the air bubbles in the soil pores. A constant water head was applied to the columns through the inlet valve installed at the base. The water supply was kept until the columns achieved a fully saturated condition through the entire soil profile, which can be roughly checked through the EC-5 sensors' readings. Finally, the water valves were closed, and the water head was removed.

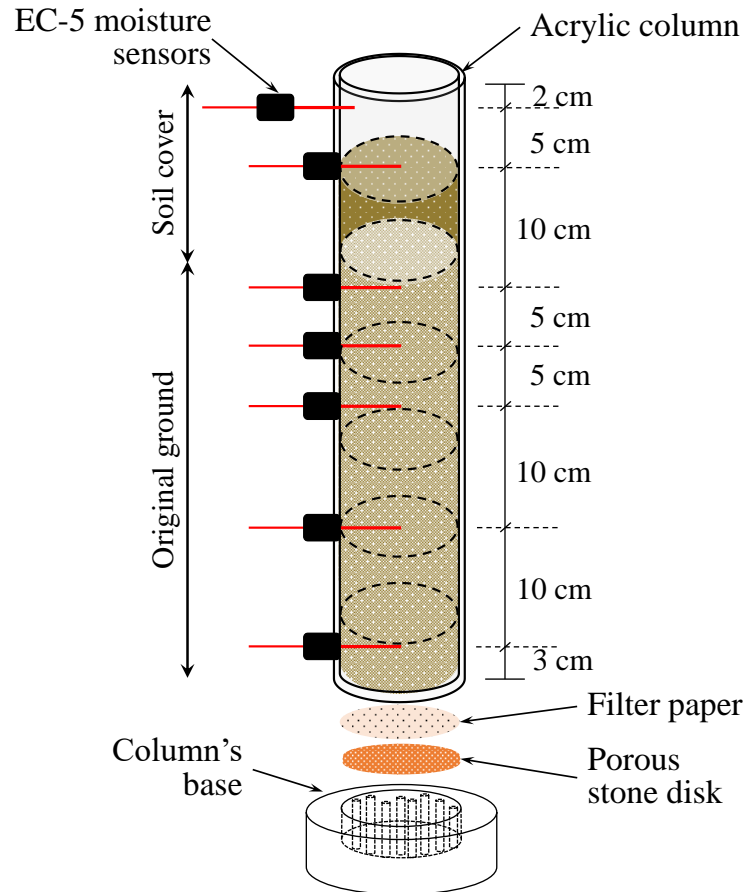


Figure 6.10: Preparation of the double-layered drying soil columns.

6.5.3 Testing procedure and boundary conditions

The six double-layered sandy soil drying column tests were conducted in two individual groups. The columns were initially fully saturated while evaporation was allowed through the top soil surface. The atmospheric potential evaporation was measured using the evaporation pan, frequently replenished to keep the water surface at the same level as the soil columns' surfaces. The average potential evaporation for the fine-overlying-coarse group equals 11.3 mm/day, while for the coarse-overlying-fine group equals 4.7 mm/day. This result was confirmed

experimentally by finding the average actual evaporation rate attained during Stage 1 in the fine-overlying-coarse group equals 11.33 mm/day, while for the coarse-overlying-fine group equals 5.66 mm/day. According to Shahraeeni et al. (2012), the actual evaporation reflects a high evaporation demand during testing (typically > 5 mm/day). The temperature and relative humidity were continuously recorded, while the average was found, as shown in Figure 6.11. Consequently, an average temperature of $24.2 \pm 2.0^\circ\text{C}$ and $19.2 \pm 2.2^\circ\text{C}$ and an average relative humidity of $55.0 \pm 8.6\%$ and $51.0 \pm 7.8\%$ was confirmed 15 cm above the soil surface for the fine-overlying-coarse and coarse-overlying-fine groups, respectively. The atmospheric conditions, amount of water loss from the soil profiles, and the water content across the profiles' depth were recorded at 15-minute intervals during the testing period. Testing was shut down once the actual evaporation rate converged to a low and constant value, announcing the onset of the residual stage, Stage 3.

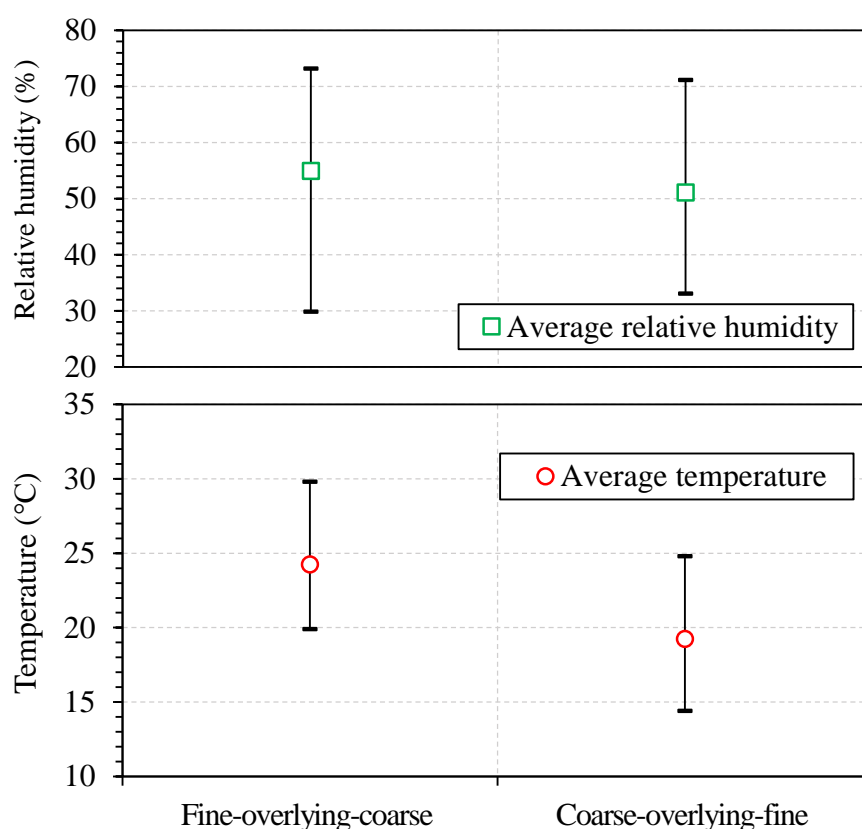


Figure 6.11: Average atmospheric conditions of the double-layered tested groups.

6.6 Validation of the Soil Cover Efficiency

In the following section, the efficiency of the proposed soil cover design concept is confirmed through the results of the tested double-layered soil profiles. The normalized actual evaporation curves, water redistribution profiles, and suction profiles are discussed and compared to investigate the importance of considering the relative retention properties and relative cover thickness on the evaporation process. Moreover, new insights related to evolved micro-mechanisms due to the textural contrast boundary and the composite characteristic length (L_{Comp}) were presented.

6.6.1 Soil cover and actual evaporation stages

The actual evaporation rate during drying was determined experimentally using the data recorded by the digital balance. The Actual Evaporation rate (AE) was determined as the amount of water loss per unit area in a specific time (mm/day). The normalized actual evaporation curves were used to study the evaporation process and determine its stages to better compare the tested profiles. The normalized actual evaporation rate (NAE) was obtained individually for each profile by dividing the actual evaporation rate at any time during drying over the constant actual evaporation rate attained during Stage 1 ($AE_{Stage\ 1}$).

Figure 6.12 (a) and (b) delineate the normalized actual evaporation rates with the elapsed time for the fine-overlying-coarse and coarse-overlying-fine groups, respectively. The actual evaporation rate during Stage 1 for each group is presented in the figures, while the duration and water loss during Stages 1 and 2 are summarized in the adjoining tables. It must be noted that the number of days is rounded to the nearest tenth.

Generally, varying the soil of the cover layer resulted in significant differences in the actual evaporation behavior, which is more pronounced in the fine-overlying-coarse group soil profiles. It can be observed that the duration of Stage 1 for the FII (Zone IV) tends to be the shortest, while during this stage, FI (Zone III) lost the highest amount of water. On the other hand, Stage 2 tends to be the shortest FI (Zone III) profile resulting in the least amount of water loss. These differences were not apparent in the coarse-overlying-fine group, where during Stages 1 and 2, the duration and amount of water loss were very close between the profiles that all fall within Zone I. It must be noted that the evaporation rate reduction slope varied for different soil profiles, which was discussed thoroughly in the previous chapters.

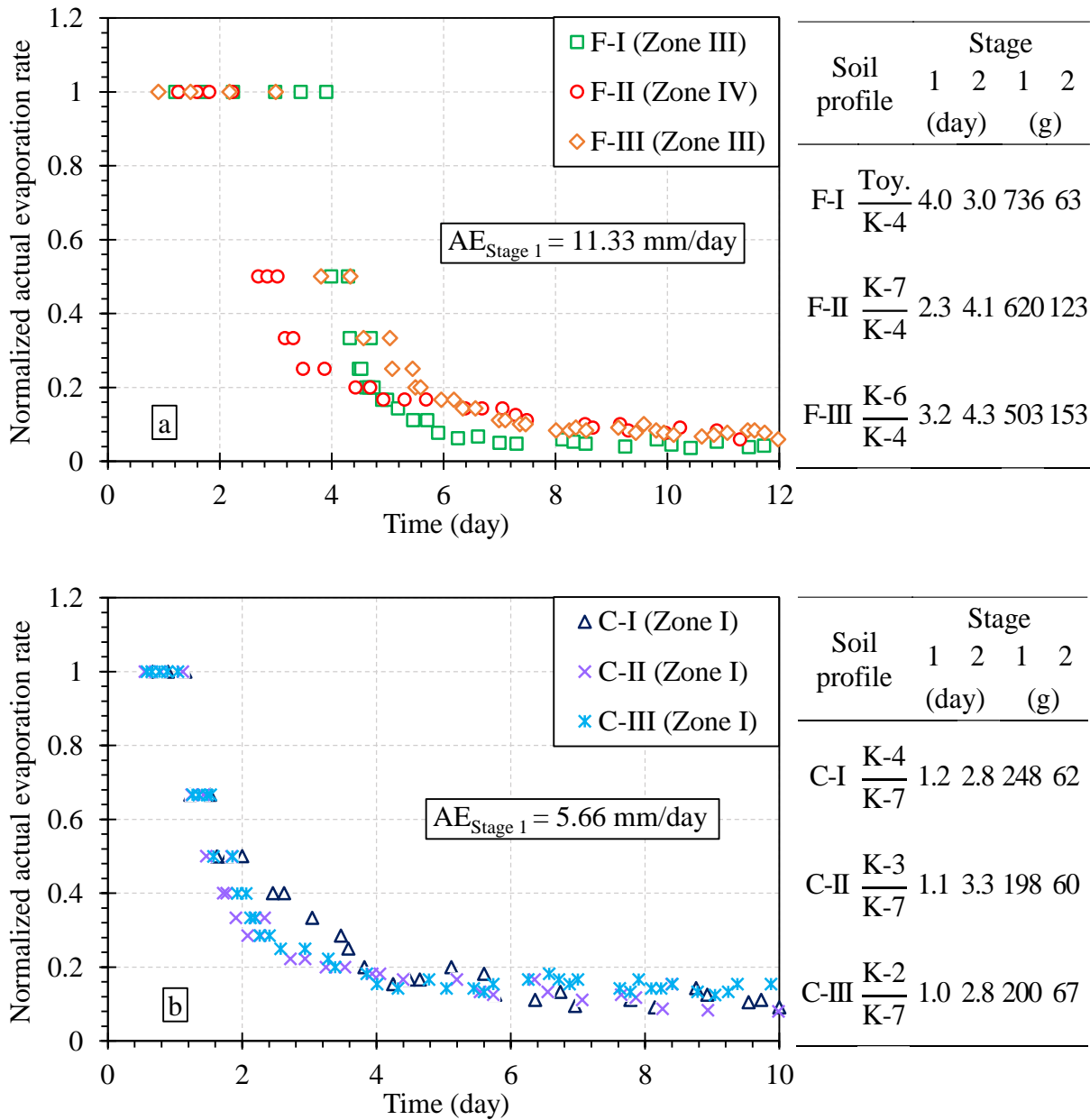


Figure 6.12: Normalized actual evaporation curves of the double-layered tested groups: a) fine-overlying-coarse. b) coarse-overlying-fine.

6.6.2 Soil cover and water redistribution

The water redistribution profiles for the tested double-layered soil profiles were determined using the data of the EC-5 moisture sensors. For that, six different times were selected during drying considering the duration of Stages 1 and 2. Chronologically, starting with the onset and middle of Stage 1, followed by the onset, middle, and end of Stage 2, and finally, 12 hours from the onset of Stage 3. In addition, to study the influence of the relative cover thickness, the

textural contrast boundary (Z_{Cover}) and composite characteristic length (L_{Comp}) were delineated with the horizontal dashed lines at each figure.

Figure 6.13 depicts the water redistribution profiles for the six tested soil profiles. It was confirmed that the columns achieved almost fully saturated conditions before starting the tests in all the tested profiles (Onset of Stage 1). During Stage 1 (red circle dashed lines), the soil cover exhibited a remarkable decrease in the degree of saturation for the coarse-overlying-fine group, while the degree of saturation decreased through the whole profile for the fine-overlying-coarse group, including the original ground. As the evaporation progresses, water continues to get lost from almost the same unsaturated layer during Stage 2 (Navy cross solid lines) in all the tested profiles. This behavior kept around 70% of the coarse-overlying-fine profiles saturated, while only 26% of the fine-overlying-coarse profiles saturated at the end of the process.

The drying front is defined as the boundary between the saturated and the unsaturated layers. In the coarse-overlying-fine group, the boundary is recognized around the textural boundary in all three samples. However, at the onset of Stage 2, the boundary was always deeper than the L_{Comp} , which, by definition, indicates the drying front at the end of Stage 1. This confirms well with the findings of Chapter 3: relying on the inflection points of the evaporation curve might not be a reliable practice since they indicate a change in the evaporation rate but do not necessarily represent the change in the transport mechanism between stages.

The behavior of the fine-overlying-coarse profiles was different from the coarse-overlying-fine profiles. The saturation of the original ground tends to be lower than the saturation of the soil cover. This result indicates the occurrence of the pumping phenomenon, where the water starts ejecting from the ground to the cover. The pumping phenomenon occurs when the L_{Comp} is deeper than the textural boundary. However, in F-I (Zone III) and F-III (Zone III), L_{Comp} is shallower than the textural boundary, yet the pumping phenomenon occurs. Therefore, for further investigations, the tested samples' suction profiles were extracted from the SWCCs, as delineated in Figure 6.14 for all the tested profiles. In the coarse-overlying-fine profiles, the suction head within the soil cover is relatively lower than the original ground, resulting in a head gradient towards the original ground. Consequently, the drying front is pinned at the textural contrast boundary, announcing Stage 3. On the other hand, for the fine-overlying-coarse profiles, the suction head within the soil cover is relatively higher than the bottom layer, resulting in an opposite head gradient towards the soil cover layer, thus ejecting water from the ground to the soil cover. This sufficient water supply to the soil surface results

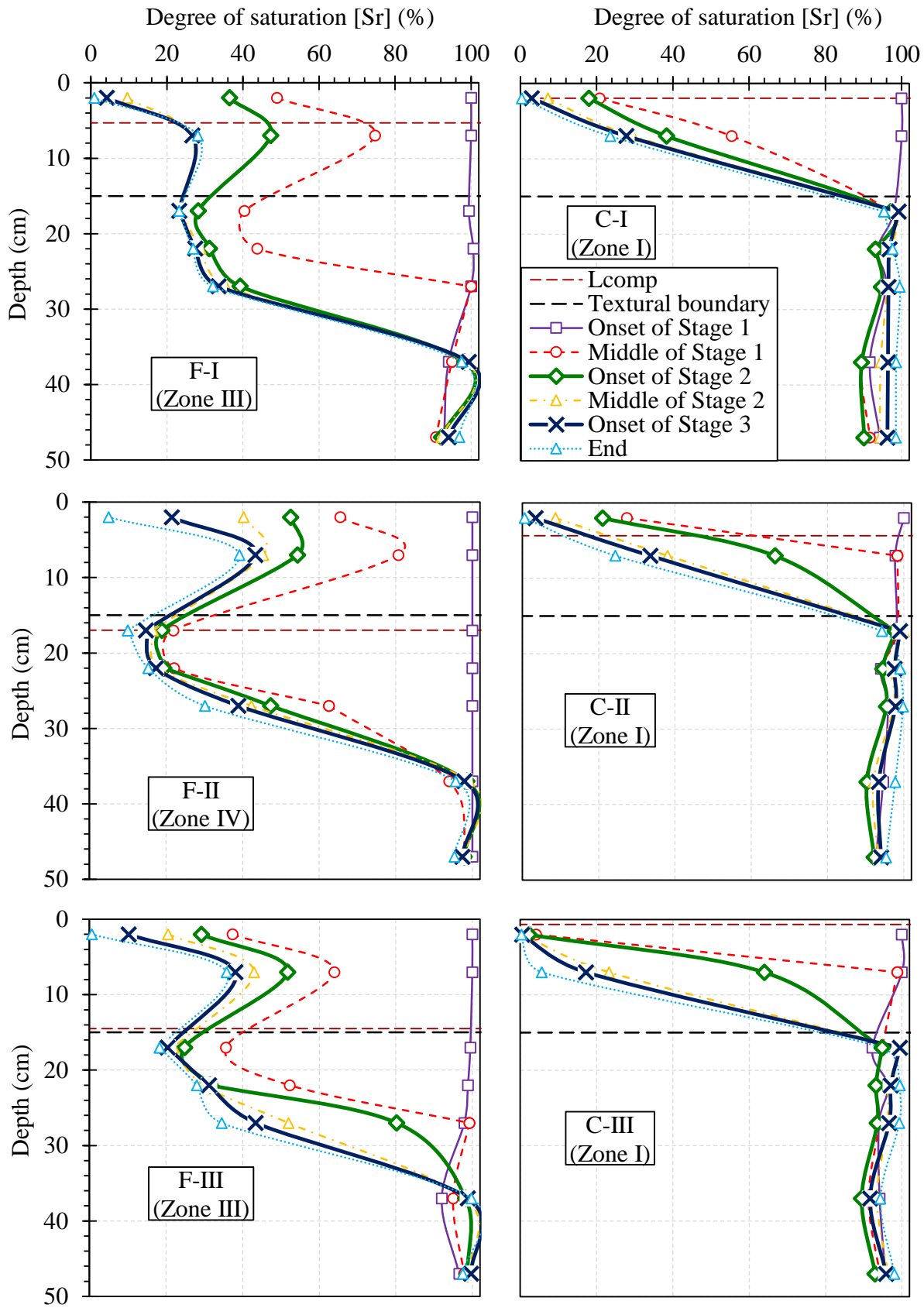


Figure 6.13: Water redistribution profiles of the double-layered tested groups during evaporation.

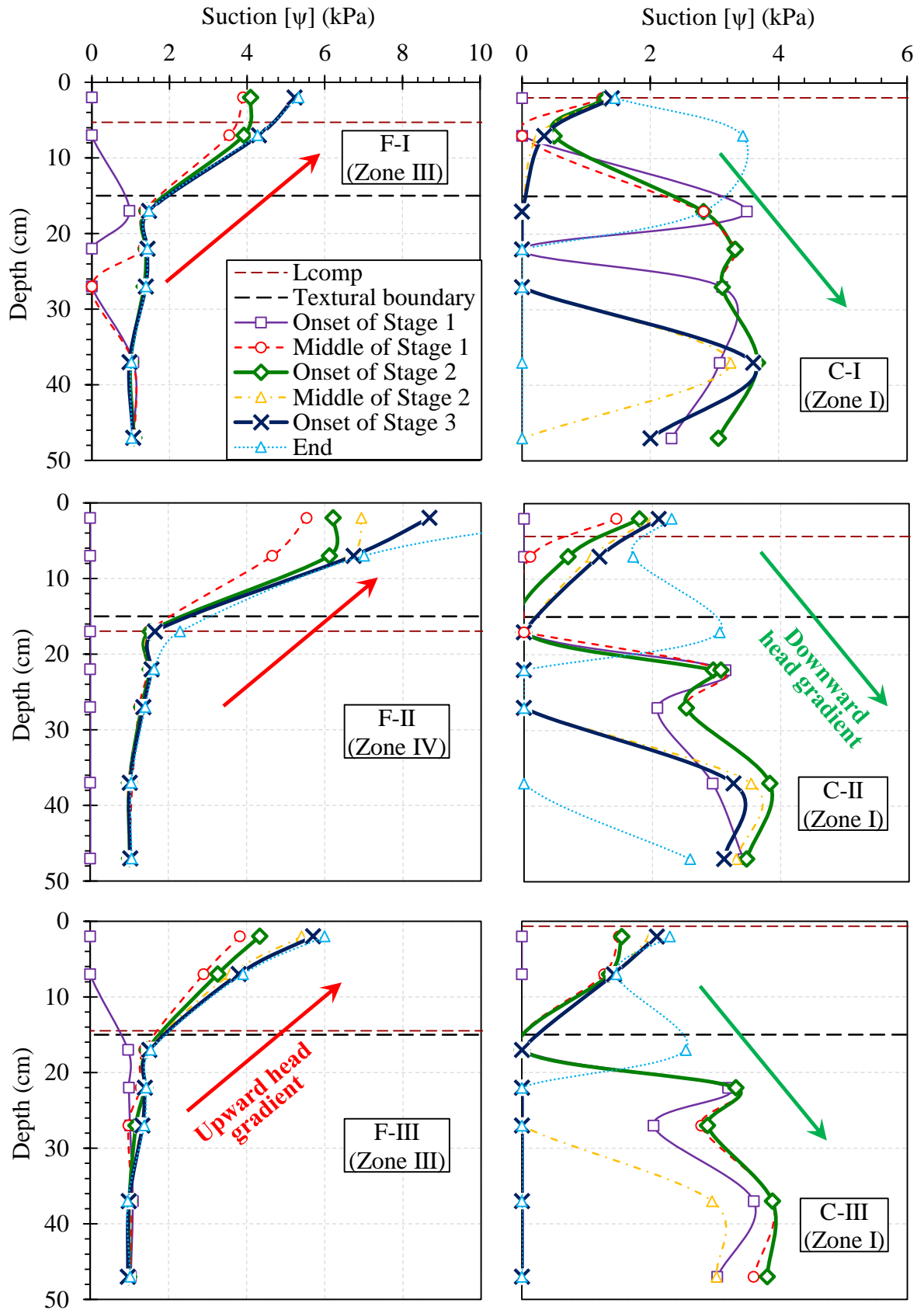


Figure 6.14: Suction profiles of the double-layered tested groups during evaporation.

in losing more water to evaporation. Therefore, in the F-I (Zone III) and F-III (Zone III) soil profiles, despite the shallow L_{Comp} , the head gradient played a significant role in intensifying the evaporation and water loss from the original ground. Therefore, it must be concluded that the relative retention properties between the soil cover and the original ground determine the orientation of the head gradient, which controls water supply in double-layered soil profiles. Consequently, such a micro-mechanism highly influences the macro-behavior of the evaporation flux in such complicated soil profiles.

6.6.3 Soil cover design concept and its efficiency

The efficiency of the soil cover design concept was studied by determining the soil cover capability of retaining water in its pores during drying. Therefore, the EC-5 sensors' readings were utilized to determine the water storage in the soil cover, original ground, and the entire profile. Figure 6.15 illustrates the tested soil profiles' water storage capabilities concerning the soil cover design concept and its zones. The empty scatter delineates the stored water in the entire profile, while the filled scatter indicates stored water in the original ground.

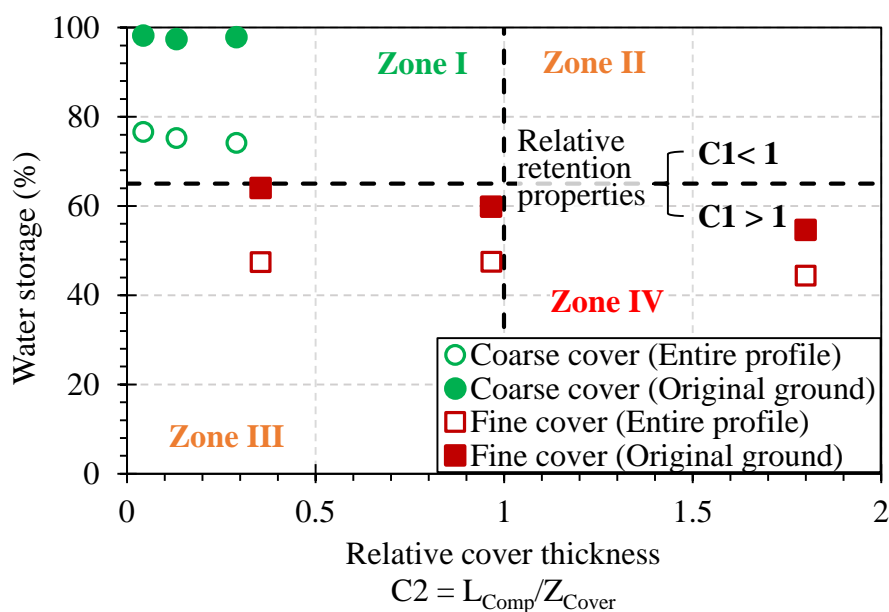


Figure 6.15: Efficiency of the proposed soil cover design concept.

It can be observed that Zone I soil profiles retained the highest amount of water among the other tested profiles. Moreover, the storage almost reaches 100% in the original ground, which indicates that most of the water is being lost from the cover rather than the soil ground. On the other hand, Zone III and IV soil profiles stored less than 60% of their soil profiles, with

Zone IV profiles storing the least amount of water. Further testing results are required to confirm the storage pattern of Zone II soil profiles. The difference between the water storage in the entire profile and the original ground tends to be smaller for the fine cover profiles (Zone III and IV), indicating that water was lost simultaneously from the cover and the original ground during drying.

Based on the experimental results, it must be concluded that the proposed soil cover design concept is reliable in predicting the water storage capabilities of a given double-layered soil profile. Additionally, it can be efficiently used to choose a suitable soil cover for an existing soil ground to suppress evaporation and increase water retention at a preferable degree.

6.7 Summary and conclusions

The following chapter proposes a novel design concept for a natural soil cover to suppress evaporation rates and increase water storage in natural soil profiles. The simple design concept is based on the micro-mechanisms and dynamics occurring during evaporation between the soil cover, natural ground, and the textural contrast boundary between them. It comprises two design criteria; the relative soil properties (C1) and the relative cover thickness (C2). C1 is deduced from the retention properties of both soils, while C2 considers the drying front during the sufficient capillary supply and its relation to the textural contrast boundary. It was found that the most effective design of the natural soil cover can be achieved by applying a proper cover material to the natural ground that keeps C1 and C2 smaller than 1. In such a case, a downward head gradient is triggered, causing a disruption in the upward water supply and thus reducing water losses. Moreover, the preferential pumping phenomenon from the original ground to the cover is eliminated, causing more water to retain within the original soil ground.

The proposed design concept is an economical and environmental-friendly solution to combat desertification in many arid and semi-arid regions and developing countries. It enables the utilization of the available soils in the field based on the relative properties of the cover and natural ground rather than the need for other ground materials, such as gravel, to suppress evaporation. The design concept is based on soil science, micro-scale mechanisms, and soil-water dynamics. However, it is simplified and requires simple soil properties that can be determined in any geotechnical laboratory.

Further considerations are required to ensure the applicability and sustainability of such soil covers in the field, including its geometry and resistance against wind erosion and soil

creep. Nevertheless, the proposed design concept is believed to be a fundamental and robust solution to combat desertification and recover degraded soils in many dry regions worldwide.

References

- Alowaisy, A.M., 2019. *Development of a Novel Evaluation Method for Water Movement and Retention Characteristics through Unsaturated Porous Mediums* (Doctoral thesis). Kyushu University.
- Alowaisy, A., Yasufuku, N., 2018. Characteristics of the second stage of evaporation and water redistribution through double layered sandy soil profiles. *Lowland Technology International* 20, 273–284.
- Alowaisy, A., Yasufuku, N., Ishikura, R., Hatakeyama, M., Kyono, S., 2020. Continuous pressurization method for a rapid determination of the soil water characteristics curve for remolded and undisturbed cohesionless soils. *Soils and Foundations* 60, 634–647. <https://doi.org/10.1016/j.sandf.2020.03.014>
- Assouline, S., Narkis, K., Gherabli, R., Lefort, P., Prat, M., 2014. Analysis of the impact of surface layer properties on evaporation from porous systems using column experiments and modified definition of characteristic length. *Water Resour Res* 50, 3933–3955. <https://doi.org/10.1002/2013WR014489>
- Benoit, G.R., Kirkham, D., 1963. The effect of soil surface conditions on evaporation of soil water. *Soil Science Society of America Journal* 27, 495–498.
- Corey, A.T., Kemper, W.D., 1968. *Conservation of soil water by gravel mulches*. (Doctoral thesis). Colorado State University. Libraries.
- Huang, M., Bruch, P.G., Barbour, S.L., 2013. Evaporation and Water Redistribution in Layered Unsaturated Soil Profiles. *Vadose Zone Journal* 12, vzj2012.0108. <https://doi.org/10.2136/vzj2012.0108>
- Kirkham, D., Rolston, D.E., Fritton, D.D., 1967. Gamma-radiation detection of water content in two-dimensional evaporation experiments, in: *Proceedings of Isotope and Radiation Techniques in Soil Physics and Irrigation Studies*. pp. 3–14.
- Lehmann, P., Assouline, S., Or, D., 2008. Characteristic lengths affecting evaporative drying of porous media. *Phys Rev E Stat Nonlin Soft Matter Phys* 77, 1–16. <https://doi.org/10.1103/PhysRevE.77.056309>
- Pillai, K.M., Prat, M., Marcoux, M., 2009. A study on slow evaporation of liquids in a dual-porosity porous medium using square network model. *Int J Heat Mass Transf* 52, 1643–1656.
- Sako, K., Kitamura, R., 2006. A Practical Numerical Model for Seepage Behavior of Unsaturated Soil. *Soils and Foundations* 46, 595–604.
- Shahraeeni, E., Lehmann, P., Or, D., 2012. Coupling of evaporative fluxes from drying porous surfaces with air boundary layer: Characteristics of evaporation from discrete pores. *Water Resour Res* 48, 1–15. <https://doi.org/10.1029/2012WR011857>
- Shokri, N., Lehmann, P., Or, D., 2010. Evaporation from layered porous media. *J Geophys Res Solid Earth* 115, 1–12. <https://doi.org/10.1029/2009JB006743>
- Unger, P.W., 1971. Soil profile gravel layers: I. Effect on water storage, distribution, and evaporation. *Soil Science Society of America Journal* 35, 631–634.
- Willis, W.O., 1960. Evaporation from layered soils in the presence of a water table. *Soil Science Society of America Journal* 24, 239–242.
- Yanful, E.K., Mousavi, S.M., Yang, M., 2003. Modeling and measurement of evaporation in moisture-retaining soil covers. *Advances in Environmental Research*. [https://doi.org/10.1016/S1093-0191\(02\)00053-9](https://doi.org/10.1016/S1093-0191(02)00053-9)

- Yang, M., Yanful, E.K., 2002. Water balance during evaporation and drainage in cover soils under different water table conditions. *Advances in Environmental Research* 6, 505–521. [https://doi.org/10.1016/S1093-0191\(01\)00077-6](https://doi.org/10.1016/S1093-0191(01)00077-6)
- Zhou, H., Li, S., Sun, S., Xu, X., Lei, J., Liu, S., Du, W., Yan, Z., Wang, Y., 2008. Effects of natural covers on soil evaporation of the shelterbelt along the Tarim Desert Highway. *Chinese Science Bulletin* 53, 137–145. <https://doi.org/10.1007/s11434-008-6016-1>

7

CHAPTER

Summary and conclusions

7.1 Research Achieved Objectives

Two main goals were defined for the current research work:

1. Investigating and evaluating the evaporation process from unsaturated soil profiles by tackling the evolving micro-mechanisms occurring at the soil pore level and reflecting them on the macroscale behavior of evaporation.
2. Developing natural soil covers to control and suppress evaporation from bare soil profiles in drylands as a step toward combating desertification.

Consequently, the objectives of the thesis, as stated in Chapter 1, were as follows:

1. To parameterize the soil pore structure through an experimental approach and investigate its influence on the evaporation behavior and the water transport mechanisms that vary between the evaporation stages.

2. To visualize the formation and development of the unsaturated soil layer and its boundaries during evaporation through an experimental approach and investigate their role in the process.
3. To formulate an empirical and theoretical framework to estimate the evaporation rate based on the soil pore structure parametrization and the visualization of the unsaturated layer dynamics.
4. To optimize a conceptual framework for a natural soil cover that suppresses evaporation and maximizes water retention in drylands by identifying the role of the relative soil properties between the natural ground and the applied soil cover.

The results of the conducted theoretical and laboratory research indicate that the objectives of the current research work were achieved. The objectives were satisfied respectively throughout the thesis. The pore structure was parameterized in a single, comprehensive, and robust index in Chapter 3. A new image-analysis-based technique was developed in Chapter 4 to trace the drying front and vaporization plane during evaporation stages and extract their dynamics. In Chapter 5, a comprehensive pore-scale-based actual evaporation estimation model was formulated from theoretical and empirical approaches. Finally, in Chapter 6, a new design concept for a natural soil cover was optimized to suppress water evaporation from soil profiles.

7.2 Conclusions

The current research studied the evaporation process from homogeneous and double-layered soil profiles. The theoretical, experimental, and image analysis results fulfilled the thesis objectives and proposed novel methods, techniques, and design concepts. The research outcomes are generally promising for water evaporation research, water movement and management, and unsaturated soil mechanics. Consequently, the specific conclusions of this thesis are summarized as follows:

1. A comprehensive and robust index that reflects the pore structure variations and considers the factors affecting the capillary and diffusion flow was proposed. The Pore Size Distribution Index (I_{PSD}) correlated well with the duration and evaporated water during Stages 1 and 2. Moreover, the influence of the pore structure was investigated where generally, it was found that sandy soils with larger I_{PSD} exhibit longer stages resulting in more water losses. The proposed index is systematically determined using only the soil retention properties, specifically the Soil Water Characteristics Curve (SWCC). The

proposed index was utilized to propose an actual evaporation estimation model. Moreover, it is expected to be a fundamental parameter in water movement and solute transport through unsaturated soil profiles.

2. Under low atmospheric demand, it was confirmed experimentally that Stage 2 comprises more than half of the evaporation process. Therefore, under severe dryland conditions characterized by hot and dry weather persisting for extended periods with high evaporation rates and seldom precipitation, Stage 2 is believed to be dominant and responsible for most of the water loss in the field.
3. A novel and effective image analysis-based technique was developed. The experimental technique is confirmed to be a reliable and definitive tool in tracing the development of the unsaturated layer during drying soil column tests. The setup included an image acquisition unit comprised of a digital camera and a lighting setup to capture high-quality images remotely. Additionally, two-reference soil columns are set up next to the primary tested soil column to calibrate the color changes in the primary column and allow the detection of the saturated, unsaturated, and dry zones within the profile. Finally, image processing operations are applied to accurately and directly detect the zones' boundaries, the drying front, and the vaporization plane.
4. The dynamics of the drying front, vaporization plane, and the film region, where capillary water flow is dominant, were studied, and new insights regarding their significant contribution to the evaporation process were concluded as follows:
 - a. The drying front tends to recede faster during Stage 1, with a slight reduction in its rate with each consecutive stage.
 - b. The unsaturated layer thickness is maintained during Stage 2, where water mainly gets lost from the smaller embedded pores rather than the large pores at the drying front, where water is lost gradually from the vaporization plane, causing an increase in the air-dry layer thickness and the length of the diffusion pathways to the surface.
 - c. The vaporization plane forms instantly at the onset of Stage 2, followed by a sudden increase in its depth at the onset of Stage 3, which explains the inflection points of the actual evaporation curve at the onset of Stages 2 and 3. The sharper reduction at the onset of Stage 2 is associated with the change of the mechanism from capillary during Stage 1 to vapor diffusion during Stage 2.
 - d. A strong correlation was found between the vaporization plane receding rate and the pore structure presented by the newly proposed I_{PSD} . Generally, soil profiles with a broader pore size distribution, characterized by bigger I_{PSD} , tend to have a slower

receding rate of the vaporization plane during Stage 2. Accordingly, a robust empirical formula was derived for homogenous sandy soil profiles under unified atmospheric conditions to predict the receding rate of the vaporization plane.

- e. The film region's thickness increases continuously during Stage 1, followed by a slight drop once reaching the characteristic length (L_C) associated with the onset of Stage 2. During Stage 2, the thickness slightly fluctuated until reaching a thickness equal to L_C , where a sudden and remarkable second drop in thickness occurred, believed to be the beginning of Stage 3, where the diffusion distance becomes limiting.
5. A semi-empirical actual evaporation rate estimation model from homogeneous soil profiles was proposed. The simple pore-scale-based estimation model is comprehensive and reliable in predicting the normalized actual evaporation rate. The model considers the evaporation process's internal and external influencing factors: the atmospheric demand and water supply capabilities. It solves Fick's law to determine the vapor diffusion flux through the air-dry layer by assuming that the evaporation occurs from a receding vaporization plane. Simultaneously, the receding rate of the vaporization plane is determined using the proposed empirical formula based on the I_{PSD} of the soil profile.
6. A novel design concept for an environmental-friendly natural soil cover was proposed to suppress evaporation rates and increase water storage in soil profiles. The simple concept considers the micro-mechanisms and dynamics occurring during evaporation between the soil cover, natural ground, and the textural contrast boundary between them. It comprises two design criteria; the relative soil properties (C1) and the relative cover thickness (C2). C1 is deduced from the retention properties of both soils, while C2 considers the drying front during the sufficient capillary supply and its relation to the textural contrast boundary. It was found that the most effective design of the natural soil cover can be achieved by applying a proper cover material over the natural ground that keeps C1 and C2 smaller than 1. The proposed design concept is a simple, economical, and environmental-friendly solution to combat desertification in many arid and semi-arid regions and developing countries.

7.3 Future Work

Although the objectives of this thesis have been achieved, further studies and research scopes are required to further improve the proposed methods and extend them to engineering practice. Some of the scopes and issues that require more investigation in the future are listed as follows:

1. The Pore Size Distribution Index (I_{PSD}) was confirmed reliable for sandy soils resistant to volume changes under variant moisture content. Therefore, considering the shrinkage and cracking effects are necessary to extend the I_{PSD} for cohesive and natural soils.
2. The robust empirical formula of the vaporization plane receding rate as a function of the I_{PSD} proved reliable for sandy soils under constant atmospheric conditions. However, more experimental results contribute to its improvement and extension to consider different types of soils. Moreover, the strong correlation between the vaporization plane dynamics and the I_{PSD} proposes a high possibility of formulating a theoretical framework for a more comprehensive and generalized formula.
3. The novel pore-scale-based estimation model predicts a bilinear normalized actual evaporation curve for sandy soil profiles. However, additional efforts to consider the sigmoidal shape of the evaporation curve are highly required for a more accurate prediction of the evaporation rate. Moreover, further research is necessary to validate the model's applicability in the field.
4. For broader research outcomes, experimental work for field testing utilizing the lysimeter is crucial to consider more realistic conditions where several boundary fluxes are active simultaneously. Additionally, a research scope that considers vegetation cover is highly required due to the significant influence of vegetation cover on evaporation behavior.
5. The simple design concept is robust in choosing a suitable material and thickness for the soil cover. Nevertheless, further considerations are required to ensure the applicability and sustainability of such soil covers in the field, including its geometry and resistance against wind erosion and soil creep.

Glossary and Parameter Notation

Notation	Meaning	Chapter
AE	Actual Evaporation (rate)	2, 3
AE _{Stage 1}	Actual evaporation rate attained during Stage 1	3, 6
AI	Aridity Index	1
AEV	Air-entry value	2, 6
BREB	Bowen Ratio Energy Balance	2
C	Coarse Soils	6
CBD	Convention on Biological Diversity	1
CCA	Climate Control Apparatus	3
CPM	Continuous Pressurization Method	3
CV	Coefficient of Variation	3
ET	Evapotranspiration	2
F	Fine soils	6
FOA	Food and Agriculture Organization	1
HCF	Hydraulic Conductivity Function	3, 4
I	Infiltration	2
IPCC	Intergovernmental Panel on Climate Change	1
IWMI	International Water Management Institute	1
JGS	Japanese Geotechnical Society standard	3

K	Kelvin	5
LND	Land Degradation Neutrality	1
MP	Mega Pixels	4
MSE	Mean Squared Error	5
NAE	Normalized actual evaporation rate	3, 6
NASA	National Aeronautics and Space Administration	1
NOAA	National Oceanic and Atmospheric Administration	1
NTP	Normal Temperature and Pressure	5
P	Precipitation	1, 2
PE	Potential Evaporation	2, 5
PET	Potential Evapotranspiration	1
PSD	Pore Size Distribution	3
R	Runoff	2
RGB	Red, Green, Blue	4
RMSE	Root Mean Squared Error	5
HSV	Hue, Saturation, Value	4
S	Sand	3
S-F	Sand with Fine fraction	3
S-layer	Saturation layer from the HSV color space	4
SWCC	Soil Water Characteristic Curve	3, 4, 6
T	Transpiration	2
TDR	Time Domain Reflectometry probes	2, 3, 5
UNCCD	United Nations Convention to Combat Desertification	1

UNFCCC	United Nations Framework Convention on Climate Change	1
USDA	United States Department of Agriculture	1
VG	Van Genuchten	3
WMO	World Meteorological Organization	1, 2
Q_H	Sensible heat flux	2
Q_E	Latent heat flux	2
q	Steady-state evaporation rate per unit of time	2
h	Pressure head	2
z	Gravitational head or the vertical distance from the water table	2
$K(\theta)$	Unsaturated hydraulic conductivity function	2, 3
θ	Volumetric water content	2, 3
H	Hydraulic head	2
ψ	Matric suction	2, 3
L_G	Gravity-limiting length	2
L_V	Viscous length	2
L_C	Characteristic length, Intrinsic characteristic lengths of a homogeneous soil profile	2, 3, 4, 5, 6
Θ	Normalized water content	2
θ_s	Saturated volumetric water content	2, 3, 4
θ_r	Residual volumetric water content	2, 3, 4
α	van Genuchten fitting parameter, inverse of the air-entry pressure	2, 3, 4
n	van Genuchten fitting parameter, function of the pore size distribution and reflects the slope of the SWCC	2, 3, 4
m	van Genuchten fitting parameter, symmetry of the SWCC sigmoidal curve shape	2

h_b	Capillary pressure equivalent to the air-entry value of the drying SWCC	2
h_r	Capillary pressure equivalent to the pressure at the residual water saturation of the SWCC	2
σ	Water-air surface tension	2
ρ	Water density	2
g	Gravitational acceleration	2
r_1	The smallest drainable pore	2
r_2	The largest drainable pore	2
Δh_{cap}	Capillary head difference	2
e_o	Evaporation rate	2
L_{Comp}	Composite characteristic length	2, 6
r_s	Surface resistance in the surface resistance model	2
r_a	Aerodynamic resistance in the surface resistance model	2
$q^*(T_s)$	Saturated specific humidity at T_s	2
T_s	Surface temperature in the surface resistance model	2
ρ_a	Air density	2
q_a	Relative humidity at a reference height in the atmosphere in the surface resistance model	2
α	Coefficient represents the relative humidity at the soil surface in the surface resistance model	2
θ	Surface volumetric water content in the surface resistance model	2
θ_{fc}	Field capacity or the volumetric water content in the surface resistance model	2
h_r	Relative humidity of the air adjacent to a flat free-water surface in the pore space in the surface resistance model	2
R	Gas constant for water vapor in the surface resistance model	2

β	Moisture availability parameter in the surface resistance model	2
r_{sw}	Resistance imposed on vapor flux while traveling from the pore of the wet soil layer to the bottom pores of the dry soil layer in the surface resistance model	2
r_d	Resistance imposed on vapor flux in the dry soil layer in the surface resistance model	2
h_a	Relative humidity of the air at a reference height in the atmosphere	2
T_a	Temperature of the air at a reference height in the atmosphere	2
$q_a^*(T_a)$	Saturated specific humidity at T_a	2
$q^*(T_e)$	Saturated specific humidity at T_e	2
T_e	Evaporative surface temperature	2
ΔNAE	Normalized actual evaporation reduction rate, Diffusion rate change	3
ΔAE	Actual evaporation reduction rate	3
G_s	Specific gravity	3, 4, 6
D_r	Relative Density	3, 4
D_{10}	Effective particle size	3, 4, 6
ρ_d	Dry density	3, 4, 6
e	Void ratio	3, 4, 6
ϕ	Porosity	3, 4, 5
k_s	Saturated hydraulic conductivity	3, 4
J	Fick's law diffusion rate	3
$\partial c / \partial L$	Concentration gradient with respect to the diffusion distance (Fick's law)	3
D	Water vapor diffusion coefficient or the diffusivity	3, 5
ΔVP	Receding rate of the diffusion distance or the vaporization plane	3

$\theta(\psi)$	Desorption path of the soil water characteristics curve, Drying SWCC	3
$\theta(d)$	Cumulative pore size distribution curve	3
d	Pore diameter	3
$f(d)$	pore size distribution curve	3
$u_a - u_w$	Matric suction	3
T_s	Water surface tension	3
α	Contact angle	3
PV	Pore volume per unit mass of solid	3
w_d	Gravimetric water content at a specific suction value	3
ρ_w	Water density	3
ΔPV	Incremental pore volume	3
PV_t	Total pore volume	3
λ	Mean of the lognormal distribution curve	3
ξ	Standard deviation of the lognormal distribution curve	3
μ	Mean value of the sample	3
σ	Standard deviation of the sample	3
logn	Lognormal distribution functions	3
d_2	The largest pore diameter	3
d_1	The smallest pore diameter	3
I_{PSD}	Pore size distribution index	3, 4, 5
$(\frac{1}{d_1} - \frac{1}{d_2})$	Width of the pore size distribution	3
∂C	Concentration gradient	5
$\Delta NAE/\Delta t$	Normalized actual evaporation reduction rate during Stage 2	5

A	Diffusion area	5
D_o	Free-air water vapor diffusion coefficient at specific temperature and pressure, Diffusion coefficient	5
b	Penman's constants for dry soils to determine D	5
m	Penman's constants for dry soils to determine D	5
$D_o(NTP)$	Diffusion coefficient at the Normal Temperature and Pressure (NTP)	5
T	Temperature	5
P	Pressure	5
T^0	Standard temperature	5
P^0	Standard pressure	5
n	Constant for the determination of the diffusion coefficient	5
C_{sat}	Water vapor density at the surface	5
C_v^*	Saturation vapor concentration at the soil surface	5
RH_{air}	Relative humidity of the ambient air 5 cm above the soil surface.	5
NAE_{S1}	Normalized actual evaporation rate during Stage 1	5
NAE_{S2}	Normalized actual evaporation reduction during Stage 2	5
VP	Vaporization depth reflects the diffusion distance to the soil surface	5
$(1/\Delta VP)/\Delta t$	Inverse of the vaporization plane receding rate with time during Stage 2	5
t_{S1}	End of Stage 1	5
$R_{E/E}$	Average ratio between the experimental and estimated values	5
$(\Delta NAE/\Delta t)_m$	Measured Reduction slope during Stage 2	5

$(\Delta NAE/\Delta t)_e$	Estimated Reduction slope during Stage 2	5
C1	Criterion one of the proposed soil cover design concept, Relative retention properties	6
C2	Criterion two of the proposed soil cover design concept, Relative cover thickness	6
Z_{cover}	Thickness of the soil cover	6
EC-5	Moisture sensors	6

